



# LES based aerothermal modeling of turbine blade cooling systems

Rémy Fransen

## ► To cite this version:

Rémy Fransen. LES based aerothermal modeling of turbine blade cooling systems. Fluid Dynamics [physics.flu-dyn]. Institut National Polytechnique de Toulouse - INPT, 2013. English. NNT: . tel-00870685v1

**HAL Id: tel-00870685**

**<https://theses.hal.science/tel-00870685v1>**

Submitted on 7 Oct 2013 (v1), last revised 15 Nov 2023 (v2)

**HAL** is a multi-disciplinary open access archive for the deposit and dissemination of scientific research documents, whether they are published or not. The documents may come from teaching and research institutions in France or abroad, or from public or private research centers.

L'archive ouverte pluridisciplinaire **HAL**, est destinée au dépôt et à la diffusion de documents scientifiques de niveau recherche, publiés ou non, émanant des établissements d'enseignement et de recherche français ou étrangers, des laboratoires publics ou privés.



# THESE

En vue de l'obtention du

## DOCTORAT DE L'UNIVERSITÉ DE TOULOUSE

Délivré par *Institut National Polytechnique de Toulouse*  
Discipline ou spécialité : *Dynamique des Fluides*

---

Présentée et soutenue par *Rémy Fransen*  
Le 13 Juin 2013

*LES based aerothermal modeling of turbine blade cooling systems*

---

### JURY

*Pierre Sagaut* Rapporteur  
*Laurent-Emmanuel Brizzi* Rapporteur  
*Eric Lamballais* Examineur  
*Emmanuel Laroche* Examineur  
*Pierre Ginibre* Invité  
*Laurence Vial* Invité  
*Laurent Gicquel* Directeur de thèse  
*Tony Arts* Codirecteur de thèse

---

Ecole doctorale : *Mécanique, Energétique, Génie civil, Procédés*

Unité de recherche : *CERFACS*

Directeur de Thèse : *Laurent Gicquel*

Co-Directeur de Thèse : *Tony Arts*

Encadrants industriels : *Laurence Vial et Gontran Martineau*





# Acknowledgments

Cette thèse CIFRE a été rendue possible grâce à la collaboration bénéfique de l'entreprise Safran Turbomeca avec le CERFACS et l'Institut von Karman, et je tiens à remercier chacun de ses membres qui y ont contribué.

Avant tout, je tiens à remercier sincèrement les membres du Jury qui ont accepté de lire et de juger mon travail. Merci donc à Laurent-Emmanuel Brizzi et Pierre Sa-gaut, qui m'ont fait part de leurs critiques, questions et remarques sur l'ensemble de mes travaux. Eric Lamballais, Emmanuel Laroche et Pierre Ginibre ont également participé à la discussion qui a contribué à élargir un peu plus ma vision et mes idées sur ces trois ans (et quelques) de thèse.

Au CERFACS, dans lequel j'ai passé la plus grande partie de mon temps durant ces trois ans, je ne peux d'abord penser qu'à mon directeur de thèse, Laurent Gicquel. Pendant une thèse on avance, on se trompe de chemin, on redémarre et de temps en temps on fait un grand bon en avant, autant sur le papier que dans la tête. A chaque fois je crois bien que tu y étais pour quelque chose, alors merci Laurent ! Un merci aussi aux différents seniors du CERFACS pour les discussions, en particulier Nicolas Gourdain, Florent Duchaine et Olivier Vermorel, conseillers respectifs informels en turbomachines, thermique et AVBP. Enfin, pour bien huiler l'ensemble, comment ne pas citer CSG pour le côté technique, une équipe efficace de support que j'aimerais pouvoir remmener avec moi, et pour le côté administratif, Chantal, Michelle, Marie et Nicole, qui mériteraient leur sigle aussi (le C2MN ?) pour leur bonne humeur et enthousiasme contagieux !

Mon passage au VKI m'a permis de rencontrer et de profiter de l'expérience de Tony Arts, avec qui j'ai pu approcher le monde expérimental dont mon clavier aurait pu avoir tendance à m'éloigner... Merci Tony, Filippo et les stagiaires de m'avoir montré comment assembler des vis, des lasers et de l'huile pour faire de belles images PIV !

Enfin, du côté de Turbomeca, un merci à Lonrenzo Pons et Laurence Vial sans qui cette thèse n'aurait jamais vu le jour. Grâce à vous j'ai pu me frotter au monde de l'entreprise à Bordes, où j'y ai rencontré d'autres collègues aussi compétents que chaleureux. Fred, Gontran, Yohan, Guilhem et tous les autres... Merci pour l'accueil et le bon esprit qui y régnait !

Je me dois également de remercier les responsables de l'ambiance qui règne au CERFACS... Au risque de m'attirer les représailles de la "communauté du café", je ne peux évidemment pas oublier les anciens, Pierre, Thomas, David, Pablo, P'tit Ju, et les "moins anciens" Abdula, Pierre, Laure, Thomas, ainsi que ceux de passage...

Merci pour toutes ces mémorables pauses où chocolats, fruits et autres touillettes ont subi la dure loi de la communauté... Parmi les thésards plus "pacifistes", je salue entre autres Greg, Basti, Geof et Mario compagnons de foot ou de sodexo nocturne... Elena, Anne et Élodie, merci de m'avoir laissé m'incruster à vos pauses gâteau, et Elena, re-merci pour ma nouvelle LV3! Ahora hablo un poco español tambien!

Les amis à l'extérieur, reconnaissables au fait qu'ils préfèrent voir des "ribs" dans leur assiette que tournant dans une turbine... Les ensmatiques et autres, éparpillés en France et ailleurs, merci pour le soutien et désolé d'avoir eu droit aux tarifs étudiants 3 ans de plus... Merci aussi aux toulousains pour les moments de décompression, et en particulier aux ludiens jamais en manque d'énergie!

Enfin, ma famille Champardennaise, qui m'a laissé cette petite marque qui contraste beaucoup ici dans le sud-ouest lorsqu'on parle du ui-end... Merci de m'avoir soutenu et encouragé quand j'en avais besoin!

Merci à toutes et à tous!

# Preamble

The aim of this thesis conducted for the Safran Turbomeca company was to study numerical cooling flows on both academical and real industrial configurations. To satisfy a non-disclosure agreement, several manuscript versions have been produced describing either both configurations or only the academic cases. The present version is the open version where all the industrial data have been removed. You may however note that some references still remain within the text (especially in introducing and concluding parts).



# Contents

<b>1</b>	<b>Introduction</b>	<b>1</b>
	Context . . . . .	1
	Objectives . . . . .	4
	Plan of the manuscript . . . . .	5
<b>2</b>	<b>Turbine blade cooling: state-of-the-art and technology</b>	<b>7</b>
2.1	Turbine cooling requirements . . . . .	7
2.2	Turbine cooling technology . . . . .	9
2.2.1	External cooling . . . . .	9
2.2.2	Internal cooling . . . . .	11
2.2.3	Cooling technology combination . . . . .	12
2.3	Ribbed Channels based internal cooling . . . . .	13
2.3.1	Ribbed channel controlling parameters . . . . .	13
2.3.2	Ribbed channels in rotation . . . . .	15
2.3.3	Realistic ribbed channels . . . . .	16
2.4	CFD of cooling channel . . . . .	16
2.4.1	Aerothermal computations . . . . .	17
2.4.2	Conjugate heat transfer . . . . .	19
2.5	Conclusions . . . . .	22
<b>3</b>	<b>Internal cooling LES in non-rotating configurations</b>	<b>23</b>
3.1	Internal cooling flow physics . . . . .	24
3.1.1	Non-dimensional approach . . . . .	24
3.1.2	General description of turbulent flows . . . . .	28
3.1.3	Turbulence Modeling . . . . .	31
3.1.4	Modeling cost . . . . .	33
3.2	Turbulent flows in a realistic cooling channels . . . . .	37
3.2.1	Smooth U-bend . . . . .	38
3.2.2	Ribbed channel . . . . .	39
3.2.3	Objectives of the following LES test . . . . .	42
3.3	LES numerical requirements for the VKI static cases . . . . .	43
3.3.1	U-bend computational domain . . . . .	43
3.3.2	Ribbed channel computational domain . . . . .	44
3.3.3	Periodic case numerical procedure . . . . .	45
3.3.4	Spatial case boundary conditions . . . . .	46
3.3.5	Domain discretization . . . . .	46
3.4	U-bend case . . . . .	47
3.4.1	Sensitivity to the upstream flow conditions . . . . .	48
3.4.2	Comparison with the state of the art . . . . .	49
3.4.3	Conclusion on the U-bend analysis . . . . .	51

3.5	Ribbed channel case . . . . .	52
3.5.1	Parametric analysis of the periodic LES . . . . .	52
3.5.2	Comparison with the industrial state of the art . . . . .	63
3.5.3	Spatial LES . . . . .	65
3.5.4	Heat transfer in the ribbed channel . . . . .	67
3.6	Conclusions . . . . .	71
<b>4</b>	<b>Internal cooling LES in rotating configurations</b>	<b>73</b>
4.1	Physics and modeling of rotating flows . . . . .	74
4.1.1	General transformation . . . . .	75
4.1.2	Governing equations in rotating frames . . . . .	76
4.1.3	Rotation and shear . . . . .	79
4.2	Simulation of rotating channels with AVBP: method and sensitivity	82
4.2.1	Modeling of rotating flows . . . . .	83
4.2.2	Numerical method in AVBP . . . . .	83
4.2.3	Validation test cases . . . . .	84
4.2.4	Conclusion . . . . .	86
4.3	Experimental rotating test bench . . . . .	86
4.4	Application of the rotating numerical methodology to the experimen- tal ribbed channel . . . . .	88
4.4.1	Domain and boundary conditions . . . . .	88
4.4.2	Expected flow topology . . . . .	89
4.4.3	Sensitivity analysis . . . . .	90
4.4.4	Results and interpretations . . . . .	90
4.4.5	Conclusion . . . . .	93
4.5	LES of the VKI isothermal rotating ribbed channel: validation against experiment . . . . .	93
4.5.1	Mean effects of rotation on the near wall flow topology . . . . .	94
4.5.2	Effect of rotation on the flow field around the ribs . . . . .	98
4.5.3	Two-point correlations . . . . .	103
4.5.4	Temporal vortex tracking . . . . .	105
4.5.5	Conclusions on LES of rotating isothermal flows . . . . .	111
4.6	LES of the VKI anisothermal rotating ribbed channel: validation against experiment . . . . .	112
4.6.1	Mean temperature in the channel . . . . .	113
4.6.2	Flow field around the ribs . . . . .	115
4.6.3	Heat transfer at the ribbed wall . . . . .	116
4.6.4	Conclusions on the anisothermal study . . . . .	120
4.7	Conclusions on LES of rotating cooling channels . . . . .	120
<b>5</b>	<b>General conclusion and future works</b>	<b>123</b>

---

<b>Appendices</b>	<b>128</b>
<b>A RANS and LES modeling details</b>	<b>131</b>
A.1 Physics and modeling of turbulent flows . . . . .	131
A.2 RANS . . . . .	133
A.3 LES . . . . .	134
<b>B AVBP solver presentation</b>	<b>137</b>
<b>C Periodicity of compressible flow in a ribbed channel</b>	<b>139</b>
<b>D Comparison of LES simulations on full-tetra meshes with PIV mea-     surement</b>	<b>141</b>
<b>Bibliography</b>	<b>151</b>
<b>Publications</b>	<b>163</b>





# Nomenclature

## Latin characters

$\mathcal{R}$	Inertial frame of reference	
$\mathcal{R}^*$	Non-inertial frame of reference	
$\mathbf{S}$	Strain rate tensor . . . . .	$[\text{s}^{-1}]$
$\mathbf{f}$	Body forces vector . . . . .	$[\text{N/kg}]$
$\mathbf{Q}$	Rotation matrix . . . . .	$[-]$
$\mathbf{u}$	Velocity vector . . . . .	$[\text{m/s}]$
$D_h$	Hydraulic diameter . . . . .	$[\text{m}]$
$E$	Specific total energy . . . . .	$[\text{J/kg}]$
$g$	Gravitational acceleration . . . . .	$[\text{m/s}^2]$
$h$	Ribs height . . . . .	$[\text{m}]$
$h_c$	Convective heat transfer coefficient . . . . .	$[\text{W}/(\text{m}^2 \cdot \text{K})]$
$h_r$	Radiative heat transfer coefficient . . . . .	$[\text{W}/(\text{m}^2 \cdot \text{K})]$
$p$	Pressure . . . . .	$[\text{Pa}]$
$q$	Heat flux . . . . .	$[\text{W}/\text{m}^2]$
$T$	Temperature . . . . .	$[\text{K}]$
$t$	Time . . . . .	$[\text{s}]$
$U$	Velocity magnitude . . . . .	$[\text{m/s}]$
$u, v, w$	3D velocity components . . . . .	$[\text{m/s}]$
$u_\tau$	Wall friction velocity . . . . .	$[\text{m/s}]$
$x, y, z$	Space coordinates . . . . .	$[\text{m}]$

## Greek characters

$\alpha$	Fluid thermal diffusivity	
$\delta_{ij}$	Kronecker delta . . . . .	$[-]$
$\lambda$	Thermal conductivity . . . . .	$[\text{W}/(\text{m} \cdot \text{K})]$
$\mu$	Dynamic viscosity . . . . .	$[\text{kg}/(\text{m} \cdot \text{s})]$
$\nu$	Kinematic viscosity . . . . .	$[\text{m}^2/\text{s}]$
$\Omega$	Rotation rate . . . . .	$[\text{s}^{-1}]$
$\rho$	Density . . . . .	$[\text{kg}/\text{m}^3]$
$\tau_w$	Wall shear stress . . . . .	$[\text{N}/\text{m}^2]$

$\tau$  Viscous stress tensor . . . . . [N/m<sup>2</sup>]

### Subscripts and superscripts

$(-)^{\prime}$  Superscript for fluctuating quantities  
 $(-)^{+}$  Superscript for quantities written in wall units  
 $(-)_b$  Subscript for bulk quantities  
 $(-)_w$  Subscript for wall quantities  
 $(-)_{SGS}, (-)_t$  Modeled quantities  
 $(-)^{*}$  Dimensionless quantities  
 $(-)_i$   $i^{th}$  tensor or vector component  
 $\overline{(-)}$  Reynolds averaged quantities  
 $\widetilde{(-)}$  Resolved (Favre averaged or filtered) quantities

### Dimensionless numbers

$Bo$  Buoyancy number  
 $Nu$  Nusselt number  
 $Pr$  Prandtl number  
 $Re$  Reynolds number  
 $Ri$  Richardson number  
 $Ro$  Rotation number

### Acronyms

2D/3D Two/three dimensional  
 CHT Conjugate Heat Transfer  
 DNS Direct Numerical Simulation  
 EF Enhancement Factor  
 LE Leading Edge  
 LES Large Eddy Simulation  
 NS Navier Stokes  
 PIV Particle Image Velocimetry  
 RANS Reynold Average Navier Stokes  
 RSM Reynolds Stress Model  
 SGS Sub-Grid Scale  
 TE Trailing Edge  
 TI Turbulent Intensity  
 TKE Turbulent Kinetic Energy

# Introduction

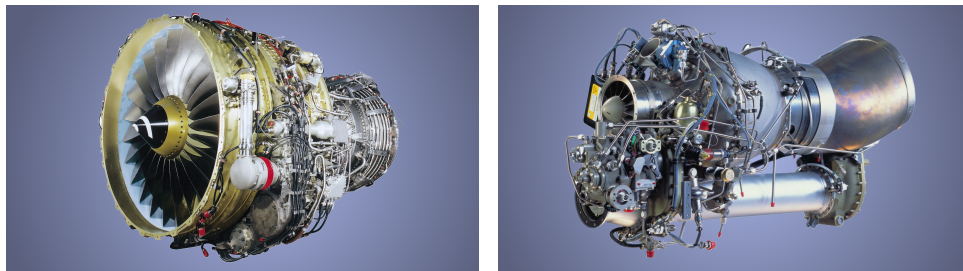
---

## Context

### Aeronautical requirements

From the first mythical attempt to reach the sky with wings made of wax and feathers to our current world traveling cargo aircraft, human has always tried to improve his air mastery. In order to meet this dream, a long technical and innovative travel has been made to propel us further, faster and longer: from the highly trained athletic human able to provide up to 400 W [70] to the world record of thrust generation by the GE90 jet engine with 565 kN [47], and a power around 65 MW on a Boeing 777 at maximum cruise speed. Today this search for thrust and performance still continues: aircraft engine design has become the aim of a highly specialized industry which tries to increase engine power output while adapting its development cycle to current economic and environmental constraints: see for example recommendations from the European Economic and Social Committee on the European aeronautics industry [40] or the European aeronautical research program Clean Sky [21].

There are two main types of powerful engines with high power-to-weight ratio. Depending on the type of application or work needed to drive the aircraft: i.e. pure thrust for turbojets or turbofans and torque for turboprops or turboshafts, two architectures are possible, Fig. 1.1. These two designs are composed of the same following main parts: an air intake, a compressor, a combustor, a turbine and a nozzle.



(a) Jet engine : CFM56

(b) Turboshaft : Safran Turbomeca Arriel

Figure 1.1: Example of the two types of aeronautical gas turbine.

These parts are shown in Fig. 1.2 with the corresponding numbers: the air intake (1) is designed to provide an air mass flow at proper conditions for the compressor

(2) to increase the air pressure prior to the combustion. The compressor can be divided into several axial or centrifugal stages, driven by the turbine via a shaft running through the engine. The high pressure air is then mixed with fuel in the combustor (3) and burns to increase the gas mixture temperature. Finally, the hot gases expand in the nozzle guide vane and a part of the flow energy is extracted by the turbine stages (4) to power the compressor. In a turboshaft, most of the flow energy is converted into mechanical energy on a shaft in the subsequent turbine stages, whereas in a jet engine the hot gases are accelerated in a nozzle (5) to create thrust.

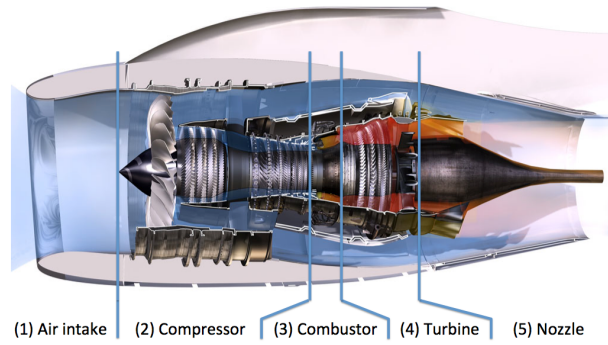


Figure 1.2: View of the different parts of an aeronautical engine (here a jet engine)

The working principle of these engine relies on the Brayton thermodynamic cycle presented in Fig. 1.3. In an ideal cycle, compression of fresh air (1-2) and expansion of burnt hot gases (3-4) are assumed to be isentropic, while the combustion of the fuel-air mixture (2-3) and the gas exhaust to the atmosphere (4-1) are considered isobaric processes.

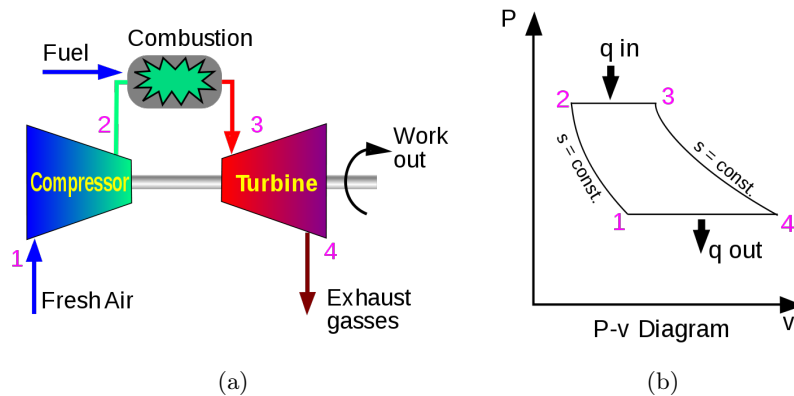


Figure 1.3: Gas turbine working principle: simplified scheme (a) and ideal Brayton cycle (b)

Output power increase and improved efficiency of aeronautical engines can be obtained by increasing the pressure ratio in the compressor and by an increase of the turbine inlet temperature. This is confirmed by the performance map of Fig. 1.4 extracted from Boyce's handbook [10] for the simple gas turbine cycle of Fig. 1.3a. Focusing on the turbine, a rise in temperature however imposes new constraints on the design of this component since the blade material melting point is already often well surpassed in existing modern gas turbine. The life duration of the turbine can therefore be greatly reduced if new protection systems are not developed to ensure the blade integrity over a reasonable time duration. The study and modeling of such systems, namely the air internal blade strategy is the point of interest of this thesis.

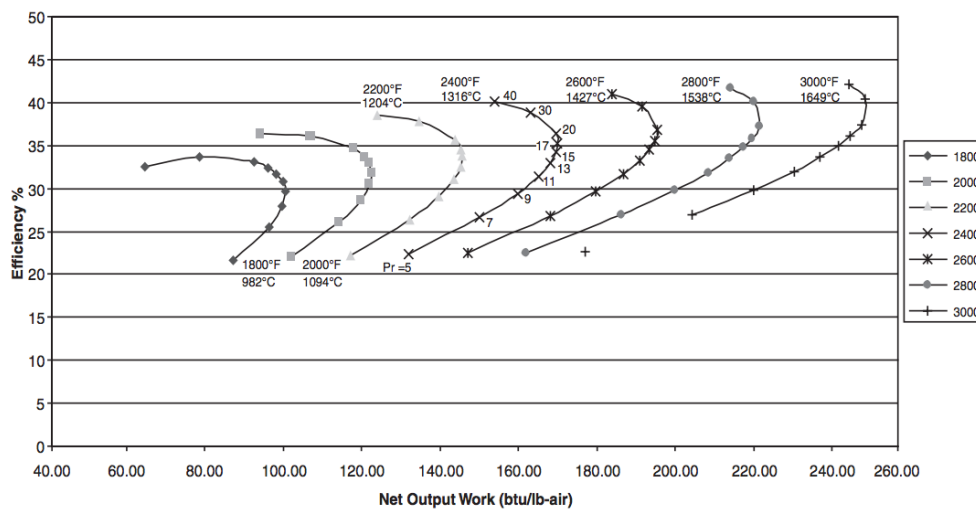


Figure 1.4: Performance map of a single cycle gas turbine [10]: efficiency and net output work are plotted against turbine inlet temperature (isolines) and compressor pressure ratio (measured values correspond to the symbols on isolines).

Internal cooling systems will be detailed in a next chapter, but an example of such a cooling design is presented in Fig. 1.5. The main principle relies on the extraction of a small portion of the compressor output fresh air. This air then by-passes the combustor and is reintroduced at the turbine stage where it flows inside the blades through especially designed cooling passages. Finally, the air is re-injected in the vein main flow through holes on the blade surface to create film cooling effect and protect it from hot burnt gases.

## Computational tools

Emergence and evolution of computer science has developed fluid flow modeling eminently. First used in the 1930s to solve the two-dimensional linearized Navier-Stokes (NS) equations (Euler equations) for a flow around a cylinder by Thom [129], the so-called Computational Fluid Dynamics (CFD) numerical codes are now able to

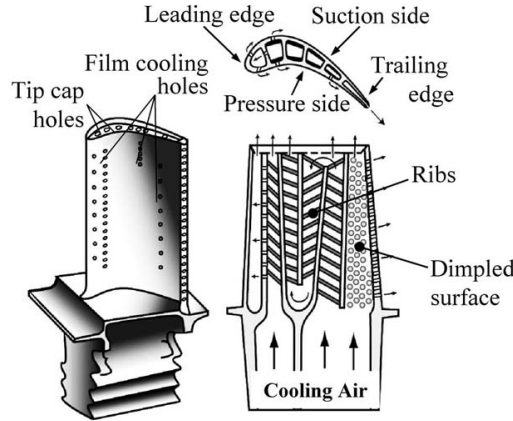


Figure 1.5: Example of turbine blade cooling system with internal passages with turbulence promoters and holes on the surface for film cooling (image from Murata Lab. website, Tokyo University of A&T)

model three-dimensional full NS equations for complex industrial flows, like among many others, the case of interest of this thesis: flows in aeronautical gas turbines.

Today, three main methods are available to compute such industrial turbulent flows: Reynolds-Averaged-Navier-Stokes (RANS), Large Eddy Simulation (LES) and Direct Numerical Simulation (DNS) (see Pope's description [102]). They are presented here in terms of increasing predictive capability, but also of increasing computational cost. Because of its low computational cost RANS remains the most frequently used CFD model by industry, while LES and DNS are essentially reserved to academic research. But thanks to the exponential development of the High Performance Computing (HPC), see Fig. 1.6, LES becomes more affordable to the industry and its contributions on flow comprehension can be now assessed, as detailed by Tucker [132].

## Objectives

In this specific framework of aeronautical demand for engine improvements and tremendous development of HPC abilities, Safran Turbomeca has launched several research and development projects [137, 26] to analyze and quantify the impact of a wider use of LES modeling for engine flow predictions. Indeed, while LES has already proved its potential for highly unsteady combustion flow computations in real gas turbine combustion chambers [85, 123], its application to turbine flows is only beginning. This thesis focuses more specifically on the prediction and understanding of the aerothermal modeling of turbine blade internal cooling systems. The study is thus devised in multiple steps linked to the modeling and flow characteristics of such systems. These are summarized in the three following points:

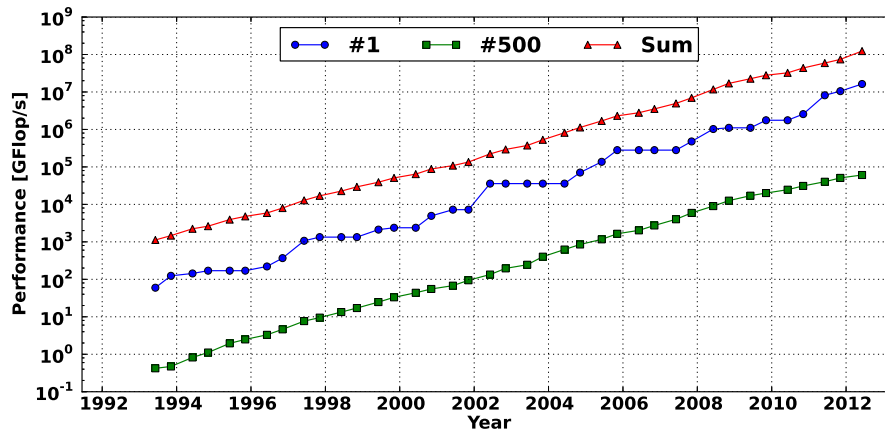


Figure 1.6: Exponential performance development of the supercomputer top500 ranking [130].

- Characterization, validation and analysis of a numerical strategy to realize aerothermal LES of highly turbulent wall bounded rotating flows through the assessment of LES in simplified typical cooling channel configurations.
- Application of this methodology to a realistic turbine blade cooling system in engine operating conditions.
- Compare LES predictions of academical and industrial configurations with the regular tool used in the research department of Safran Turbomeca, i.e. the RANS modeling approach.

## Organization of the manuscript

To achieve the previously defined objectives of this PhD dissertation, multiple subjects and developments have been investigated. This manuscript recapitulates these steps and is organized as follows:

- In **Chapter 2**, a state-of-the-art of turbine cooling systems is presented and previous reference works on the typical configurations studied in this thesis are recalled.
- In **Chapter 3**, physics of turbine blade cooling, fundamentals of fluid mechanics and turbulence modeling are first recalled. Two stationary static flow configurations, a straight ribbed channel and a smooth U-bend, are then computed with LES. Descriptions, validations and comparisons with measurements and RANS results are proposed. LES numerical parameters such as mesh resolution, cell topology or inflow specifications (turbulence injection) are evaluated. Detailed aerodynamical and thermal analyses of these unsteady predictions are finally performed.



- In **Chapter 4**, the ribbed channel is set in rotation: physics changes and the corresponding modeling are presented and discussed. Results of clock-wise and anticlock-wise wall-normal rotating computations are detailed and a numerical sensitivity assessment is proposed. Note that a validation of these LES results is also provided thanks to measurements obtained on an experimental test bench using time resolved Particle Image Velocimetry (PIV). Change of heat transfer performances caused by the flow modifications are analyzed.
- In **Chapter 5**, *not present in this manuscript version*, the industrial cooling channel is investigated with LES based on the previous physical analysis and developed methodologies. Flow descriptions and conjugate heat transfer computations are given with comparison of predictions obtained with the Safran Turbomeca in-house tools.
- Finally, **conclusions** are drawn on the introduced methodology and on the assessment of the LES for internal cooling flow simulation. **Perspectives** are also proposed in the form of areas for improvement and further investigations.

# Turbine blade cooling: state-of-the-art and technology

---

## Contents

---

<b>2.1</b>	<b>Turbine cooling requirements</b>	<b>7</b>
<b>2.2</b>	<b>Turbine cooling technology</b>	<b>9</b>
2.2.1	External cooling	9
2.2.2	Internal cooling	11
2.2.3	Cooling technology combination	12
<b>2.3</b>	<b>Ribbed Channels based internal cooling</b>	<b>13</b>
2.3.1	Ribbed channel controlling parameters	13
2.3.2	Ribbed channels in rotation	15
2.3.3	Realistic ribbed channels	16
<b>2.4</b>	<b>CFD of cooling channel</b>	<b>16</b>
2.4.1	Aerothermal computations	17
2.4.2	Conjugate heat transfer	19
<b>2.5</b>	<b>Conclusions</b>	<b>22</b>

---

The introduction has pointed the interest and need of the industrial LES modeling for turbine blade internal cooling design and validation. To fully understand the possible issues raised in the introduction, it is necessary to understand the industrial requirements and what are the current technologies present today. Therefore, this chapter provides first an overview of the turbine cooling technology through its needs and the currently available answers. CFD modeling of such devices is then addressed giving the current state-of-the-art of internal cooling flow simulations as well as the Conjugate Heat Transfer (CHT) approach proposed today.

## 2.1 Turbine cooling requirements

As presented in the introduction, internal cooling of turbine blade has become an indispensable requirement for modern gas turbines to meet the increasing power demand, also synonym of higher gas temperature in the turbine which may surpass the material melting point. Cooling systems are already present in gas turbines for all static parts but its extension to rotating turbine blades is a task which has

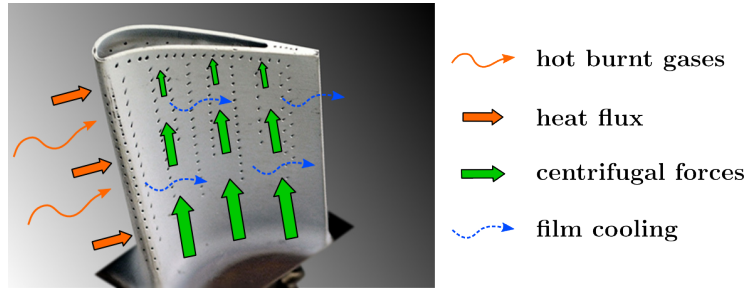


Figure 2.1: Physical environment of a working turbine blade with major physical phenomenon.

to fit in the entire turbine design process in a more complex equilibrium than for the static parts. Figure 2.1 summarizes the environment of a cooled turbine blade with high temperature coming from the combustor and the strong mechanical stress induced by the rotation. To guarantee the blade resistance to this medium, turbine blade internal cooling design is mandatory although a tricky process in which a compromise has to be found between multiple physical parameters. Figure 2.2 illustrates this problematic comparing the designer to a juggler who has to care about all the aforementioned constraints.

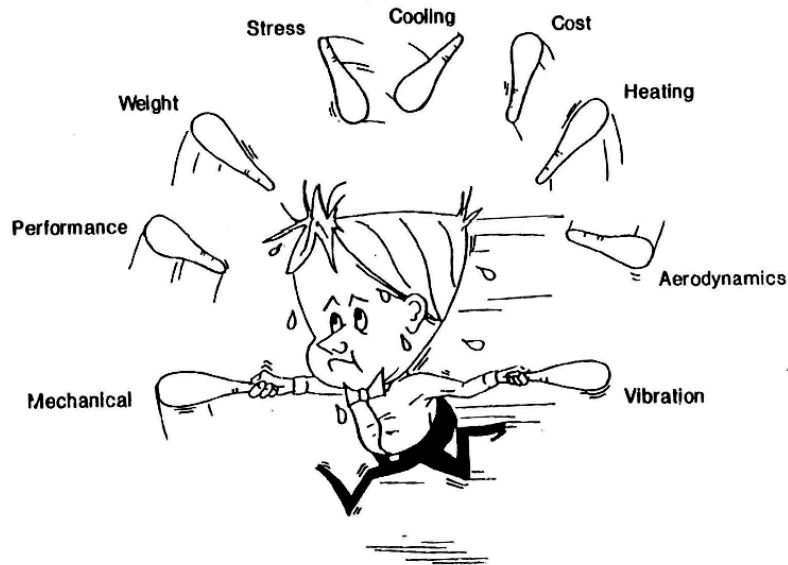


Figure 2.2: The technical "juggling" problem of the turbine blade cooling system designer [60].

The determining consequence of all this parametric choice is finally the blade life duration, and bad parameters may lead to premature failures. Table 2.1 describes the four main blade turbine failures and their temperature dependency following Ireland [60]. The result shows actually the influence of small metal temperature

differences on the blade lifetime which may be halved with some dozen degrees higher temperatures. However, Ireland also notes, using an uncertainty analysis, that the state-of-the art industrial tools is not able today to achieve the required accuracy for proper lifetime prediction (his computation leads to a temperature uncertainty of 35 °C to 80 °C). If prediction improvements are of great interest, Ireland also concludes that internal heat transfer predictions would require an accuracy of about  $\pm 2\%$  when current CFD solution typically reaches  $\pm 20\%$ .

Table 2.1: Four main turbine blade failures and their temperature dependency [60].

Mechanism	Metal temperature change to double/halve life
Creep	15 °C
Corrosion	20 °C
Low cycle fatigue	30 °C
High cycle fatigue (vibrations)	Not primarily temperature driven

## 2.2 Turbine cooling technology

The lack of blade metal temperature prediction accuracy pointed out in the previous section has not prevented the blade technology development and a increased resistance to the always increasing turbine inlet temperature. Turbine blade improvements have relied on two main strategies: enhancements in material characteristics and cooling systems. The former was the first to be developed, while the latter has appeared in the 1960's [42]. Figure 2.3 presents the performance gain (linked to the turbine inlet temperature) evolution thanks to the combined use of both improved technologies. As already presented, the present study only focuses on cooling systems, but the reader interested in the mechanical aspects may look at other recent Safran Turbomeca modeling works by Ghighi [48]. Note also that Fig. 2.3 gives an idea of the potential room for improvement indicating the approximate stoichiometric temperature of the fuel in comparison to the operating turbine inlet temperature.

To describe now the different cooling systems available today on most engines, we consider the common blade construction pattern, Fig. 2.4. The starting point consists in a blade root with an inlet channel feeding the blade airfoil cooling system(s) with a relatively cold air extracted from the compressor. This cold air then flows through one or several cooling channels, to finally exhausts in the turbine main vein. Two types of cooling can be used depending on whether the coolant air flow interacts primarily with the *external* or *internal* faces of the blade.

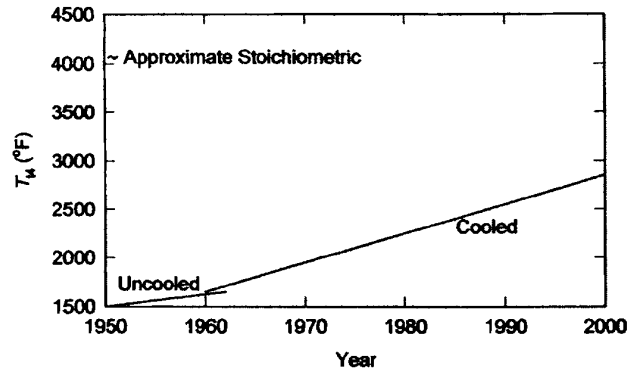


Figure 2.3: History of the turbine inlet temperature [42].

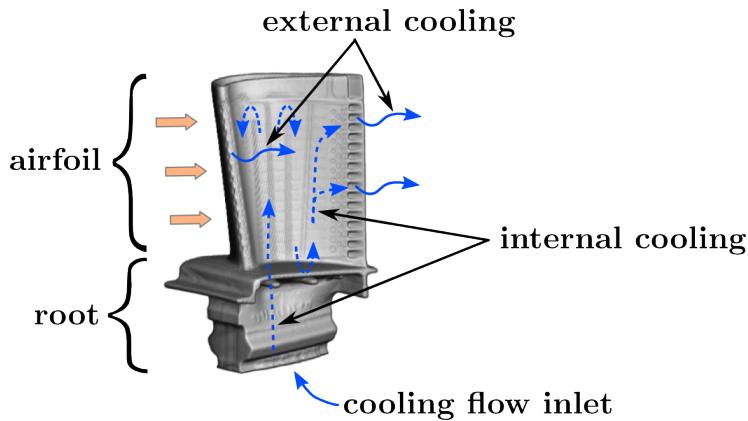


Figure 2.4: Cooling flow in a turbine blade. Internal serpentine channels are visible by transparency.

### 2.2.1 External cooling

The aim of external cooling is the protection of the external blade surfaces exposed to hot combustion gases [54]. Two techniques may be used: film cooling and transpiration cooling, which is actually a generalized form of the former. Following the general description of Goldstein [50], *film cooling is the introduction of a secondary fluid (coolant or injected fluid) at one or more discrete locations along a surface exposed to a high temperature environment to protect that surface not only in the immediate region of injection, but also in the downstream region*. In the application, film cooling consists in ejecting cold air from the internal cooling system through small holes on the blade airfoil. Despite the principle simplicity, the technology faces a large amount of parameters which may depend for example on the flow properties, the injection geometry, the wall properties... Details on these effects can be found in Han [54].

As already pointed out, transpiration cooling may be considered as a generalized film cooling: instead of discrete cold air release locations, the entire blade walls (or only areas) releases cold air continuously through the surface. This can be made

possible thanks to naturally porous material, or using an in-wall small channel network, as presented for example in Fig.2.5. Transpiration offers a more uniform blade protection coverage than film cooling. It also yields additional cooling in the course of the fluid passing through the wall of the body thereby absorbing a part of its internal energy.

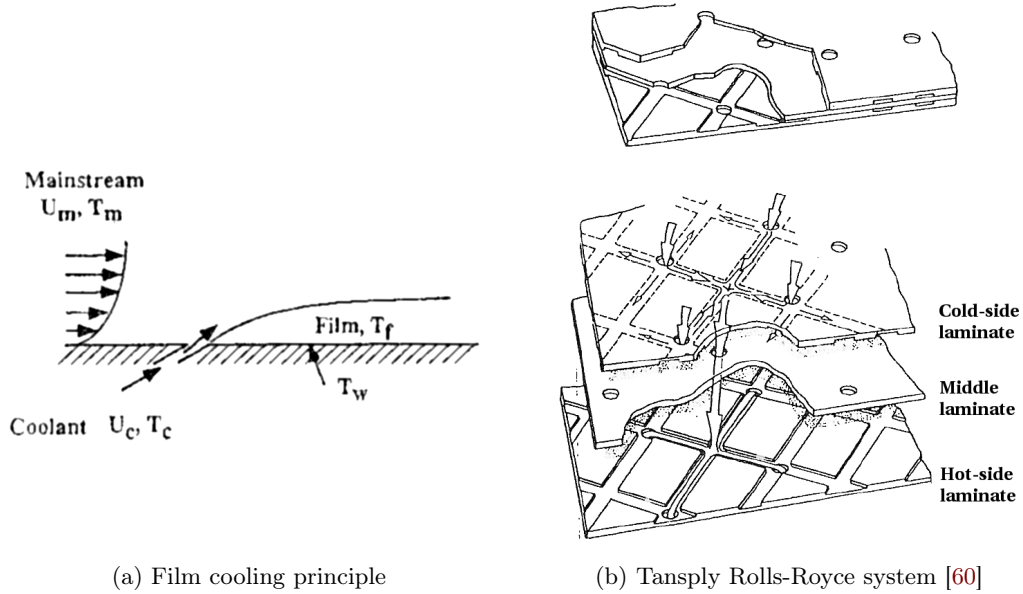


Figure 2.5: External cooling example

### 2.2.2 Internal cooling

Internal cooling consists mainly in using convective heat transfer in internal channels to extract heat from the blade metallic wall to cool it down. To do so, more or less complex channels are hollowed out of the blade metal. Internal designs may therefore go from simple radial straight smooth channels extending from the hub to the tip, to long serpentine channels with turbulence promoters. A large panel of internal convective cooling systems has been developed since the first smooth channels in the 1960's to improve heat exchanges. A list of the available designs may be the following: surface roughness, rib arrays, jet impingement, dimples, pin fins and swirl chambers (listed with corresponding references in Table 2.2).

The main principles on which these systems are based are the augmentation of exchange surface through flow turbulence increase. A lot of different arrangements are possible and they may be classified following the heat transfer increase in comparison to a similar smooth channel without any cooling enhancement system. To be able to take into account any geometry, this parameter is commonly define as the ratio of the cooling system Nusselt number  $Nu$  to the smooth channel Nusselt number  $Nu_0$ . As the main objective of blade cooling, heat transfer maximization

Table 2.2: Advantages and drawbacks of the common blade internal cooling systems

System	Pros	Cons
rough surface [135]	low weight, low pressure drop	low heat transfer rate
dimples [1]	low weight, low pressure drop	low heat transfer rate, better than rough surface
pin fins [78]	reduce temperature between faces	not self-supporting in high rotation rate
impingement [136]	localized high heat transfer	decreased efficiency with cross-flow, dirt blockage
ribs [53]	high heat transfer rate	high pressure loss
swirl chamber [55]	good heat transfer/pressure loss ratio, low weight	

while minimizing the pressure drop penalties, the cooling systems may also be classified following ratio comparing modified channel friction factors  $f$  to smooth channel friction factors  $f_0$ . Very early on Webb [135] has for example proposed a parameter to quantify the efficiency of roughness elements taking into account both pressure drop and heat transfer and known as thermal performance  $\eta$ :

$$\eta = \frac{Nu/Nu_0}{(f/f_0)^{1/3}} \quad (2.1)$$

Figure 2.6 proposed by Ligrani [83] presents the thermal performances showing the wide disparity between all the different cooling systems. A short review of the advantages and the drawbacks of each of solutions taken from [60, 83, 54] is also provided in Table 2.2. Naturally the perfect cooling design offering the best thermal performance does not exist yet and blade designers have to adapt their choices following the specific engine characteristics and geometrical requirements.

### 2.2.3 Cooling technology combination

All the above internal and external cooling technologies are usually mixed together to improve the heat transfer efficiency. A lot of examples are available as patented arrangement. An actual example may be the blade of Kercher [68] using an internal serpentine smooth channel with transpiration stripes. One can also present the overall cooling effectiveness  $\varphi$  of a cooling system. By definition, this parameter is a dimensionless temperature ratio of gas-to-metal temperature difference over the gas-to-inlet-coolant temperature difference:

$$\varphi = \frac{T_{gas} - T_{metal}}{T_{gas} - T_{c,in}} \quad (2.2)$$

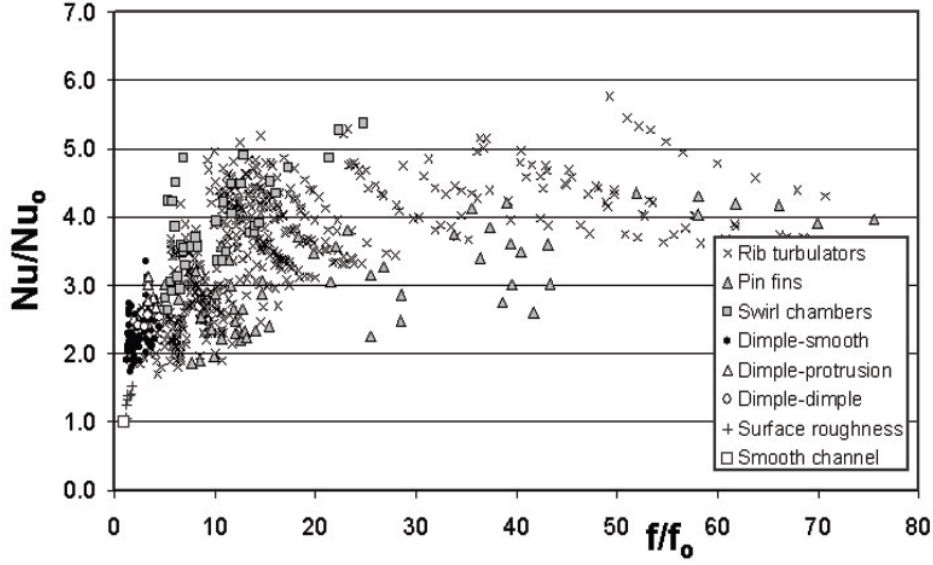


Figure 2.6: Comparison of relative performance of different internal cooling systems. Globally-averaged Nusselt number ratios are presented as in function of channel friction factor ratios [83].

with  $\varphi = 0$  being the worst case when the metal has the same temperature as the hot gases, and  $\varphi = 1$  the ideal case when the metal has the same temperature as the coolant. Figure 2.7 gives a summary in a graph by comparing some technological arrangements from the low efficiency radial convective internal cooling to the highly efficient transpiration cooling approach.

## 2.3 Ribbed Channels based internal cooling

In the application case of this thesis, only internal cooling is studied. Works of Collado [26] may provide more information on external heat transfer predictions. Focusing on the internal cooling system of the studied turbine blade shows that it has been designed mainly with ribbed cooling channels. There have been a lot of studies addressing the heat transfer performance of ribbed channels. This first subsection presents therefore a general description of the main influent heat transfer parameters for static cases, while the second extends it for rotating cases. For a complete review of this specific cooling system (among the others), Han [54] may be greatly recommended.

### 2.3.1 Ribbed channel controlling parameters

For heat transfer efficiency, Han [54] has identified major dependencies from the following three parameters of ribbed channels: the channel Aspect Ratio (AR, width to height ratio), the rib configuration and the flow Reynolds number  $Re$ . Mainly



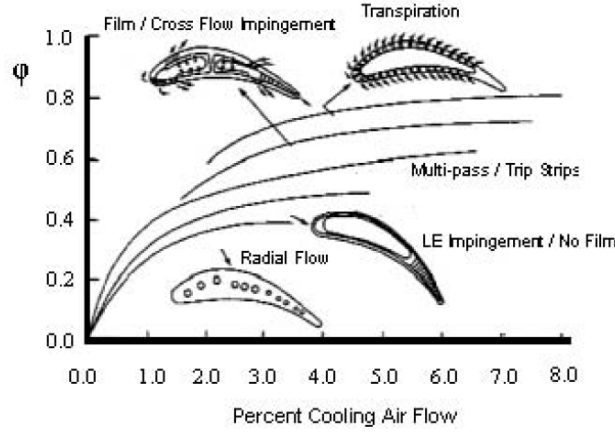


Figure 2.7: Cooling effectiveness illustration for different modes of cooling [91].

geometrical parameters are detailed here, but flow dependency may be summarized by a slightly decreasing heat transfer with increasing  $Re$  (with  $10^4 < Re < 10^5$  for typical applications).

The main physical phenomenon desired using ribs is the turbulence generation thanks to the creation of a separated flow. Figure 2.8 depicts this behavior with the commonly studied main features characterizing a rib arrangement: rib height  $e$ , pitch  $p$  and angle of attack  $\alpha$ . Additional parameters are the rib cross-section (may be square, triangular, semicircular, trapezoidal; with sharp or round corners) and whether the ribs are continuous or broken for example. Concerning the channel where the ribs are placed, some parameters of importance are the cross section (often rectangular but may be triangular considering the blade leading edge cooling channel), the AR (square or rectangular with very flattened forms/shapes), the number of ribbed walls and the relative rib pattern along the wall (symmetric or staggered).

Among all these characteristics, the most commonly accepted for good heat transfer performance referring to a simple static channels is a rib height to channel hydraulic diameter ratio of around 0.1 and a pitch around 10. Angled ribs with  $\alpha = 45^\circ \sim 60^\circ$  have also shown good heat transfer efficiency with relatively lower pressure losses if compared to  $\alpha = 90^\circ$  ribs. Performance of the  $60^\circ$  arrangement may reach an averaged  $Nu/Nu_0$  up to 3 with a  $f/f_0$  ratio equal to 5 [97]

### 2.3.2 Ribbed channels in rotation

The study of rotor blade cooling introduces additional physical effects that need to be considered and in comparison to the stator blades for which previous observations were more dedicated. The primary changes caused by rotation can significantly modify the coolant flow in internal channels. Rotating channel experimental observations have been early obtained (see for example the work of Johnston [65] in 1972 on developed 2D rotating channel flow) and more recently with the study of

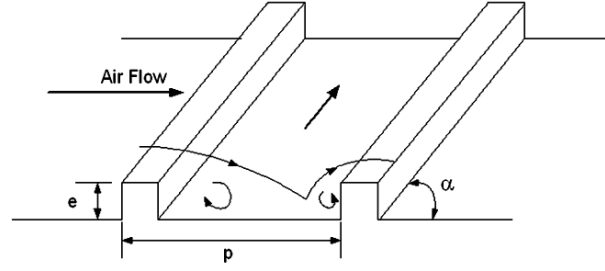
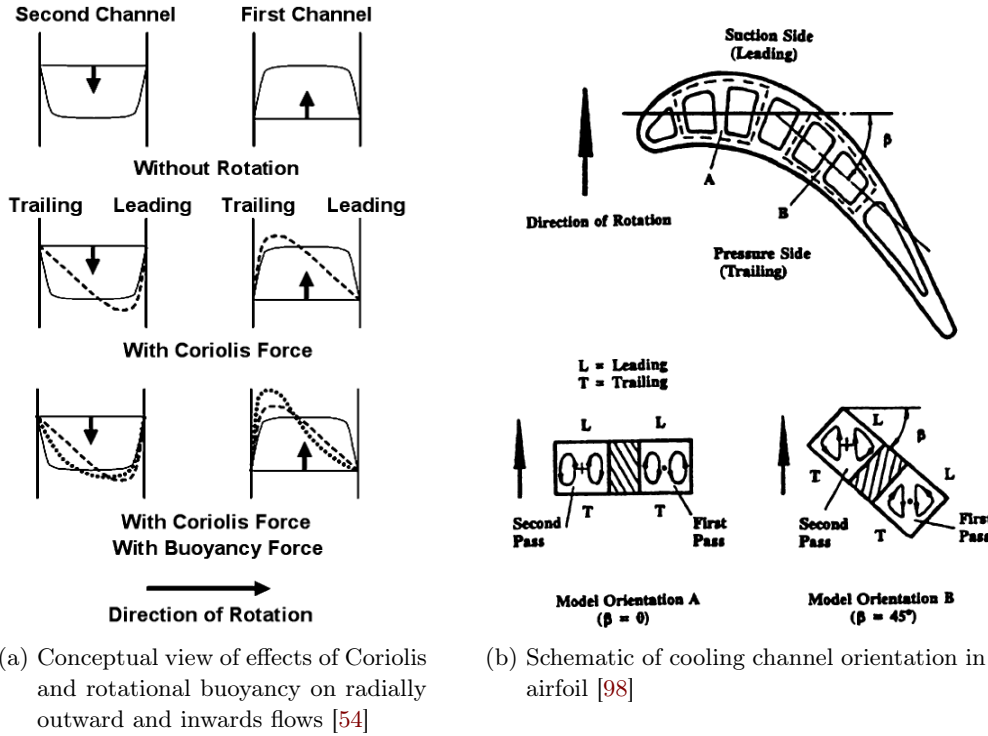


Figure 2.8: Schematic of flow separation from ribs and secondary flow between angled ribs in a rib-turbulated cooling channel [53].

Chang [18] in 2012 with 2D heat transfer detailed measurements in rotating ribbed channels. Following the nomenclature proposed by Wu [138] rotation will mostly refer in this document to a *wall-normal* rotation. Streamwise channel rotation will not be addressed here, while spanwise rotation may be similar to the wall-normal rotation considering finite AR channels. Therefore, in the considered rotation framework, non-inertial forces will redistribute the velocity, altering its fluctuations and generating streamwise large secondary flows. It results a channel flow with a symmetry loss and the appearance of a destabilized side and a stabilized side, where turbulence levels is increased and decreased respectively. These effects depend on the rotation rate, which is characterized by the rotation number  $Ro$ :  $Ro = 0$  for no rotation and increases with the rotation speed (further details are given in the next chapter).

Influence of the rotation induced forces may first be observed in smooth channels to understand how they affect the flow. Figure 2.9a shows velocity profiles in rotating channels with radially outwards and inwards flows to be compared to a non rotating channels. First, Coriolis forces alone induce asymmetric velocity profiles depending on the radial flow direction. Then, buoyancy forces being always radially outward reinforce or damp the asymmetry when the flow has the same or opposite direction respectively. Figure 2.9b gives an example of the streamwise secondary flow which may be observed in a curved turbine blade and for which different channel orientation  $\beta$  with respect to the rotation axis appear. In this square cross section channel configuration, two counter rotating cells are detected with their center being aligned and parallel to the rotation axis. When  $\beta$  is modified, both vortices may not be heated by the same walls: in addition to one side wall, both leading and trailing walls for  $\beta = 0^\circ$  and either leading or trailing for  $\beta = 45^\circ$  for example. Such changes may hence generate higher temperature differences when the walls are not uniformly heated [98].

All the cooling parameters presented for the static cases can be extended to the rotating context. In the specific case of ribbed channels and following the recent work of Coletti [24], rotation visibly alters the turbulence generation following the stabilized / destabilized principle. Moreover, the flow topology may also be strongly impacted by the buoyancy forces. The main effect is visible on a stabilized heated



(a) Conceptual view of effects of Coriolis and rotational buoyancy on radially outward and inwards flows [54] (b) Schematic of cooling channel orientation in an airfoil [98]

Figure 2.9: Influence of rotation on turbine blade internal cooling channel flows.

ribbed wall where the recirculation bubbles generated behind the ribs can grow until taking all the space between two consecutive ribs. Since the core flow does not more reattach, heat transfer is reduced compared to the corresponding static case. One can also note that when buoyancy is further increased, heat transfer surprisingly re-increases, while the recirculation bubble thickness becomes larger than the rib height. An explanation for this phenomenon provided computationally by Sewall [116] will be detailed in the next section.

### 2.3.3 Realistic ribbed channels

The aforementioned works and the majority of the studies addressing ribbed channels investigates simple geometries with often fully developed flow. However, in realistic turbine blades the cooling channels have to be adapted to the airfoil profile leading to non uniform channel shapes where the flow may never really reach a developed state. A recent study by Leblanc [81] has presented detailed heat transfer measurements in a realistic cooling serpentine passage. It is shown that thermal correlations obtained in simple geometries over-predict the cooling performance in comparison to the experimental observations in the complex channel. This result provides insight into using correlations developed for simplified geometries and idealistic flow conditions to predict heat transfer for more realistic geometries.

## 2.4 CFD of cooling channel

Convective heat transfer in channel flows has been widely studied and offers a large amount of theories and computation. In this section and following the focus of this chapter, we only address the presentation of turbine blade internal cooling results and more specifically ribbed channels. Aerothermal investigations are first presented comparing turbulence modeling and numerical approaches. Then, extensions to CHT computation are addressed.

### 2.4.1 Aerothermal computations

In industrial applications, RANS is the dominant form of turbulence modeling. Many industrial applications however evidence the limitation of the RANS approach, and DES as well as LES computations provide viable alternatives [28]. The two following subsections give examples of computations using RANS, LES and DNS along with the conclusions issued by these works.

#### RANS

RANS of cooling channels are numerous and some recent studies describe different behaviors depending on the RANS model. For eddy viscosity modeling, Iacovides [58] concludes in his study of a ribbed channel with a U-bend that it is necessary to use low- $Re$  closures for heat transfer. Ooi [95] compares three eddy viscosity models ( $k - \varepsilon$ ,  $v2 - f$ , Spalart-Allmaras ) and finds that even if in a 2D ribbed channel  $v2 - f$  yields results in good agreement with experimental data, in a 3D case none of the tested models is able to predict the secondary flows leading to inaccurate heat transfer results (especially on the side walls). The same kind of conclusions is drawn by Phibel [99] for cooling channels with high blockage ratios. For modeling, the last authors point out the anisotropy assumption that is no more valid in ribbed channels and the unsteady nature of the large separated flow generated by the ribs.

Following these remarks, the use of more advanced RANS modeling like Reynolds Stress Model (RSM) [77] yields satisfactory results. Sleiti [117] performs a RANS computation with a RSM model providing good thermal predictions in a rotating two-pass ribbed channel with a U-bend. To capture the unsteadiness, one can note the work of Saha [111] who compares ribbed channels with different AR (1:4, 1:1, 4:1) in rotating cases using an unsteady RANS approach. He reports that AR has a strong influence on Coriolis induced secondary flows, leading to a high heat transfer difference between the trailing and the leading walls, while almost no significant difference in the 4:1 case. However neither experimental data nor more accurate modeling is available to assess his conclusions.

## LES

As reported by Corson [28], the universality qualities of LES over RANS are becoming affordable thanks to the increasing computational power. This has of course not prevented early cooling channel studies to be performed.

One of the first LES on a ribbed channel geometry was performed by Murata [92]. He investigated the heat transfer in a periodic ribbed channel and described several features as the high correlations between the wall shear stress and the wall heat transfer. Locations of the high heat transfer regions were also predicted by LES in good agreement with the measurements in the front of the rib and near the rib on the smooth side walls. He reported a dissimilarity between the velocity and the temperature field in the channel cross-section when the channel rotates.

The latter observation was also observed by Ahn [2] in a LES of a rotating ribbed channel with a similar geometry. Using vortex identification in the unsteady LES data, Ahn enlightened that the ribs created vortices inducing high wall-normal fluctuations and leading to heat transfer enhancement on the ribbed wall. In comparison to a non-rotating channel, this heat transfer was increased and decreased on the trailing (destabilized) and leading (stabilized) ribbed wall respectively. Figure 2.10 presents the time averaged  $Nu$  computed by Ahn compared to a similar (but not identical) experiment to describe this trend.

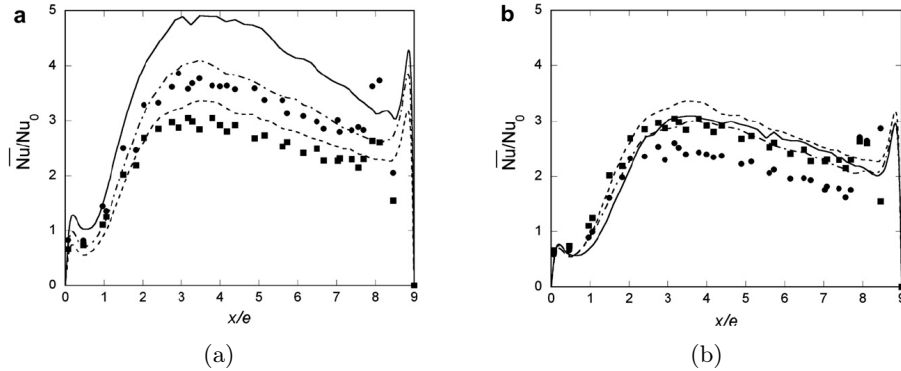


Figure 2.10: Effect of the rotation on the time averaged Nusselt number between two ribs computed by LES on a destabilized (a) and a stabilized wall (b) of a ribbed channel [2]. LES (lines) are compared to measurements (symbols):  $---$  and square:  $Ro = 0$ ;  $- \cdot -$  and circle:  $Ro = 0.1$ ;  $—$ :  $Ro = 0.3$ .

The same author also used LES to recently compare thermal efficiency of channels with a more exotic rib configuration based on detached ribs [3]. Again, good agreement with experiment allowed Ahn to explore the 3D topology of the complex flow. He concluded finally in this case that detached ribs do not provide higher thermal performance than ribs on the wall due to higher pressure losses.

Cui [29] also relied on good LES validations against measurements to analyze different rib spacings. He showed that LES was able to predict correctly roughness

function at the wall and suggested the use of this approach to explore parametric variations in rib roughness.

If previous works addressed periodic flows, an interesting LES study on developing flow is the investigations of Sewall [116]. He made a LES of a rotating straight cooling channel with 90° ribs and performed comparisons of  $Nu$  at different buoyancy number ( $Bo$ ). Sewall's analysis gave an explanation for a particular evolution of the  $Nu$  on a stabilized ribbed wall observed in several experiments. Namely, it has been observed that with increasing  $Bo$ , mean  $Nu$  first decreases (below  $Bo = 0.25$ ) and then re-increases for higher  $Bo$ . Thanks to the LES, he proposed an explanation for this behavior as being due to the competition of first the growth of the separated flow behind the rib, and then an stronger entrainment of the fresh air in the core flow. The corresponding flow field and heat transfer results are presented in Fig. 2.11.

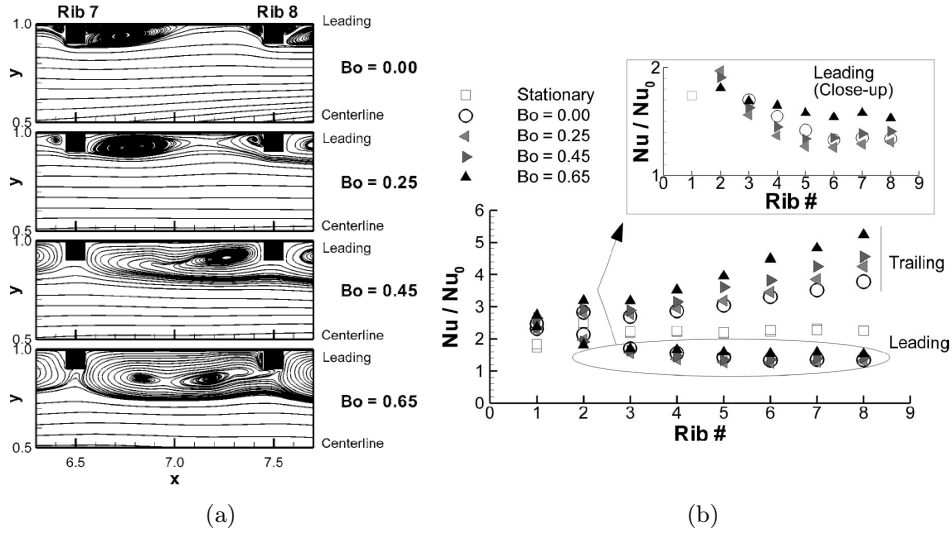


Figure 2.11: Recirculation bubble size between the ribs with increasing buoyancy (a) and corresponding  $Nu/Nu_0$  ratios (b) [116].

## DNS

Finally, one can note several DNS confirming the experimental data and providing deeper flow comprehension. A DNS of a infinite AR channel provided with two ribs on a wall is performed by Labbé [73] with thermal analysis. Three dimensional vortical structures are highlighted and found to be responsible of increased heat transfer when they splash on the hot wall. The DNS of Nagano [93] investigates a finite-ratio channel with different transverse-rib roughness with varied spacing, width and height. It results that these parameters show significant influences on the heat transfer and pressure losses. Finally, one may mentioned the first DNS of a rotating channel by Kristoferssen [72] which issues numerous statistical data in a

wide range of rotation rates.

A non exhausting list of numerical studies performed on cooling channel configurations and addressed here are summarized in Table 2.4, while significations of abbreviation used to characterize them are given in Table. 2.3.

### 2.4.2 Conjugate heat transfer

In addition to the fundamental knowledge of the convective process in fluid flow, accurate heat transfer predictions in turbine blade cooling channel are basically also desired by the designers to estimate the blade lifetime. Toward this objective, coupled thermal computations between a fluid flow and a solid body also known as CHT computations have been already studied and used in the industry. But following the industrial state-of-the-art, CHT computations have been until now most widely performed with 1D networks or RANS modeling for the fluid part [104, 8, 84, 66]. In this way, the exchange methodology is simplified since only mean information are used. But looking at the advances in LES, it may be interesting to consider this turbulent flow modeling for CHT computations. This approach introducing unsteady computations with a wide frequency spectrum raises new coupling strategy questions (computational cost optimization and numerical stability for instance [34]). Investigations of such issues have been the subject of several studies, as for example the works of Chatelain [20] and Jauré [63]. Chatelain has studied the temperature fluctuations near the wall to propose the One Dimensional Variance Model (ODVM). This approach may be applied in the near wall region and reduce the LES computational time by transporting statistical information to the wall. Recently, Jauré [63] has more specifically performed a stability analysis studying the setup and the convergence of asynchronous fluid and solid coupled computations for massively parallel environments.

Table 2.3: Legend of abbreviations used to characterize the numerical studies presented in Table 2.4

Abb.	signification	options
y.	year	-
w.t.	wall type	smooth (s), ribs (r), detached ribs (d.r.) dimples( di.)
be.	has a bend ?	yes (x), no (.)
he.	heated channel ?	yes (x), no (.)
mod.	modeling	for RANS: eddy viscosity (1), RSM (2)
AR	aspect ratio	-
p.	pitch	-
bl.	blockage ratio	-
r.w.	ribbed wall	faced (fa.), staggered (st.)
r.a.	rib angle	-
r.s.	rib shape	square (sq.), rounded (ro.)
f.t.	flow type	developing (d.), periodic (p.)



Table 2.4: Description of some numerical studies of cooling channel. Significations of abbreviation are given in Tab. 2.3.

Author	y.	w.t.	be.	$Re$ [ $10^3$ ]	AR	Ro	he.	p.	bl.	r.w.	r.a.	r.s.	mod.	t.f.
Iacovides [58]	1999	r	x	64	$\infty$	–	x	10	0.1	2 st.	90°	sq.	RANS (1,2)	d.
Jang [62]	2001	s,r	.	25	1	0.0, 0.24	x	10	0.1	2 st.	45°	ro.	RANS	d.
Al-Qahtani [4]	2002	s	x	10	2:1	0 to 0.22	x	–	–	–	–	–	RANS	
Ooi [95]	2002	r	.	30	1	–	x	6,9,12	0.1	1, 2 fa.	90°	sq.	RANS (1)	p.
Al-Qahtani [5]	2005	s	.	10	4:1	0 to 0.28	x	–	–	–	–	–	RANS	
Sleiti [117]	2008	r	x	25	1	0 to 1	x	10	0.1	2 st.	90°	ro.	RANS (2)	d.
Saha [111]	2005	r	.	25	0.25,1,4	0.12 to 0.5	x	10	0.1	2 st.	90°	sq.	URANS (1)	p.
Murata [92]	2000	r	.	4,1,9,2	1,4	1.0	x	10	0.1	2 fa.	90°	sq.	LES	p.
Cui [29]	2003	r	.	10	$\infty$	–	.	1,4,9	0.1	1	90°	sq.	LES	p.
Tafti [126]	2004	r	.	20	1	–	.	10	0.1	2 fa.	90°	sq.	LES	p.
Qin [103]	2006	s	.	4.5,5,10	1	0.01 to 0.09	.	–	–	–	–	–	LES	p.
Ahn [2]	2007	r	.	30	$\infty$	0.0 to 0.3	x	10	0.1	2 fa.	90°	sq.	LES	p.
Sewall [116]	2008	r	.	20	1	0.3	x	10	0.1	2 fa.	90°	sq.	LES	d.
Ahn [3]	2010	d.r.	.	30	$\infty$	–	x	10	0.1	2 fa.	90°	sq.	LES	p.
Elyyan [39]	2012	di.	.	12.5	$\infty$	0.0, 0.7	.	–	–	–	–	–	LES	p.
Kristoferssen [72]	1993	r	.	25	0.25,1,4	0.12 to 0.5	x	–	–	–	–	–	DNS	p.
Nagano [93]	2004	r	.	25	0.25,1,4	0.12 to 0.5	x	10	0.1	2 st.	90°	sq.	DNS	p.

## 2.5 Conclusions

A review of the state-of-the-art turbine blade cooling has been presented in this chapter. Addressing first the industrial requirements and the current technologies, second the CFD approaches for modeling the cooling systems, the following conclusions may be reported:

- The turbine blade cooling channel design is at the meeting point of several physical constraints requiring therefore to satisfy multiple criteria. In this scope, the blade metal temperature is the parameter of primary importance driving the blade lifetime. However, current industrial tools do not provide sufficient accuracy for this critical data. As a consequence, all areas require improvements, including CFD methods.
- Rib setups on channel walls are one of the most efficient turbulence promoter system. Numerous designs exist providing a large range of thermal performances which may also induce strong pressure penalties.
- Ribbed channels have been widely studied computationally with the common RANS and LES modeling. RANS with isotropy assumption is shown to be strongly dependent on the model used and leading to results with poor accuracy in 3D especially in regions where the flow is highly separated. More complex models such as RSM have shown satisfactory estimations for this specific issue. LES computations have proven a real gain over the RANS predictions in ribbed channels.
- Considering the methods for a potential industrial application, one can note that most of the LES studies have been performed on periodic structured meshes. Some of them have addressed developing channel flows but none have been found to investigate developing flow with unstructured meshes.
- CHT computations are well studied in RANS. The use of LES for CHT raises new issues due to unsteady flow solution which may cause physical data exchange and stability problems [63].



# Internal cooling LES in non-rotating configurations

---

## Contents

---

<b>3.1</b>	<b>Internal cooling flow physics . . . . .</b>	<b>24</b>
3.1.1	Non-dimensional approach . . . . .	24
3.1.2	General description of turbulent flows . . . . .	28
3.1.3	Turbulence Modeling . . . . .	31
3.1.4	Modeling cost . . . . .	33
<b>3.2</b>	<b>Turbulent flows in a realistic cooling channels . . . . .</b>	<b>37</b>
3.2.1	Smooth U-bend . . . . .	38
3.2.2	Ribbed channel . . . . .	39
3.2.3	Objectives of the following LES test . . . . .	42
<b>3.3</b>	<b>LES numerical requirements for the VKI static cases . . . . .</b>	<b>43</b>
3.3.1	U-bend computational domain . . . . .	43
3.3.2	Ribbed channel computational domain . . . . .	44
3.3.3	Periodic case numerical procedure . . . . .	45
3.3.4	Spatial case boundary conditions . . . . .	46
3.3.5	Domain discretization . . . . .	46
<b>3.4</b>	<b>U-bend case . . . . .</b>	<b>47</b>
3.4.1	Sensitivity to the upstream flow conditions . . . . .	48
3.4.2	Comparison with the state of the art . . . . .	49
3.4.3	Conclusion on the U-bend analysis . . . . .	51
<b>3.5</b>	<b>Ribbed channel case . . . . .</b>	<b>52</b>
3.5.1	Parametric analysis of the periodic LES . . . . .	52
3.5.2	Comparison with the industrial state of the art . . . . .	63
3.5.3	Spatial LES . . . . .	65
3.5.4	Heat transfer in the ribbed channel . . . . .	67
<b>3.6</b>	<b>Conclusions . . . . .</b>	<b>71</b>

---

The great majority of the previous numerical studies has already yield a large amount of data for flows in academical cooling channel. To perform the desired computation of an industrial configuration, these results although of great value,

are however not applicable directly since not fully representative of a real cooling system. The objectives of this chapter are to present and evaluate preliminary numerical requirements and developments needed for LES of such flows which will be then used in the final application of this work.

The first section provides a non-dimensional analysis of the cooling channel issue in order to categorize all the physical phenomena at play. A general description of turbulent flows in an inertial reference frame, out of which static channel flow is a particular case is then provided. Physical and classical modeling approaches of such a flow are also presented at this occasion. Computational requirements for the particular case of wall bounded flows is detailed to propose alternative LES wall treatment based on a hybrid mesh. To focus on the concrete case of turbine blade cooling channels, the second section introduces two experimental academic cooling configurations drawn from industrial realistic channels. These experimental geometries for which preliminary tests will be detailed afterwards are a U-bend and a ribbed channel. The third section describes the different numerical domains of interest chosen for simulating the both experimental test channels with LES. The fourth and fifth sections present results of LES flow analysis in the U-bend and the ribbed channel respectively. In the bend, the sensitivity of the flow topology to the turbulent state is first investigated and validated with the experimental measurements. Then, the turbulence generation is directly addressed with the ribbed channel study. The latter examines the turbulent flow predicted by LES and assess the adaptation proposed based on hybrid meshes. In this scope, several meshes, wall treatments and LES model are tested. For both channel type analyzes, comparison of LES with RANS is also given to quantify the potential contribution of LES modeling for turbine cooling channel flows. Finally, the sixth section gives a summary of the results and conclude on the computational method recommendations.

## **3.1 Internal cooling flow physics**

The internal cooling in turbine blades involves fluid dynamics and heat transfer in rotating systems. In this section, a non-dimensional analysis is first provided to describe all the physical phenomena at play and their respective importance. Then physics and modeling of turbulence, which link all of them in the present study, are introduced.

### **3.1.1 Non-dimensional approach**

The combination of flow dynamics, thermal conduction and rotation may have different relative influences on the flow behavior. Such effects can be quantified thanks to the use of classical dimensionless numbers.

### Flow dynamics

The initial and preponderant physical mechanism used for internal blade cooling involves a fluid flow. To characterize such a flow, the common approach is to evaluate the ratio of inertial forces to viscous forces through the Reynolds number:

$$Re = \frac{D_h U_b}{\nu} \quad (3.1)$$

$D_h$  is the hydraulic diameter of the channel,  $U_b$  the bulk velocity of the flow, and  $\nu$  is the kinematic viscosity of the fluid. A low value of  $Re$  characterizes a flow dominated by viscosity forces (laminar flow), while high values of  $Re$  give a flow with predominant inertial forces (turbulent flow). The choice of this flow regime has a strong influence on the fluid mixing, and therefore on the heat transfer.

### Convective heat transfer

The desired main heat transfer mode in a cooling channel is the convective heat transfer. Convection characterizes heat transfer between a fluid and a surface or a solid. It is usually described by the *Newton's Law of Cooling* which introduces the heat transfer coefficient  $h$  quantifying the proportionality between the wall heat flux  $q_w$  and a temperature difference between  $T_w$  the wall temperature and  $T_{ref}$  a reference temperature to choose:

$$h_c = \frac{q_w}{T_w - T_{ref}} \quad (3.2)$$

Note that for convection dominated problems, the determination of a good reference temperature to compute the convective heat transfer coefficient is an often raised problem [108]. But two other heat transfer modes exist and remain potential importance in our study: conductive and radiative heat transfer. The following paragraphs give methods to compare both of them against convection.

**Convection and conduction** The first heat transfer mode to be compared with convection is conduction. Conduction generates a heat flux  $q_j$  which comes from the Fourier's law [59] involving the fluid thermal conductivity  $\lambda$ :

$$q_j = -\lambda \frac{\partial T}{\partial x_j} \quad (3.3)$$

For a problem involving a fluid/solid interface, one can consider that temperature and heat flux have to be equal at any time at the wall surface in the fluid and the solid. The convective coefficient  $h$  can hence be re-written with the Fourier law at the wall of normal  $n$ :

$$h_c = \frac{-\lambda \left( \frac{\partial T}{\partial n} \right)_w}{T_w - T_{ref}} \quad (3.4)$$

Equation (3.4) can then be non-dimensionalized, leading to Nusselt number  $Nu$ , which compares the relative importance between the convection and the conduction:

$$Nu = \frac{D_h h_c}{\lambda_f} \quad (3.5)$$

$D_h$  being the hydraulic diameter,  $\lambda_f$  the fluid thermal conductivity and  $h$  the convective heat transfer coefficient. Note that Eq. (3.4) also shows that  $Nu$  represents the dimensionless temperature gradient at the wall.

**Convection and radiation** Heat transfer through radiation takes place in the form of electromagnetic waves. Therefore, in our wall bounded flows, radiation due to hot walls can heat all the gas flowing in the channel. The hot wall emissivity and the fluid absorptivity need therefore to be evaluated to be compared to convection. To do so, a radiative heat transfer coefficient of the wall may be built and approximated with the following expression using the black body assumption [59]:

$$h_r \approx 4\sigma T^3$$

Therefore, one can compare  $h_r$  with the convective heat transfer coefficients  $h_c$  to evaluate their relative importance.

### Heated fluid

Cooling issues involve necessarily a thermal changes in the fluid flow so that any fluid with a non uniform temperature distributions may be subjected to buoyancy effects. To evaluate the gravitational buoyancy influence on the fluid motion, one can use the Richardson number:

$$Ri = \frac{g D_h \beta (T_w - T_b)}{U_b^2} \approx g \frac{D_h}{U_b^2} \frac{T_w - T_b}{T_b} \quad (3.6)$$

where  $g$  is the gravitational acceleration and  $\beta \approx 1/T$  is the thermal expansion coefficient.  $Ri$  quantifies therefore the importance of gravity in thermal flow studies.

### Rotating fluid

Another characteristic of the flow inside a working turbine blade is that the fluid is subjected to rotation. Following the flow in the corresponding rotating frame of reference may show an influence in comparison to the same non-rotating configuration because of the rotation induced inertial forces. The importance of one of them, the Coriolis force, is characterized by the rotation number:

$$Ro = \frac{\Omega D_h}{U_b} \quad (3.7)$$

with  $\Omega$  the blade rotation rate.

### Rotating heated fluid

The second inertial force due to the rotation is the centrifugal force. This force may have the same influence as the gravity on fluids with a non-uniform temperature distribution. As a consequence and similarly to the  $Ri$ , the importance of rotation on such a flow is characterized by the Buoyancy number  $Bo$ , exchanging the gravity by the centrifugal force  $r\Omega^2$  in the expression of  $Ri$ :

$$Bo = r\Omega^2 \frac{D_h}{U_b^2} \frac{T_w - T_b}{T_b} \quad (3.8)$$

$r$  is the mean radius of the rotating system. One can note that  $Bo/Ri = r\Omega^2/g$  showing that when the rotation increases, natural buoyancy becomes negligible in comparison to the rotating buoyancy.

### Summary of the non-dimensional approach

All potential physical effects in turbine blade cooling channel flows have been introduced in the previous section. The appearance of the associated characteristic number for all cases addressed in this thesis is summarized in Table 3.1:

Table 3.1: Potential physical phenomenon in turbine blade cooling channel flows.

study case	$Re$	$Nu$	$h_r$	$Ri$	$Ro$	$Bo$
stationary & isothermal	×	—	—	—	—	—
stationary & heating	×	×	×	×	—	—
rotating & isothermal	×	—	—	—	×	—
rotating & heating	×	×	×	×	×	×

### First simplification assumptions

**Gravity buoyancy** It has been shown above that in a moderately to strongly rotating configurations, gravity buoyancy becomes negligible in comparison to the rotating buoyancy. Therefore, for the target rotating academic and industrial cases with a rotation rate of  $\sim 10$  rad/s and  $\sim 1000$  rad/s respectively, the gravity can be neglected. Note that in the intermediate non-rotating heated case, the temperature differences in the fluid will be low in comparison to the turbulent flow induced by the velocity addressed in this work. Gravity will therefore not be taken into account.

**Radiation** In view of the working temperatures of the academic and industrial configurations studied in this thesis, it can be expected that radiation may be negligible in comparison to convection. A posteriori computed convective coefficients  $h_c$  are compared to  $h_r$  in Table 3.2 confirming the hypothesis:



Table 3.2: Comparison of radiative and convective heat transfer coefficient orders of magnitude for the typical academic and industrial configurations.

study case	$h_r$	$h_c$
academical	$\sim 10$	$\sim 80/100$
industrial	$\sim 150$	$\sim 1500/2000$

The maximum radiative flux will therefore always be under 10% of the convective flux. Noting finally that the gas used in the cooling channels is always fresh air without highly absorbing molecules (such as  $H_2O$  and  $CO_2$ ), one can reasonably consider that radiative heat transfer can always be neglected in the framework of this thesis.

### Conclusion of the non-dimensional analysis

Following the Table 3.1 and the above simplifications, the main physical effects that require to be taken into account in this thesis are turbulent flows, convective heat transfer, rotating flows and rotating buoyancy. This leads to the final Table 3.3 presenting the remaining main physical phenomenon of the cooling configurations studied in this thesis and the corresponding chapters where they are addressed.

Table 3.3: Dominant physical phenomenon in turbine blade cooling channel flows.

study case	$Re$	$Nu$	$Ro$	$Bo$	Chapter
stationary & isothermal	$\times$	–	–	–	3
stationary & heating	$\times$	$\times$	–	–	3
rotating & isothermal	$\times$	–	$\times$	–	4
rotating & heating	$\times$	$\times$	$\times$	$\times$	4

#### 3.1.2 General description of turbulent flows

The previous discussion has suggested that convective heat transfer is the key mechanism for blade cooling system. To increase its effects, turbulence is the best flow regime found, as presented in Fig. 3.1 where experimental data and conventional correlations show that  $Nu$  is strongly increased with increase of turbulent  $Re$ .

Figure 3.2 portrays two views of the turbulent flow regimes that one encounters in everyday life for both main fluids present on Earth, air and water. Already studied by Leonardo da Vinci in the sixteenth century [107], and more recently characterized by Osborne Reynolds in the end of the nineteenth century [105, 61], turbulence still keeps today a part of its secrets.

Before entering into a more mathematical and physical description of turbulence, one can describe how this phenomenon appears and identify the accepted underlying mechanism from the works of Reynolds [105] and Kolmogorov [69]. Using the

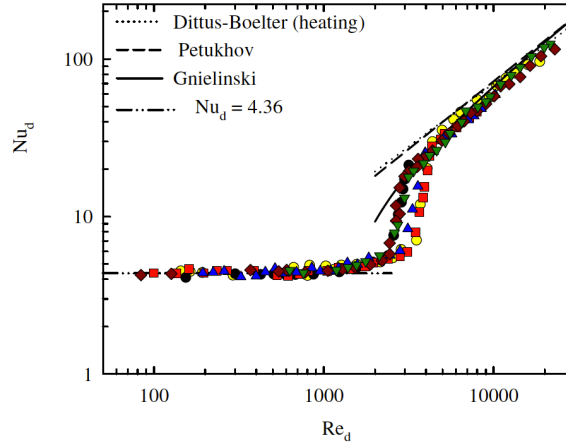


Figure 3.1: Nusselt number in pipe flows versus Reynolds number: example of Yang’s experiment [139] with conventional correlations.

previously presented dimensionless number introduced by the former, one can characterize a fluid flow state by measuring the ratio of inertial forces to viscous forces: that is the Reynolds number  $Re = UL/\nu$  where  $U$  and  $L$  are respectively a characteristic velocity in m/s and length in m of the flow, while  $\nu$  is the kinematic viscosity in  $\text{m}^2/\text{s}$  of the fluid. Three main regimes are usually identified based on  $Re$ : the laminar regime for low  $Re$  for which viscous forces dominate; the turbulent regime for high  $Re$  where inertial forces become the major contributors to the fluid motion; and in-between a narrow range of  $Re$  which is still today not fully mastered. The latter is usually qualified as the transitional regime where the laminar flow becomes intermittent before to become fully turbulent. In most aerothermal problems, like the one addressed in this thesis, the turbulent regime is of primary interest because its agitation creates more fluid mixing, which always enhances heat exchanges in air cooling systems, Fig 3.1.

To describe the turbulent regime, Chassaing [19] proposes among others the following terms: random behavior, tri-dimensional geometry and non linear dynamics. These characteristics explain the difficulties in understanding and handling this common physical phenomenon. A proposition — because the issue is still an open problem — of definition is also given by the latter:

*Turbulence is a natural mode of a viscous fluid flow where internal mechanisms of energy exchange carry out creation and conservation of continuously distributed chaotic motions hierarchy on a wide macroscopic scale range.*

In the 1940s, Kolmogorov [69] proposed a mechanism to describe this continuously chaotic hierarchy and associated internal energy exchange, presented in a turbulent flow energy spectrum of Fig. 3.3. The spectrum shows the amount of energy carried by all the different scales in a turbulent flow. The largest structures,



(a) Sketch of Leonardo Da Vinci [107].



(b) Plume of smoke (Bohunice nuclear power plant, Slovakia)

Figure 3.2: Historical and modern observations of turbulent flows.

typically comparable in size to the characteristic length of the mean flow, bear most of the energy of the turbulent flow. In contrast the smallest scales, limited in size by the existence condition of  $Re = 1$  where the flow becomes entirely viscous, contain low energy. The concept of an energy cascade between these scales has thus been introduced by Kolmogorov and assumes that the turbulent energy produced by the largest turbulent structures is transferred toward the smallest scales. The latter, also called Kolmogorov scale  $\eta = \kappa_\eta^{-1}$  in Fig. 3.3, finally dissipates flow kinetic energy by viscous effects. This cascade is assumed to be the consequence of vortex stretching of intermediate eddies, with a  $-5/3$  energy decrease characteristic law. In this theory, the major hypothesis which is the foundation of the different main flow modeling presented in the following section, concerns the separation between the large and the small scales. Whereas the former are always geometrically dependent and so always considered anisotropic, the latter tend to become completely isotropic when the Reynolds number becomes high enough [19]. This assumption is at the root of the classification of the continuous range of turbulent motions in flows and is often applied in specific modeling concepts as detailed hereafter.

### Governing equations

Instantaneous governing equations for a compressible Newtonian turbulent flow as studied in this thesis are written in Cartesian coordinates and using the Einstein notations (indices ranging over the set  $\{1, 2, 3\}$  for the three space coordinates):

$$\frac{\partial}{\partial t} (\rho u_i) + \frac{\partial}{\partial x_j} (\rho u_i u_j + p \delta_{ij} - \tau_{ji}) = \rho f_i \quad (3.9)$$

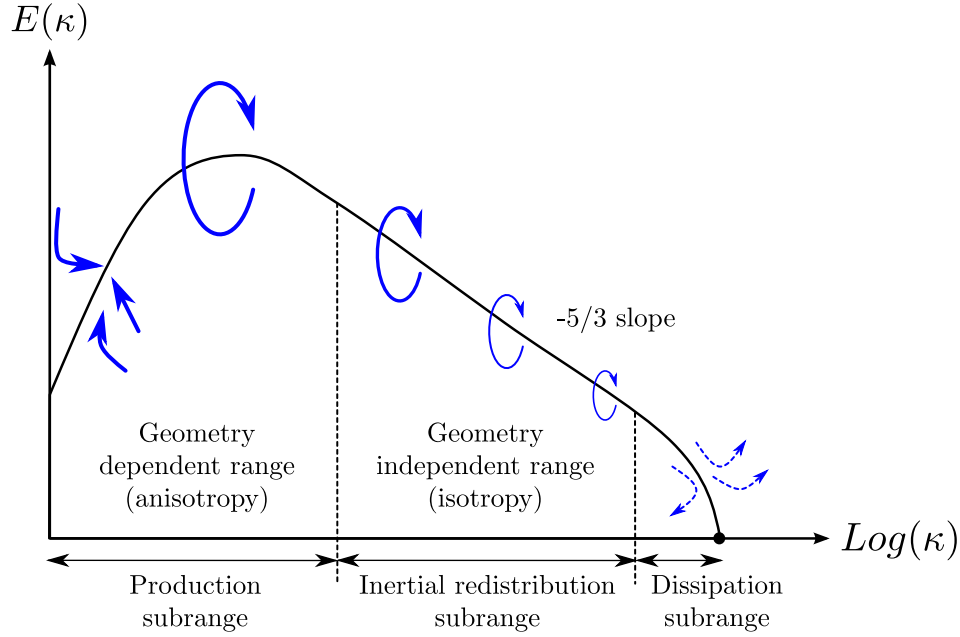


Figure 3.3: Energy spectrum as a function of the wave number  $\kappa$ , and schematic energetic cascade (blue arrows)

In Eq. 3.9  $u_i$  is the  $i$ th velocity component of the fluid,  $\rho$  its density,  $p$  the pressure,  $\tau_{ij}$  the viscous stress tensor and  $f_i$  the body forces. In order to fully describe fluid flows, one must add to the previous equations the following conservation laws for mass, Eq. 3.10, and energy, Eq. 3.11:

$$\frac{\partial \rho}{\partial t} + \frac{\partial}{\partial x_j} (\rho u_j) = 0 \quad (3.10)$$

$$\frac{\partial}{\partial t} (\rho E) + \frac{\partial}{\partial x_j} (\rho u_j E + u_i p \delta_{ij} + q_j - u_i \tau_{ij}) = \rho u_j f_j \quad (3.11)$$

$E$  is here the total energy per volume unit, which depends in addition to pressure on the viscous dissipation and the body forces already present in the momentum equations, as well as on the heat flux vector  $q_j$ .

In the following, the entire set of these conservation equations will be called the Navier-Stokes (NS) equations and is the starting point of all the works presented in this document.

### 3.1.3 Turbulence Modeling

With the previous NS equations, we are now able to look into turbulence modeling to perform the computational resolution of a flows. In CFD, three main types of resolutions are present. These three methods, Direct Numerical Simulation (DNS), Large Eddy Simulation (LES) and Reynolds Averaged Navier Stokes (RANS), allow to solve the NS equations with different proportions of resolved / modeled fluid

scales and different associated computational costs. Figure 3.4 presents a scheme based on the energy spectrum and compares RANS, LES and DNS modeling, each method and its specificities being given in the following paragraphs and details in App. A.

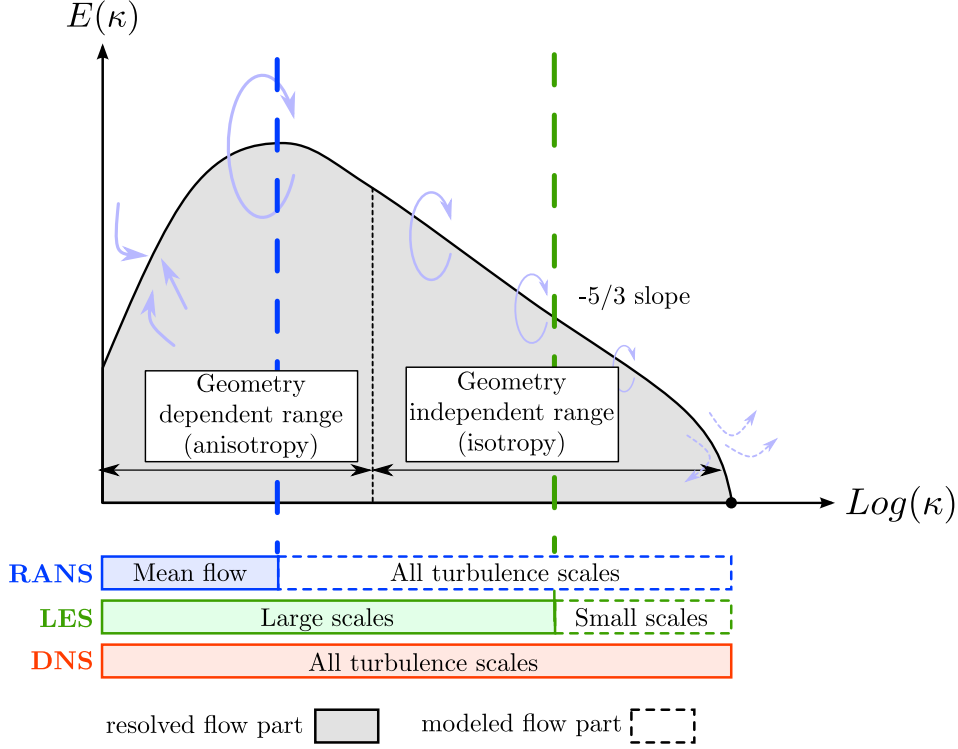


Figure 3.4: Presentation of the three main methodologies to compute turbulent flows.

## DNS

In DNS, a *direct* resolution of the NS equations is computed, which means that no turbulence modeling is needed. To resolve all the scales of turbulence, a very fine mesh is required since the spatial discretization needs to properly simulate the effect of the Kolmogorov dissipation scale on the spectrum evolution as well as the large scales of the flow. Considering that the ratio of the smallest turbulent eddies to the largest scales in a flow is inversely proportional to  $Re^{3/4}$ , Pope [102] determines the total computational requirement to perform a DNS of a 3D homogeneous isotropic turbulence. This results for the predictions of one large scale characteristic time into a number of floating point operations scaling as  $Re^3$ . Since the objective of this thesis is to evaluate available turbulence modeling in an industrial context with flow Reynolds number of the order from  $10^5$  to  $10^7$ , DNS still and for a long time will remain unaffordable.

## RANS

Opposite to DNS in Fig. 3.4 is the RANS method. This modeling introduces the notion of *average* so only mean flow values are solved while all turbulent scales are modeled. RANS computations are thus available with a very low computational cost which makes this method the most widely used today for engineering work [9, 28] (in its fully statistically steady formalism). The principle is based on the Favre averaging of the compressible NS equations [41], splitting each quantity, except density, into a Favre averaged steady mean and a fluctuating component. RANS modeling details and references are given in App. A.2.

## LES

Halfway between DNS and RANS in Fig. 3.4 is the LES method. In comparison to RANS, this modeling relies on the filtering of the NS equations so that the most energetic part of the flow is resolved and directly simulated. The assumption behind this method is that all turbulent flows can be divided into two parts (see Fig. 3.4):

- a high energy anisotropic large scales range, above the filter length scale
- a lower energy and dissipative isotropic small scale range, below the filter length scale

Generally filtering is linked to the mesh cells size and the first geometry-dependent range of scales can be resolved without paying a too expensive computational price thanks to a not too fine mesh. Note that scales smaller than the grid size still need to be modeled to simulate the turbulent dissipative effect of the removed information which is done using a so-called Sub-Grid Scale (SGS) model. LES of compressible flows involves the same formalism as RANS with the spatial Favre filtering splitting this time each quantity into a low frequency and a high frequency part. LES details and references can be found in App. A.3.

### 3.1.4 Modeling cost

The previous modeling presentations have introduced as comparison the key point of the computational cost. This point makes RANS the most interesting approach with in compensation well-known limitations in the model accuracy. On the contrary, the limitations of LES and even more of DNS are specifically their computation cost. As previously presented, one of the objectives of this thesis is to improve the prediction of industrial turbine internal cooling flows currently obtained by RANS. Keeping DNS for the fundamental fluid dynamics research due to its cost not yet applicable to the industry world, LES is a good candidate for the desired precision increase. However, the use of this modeling has an additional cost or modeling difficulty due to wall turbulence which is necessary to be quantified to determine the numerical methodology to adopt with LES modeling.

To illustrate the difficulty of LES and wall modeling, Fig. 3.5 given by Piomelli presents an evaluation of LES computational costs with respect to the Reynolds

number. Dividing a computation between the resolution of boundary layers (or inner layers) and of the non-bounded remaining fluid part (outer layers), it is shown that LES costs are mainly due to either outer layers or inner layers resolution for  $Re < 5000$  or  $Re > 10000$  respectively (in-between costs for both of them being equivalent). For his demonstration, Piomelli assumes between 15 and 25 points in the inner layers. LES using such a resolution criterion is called a *wall-resolved* LES.

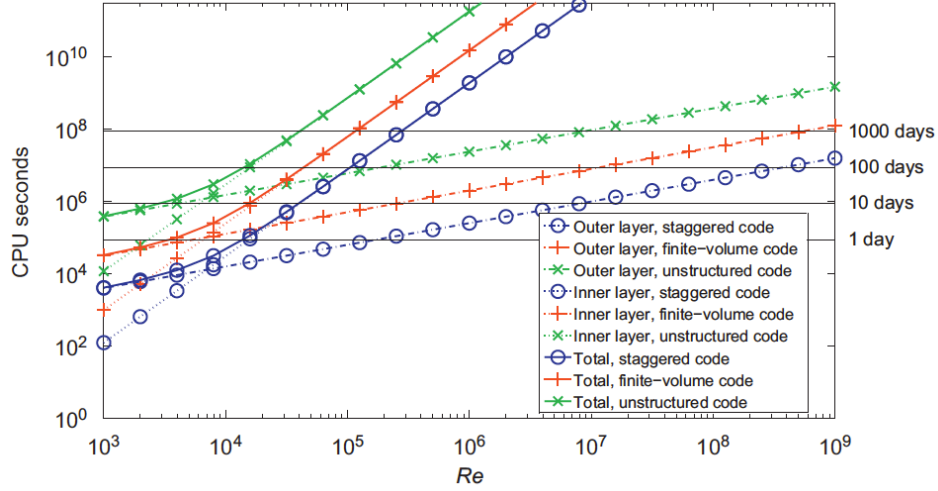


Figure 3.5: Cost, in CPU seconds, of the LES of a flat-plate boundary-layer flow. The calculations were performed on an AMD Opteron, using two in-house codes and an opensource unstructured one. Graph from Piomelli [100]

To define our computational cost and so our numerical methodology, we need therefore some information on the flow regime and the possible mesh type. However, in the present case, the choice of an industrial application as final objective imposes constraints:

- Flow regime: target flow regimes for industrial turbine cooling channels aim at enhancing heat transfer with the turbine blade and are therefore chosen turbulent. In the present case, the typical average is  $Re \sim 20000$ .
- Mesh type: the literature gives a lot of computation examples of academic configurations of cooling channels. In these works, the great majority of the numerical methodologies relies on the choice of fully structured meshes thanks to well-fitting simplified geometries. However, a structured mesh is not necessarily convenient for a complex internal cooling channel discretization and the use of an unstructured mesh is selected as a prerequisite.

Following the indications of Fig. 3.5, we can see that wall-resolved LES of the desired industrial case would require most of the computational power for the resolution of the inner layers, and an extra computational time for the use of an unstructured grid. Since internal cooling channels induce a large amount of boundary



layers, it may be of interest to consider near-wall flow modeling to reduce the computational effort. Three main methods available for the near wall region modeling are detailed by Piomelli [100] and summarized below:

- Equilibrium stress model: wall functions are used to bypass the near-wall region.
- Zonal approaches: a separate set of equations is solved on a specific mesh in the near-wall region and weakly coupled to the outer flow.
- Hybrid RANS/LES methods: the near-wall region is simulated in a global, Reynolds-averaged sense.

To avoid the introduction of more complicated modeling in the view of the industrial configuration, only the wall-law approach will be assessed from the list above. Moreover and thanks to the AVBP code abilities, another near-wall treatment can be considered in this thesis using hybrid meshes. So that two types of grids will be evaluated in the wall-resolved context: full tetra and hybrid grids. Here, the hybrid mesh has been chosen to be always a full tetrahedral mesh with one prism layer along all the wall boundaries, as presented in Fig. 3.6. In this context a pseudo wall-resolved LES can be addressed since hybrid meshes are chosen to reduce the overall number of points in the boundary layer compared to full tetra meshes while ensuring a prism layer located in the viscous sublayer. Note that in such meshes the flow preferential direction are also better preserved. However and compared to prior resolution criteria, here wall-resolved LES more exactly corresponds to a number between 3 and 5 points in the inner layers.

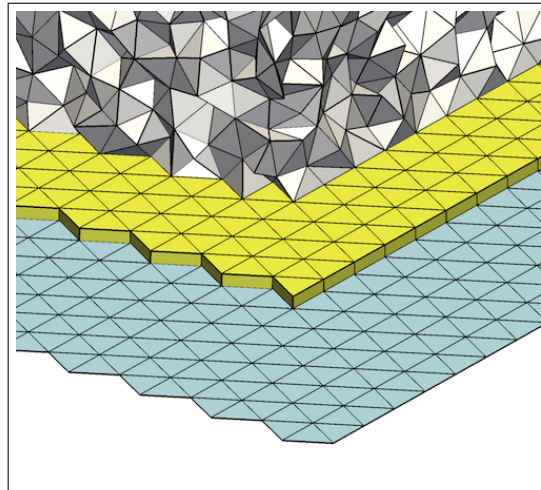


Figure 3.6: Hybrid mesh type composition: one prism layer (yellow) on every wall (blue) and remaining volume filled with tetrahedra (grey).



### Dimensionless units for wall description

The near-wall flows are commonly described using a new velocity reference (instead of the bulk velocity) called the wall friction velocity  $u_\tau$ . This quantity is computed from the wall shear stress  $\tau_w$  as follows:

$$u_\tau = \sqrt{\tau_w / \rho} \quad (3.12)$$

while  $\tau_w$  is defined as:

$$\tau_w = \mu \left( \frac{\partial \mathbf{u}}{\partial n} \right)_{y_{wall}} \quad (3.13)$$

with  $\mu$  the dynamic viscosity and  $n$  the wall normal direction.

With this new reference, additional characteristic values may be introduced, as a dimensionless wall velocity  $u^+$  obtained from the wall velocity  $\mathbf{u}$ :

$$u^+ = \frac{\|\mathbf{u}\|}{u_\tau} \quad (3.14)$$

Additional Reynolds numbers are also introduced based on  $u_\tau$ , the fluid viscosity and a characteristic length. If the latter length is chosen as being the wall-normal distance  $y_{wall}$ , one obtains the dimensionless wall distance  $y^+$ :

$$y^+ = \frac{u_\tau y_{wall}}{\nu} \quad (3.15)$$

This new length scale is widely used to describe near-wall flow scalings and to quantify mesh resolutions. Note that two others dimensionless wall spacing may be used to qualify a mesh at the wall:  $\Delta x^+$  and  $\Delta z^+$ . In the case of a channel,  $\Delta x^+$  and  $\Delta z^+$  are the streamwise and the spanwise mesh wall resolution respectively. They are expressed as  $y^+$  replacing the wall distance  $y_{wall}$  with the mesh spacing in the streamwise and the spanwise direction respectively.

### Thermal behavior at the walls

The previous discussions on computational cost was based only on the assumption of the resolution of the flow boundary layer. In our heat transfer application, one also has to consider the existence of a thermal boundary layer. The numerical methodology for a cooling channel LES should therefore be designed to fit the most restrictive resolution for both of these layers. The evaluation of their relative importance may be done thanks to the Prandtl number  $Pr$ :

$$Pr = \frac{\nu}{\alpha} \quad (3.16)$$

$\nu$  is the kinematic viscosity and  $\alpha$  the thermal diffusivity of the fluid. In the framework of LES turbulence modeling, a SGS turbulent Prandtl number  $Pr_t$  may also be defined similarly to link the SGS turbulent thermal diffusivity  $\alpha_t$  to the computed SGS viscosity  $\nu_t$ :  $Pr_t = \nu_t / \alpha_t$ . Therefore, the ratio between the dynamic

and the thermal boundary layer thicknesses  $\delta$  and  $\delta_{th}$  respectively is expected to be of the form of  $Pr_{eff}$  such as:

$$Pr_{eff} = \frac{\nu + \nu_t}{\alpha + \alpha_t} = Pr Pr_t \frac{\nu + \nu_t}{Pr_t \nu + Pr \nu_t} \quad (3.17)$$

In our case, only air will be considered as coolant fluid. With  $Pr_{air} \approx 0.7$  and  $Pr_t$  constant chosen to be  $Pr_t = 0.6$  (in the common range between 0.5 and 1.1 [67]), one can deduce that both boundary layers will have a similar thickness since  $Pr_{eff} \sim Pr$  (thermal one being slightly thicker). Therefore, all conclusions on the numerical methodology drawn from dynamic observations may be applied in the same fashion for the thermal problem.

## 3.2 Turbulent flows in a realistic cooling channels

The assessment of the LES turbulence modeling with the specific numerical methodology discussed in the previous section for the cooling channel configuration clearly underlines the need for an a priori experimental validation prior to any use of LES on a real industrial configuration. Among the large variety of available cooling channel test benches, two have been chosen since they represent the two typical shapes encountered in real turbine cooling channels: a smooth U-bend and a straight ribbed channel. Such zones are circled in Fig. 3.7 in a cooled industrial blade example. In this section, the two von Karman Institute (VKI) test benches reproducing the smooth channel with a U-bend and the ribbed channel are presented along with the available aerodynamic and thermal measurements.

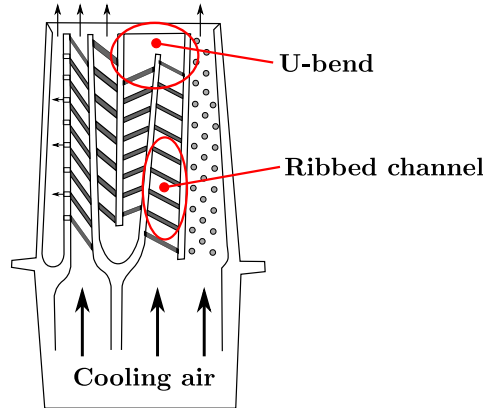


Figure 3.7: Example of application of this study : flow inside a turbine blade.

### 3.2.1 Smooth U-bend

#### Experimental facility

The U-bend configuration chosen for this study is a 3D smooth channel with a rounded 180° turn. Data come from a VKI test bench where Particle Image Ve-

locimetry (PIV), thermal and pressure loss measurements, as well as optimization studies have been performed. A detailed presentation of the setup can be found in Coletti [24].

The 3D channel geometry is designed from an extrusion of a 2D contour made of two parallel rectilinear parts forming the inlet and outlet legs of the bend. The bend itself is obtained thanks to splines where the control points are used as optimization parameters [133]. In our non-optimized case, the splines simply have a circular shape leading to a constant section. Extrusion is then performed to obtain a square section channel with a hydraulic diameter equal to  $D_h = 0.075$  m. Experimentally, this smooth channel is fully built from Plexiglas machined blocks or plates, allowing optical access for PIV measurements, as shown by the picture of Fig. 3.8. Air at ambient temperature is used and is set to flow through the channel at a Reynolds number of 40 000 based on  $D_h$ . A honey comb is also placed at the channel entrance to reduce the disturbance of the flow. Geometric parameters and operating conditions are summarized in Table 3.6.

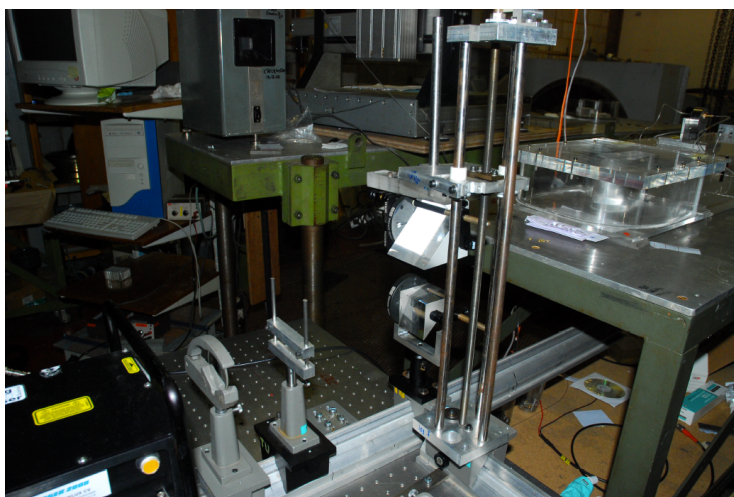


Figure 3.8: Experimental test bench used for validation of stationary numerical simulations. PIV optical rail at the bottom and Plexiglas channel on the table on the right.

Table 3.4: Physical parameters of the smooth U-bend experimental facility.

Channel section	square
Hydraulic diameter $D_h$	0.075 m
Fluid	<i>Air</i>
Inlet bulk velocity $U_b$	$8.8 \text{ m} \cdot \text{s}^{-1}$
Inlet bulk temperature	293 K
$Re$	40 000

### Experimental reference flow topology

Figure 3.9 shows the PIV measurements in the mid-height plane (ie.  $Z/D_h = 0.5$ ) with three reference lines L1, L2 and L3 used for more quantitative diagnostics. The inlet leg is located on the left, under line L1, while the outlet leg is on the right under line L3 and the bend is located between L1 and L3, L2 dividing the bend in two equal parts. The magnitude of the mean velocity is here presented non-dimensionalized by the experimentally measured bulk velocity and complemented by flow streamlines.

In the inlet leg, a classical channel flow is more and more curved because of the presence of the bend. The fluid accelerates along the inner wall of the first mid-part of the turn (between L1 and L2) with a maximum velocity value above  $1.8U_b$  reached at around 25% of the inner chord. Then the flow separates near the inner extremity of line L2 at a position near 46% of the chord. As a consequence, a recirculation bubble is created in the second part of the bend (between L2 and L3), which then develops downstream of the bend until about  $1D_h$  on the inner wall of the outlet leg. On the outer wall, when the fluid enters the turn, its velocity initially decreases reaching  $0.1U_b$ , then progressively increases all along the bend to reach a maximum value around  $1.8U_b$  at the entrance of the outlet leg. This acceleration is of course linked to the large recirculation zone on the inner wall restricting the flow passage section.

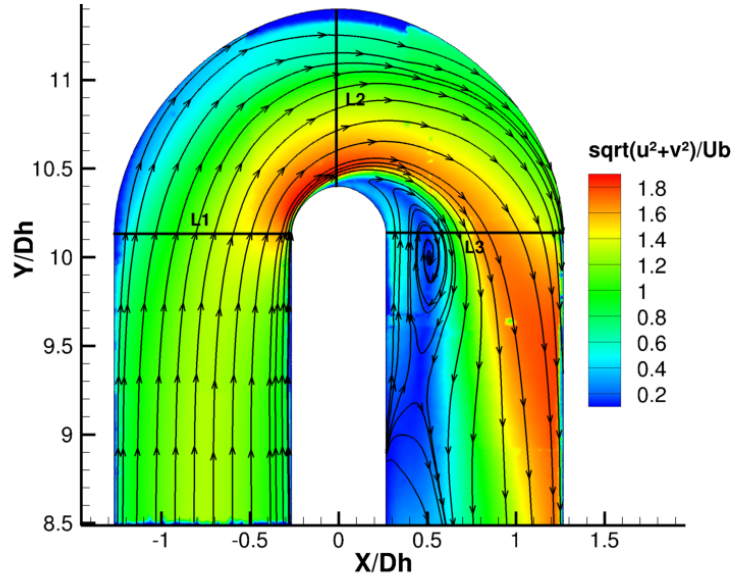


Figure 3.9: PIV measurements in the symmetry plane of the U-bend: streamlines plotted on 2D mean velocity magnitude contours  $\sqrt{U_x^2 + U_y^2}/U_b$ . L1, L2 and L3 black lines divide the domain between inlet leg, first half of the bend, second half of the bend and outlet leg.

### 3.2.2 Ribbed channel

#### Aerodynamic measurements

The chosen ribbed channel experimental test bench is a VKI channel in which Casarsa [16] has carried out PIV measurements. The configuration is a square channel with a hydraulic diameter  $D_h = 0.1$  m and an aspect ratio of 1. Square ribs normal to the flow are mounted on one wall with a pitch-to-height ratio ( $p/h$ ) of 10 leading to a high-blockage ratio,  $h/D_h = 0.3$ ,  $h$  being the rib height. The Reynolds number of the mean flow based on the bulk velocity and  $D_h$  is set at 40 000, a regime similar to the flow inside real cooling channels. This equipment is portrayed in Fig. 3.10 and flow as well as geometry parameters are summarized in Table 3.5. In this experiment, the flow has been measured in a section located between the 4th and 5th rib, where the flow is assumed to be established and periodic. Particle Image Velocimetry (PIV) has been used in several planes across the channel in the three directions, as shown in Fig. 3.11, yielding among others the flow in the symmetry plane and in a plane parallel and close to the ribbed wall.

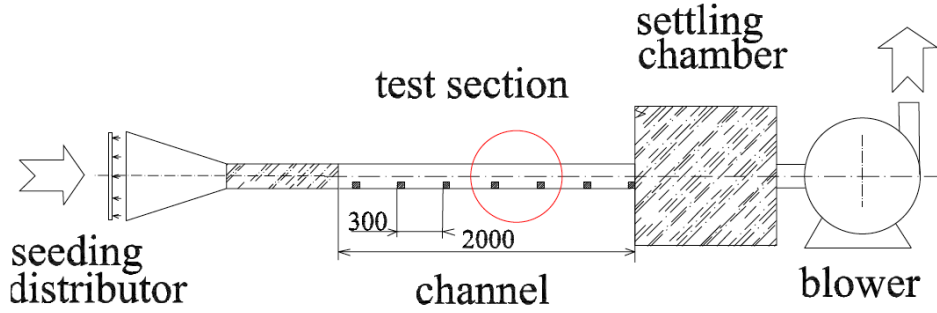


Figure 3.10: Experimental test bench from [16] used for validation of stationary numerical simulations. PIV measurements are located in red circled area.

Table 3.5: Physical parameters of ribbed channel experimental facility

Channel section	square	Fluid	<i>Air</i>
Hydraulic diameter $D_h$	0.1 m	Inlet bulk velocity $U_b$	$8.8 \text{ m} \cdot \text{s}^{-1}$
Number of ribbed wall	1	Inlet bulk temperature	293 K
Ribs angle	$90^\circ$	$p/h$	10
Ribs height $h$	0.03 m	$h/D_h$	30%
Ribs pitch $p$	0.3 m	$Re$	40000

#### Experimental flow topology in the channel symmetry plane

As for the U-bend, an overview of the different phenomena appearing in the flow caused by the ribs and in the symmetry plane is presented based on the measured

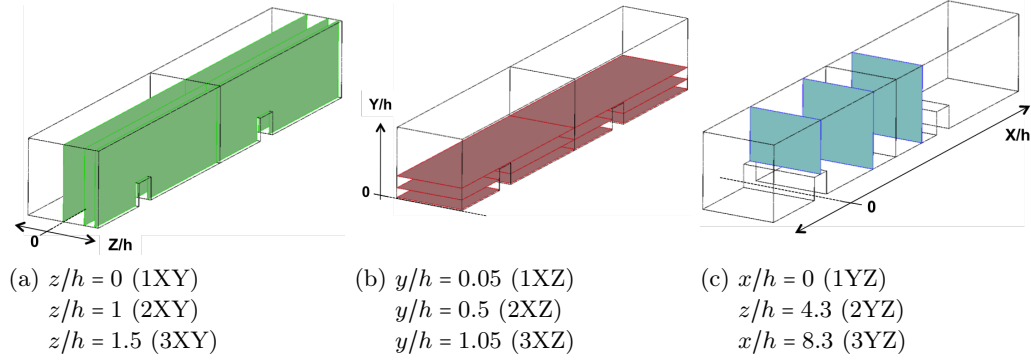


Figure 3.11: PIV measurements planes.

fields, Fig. 3.12. First, the narrowing of the section due to the presence of the ribs forces the fluid velocity to increase and a maximum is detected in the middle of the channel. A boundary layer separation appears at the upstream rib top corner coinciding with a small flattened recirculation bubble on the top surface of the rib, Fig. 3.12 ①. Just after the rib the flow massively separates at the rib down wind side due to the sharp angle, which is typical of a backward facing step flow. Along with this separation, an elongated recirculation bubble appears behind the rib, Fig. 3.12 ②, accompanied by a smaller counter-rotating vortex located at the rib downstream bottom corner, Fig. 3.12 ③. Further downstream the flow fully re-expands in the channel and eventually reattaches on the bottom wall near  $x/h = 4.5$ . Finally, when the fluid reaches the next rib, the flow streamlines strongly curve upward, leading to a new small recirculation bubble near the upstream bottom corner of the rib, Fig. 3.12 ④.

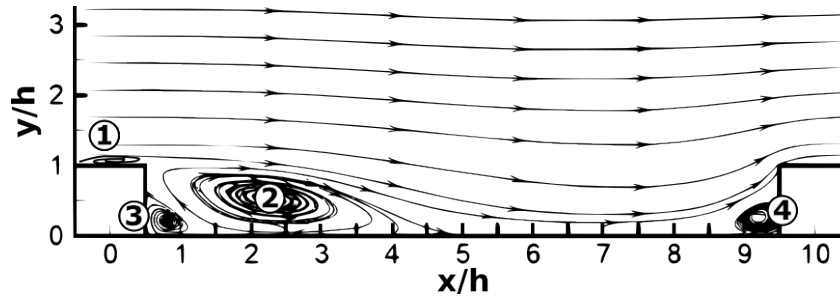


Figure 3.12: Mean flow topology in the ribbed channel symmetry plane 1XY with the four characteristic vortices.

### Thermal measurements

In addition to the aerodynamic experimental data, thermal measurements were also carried out on this ribbed channel configuration. In this case, Cakan [13] used Liquid Cristal Thermography (LCT) to calculate heat transfer wall maps in a developed

flow area. The thermal procedure consisted in imposing a constant heat flux, chosen here equal to  $650 \text{ W/m}^2$ , on all the walls and ribs of the channel.

The heat transfer maps are given in terms of *Enhancement Factor* (EF). Qualitatively, EF represents the ratio between the heat transfer in the ribbed channel and the heat transfer in a similar reference smooth channel operated at the same  $Re$ . Therefore,  $EF > 1$  and  $EF < 1$  denote a higher and lower heat transfer respectively, leading to the characterization of the rib influence on the channel cooling efficiency. Quantitatively, EF is the ratio between the measured Nusselt number at the wall and  $Nu_0$ , the Nusselt number computed from the Dittus-Boelter correlation for a smooth circular duct, as introduced by McAdams [86]:

$$Nu_0 = 0.023 \cdot Re^{0.8} \cdot Pr^{0.4} \quad (3.18)$$

The reference temperature  $T_{ref}$  required for the  $Nu$  computation is built here from the inlet and outlet bulk temperatures: a linear increase between both of them is assumed, and a stepwise approximation is deduced, each constant value covering a ribbed wall pattern (a rib and its downstream smooth wall).

### 3.2.3 Objectives of the following LES test

The objectives of this part are to validate the LES approach for cooling channel flows prior to its application to thermal, rotating and industrial studies. To do so, a numerical parameters sensitivity analysis for both the U-bend and the ribbed channel is applied and results are compared to classical reference RANS computations as well as experimental data. Four categories of parameters detailed in the following sections of this chapter have been tested and are summarized in the list below:

- Inlet flow condition (U-bend case): unsteady flow simulated by LES may require more fluctuating complex information for the inlet boundary conditions than in RANS. Therefore, which upstream turbulence level has to be taken into account for LES predictions to reproduce accurately the physics ?
- Mesh type and size (ribbed channel case): the majority of the previous computations on cooling channels used structured meshes. The objective of this thesis being an industrial application with a complex geometry, an unstructured mesh is preferred but may lead to additional computational time. Therefore, how does one choose a meshing strategy with unstructured grids to reduce the computational time without affecting physical accuracy ?
- With or without wall-law (ribbed channel case): as shown previously, LES computational efforts in high  $Re$  configurations become mainly dedicated by the near-wall turbulence resolution. Different strategies exist to reduce these efforts, but in our case, does a simplified equilibrium model allow to alleviate near-wall resolution in these largely separated flows ?

- Turbulence model (ribbed channel case): the Smagorinsky classical LES model allows to reproduce with good accuracy a large range of physical flows. But it is also known to show some theoretical discrepancies near the wall [94]. In the framework of this thesis where wall-bounded flows are exclusively studied, the WALE model contribution is illustrated.

### 3.3 LES numerical requirements for the VKI static cases

This section provides the numerical framework retained and tested for a LES modeling assessment of the two VKI experimental test cases. First the computational domains chosen for both the U-bend and the ribbed channel are presented considering the previously raised physical issues. Note that the particular case of the periodic ribbed channel is depicted before spatially simulating the full channel.

#### 3.3.1 U-bend computational domain

For the present LES, a 3D domain reproduces the bend thanks to two  $10 D_h$  long inlet and outlet legs. The dimensions of this domain are presented in Fig. 3.13a along with a view of the resulting 3D geometry including the inlet leg (green arrow) and outlet leg (red arrow) in Fig. 3.13b.

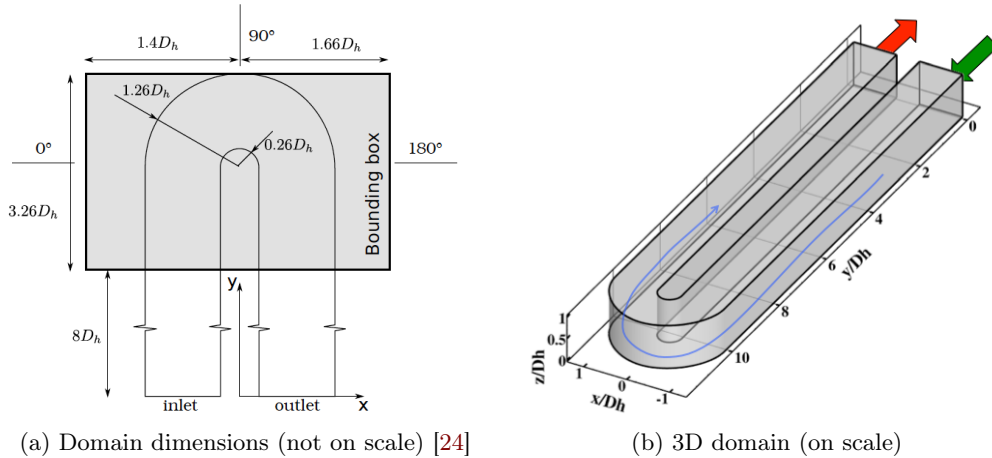


Figure 3.13: 2D source contour with dimensions (a) and overview of the 3D resulting computational domain with inlet and outlet leg (green and red arrow respectively) (b) of the U-bend case.

#### 3.3.2 Ribbed channel computational domain

Since measurements have been performed in a channel section where the flow is assumed to be periodic, to reduce the computational cost of LES, a first comparison domain is chosen to be only one section of the channel corresponding to a  $10 x/D_h$



long periodic pattern, Fig. 3.14. This first periodic domain is used to perform a numerical sensitivity analysis. Note that in reality, turbine blade cooling channels may not reach a periodic regime due to the small number of ribs in one straight channel. To investigate the periodicity hypothesis, a second full length straight channel is also considered. The second domain of study has been for this case chosen to be composed of 7 ribs as the experimental test bench and is called in the following the spatial case. Practically, the latter is made of 7 repetitions of the domain seen in Fig. 3.14, slightly extended at both extremities (inlet located at  $3D_h$  before rib#1 and outlet at  $4D_h$  after rib#7).

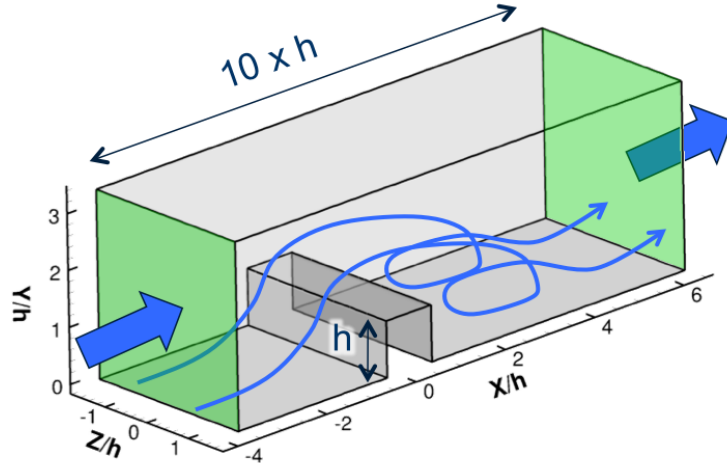


Figure 3.14: Periodic computational domain of the ribbed channel (periodic surfaces in green).

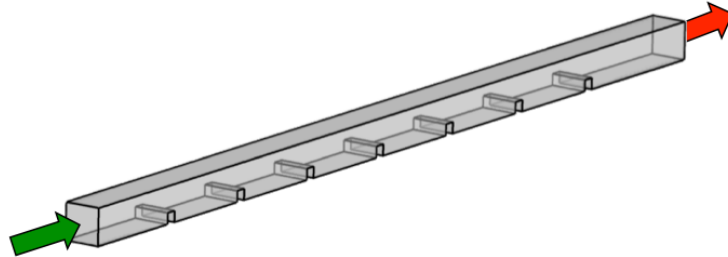


Figure 3.15: Spatial computational domain of the ribbed channel (inlet and outlet pointed with green and red arrow respectively).

### 3.3.3 Periodic case numerical procedure

As introduced before, a periodic ribbed channel numerical domain is used to perform a sensitivity analysis first. Periodicity is hence set between both streamwise boundaries (in green in Fig. 3.14). This subsection presents the numerical procedure and wall boundaries chosen to perform the periodic computation.

**Wall boundary conditions** All non periodic boundaries are in the framework of this parametric analysis one of the followings:

- Walls with a no slip condition: zero velocity is imposed at all boundary points. LES with such configuration is hence called a *wall-resolved* LES, provided with the proper modeling requirements (i.e.  $y^+$ ,  $\Delta x^+$ ,  $\Delta z^+$  and SGS model).
- Walls with log law: classical wall-law implemented in AVBP, App. B, imposing a slip velocity on the wall to match the linear/logarithmic velocity profile.

**Additional source term for the fluid motion** Since there is no inlet/outlet condition in this configuration, the fluid displacement is obtained by adding a source term similar to a fictive pressure gradient in the momentum equation, following the method of Cabrit [12].

$$\frac{\partial(\rho u_i)}{\partial t} + \frac{\partial(\rho u_i u_j)}{\partial x_j} = -\frac{\partial p}{\partial x_i} + \frac{\partial \tau_{ij}}{\partial x_j} + S_{qdm} \quad (3.19)$$

In our case, the source term is only activated on the axial component of the momentum equation ( $x$  axis in Fig. 3.14). It is applied in a dynamic way; its value is adjusted at each iteration in order to maintain the user defined flow characteristics target values. The expression of this term is given by Eq. (3.20):

$$S_{qdm,x} = S_x^{cst} + \frac{\rho_{bulk}^{target} u_{bulk}^{target} + \frac{1}{V} \iiint \rho u dv}{\tau_{S_{qdm}}}, \quad (3.20)$$

with  $S_x^{cst}$  a constant source term to minimize the dynamic part fluctuation,  $\tau_{S_{qdm}}$  a relaxation constant,  $\rho_{bulk}^{target} u_{bulk}^{target}$  the target bulk x-momentum in the channel,  $\frac{1}{V} \iiint \rho u dv$  the current bulk x-momentum. Then, the following procedure is applied to set up a stationary periodic computation:

- $\rho_{bulk}^{target}$  and  $u_{bulk}^{target}$ : chosen from a target operating point (ambient pressure and temperature at  $Re = 40\,000$ )
- $S_x^{cst}$  and  $\tau_{S_{qdm}}$ :
  - Transient state:  $S_x^{cst}$  is set equal to the experimental pressure loss, while  $\tau_{S_{qdm}}$  is set equal to one flow-through time.
  - Steady state:  $S_x^{cst}$  is adjusted to the mean value of the total source term (constant + fluctuating), and  $\tau_{S_{qdm}}$  is set equal to ten flow-through time to minimize source term fluctuations while keeping possible drift correction due to heat increase for example.

Some assumptions are made, with this method, on entropy increase and influence on the 3D flow topology. Both are addressed in App. C and an a posteriori comparisons with experimental data (see following sections) will show that these hypotheses were reasonable for this preliminary study. Note also that such approaches

were successfully used in previous works such as Cabrit for wall modeling of reacting flows [12] and Mendez for multi-perforated plate simulations [87].

### 3.3.4 Spatial case boundary conditions

This subsection details the spatial cases boundary conditions for the ribbed channel and the U-bend. Here, the stationary isothermal ribbed channel spatial case is considered as a validation transition point between the periodic case and the next thermal and rotating spatial cases. Both cases are grouped together since they both have similar boundary conditions with only one inlet and one outlet separated by a channel surrounded by walls.

**Walls** For both spatial cases, no wall-law is used in order to perform wall-resolved LES. So, a zero velocity (no slip) condition is applied.

**Fluid inlet and outlet** Both inlet and outlet boundary conditions have Navier Stokes Characteristic Boundary Conditions (NSCBC) for LES of compressible flows [101]. For each case, the outlet imposes a uniform ambient pressure, while the inlet treatment differs:

- For the ribbed channel, the mean theoretical turbulent velocity profile is imposed, considering that low fluid disturbances are present in the experimental setup and negligible compared to the turbulence created by the ribs for the zone located between rib#4 and rib#5.
- For the U-bend, since no rib can generate turbulence before the bend, a reference LES computation with velocity profile used from a RANS computation is first applied. Different synthetic turbulence intensity levels with a given fixed length scale are then added to assess their potential impact on the predictions (despite acknowledged limitations of the synthetic turbulence model).

### 3.3.5 Domain discretization

In this thesis, all the LES computational domains are discretized with unstructured grids. Two types of grids can be used: full tetra or hybrid grids, described in Section 3.1.4. The wall resolution is dependent on the wall treatment presented in the previous subsection, i.e. no slip or wall-law conditions. In our cases, only one full tetrahedron mesh will be used for the U-bend simulations, see Fig. 3.16, whereas a mesh convergence analysis will be performed on the periodic ribbed channel with both full tetra and hybrid meshes. The spatial ribbed channel of the following chapters will then be computed with the best meshing compromise solution found in the current analysis.

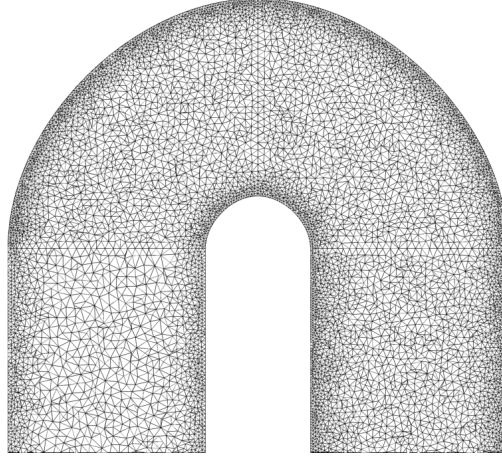


Figure 3.16: Full tetrahedron mesh type overview: U-bend symmetry plane, zoom on the bend.

### 3.4 U-bend case

This section presents the flow computation in the first typical cooling geometry, that is the U-bend. The dependency of the bend generated flow to the turbulent state of the upstream flow is analyzed. Mesh characteristics and turbulence model used in this study are given in Table 3.6. These choices are in agreement with the requirements mentioned in the previous section.

Table 3.6: Numerical parameters of the smooth U-bend LES.

<b>mesh cell number</b>	6 000 000
<b>mean <math>y^+</math> in the bend (<math>y/D_h &gt; 8</math>)</b>	4
<b>max <math>y^+</math> in the bend (<math>y/D_h &gt; 8</math>)</b>	8.7
<b><math>\Delta x^+, \Delta z^+</math></b>	$\sim y^+$
<b>SGS model</b>	WALE

#### 3.4.1 Sensitivity to the upstream flow conditions

As explained in the boundary conditions section 3.3, an initial LES computation has been performed with the same mean velocity profile as for the RANS computation to be discussed later on. To create a more physical turbulent flow, two cases with modified upstream flow conditions have also been tested to evaluate the influence on the final result. To do so, the isotropic turbulence generation method of Kraichnan [71] extended by Celik [119] for anisotropic LES boundary conditions is used. Two different turbulent intensity levels equal to 1% and 10% respectively are added to the RANS velocity profile. The characteristic length scale is chosen being a compromise between the experimental inlet honey comb cell size and the grid cell

size to avoid aliasing. The resulting three LES compared here are summarized in Table 3.7:

Table 3.7: Summary of the different upstream conditions with inlet synthetic turbulence compared in the U-bend computations.

Case name	Intensity	Length scale
w/o	0%	–
1%	1%	$D_h/5$
10%	10%	$D_h/5$

Validations of the three LES cases with PIV measurements are presented in Fig. 3.17 with mean velocity comparisons in the U-bend symmetry plane:

- First, inlet flow with synthetic turbulence has no influence on the small separation zone on the outer wall at the bend entrance (see red dashed surrounded zone in Fig. 3.17), which is a proof that this phenomenon is not solely due to the inlet flow condition.
- Second, disrupted inlet flow has a significant consequence on the large recirculation zone due to separation on the inner wall: here, turbulence seems to influence the flow curvature, leading to a thickness and length modification of the recirculation bubble. The more turbulent the flow is, the thinner and the longer the bubble is. This observation is shown in Fig. 3.17 with blue double arrows indicating the bubble length.

Such behaviors are confirmed by the experiment where the flow was naturally not without any disturbance in the inlet leg, leading to a thinner and longer recirculation than the 0% LES case. Figure 3.18 also supports the assumption on the recirculation sizes made from 2D planes where the streamwise velocity profiles extracted on line L3 at the bend end from PIV and LES are presented. The recirculation zone is found on the left of the graph in the inner quarter of the channel between  $x/D_h$  equal to 0.25 and 0.5. Most of the fluid flows in the outer part of the channel and the maximum velocity point is measured at the position  $x/D_h = 0.75$ , i.e. right in the middle of the channel. The 0% LES case gives a similar result for the recirculation bubble, but the flow is more constrained against the outer wall leading to a maximum velocity location at  $x/D_h = 1.0$ , in the last channel quarter. Increasing turbulence before the bend modifies the LES velocity profiles in such a way that the maximum velocity point slides toward the center of the channel and fits much better the experimental measurements. Note however that inlet turbulence also reduces the recirculation velocity near the wall and so adds discrepancy with respect to the PIV in this region.

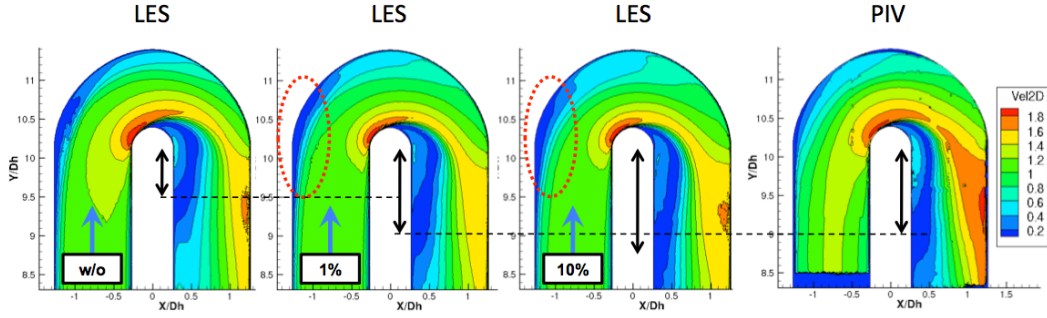


Figure 3.17: Extension of the recirculation bubble with respect to the inlet turbulence intensity level.

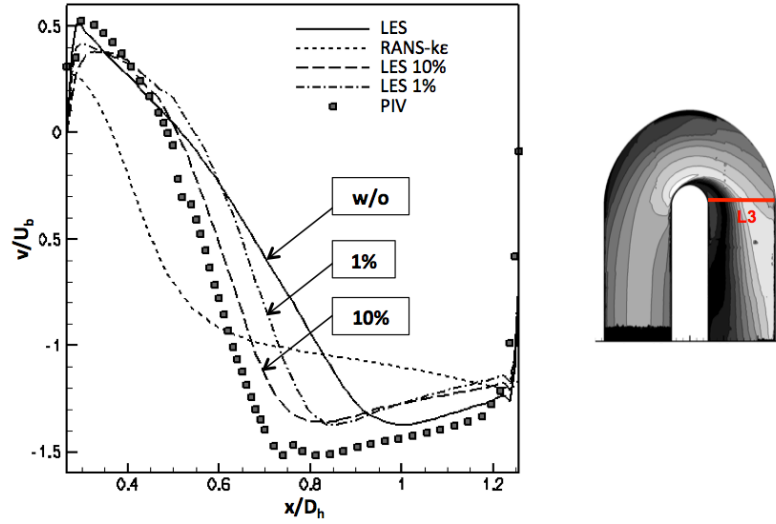


Figure 3.18: Extension of the recirculation bubble with respect to the inlet turbulence intensity level.

### 3.4.2 Comparison with the state of the art

U-bend RANS computations were extracted from the geometry optimization works of Verstraete [133]. The open source solver OpenFOAM [96] was here used with two RANS models:  $k - \varepsilon$  and RSM [31]. The simulations were carried out on the same domain with structured and unstructured meshes for RANS and LES respectively. The comparisons with the PIV measurements are presented in Fig. 3.19 and Fig. 3.20, showing in the symmetry plane the mean and fluctuating velocities respectively.

#### Mean velocity

RANS and LES predict a similarly correct flow in the inlet leg, as well as the velocity maximum value location at 25% of the inner chord. Differences appear when the flow

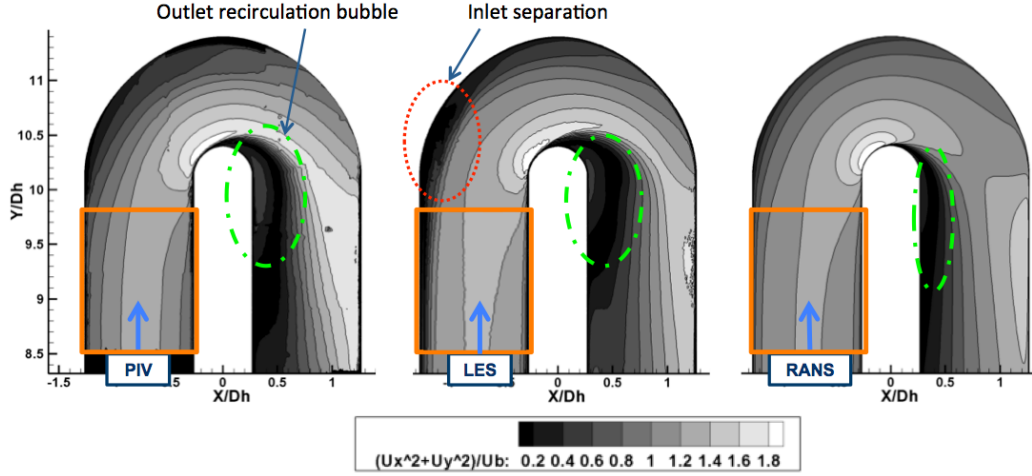


Figure 3.19: Symmetry plane RANS LES PIV, 2D velocity magnitude  $\sqrt{U_x^2 + U_y^2}/U_b$

separates: RANS over-estimates the shear layer curvature and so predicts a thinner recirculation zone than in the PIV measurements. In contrast, LES leads to a better accuracy even if a slight under-estimation of the curvature makes the recirculation bubble a bit wider. In the outlet leg, both models give a flow acceleration on the outer wall with a magnitudes in accordance with the section reduction caused by the recirculation bubble.

It has to be noticed that LES also predicts a small separation at the entrance of the bend on the outer wall which seems not to be detected in PIV and RANS. This recirculation appears regularly in all LES simulations (with and without turbulence injection). Its 3D topology is complex with a small vertically (i.e.  $z$  axis) moving recirculation bubble for which mean results need extra convergence time to obtain a symmetrical shape with respect to the mid-plane.

### Fluctuating velocity

The fluctuating velocity analyses allows to contrast the observations described in the previous paragraph. The PIV results show a very low fluctuating velocity in the inlet leg and at the bend entrance until the flow separation, which is detected through the high Turbulent Kinetic Energy (TKE) zone created by the shear layer on the inner walls, slightly before 50% of the chord (corresponding to the separation point). This zone gets thicker with high TKE values in the second part of the bend until the outlet leg entrance because of the recirculation bubble which feeds the turbulence, and finally the TKE decreases in the wake. Some turbulence is also created on the outer wall to a lesser extent with values under 25% of the inner wall turbulence.

LES predicts very well these two phenomena, but over-estimates the TKE. Turbulence also appears due to the small separation at the bend entrance discussed



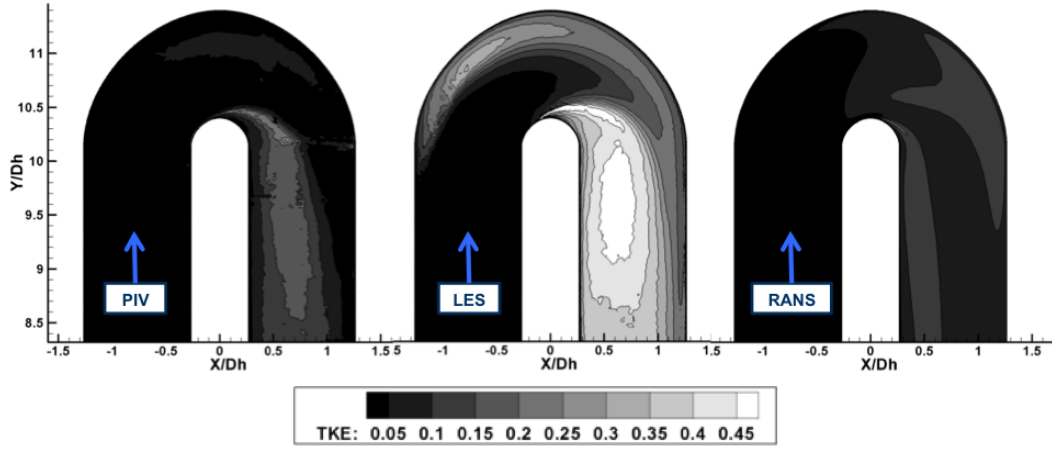


Figure 3.20: Comparison of turbulent kinetic energy (TKE) for PIV, LES and RANS. Expression of dimensionless TKE:  $3/2(u_x'^2 + u_y'^2)/U_b^2$  (PIV),  $(u_x'^2 + u_y'^2 + u_z'^2)/U_b^2$  (LES) and  $k/0.5U_b^2$  (RANS)

in the previous paragraph, which then propagates all along the outer wall until the outlet leg. RANS logically predicts turbulence creation in the shear layer of the thin recirculation zone, but also in the last bend quarter near the outer wall. However, no high turbulence peak downstream of the inner wall separation point is computed.

### 3.4.3 Conclusion on the U-bend analysis

This section has studied the flow in a characteristic U-bend configuration of a cooling channel. Since in industrial configurations, flow perturbations *a priori* exist due to the presence of turbulence promoters in the cooling channel, sensitivity of the LES results to the turbulent condition upstream the bend have been analyzed. LES accuracy has also been compared to a RANS computation as being a common model used in industry.

Conclusions here are that LES provided predictions closer to the experiment with more perturbed upstream flow conditions. Synthetic turbulence has been used here but in realistic channel the main flow activity is created by turbulence generators. Therefore the next discussion proposed in the following section address the capacity of the LES to predict realistic turbulent conditions in channels with turbulence promoters (ribs in the present case). Note also that LES has shown a better accuracy than the present RANS predictions, even if overestimations are still visible on the velocity fluctuation magnitudes.

## 3.5 Ribbed channel case

Channels with ribs on the wall allow to generate strong turbulence to increase the heat transfer at the wall. 3D complex flows with large separations are expected. Correctly predict this unsteady flow and the consequent heat transfer at the wall



represents a interesting challenge for the LES. The analyzis of the ribbed channel configuration is organized as follows: first the numerical setup is chosen from a sensitivity study using a periodic fully developed ribbed channel. Then the extension to the spatial case is assessed and predictions of the wall heat transfer are proposed. Along these steps, summarized in Tab. 3.8, experimental measurements and RANS computations are proposed for comparisons and validations of the LES results. Note that the LES statistical results given in this section have been converged for 15 flow-through time.

Table 3.8: Guidelines for the thermal ribbed channel study.

Step	Objectives	Exp. and RANS
Periodic channel	Determine the domain discretization and the associated wall treatment for ribbed channel LES computations	×
Spatial channel	Assess the periodic results in a more realistic channel	–
Heated spatial channel	LES wall thermal predictions	×

### 3.5.1 Parametric analysis of the periodic LES

This first sub section proposes to determine and validate the requirements to perform the targeted wall-resolved LES introduced in Section 3.1.4. Mesh resolution, wall treatment and LES SGS model are proposed to be the most influent parameters and are therefore studied in the following.

**Mesh convergence** Three periodic meshes are tested to see the influence of the discretization on the LES results. The first one, called M1, is a coarse full-tetra mesh with low wall resolution and a small number of cells allowing longer physical time simulations as well as fast simulations, Fig. 3.21a. The second mesh, M2, is a fine full-tetra mesh with a more suitable wall resolution for wall-resolved LES and approximately ten times more cells than M1, Fig. 3.21b. Finally, Fig. 3.21c, M3 is a hybrid mesh with prisms and tetrahedron constructed as explained in Fig. 3.13b. This mesh combines a relative small number of cells with good wall resolution thanks to the use of prisms at the walls. The characteristics of these three meshes are summarized in Table 3.9.

**Wall treatment** While M2 and M3 meshes have a sufficient wall resolution with a mean  $y^+$  below 10 to assume a wall-resolved LES, M1 has the main part of its  $y^+$  values around and above 30. Since this  $y^+$  range could be reached in more complex

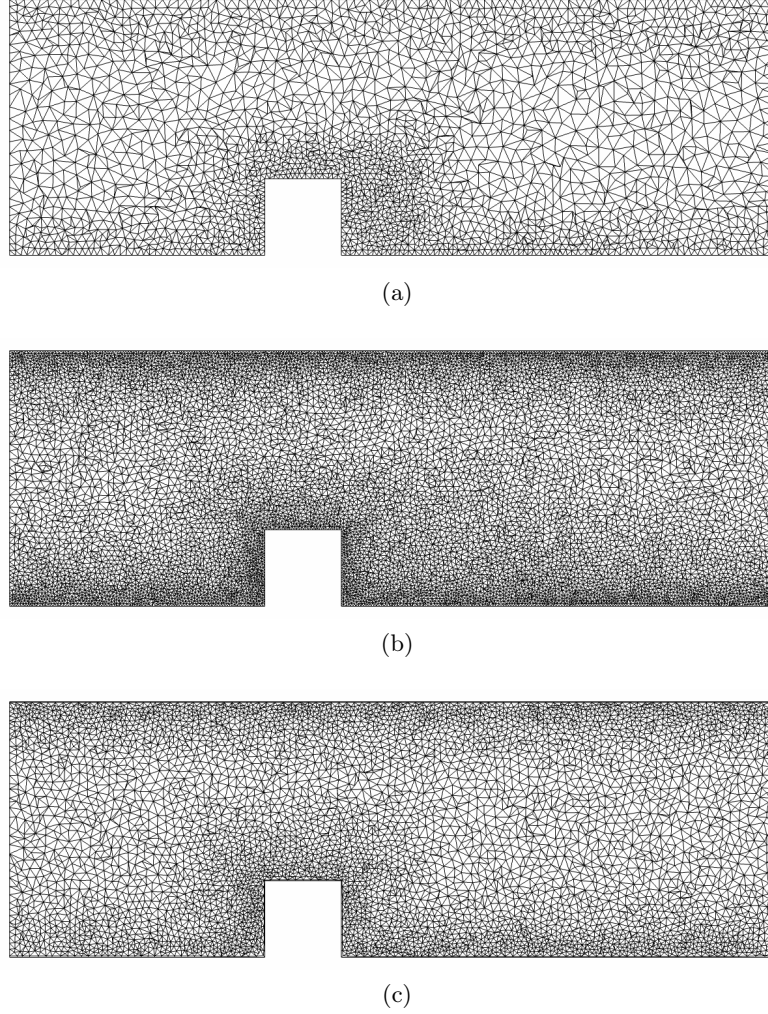


Figure 3.21: Meshes used for LES: (a) M1, (b) M2 and (c) M3.

cases as will be studied in following chapters, possible use of the classical log wall-law as presented in section 3.3.3 may be required. Since compliant only with the M1 mesh, only this configuration is here tested with this modeling technique.

**Turbulence SGS modeling** Two LES turbulence modeling strategies have been tested in this first study: the classical Smagorinsky [118] and the WALE [94] models. The first is used as reference model while the latter is a dedicated wall bounded flow model correcting the SGS viscosity near the wall as explained in App. A.3 (recovering of the proper  $y^3$  near wall scaling for eddy viscosity). For the wall-law computations, only the Smagorinsky model is used.

**Parametric analysis results** Mesh convergence, wall treatment and turbulence modeling have been mixed in order to form a seven case matrix presented in Ta-

Table 3.9: Characteristics of the meshes used for computation of the ribbed channel.

Mesh	Nb. of cells / rib	$y^+$	$x^+, z^+$
M1	550 000	[20; 50]	$\sim 1y^+$
M2	5 500 000	[2.5; 10]	$\sim 1y^+$
M3	1 800 000	[1; 5]	$\sim 5y^+$

ble 3.10. Results are presented first comparing full tetrahedron meshes M1 and M2, then hybrid with the best full tetrahedron mesh predictions.

Table 3.10: Summary of LES parameters in ribbed channel configuration.

	M1		M2	M3
	w/o WL	w/ WL	w/o WL	w/o WL
<b>Smagorinsky</b>	M1.Smago	M1.Smago.WL	M2.Smago	M3.Smago
<b>WALE</b>	M1.WALE	-	M2.WALE	M3.WALE

### 3.5.1.1 Full tetra mesh results

**Mean velocity maps** Looking at Fig. 3.22 and 3.23 comparing PIV measurements for streamwise and wall-normal mean velocities with LES in the 1XY plane, one can see that all five predicted flow topologies are in a general good agreement with the experiment. Acceleration of the fluid over the rib is well predicted at the correct  $y/h$  location between 1.5 and 2. In addition, three among the four recirculations shown in Fig. 3.12 are captured: the one upstream the rib and both downstream. The fourth on top of the rib, very flat, is only detected with the fine mesh and the coarse mesh with the wall-law. The latter mesh has a too poor resolution to find thin near wall structures. However, one can see in Fig. 3.22e that if a wall-law can simulate the top rib recirculation, it overpredicts the length of the upstream bottom corner (almost  $1.5h$  instead of  $0.5h$  in PIV). Appendix D gives additional comparisons in the 2XY and 3XY planes leading to similar conclusions. In order to perform a deeper analyses, streamwise velocity profiles have been extracted from Fig. 3.22 in the symmetry plane 1XY of each simulation and are plotted in Fig. 3.24.

**Channel core flow - mean velocity profiles** Predictions of the core flow maximum velocity at the vena contracta (Table 3.11) show that only the coarse mesh without wall-law leads to an error above 5% of the mean experimental velocity value. This is again simply caused by the poor near wall resolution giving thicker boundary layers and so a more important contraction of the flow above the rib. A finer mesh decreases the error below 1% while the use of the wall-law on the coarse mesh improves the result by 50%.

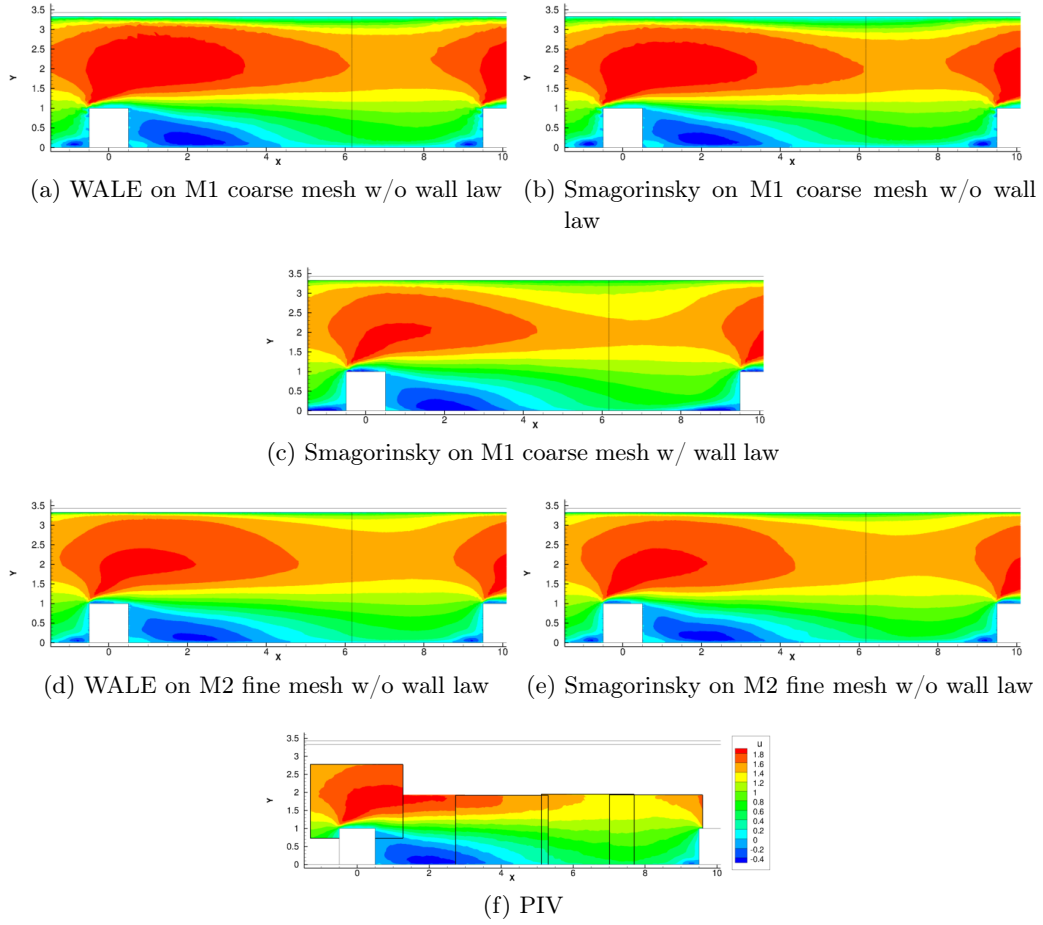


Figure 3.22: Non-dimensionalized mean streamwise velocity  $\bar{u}$  in 1XY plane: comparison of WALE and Smagorinsky modeling with PIV.

Table 3.11: Mean error on streamwise mean velocity for the five full tetra LES simulations with respect to the PIV at location  $x/h = 0$  between  $1.2 < y/h < 2.5$  (channel center above the rib)

M1.Smago	M1.Smago.WL	M2.Smago	M1.WALE	M2.WALE
5.1%	2.5%	0.092%	5.3%	0.79%

**Near wall behavior** On the bottom ribbed wall, Fig. 3.24, the wall-law simulation predictions differ from all the other LES computations until  $y/h = 0.2$ . Even if the wall-law results fit the experimental data better at this location, all LES computations converge to the same profile above  $y/h = 0.2$  at all stations. Note that more detailed observations on the ribbed wall friction maps are discussed later on.

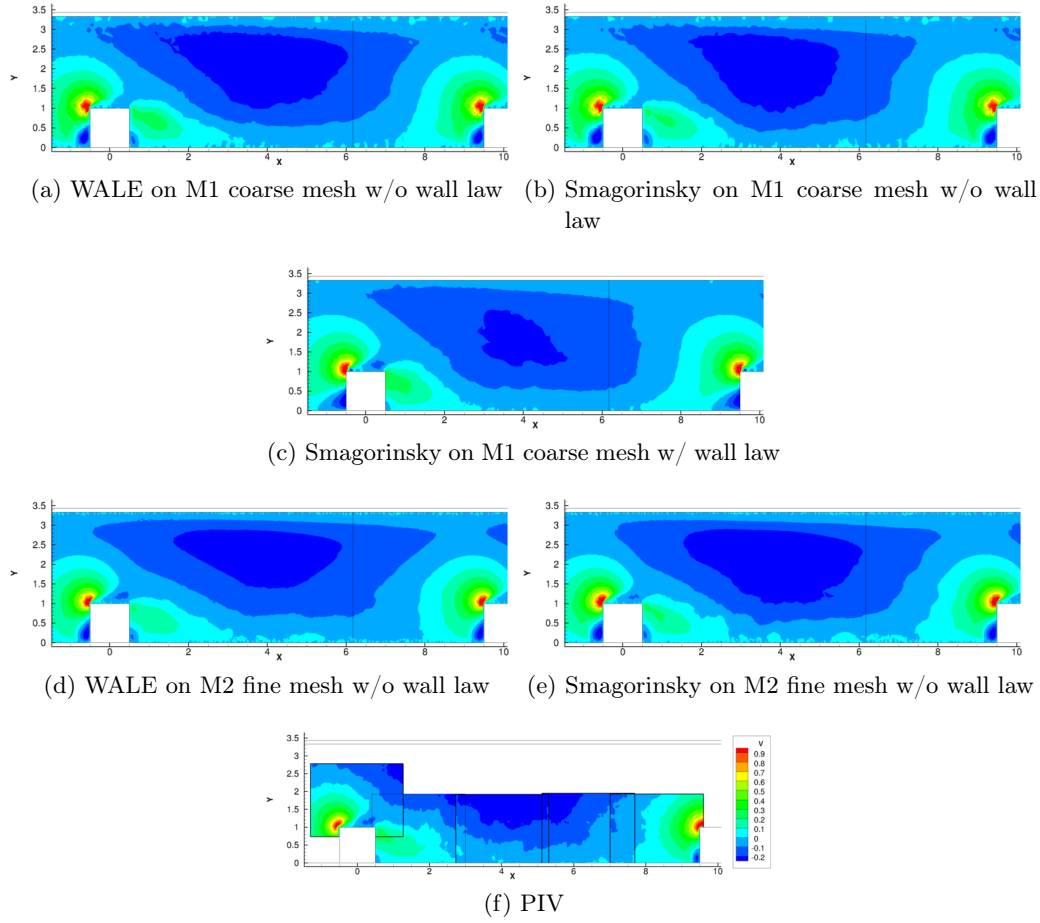


Figure 3.23: Non-dimensionalized mean wall-normal velocity  $\bar{v}$  in 1XY plane: comparison of WALE and Smagorinsky modeling with PIV.

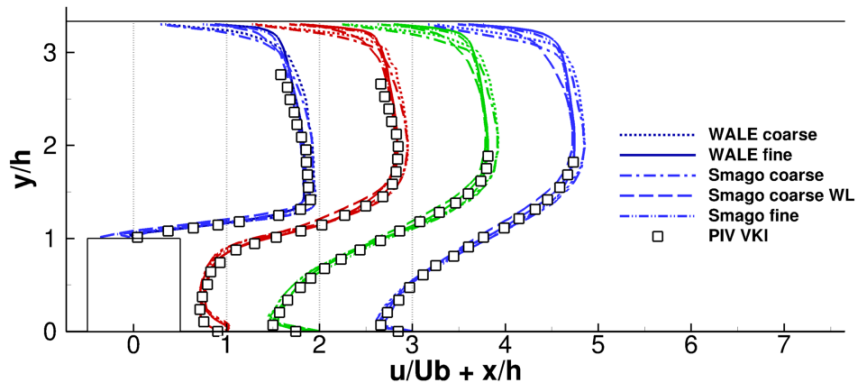


Figure 3.24: Comparison of the five full-tetra LES computations with PIV measurements: streamwise velocity  $\bar{u}$  in the symmetry plane 1XY.

On the top flat wall, no experimental data are available so only the comparison between simulations is given here. One distinguishes three behaviors regardless of the model used:

- a coarse mesh without wall-law leads to a thicker boundary layer predictions than in other simulations
- a coarse mesh with wall-law gives a profile with nearby parabolic shape
- a fine mesh gives a flatter velocity profile above the boundary layer

Since the flow regime is turbulent here, the flatter velocity profile would be the most logical behavior, but a three dimensional flow topology due to the presence of side walls may modify this expected turbulent mean velocity profile.

**Channel core flow - fluctuating velocity maps** RMS values presented in Fig. 3.25 confirm the globally good predictions of the velocity fluctuations by LES, especially for the wall-law and the fine mesh computations.

Figure 3.26 shows the position and the value of the Turbulent Intensity ( $TI = \sqrt{\frac{2}{3}TKE}$ ) predicted by LES in comparison with PIV. Maximum and 50% locations of TI have been computed for all  $x$  positions from the upstream top corner of a rib ( $x/h = -0.5$ ) until the next one ( $x/h = 9.5$ ). This result is plotted in Fig. 3.26a where the different locations draw three lines: the TI maximum location is on the center line, surrounded with two lines for the 50% TI maximum locations. Comparisons with PIV give very good predictions of both position and size of the zone where the most turbulent structures occur and travel. This zone begins in a thin layer at the location of the thin recirculation bubble above the rib, Fig. 3.12 ①, and then extends vertically. The zone envelope width increases from  $0.5h$  at position  $x/h = 0.5$  to  $1.5h$  at  $x/h = 4.5$  where it reaches the bottom wall. After this point, the envelope width grows more slowly but stays mainly in the bottom half part of the channel while the maximum line maintains a constant height between  $y/h = 0.5$  and  $y/h = 1.5$ .

Figure 3.26b presents the TI evolutions along the maximum line with respect to the streamwise direction. The reference PIV measurements detect high turbulence intensity levels between 0.55 and 0.6 above the rib, then TI decreases until it levels off to a mean value of 0.48 between  $x/h = 1$  and  $x/h = 2.5$ . These two parts coincide with the location of the shear layers generated by the recirculation bubble ① and the thick part of the recirculation bubble ② identified in Fig. 3.12. In the second part of the channel where there is no more intense recirculation, TI follows a linear decrease until 0.3 in front of the next rib. The LES results give the same evolution of TI but with lower levels. The computations on the finer meshes M2 and M3 reproduce the peak of turbulence above the rib, the lower flat portion and the linear decrease being very well captured. M1 predictions show a not so contrasted difference between the peak and the flat portion but a similar decrease rate around 0.025 point of TI per  $x/h$ . Note that these results do not take into account the subgrid scale contribution to TI, which could reduce the discrepancy between PIV and LES values.



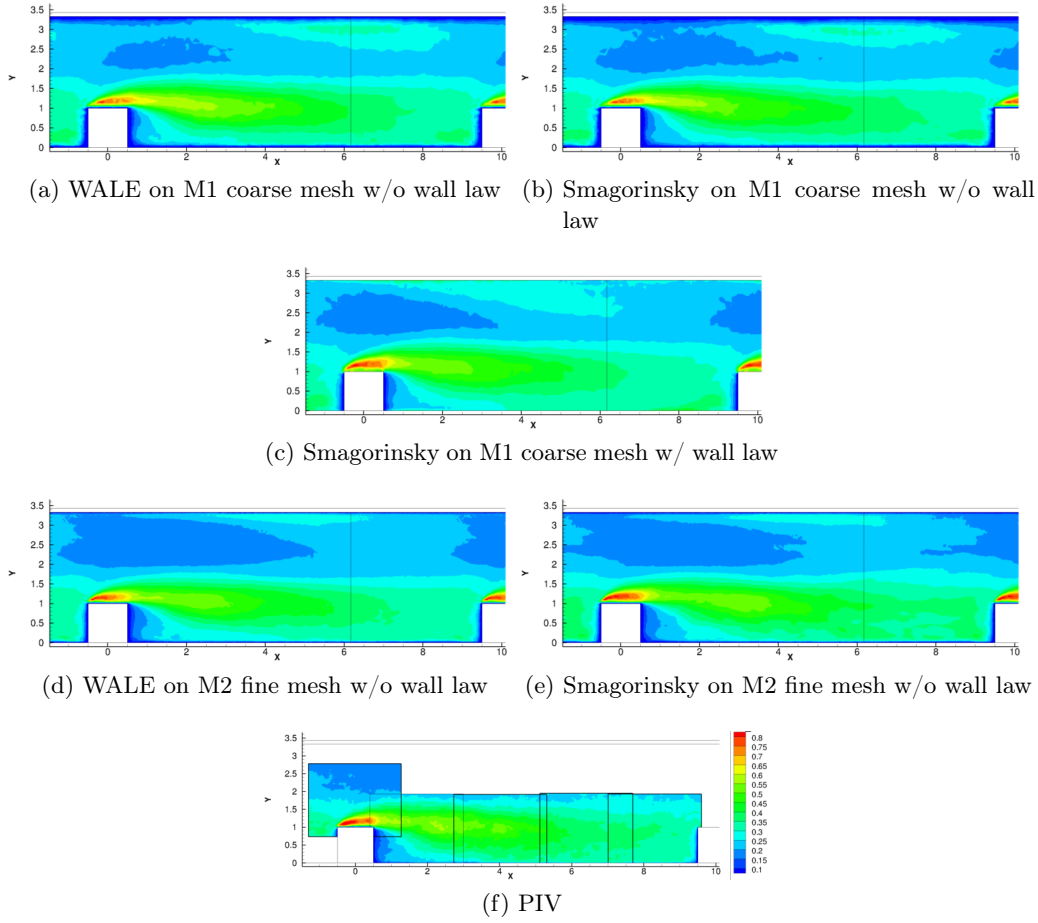
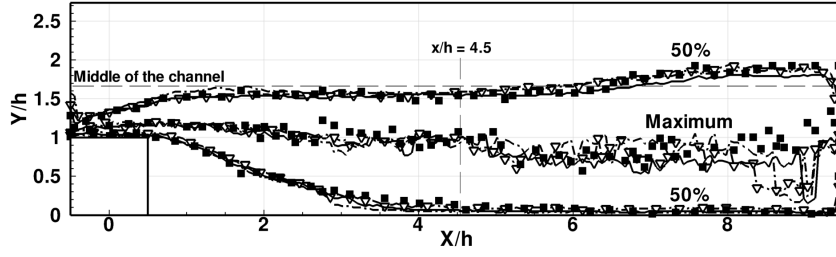
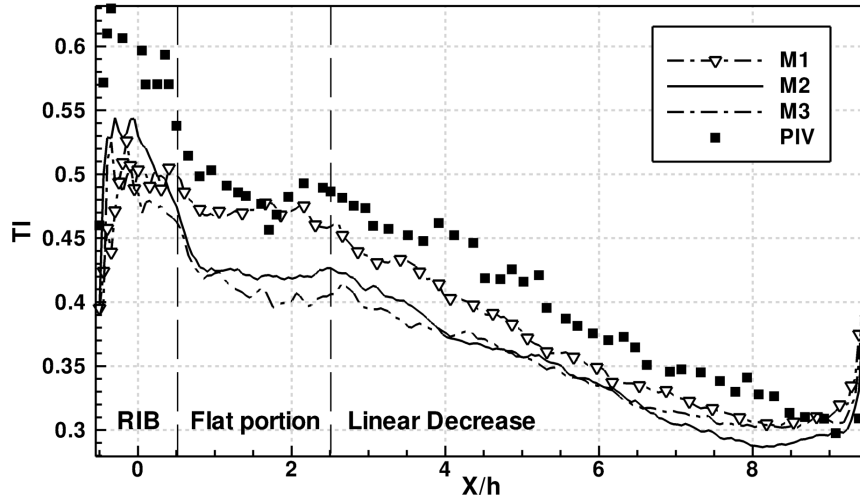


Figure 3.25: Non-dimensionalized fluctuating streamwise velocity  $\overline{u'u'}$  in 1XY plane: comparison of WALE and Smagorinsky modeling with PIV.

**Walls - fluctuating velocity** The three profile groups proposed at the top wall in Fig. 3.24 with mean streamwise velocity (i.e. coarse mesh with and without wall-law and fine mesh) are still represented here at the bottom wall. As shown by Fig. 3.27b, fluctuating velocity predictions with wall-law give here the largest discrepancy with non zero values comparing to the experiment where no fluctuation are seen on the wall. This was however expected since the wall-law naturally imposes a non-zero velocity at the wall to yield the correct velocity gradient, without guaranteeing the resulting fluctuations. The two other groups without wall-law give the same type of profiles, only the wall gradient thickness differs due to more or less adequate wall resolution. As previously observed, a coarse mesh leads to a thicker boundary layer, leading here to a twice weaker wall gradient compared to the fine mesh which fits correctly the PIV data.



(a) Maximum and 50% turbulent intensity locations along the streamwise direction



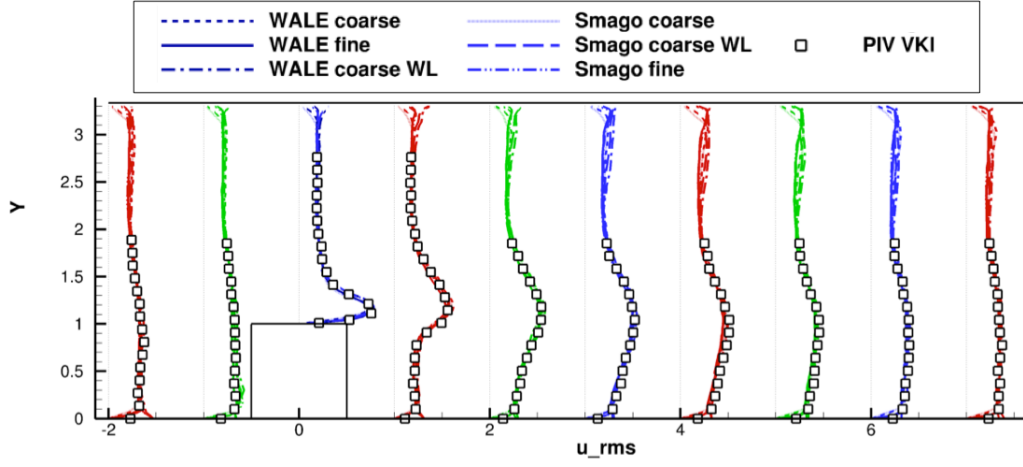
(b) Turbulent intensity maximum value in the streamwise direction.

Figure 3.26: Comparison of turbulence intensity ( $TI = \sqrt{\frac{1}{3}(u_{x,rms}^2 + u_{y,rms}^2 + u_{z,rms}^2)}/u_b$ ) computed with LES: (a) maximum line and envelope (50% of maximum) and (b) value on the maximum line (same legend for both graphs).

**Wall friction maps** The streamwise mean velocity component comparisons are presented in Fig. 3.28 in the 1XZ plane ( $y/h = 0.05$ ). The PIV measurements show three zones in the stream direction:

- The large recirculation bubble downstream of the upstream rib (on the left) until  $x/h = 4.5$  with streamwise velocity values up to  $-0.4U_b$  at  $x/h = 1.8$ .
- After the recirculation, the fluid from the channel reattaches on the ribbed wall and accelerates with a maximum of  $0.5U_b$  reached at  $x/h = 7$ .
- Finally, at the upstream bottom corner of the downstream rib (on the right) a thin recirculation bubble due to flow separation to pass over the rib is present. The streamwise size of this recirculation is  $0.5h$  and the maximum velocity reaches  $0.2U_b$ .





(a) Velocity fluctuations in the channel

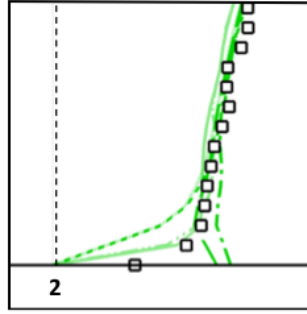
(b) Detailed velocity fluctuations at the bottom wall ( $x/h = 2$ )

Figure 3.27: Streamwise velocity fluctuation profiles in 1XY plane (a) in the entire channel and (b) detailed at the wall at  $x/h = 2$ .

Figure 3.28 displays comparison of the near wall streamwise velocity field for three LES computations and the PIV. These cases have been selected as they represent the three possible cases for full-tetra meshes. First, looking at extremum velocity values one can see that the coarse mesh is not able to predict neither the minimum nor the maximum values (20% error for the minimum in the large recirculation, 50% for the maximum at reattachment). Again, this points out the lack of resolution since the considered plane is located inside the first cell layer. The use of a wall-law with this mesh changes dramatically the results with an error only about 20% for the maximum, and this time an overestimation of the mean velocity in both recirculations (between 25% and 40% error).

Analyzing the iso-contour shapes, one can see that both meshes without wall-law predict dimensions in good agreement with the measurements for the three previously presented zones visible in PIV. Improvement is obtained as expected with the finer mesh, especially for the large recirculation bubble. By contrast, the

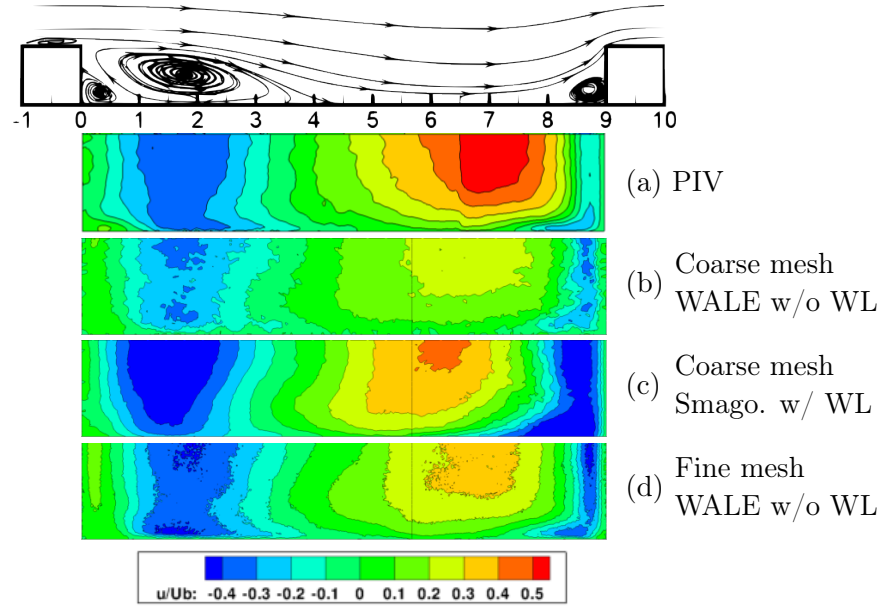


Figure 3.28: Comparison with PIV measurements of streamwise velocity in the near wall plane 1XZ ( $y/h = 0.05$ ) for LES with full tetrahedron meshes M1.WALE, M1.Smago.WL and M2.WALE. Flow is assumed to be symmetrical, only an half part of the 1XZ plane is presented for each case: symmetry axis at the top and wall at the bottom.

wall-law computation overestimates the size of the upstream bottom corner of the downstream rib with an error above 100%. This points here to a classical problem for a simple wall-law in presence of an adverse pressure gradient [100].

### 3.5.1.2 Hybrid mesh results

In this section, a hybrid mesh computation is compared with the selected most accurate full-tetra case, that is LES with the WALE model on the fine mesh. The same analysis as before are presented.

**Mean and fluctuating velocity maps** Figure 3.29 shows that on the symmetry plane the hybrid computation gives almost the same result as with the fine full-tetra mesh, despite the fact that the cell number that has been divided by 3. One can see here the importance of the  $y^+$ : with a reduced cell number and a non optimal transversal resolution  $\Delta x^+$  and  $\Delta z^+$ , results are still very close to the measurements.

Figure 3.30 leads to the same conclusion as the previous paragraph: the hybrid computation reaches the same accuracy as the fine mesh. RMS values are however slightly lower above the rib, which can be justified with the lower spatial resolution due to prisms in this high turbulence zone.

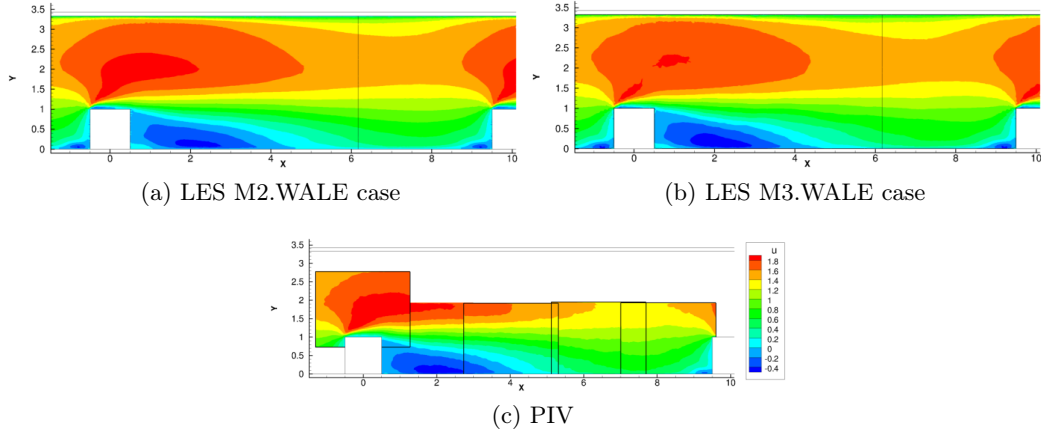


Figure 3.29: Comparison with PIV of the non dimensionalized streamwise mean velocity  $u$  in the symmetry plane 1XY for LES with fine mesh M2.WALE (a) and hybrid mesh M3.WALE (b).

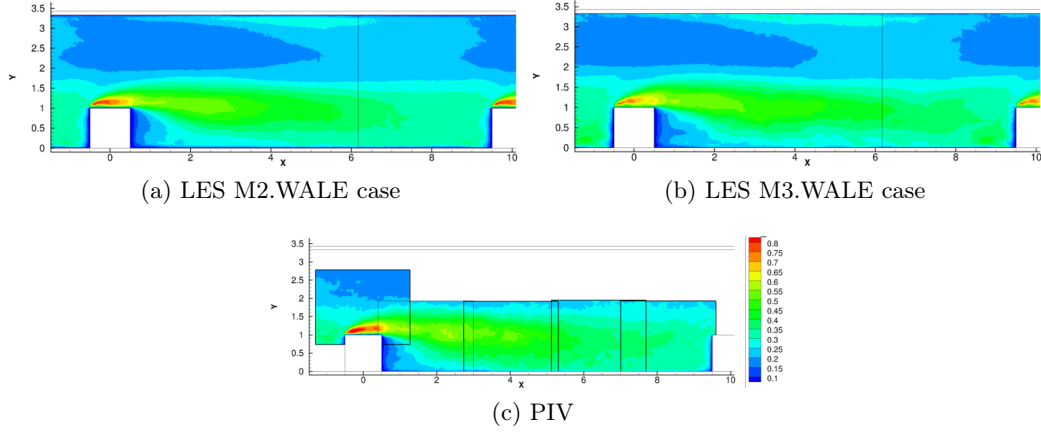


Figure 3.30: Comparison with PIV of the non dimensionalized streamwise fluctuating velocity  $\overline{u'u'}$  in the symmetry plane 1XY for LES with fine mesh M2.WALE (a) and hybrid mesh M3.WALE (b).

**Near wall behavior** Again, no major difference is observed when using the hybrid mesh to compute the ribbed channel case, Fig. 3.31. The size of the three characteristic zones are as well predicted as with the fine full-tetra mesh. Extrema are also similar, with an underestimation of the maximal velocity in the reattachment zone.

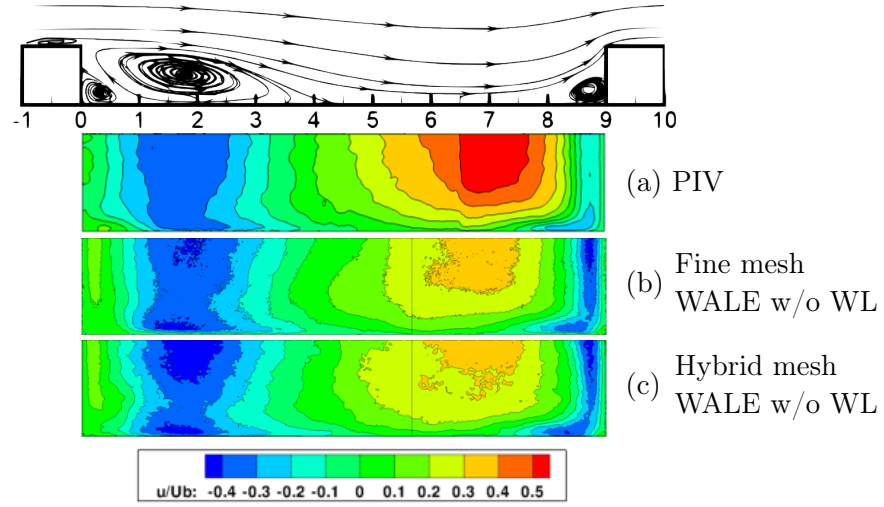


Figure 3.31: Comparison with PIV measurements of streamwise velocity in the near wall plane 1XZ ( $y/h = 0.05$ ) for LES with fine mesh M2.WALE and hybrid mesh M3.WALE. Flow is assumed to be symmetrical, only an half part of the 1XZ plane is presented for each case: symmetry axis at the top and wall at the bottom.

### 3.5.1.3 Global conclusion and recommendations

Given the previous different observations and diagnosis on the symmetry plane 1XY and the near wall plane 1XZ, the requirements proposed to compute the aerodynamics of the wall bounded flow in this ribbed channel with LES are the following:

- Use of a fine mesh (i.e.  $y^+ < 10$ ) with the WALE model.
- Use of a wall-law possible (with the Smagorinsky model) to reduce computational cost.

These observations are in full agreement with the literature recommendation [100]. To satisfy the first point on the mesh resolution, it has also been shown that the use of a hybrid mesh (tetrahedron with a prism layer on all walls) has allowed a reduction of the computational cost in comparison to a full tetra mesh while offering the same accuracy and a more regular wall discretization. A hybrid mesh with the WALE model are therefore recommended in the following for LES of ribbed channels.

## 3.5.2 Comparison with the industrial state of the art

After the LES parametric studies, it is now possible to compare this modeling with the classical commonly used RANS. Computations using different RANS models have thus been performed on the same ribbed channel. Two equation and Reynolds stress models with steady and unsteady formalisms have been tested, and the results are compared with LES predictions in the following sections.

RANS simulations on the ribbed channel have been performed with the *elsA* solver [14], a structured code used among others for turbomachinery applications. The two equation model of Smith [120] based on a  $k - L$  formulation and the anisotropic Explicit Algebraic Reynolds Stress Model (EARSIM) developed by Gatski [46] have been tested. Since RANS requests less computation time, no periodic reduction has been applied and a full channel was discretized with  $18.5 \cdot 10^6$  points and a  $y^+$  near 1 on walls. Results are extracted where periodicity establishment is noticed. The retained LES case for comparison is the hybrid case giving the best compromise between resolution and computational cost.

### Mean velocity

Figure 3.32a presents the comparisons of the mean velocity predictions with RANS, LES and PIV measurements. In this study,  $k - L$  and *EARSIM* RANS have led to similar flow predictions, so only the  $k - L$  case will be presented and discussed. As a reminder, the LES hybrid case shows very good agreement with PIV for the broad trend, when both RANS simulations miss representing the main flow features previously described. Indeed in Fig. 3.32b RANS detects the acceleration near the top wall at  $y/h = 3$  while LES averages give the good position in the center between  $y/h = 1.5$  and  $y/h = 1.5$ . As a consequence, in RANS computations the main flow tends to stagnate in the upper part of channel and is only slightly pushed toward the ribbed wall, which reduces the flow magnitude between the ribs. Both effects are confirmed by Fig. 3.33 where streamwise velocity profiles are detailed in the middle plane. It shows the good agreement of the LES in all the channel, while the RANS velocity profile has its maximum near the top wall as previously said, and also an inverted evolution in all the upper part in the range  $1.5 < y/h < 3$  with  $\partial u / \partial y < 0$  while PIV and LES give  $\partial u / \partial y > 0$ . A lower velocity magnitudes behind the rib are also shown in the recirculation at  $x/h = 2$ , and a positive velocity at  $x/h = 1$  is predicted where the flow has been measured going in the opposite direction so impacting the rib.

A possible explanation of the RANS behavior could be the non-predicted unsteadiness of the shear layer behind the rib. This phenomenon contributes to most of the turbulent activity in the main flow which is redirected toward the ribbed wall. To investigate these unsteadinesses an Unsteady RANS (URANS) computation has been performed in order to see if it could improve the prediction. Results of this new simulation are displayed in Fig. 3.34 giving streamwise velocity maps in the near ribbed wall plane 1XZ. PIV and LES are here reminded and compared to both  $k - L$  computations with the RANS and the URANS approaches. It is shown that URANS slightly improves the streamwise velocity prediction with higher values in the reattachment zone, but still underestimated by more than 60%. Also, no other flow characteristic is really modified with the unsteady approach so no improvement can be achieved here. Nevertheless, even if it is not the case here, it has to be noticed that previous computations on rectangular ribbed channel with a low Reynolds  $k - \omega$  RANS modeling could give better predictions of the velocity field, see for example

Stephens [124]. Further comparisons with this RANS approach could be therefore proposed on the present ribbed channel configuration.

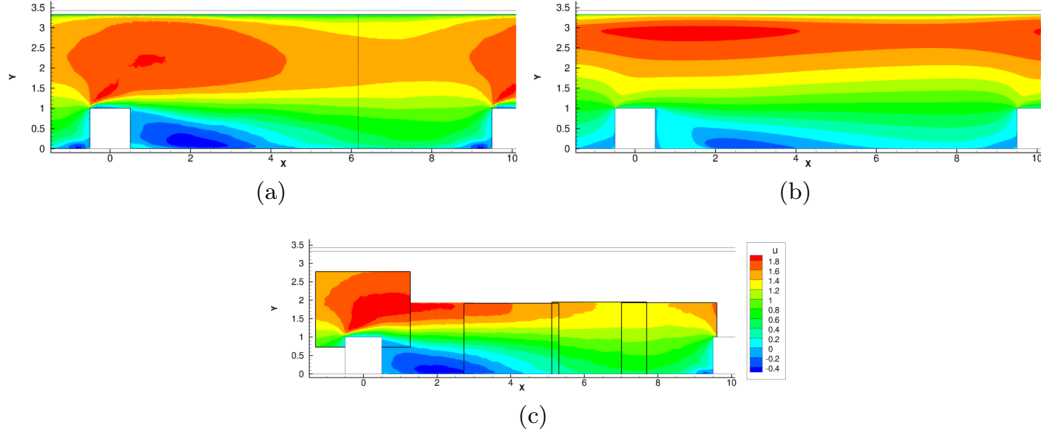


Figure 3.32: Comparison of the non dimensionalized streamwise velocity in the symmetry plane for (a) LES with WALE model on hybrid mesh M3, (b) RANS  $k-L$  and (c) PIV [16]

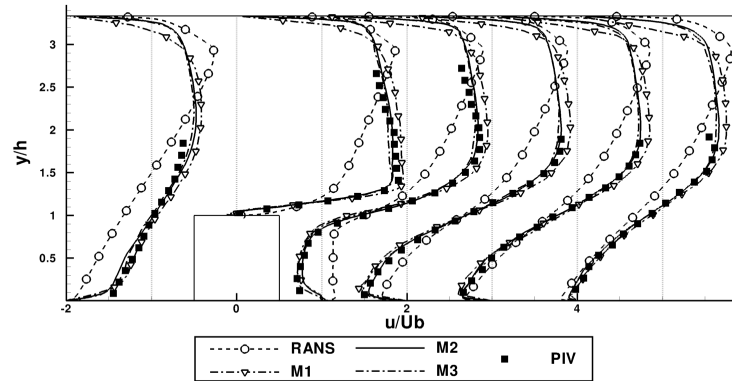


Figure 3.33: Comparison of LES, RANS and PIV streamwise mean velocity at different positions in the channel symmetry plane ( $x/h = -2, 0, 1, 2, 3, 4$ )

### 3.5.3 Spatial LES

LES has been assessed satisfactorily in the previous sections with the hybrid method and compared to the industrial state-of-the-art RANS modeling. In this last exercise a ribbed channel periodic configuration has been used to perform the analysis, but for the following thermal, rotating and industrial cases, a spatial flow development study is necessary. To evaluate how the periodic results are transposable to the spatial case, a differential analysis between both cases is performed in this chapter to evaluate the periodicity establishment in the spatial case. Note that such evaluations

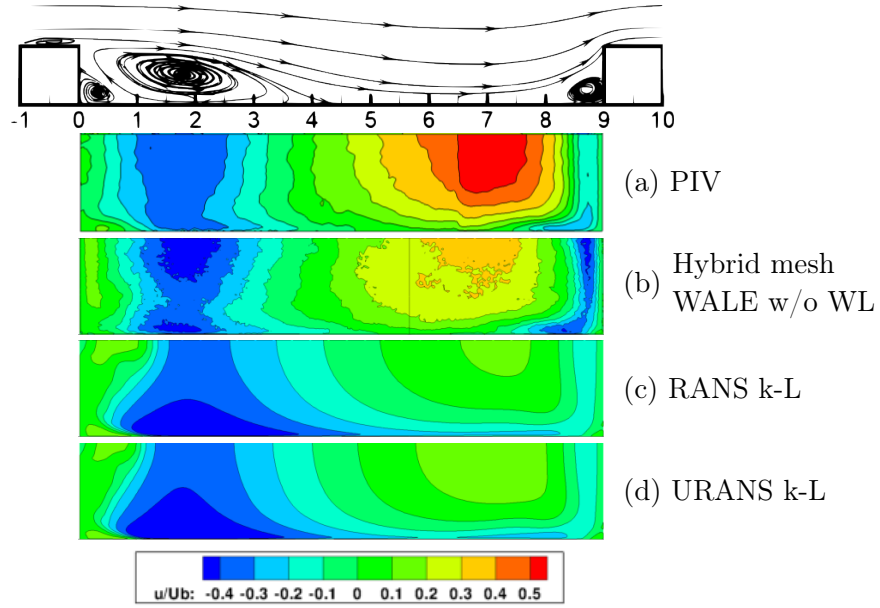


Figure 3.34: Comparison with PIV measurements of streamwise velocity in the near wall plane 1XZ ( $y/h = 0.05$ ) for LES with hybrid mesh M3.WALE and RANS. Flow is assumed to be symmetrical, only an half part of the 1XZ plane is presented for each case: symmetry axis at the top and wall at the bottom.

are of clear interest since most industrial cooling channels do not reach a fully developed state as evidenced in the experience and postulated in the periodic LES. Through such spatial simulations, one can illustrate and quantify such effects and differences.

Periodicity establishment is investigated from a statistically converged mean LES solutions obtained with the periodic M3 mesh and a spatial mesh. To do so, the finer mesh M2 is used as the reference case: the periodic solution from M3 and each of the 7 ribs of the spatial mesh are interpolated on M2 and Normalized Root-Mean-Square Deviation (NRMSD) are computed between the 3D fields of the periodic rib and each of the spatial ribs for the mean and fluctuating velocity components. If  $X_i^P$  is the value of the periodic mean solution (P) interpolated on the  $i^{th}$  point of the neutral mesh M2 made of N points, and  $X_i^{Sj}$  the value of the spatial mean solution of the  $j^{th}$  rib (Sj) interpolated on the  $i^{th}$  point of M2, then one obtains the NRMSD for each spatial rib spacing with Eq. (3.21):

$$NRMSD(P, Sj) = \sqrt{\frac{\frac{1}{N} \sum_{i=1}^N (X_i^P - X_i^{Sj})^2}{(\max(X_i^P) - \min(X_i^P))^2}} \quad (3.21)$$

Figure 3.35 shows the result of this analysis. All 6 curves follow the same evolution, ie. a high NRMSD at the first rib spacing, then a decreasing or more or less flat evolution from rib#2 spacing to rib#5 spacing with a NRMSD between 1.5% and 3.5%, to finally reincrease around the two last ribs spacing (except for the  $w$

component which stays flat at the end and even gets a bit lower). Such curves allow to draw two conclusions: first, since all the 6 components do not have a flat portion, 7 ribs are not enough and local effects avoid reaching a fully reference periodic regime. The most pathological case is for the  $u$  component, which has an inverted bell shape curve. The second conclusion is that there is a rib where one can assume a nearby periodic flow: for all curves NRMSD falls down to a minimum at the rib#5 spacing with NRMSD values below 3% for 5 of the 6 components, and below 4% for  $u$ .

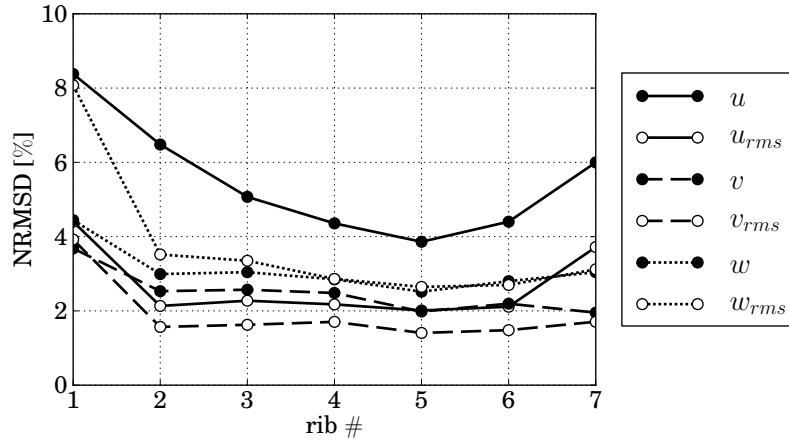


Figure 3.35: Deviation between periodic and spatial flow for mean and fluctuating velocity components

It must be noticed that for the needs of this analysis, since the periodic and spatial meshes were not exactly identical an interpolation has been used so an error has been introduced. Both cases are comparable here since they had the same process, but employing another neutral mesh for interpolation could slightly change the values of the results.

### 3.5.4 Heat transfer in the ribbed channel

The LES prediction of the flow topology in the ribbed channel has been presented in the previous section. High turbulence and mixing flow generated by the ribs have been enlightened. In this section, we focus on the purpose of such flows, that is increasing heat transfer at the wall. Therefore, comparisons of heat transfer efficiency wall maps are given here. These are obtained by LES, RANS and experimental measurements.

Figure 3.36 illustrates the heated ribbed channel LES in the symmetry plane. Instantaneous velocity and temperature fields, Fig. 3.36a and 3.36b respectively, show the unsteadiness of the flow in the channel with hot and cold air mixing. Mean fields of both quantities are given in Fig. 3.36c and 3.36d respectively after five through flow time. Periodicity previously analyzed in Fig. 3.35 is visible on the mean velocity map where characteristic mean flow patterns are recognized. The



mean temperature field shows a globally constant flow heating along the channel. More precisely, one can note hot air pockets behind each rib of equivalent size, except behind the first rib where the pocket is twice as large. Following the isothermperature contours in the channel also indicate a periodic pattern: first cold air is present near the channel top wall, then it is directed to the ribbed wall where it flows above the hot air pocket and plunges to the bottom wall following the flow reattachment, where it finally gets hotter.

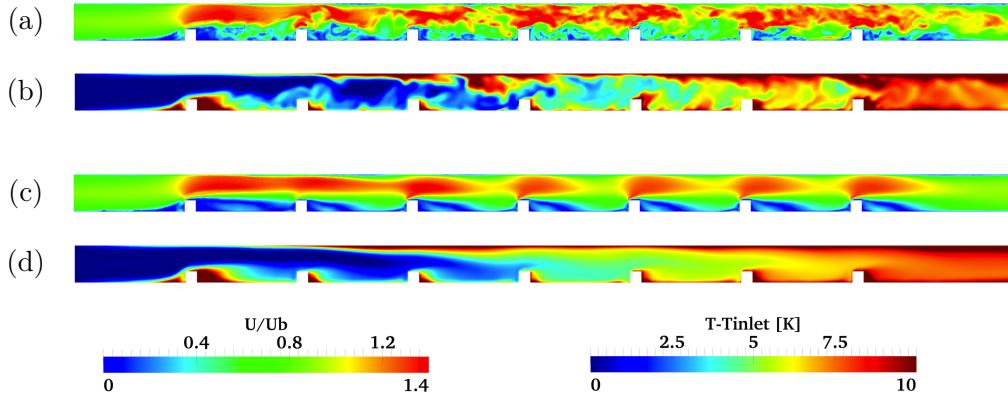


Figure 3.36: Instantaneous (a) and mean (b) flow LES computation of the spatial ribbed channel. Dimensionless velocity magnitude  $U/U_b$  (1) and fluid heating  $T - T_{inlet}$  (2) fields are given in the symmetry plane.

**Bulk temperature** In external flow heat transfer problems, a reference temperature can be easily chosen as the far-field temperature which can be considered as uniform. This choice is no more possible for internal flows where the flow is surrounded by hot or cold walls which makes the fluid temperature never really uniform, so that  $T = T(x, y, z)$ . To recover a similar concept of reference uniform temperature, the notion of bulk temperature  $T_b$  has been introduced for internal flows. The idea is to determine as reference temperature the temperature of a particular finite domain which would have been adiabatically well-mixed. The choice of this particular finite domain can be a hard task in a complex geometries, but in our case of internal forced convection situations, a common approach is to estimate  $T_b$  in a cross section of the pipe. Thus, a general definition of  $T_b$  could be evaluated as follows:

$$T_b = \frac{\text{enthalpy flow rate through a cross section}}{\text{heat-capacity flow rate through a cross section}} \quad (3.22)$$

Considering a compressible fluid, a general expression of  $T_b$  can therefore be written as:

$$T_b = \frac{\int_A \rho u c_p T \, dA}{\int_A \rho u c_p \, dA} \quad (3.23)$$

with  $A$  the cross section and  $u$ ,  $c_P$  and  $T$  the fluid velocity, heat capacity and temperature respectively of a fluid particle at the location  $dA$  on  $A$ . In our case and to be consistent with the experimental methodology,  $T_{ref}$  required for the  $Nu$  computation is obtained as Cakan [13] and explained in Section 3.2.2.

### Heat transfer on the wall between two ribs

In this section, previous LES and RANS results computed by Phibel [99] are compared against experimental data. Two models have been tested in his study [99]: the common  $k - \varepsilon$  model and the  $v2 - f$  model [82] which uses the streamline normal velocity fluctuations rather than the turbulent kinetic energy to compute the turbulent viscosity as well as the damping at the wall for the redistribution terms in the Reynolds stress equation.

Figure 3.37 shows the comparison of EF obtained from RANS, LES and measurements. Both RANS simulations give the same main pattern of EF on the wall between the two ribs: only one zone of high Nusselt number is detected in the middle of the wall, which is not present in the experimental thermography where a second high heat transfer zone in front of the rib is measured. LES reproduces both patterns very well and at better locations: between  $x/h = 3$  and 4.5 for LES and measurements but after  $x/h = 4.5$  for both RANS computations. The tightening of the isolines between  $x/h = 7$  and 8 towards the center of the channel is also well predicted with LES, which allows to draw the overall fish-tail shape of the pattern visible in the experiment.

Note that the maximum of enhancement factor is as well predicted by the RANS  $v2 - f$  model as by the LES ( $\sim 2.8 - 2.9$ ), whereas  $k - \varepsilon$  underestimates it by more than 20%. The LES overestimates the second zone in front of the rib with a level comparable to the maximum between  $x/h = 3$  and 4.5 instead of 2.19 in the measurements, that is an error of 30%.

Figure 3.38 presents the comparison of the EF on the 3 faces of the rib. This part is a very challenging zone to test the models since the fluid impacts these faces with very different angles and velocities depending on the faces.

LES and RANS show the same isoline pattern on the upstream surface, Fig. 3.38b and Fig. 3.38a respectively, which are not the same as for the experiment: the latter presents a bulge near both channel side walls (on top and bottom sides of Fig. 3.38c) while the isoline curvatures of the computations do not invert. Both models overestimate experimental findings since EF is measured between 1.9 and almost 3 while the numerics predict respectively more than 5 and 12 for RANS and LES.

It is noticed that LES detects very high EF values around the upstream corner of the rib (the right side of the upstream surface and the left side of the top surface). This behaviour is due to the fluid acceleration over the rib, for which mesh refinement at the upstream corner becomes too coarse for the high gradient in presence.

On the top surface, none of the models detects the maximum located in the middle of the rib. However, the order of magnitude is relatively well predicted,

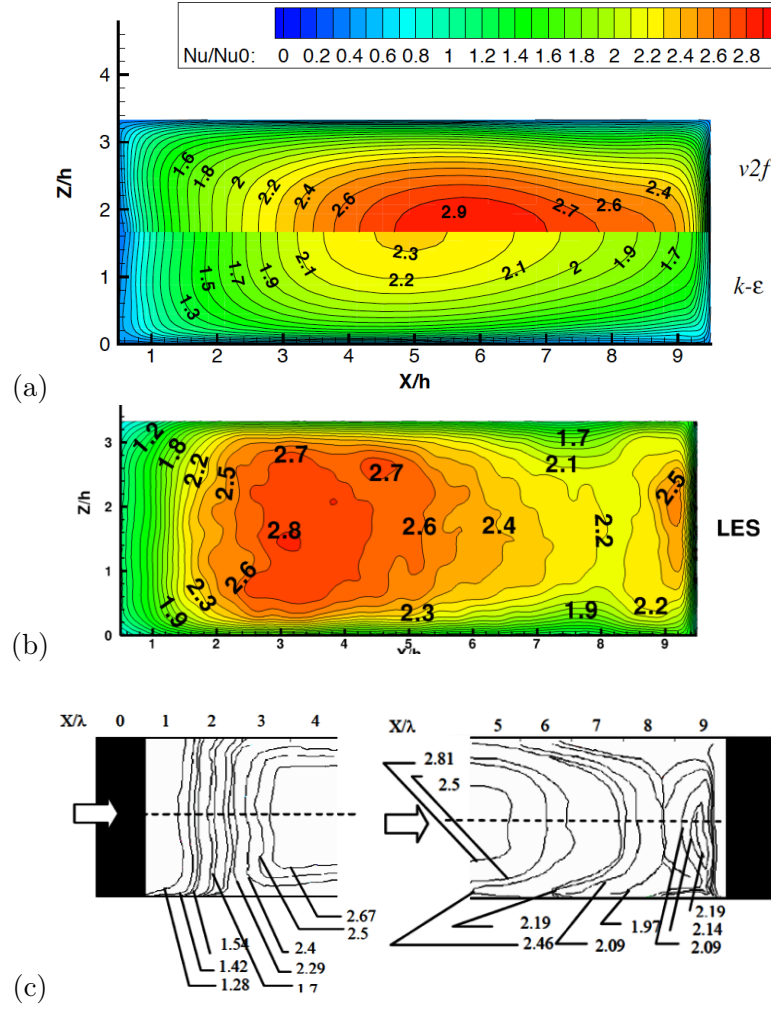


Figure 3.37: Enhancement factor on the wall between two rib for (a) RANS [99], (b) LES and (c) experimental data [13]

even it is slightly overestimated for the maximum value: measurements show EF being mainly between 2.5 and 3.1, and LES and RANS give a range from 2.5 to 3.5 (without taking into account the overpredicted left side).

The back rib side shows more differences between RANS and LES. Indeed, RANS predicts very low EF, mainly less than 1.1, whereas measurements give a range from 1.5 to 2. Patterns of RANS isolines are also completely different. Limits of this modeling are here pointed out: the massive recirculation, Fig. 3.12 ②, is badly computed by RANS resulting in wrong estimates of heat transfer behind the rib. In contrast, as seen in the aerodynamic results section, LES predicts very well all the recirculation zones in the channel yielding here a better EF field on the rib downstream face. Values from 1 to 2 are reached on the main part of the face, which is in good agreement with the thermal measurements, even if the elongated maximum zone in the middle of the face is not predicted.

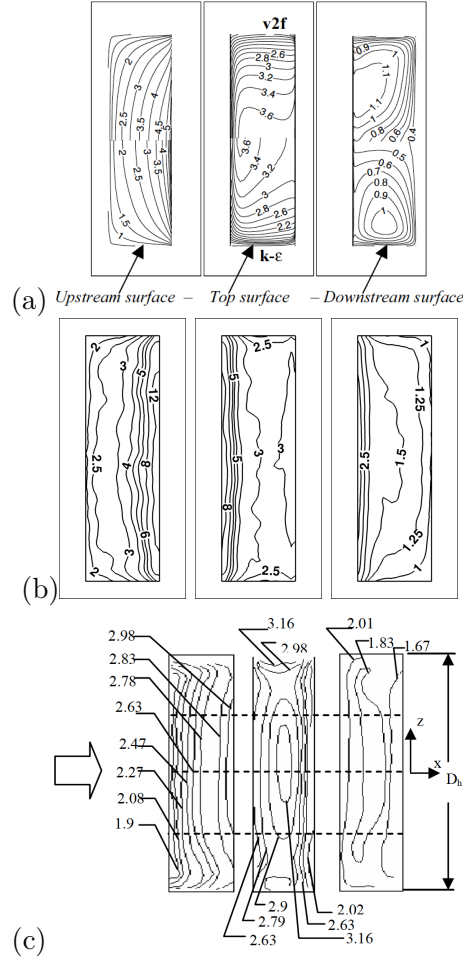


Figure 3.38: Enhancement factor on the rib wall for (a) RANS [99], (b) LES and (c) experimental data [13]

### 3.6 Conclusions

In light of the results presented in this chapter, conclusions can be reported on the LES methodology available for this operating point encountered in typical cooling channel geometries and in comparison to RANS:

- The selected approach for thermal and rotating studies of the ribbed channels is the following: the use of a fine mesh (i.e.  $y^+ < 10$ ) near the wall using hybrid approach (tetrahedron with one prism layer on all the wall) and perform a wall-resolved LES (with WALE). The use of a wall-law is however possible to reduce the computational cost on larger configurations.
- The periodicity is valid so that the methodology built on periodic simulations can be applied directly to more realistic spatial cases.

- Massive separations created in the cooling channels by the ribs and the  $180^\circ$  bend are seen to be handled with difficulties by RANS models: even if it is possible to obtain good prediction with a particular modeling, the lack of universal closure makes it a dangerous option to simulate such complex flows. By contrast, every LES test case (even poorly designed one) leads to similar mean and fluctuating flows in good agreement with measurements, showing its good reliability for this typical configuration. Note that if unsteady modeling has proven its interest, the associated requirement of more realistic unsteady boundary conditions for more accurate results has also been highlighted. Beside the proposed hybrid mesh approach, more fundamental researches on wall modeling remain however needed for fully predictive capabilities.
- The thermal behavior at the wall is seen to be strongly related to the near-wall flow topology: following this observation the thermal efficiency computed by LES is seen to be in very good agreement with experiments, as well for heat transfer levels or maps.

Finally, this chapter has validated the alternative approach based on hybrid meshes with prisms at the walls for the LES of ribbed channels. Significant computational time saving and preserved physical accuracy makes this strategy applicable to the more complex LES rotating studies which have been identified before the final application of the industrial cooling channel. In the next chapter, the LES approach with hybrid mesh is extended at this intermediate step with a same academic ribbed channel geometry from now on set in rotation. Flow modeling changes, aerodynamic and thermal predictions in this new non-inertial reference frame is therefore addressed.

# Internal cooling LES in rotating configurations

---

## Contents

---

<b>4.1</b>	<b>Physics and modeling of rotating flows</b>	<b>74</b>
4.1.1	General transformation	75
4.1.2	Governing equations in rotating frames	76
4.1.3	Rotation and shear	79
<b>4.2</b>	<b>Simulation of rotating channels with AVBP: method and sensitivity</b>	<b>82</b>
4.2.1	Modeling of rotating flows	83
4.2.2	Numerical method in AVBP	83
4.2.3	Validation test cases	84
4.2.4	Conclusion	86
<b>4.3</b>	<b>Experimental rotating test bench</b>	<b>86</b>
<b>4.4</b>	<b>Application of the rotating numerical methodology to the experimental ribbed channel</b>	<b>88</b>
4.4.1	Domain and boundary conditions	88
4.4.2	Expected flow topology	89
4.4.3	Sensitivity analysis	90
4.4.4	Results and interpretations	90
4.4.5	Conclusion	93
<b>4.5</b>	<b>LES of the VKI isothermal rotating ribbed channel: validation against experiment</b>	<b>93</b>
4.5.1	Mean effects of rotation on the near wall flow topology	94
4.5.2	Effect of rotation on the flow field around the ribs	98
4.5.3	Two-point correlations	103
4.5.4	Temporal vortex tracking	105
4.5.5	Conclusions on LES of rotating isothermal flows	111
<b>4.6</b>	<b>LES of the VKI anisothermal rotating ribbed channel: validation against experiment</b>	<b>112</b>
4.6.1	Mean temperature in the channel	113
4.6.2	Flow field around the ribs	115
4.6.3	Heat transfer at the ribbed wall	116
4.6.4	Conclusions on the anisothermal study	120

---

4.7 Conclusions on LES of rotating cooling channels . . . . . 120

---

In the previous chapter, the flow in non-rotating configurations has been studied to identify a numerical methodology for heat transfer predictions in ribbed channels. In this chapter, the latter recommendations will be applied to the similar straight ribbed channel configuration but with rotation. As a reminder, two non-dimensional numbers are proposed to evaluate the influence of the non-inertial forces issued by rotation. For isothermal flows, the rotation number  $Ro$  corresponds to the ratio between convection and Coriolis forces. Within the notations of this thesis and in the particular case of rotating channels,  $Ro$  can be expressed as:

$$Ro = \frac{\Omega D_h}{U_b} \quad (4.1)$$

where  $\Omega$  is the rotation rate,  $D_h$  is a characteristic length (chosen equal to the hydraulic diameter of the studied case) and  $U_b$  is the bulk velocity of the fluid. When the rotating flows become anisothermal, buoyancy forces issued by the non inertial forces may appear. The impact of the buoyancy is then quantified by the Buoyancy number  $Bo$ :

$$Bo = r\Omega^2 \frac{D_h}{U_b^2} \frac{T_w - T_b}{T_b} \quad (4.2)$$

$r\Omega^2$  being the centrifugal force while  $T_w$  and  $T_b$  are respectively the wall and bulk temperature.

Before simulating such flows, Section 4.1 describes theoretically the impact of rotation on the governing equations as well as their effects on the flow. The corresponding modeling adopted in the AVBP solver is then introduced in Section 4.2, before the presentation of the VKI experimental test bench for which the steady and unsteady data is presented in Section 4.3. The corresponding computational setup and parametric analyses are discussed in Section 4.4 in order to validate the behavior of the numerical tool in this rotating context. Finally, the LES of the rotating channel is investigated for isothermal and anisothermal flows and is compared to the experimental measurement providing mean and fluctuating velocity fields, two-point correlations and temporal analyses.

## 4.1 Physics and modeling of rotating flows

Rotation is one of the fundamental increments of motion. In fluid dynamics, its study has motivated a lot of works since it plays a major role not only in man-made rotating machines but also in the huge atmospheric or oceanic flows. In this thesis, we will only focus on the first type of application, but the latter should not be forgotten since it is at the root of several results on rotating flows [118, 49, 30].

This chapter is divided in three parts: first the theoretical description of a rotating motion for which the flow governing equations of Chapter 3 are extended

to take into account the rotating frame. A particular case of interest present in this thesis are sheared flows with background rotation which are also addressed at this occasion.

#### 4.1.1 General transformation

This section introduces the general physical framework for rotating frames and provides some definitions used to describe its impact on flow quantities.

##### Inertial frame of reference

By definition, a frame of reference  $\mathcal{R} = \{(O, \mathcal{B}), t_0\}$  allows to fix a space origin  $O$  and a temporal origin  $t_0$  from which an observer can define the notion of motion. The space origin is usually completed by an orthonormal vector basis  $\mathcal{B}$ , which is defined here in the three dimensional spatial case of interest by  $\mathcal{B} = (\mathbf{e}_1, \mathbf{e}_2, \mathbf{e}_3)$ . The derivation of the NS equations (Eq. 3.9) using Newton's second law of motion requires the assumption for the frame of reference to be inertial (or a Galilean reference frame). This kind of frame can be defined from Newton's first law as a frame where an object experiencing no net force has a constant velocity: the object is either at rest (if its velocity is zero), or it has a uniform straight motion (if its velocity is non-zero). A change of frames and of corresponding reference frame not satisfying these conditions are called *non-inertial* frames. Practically, a frame could be approximated as inertial depending on the space and time scale of the considered observed problem. In the following, an inertial (or assumed) frame of reference will be represented by  $\mathcal{R}$ , and a non inertial frame by  $\mathcal{R}^*$ . The respective relative variables are written with the following notation, i.e. without additional symbol in  $\mathcal{R}$  and with a star in  $\mathcal{R}^*$ .

##### Transformations

In this thesis only space transformations are considered, and a unique temporal origin is used. Possible space transformations between  $\mathcal{R}$  and  $\mathcal{R}^*$  are set under the Euclidean group of transformations composed by orthogonal transformations and translations, which can be generally written as:

$$\mathbf{x}^* = \mathbf{Q}(t)\mathbf{x} + \mathbf{b}(t) \quad (4.3)$$

where  $\mathbf{Q}(t)$  is an orthogonal matrix verifying:

$$\mathbf{Q}\mathbf{Q}^T = \mathbf{Q}^T\mathbf{Q} = \mathbf{I} \quad (4.4)$$

$\mathbf{I}$  is the identity matrix. The second term of Eq. 4.3,  $\mathbf{b}(t)$ , is the change of space origin. In all our rotating cases, no translation is assumed, i.e. we always have  $\mathbf{b}(t) = 0$ . In practical applications issued by typical aeronautical applications, one can note that accelerating transient phases exist for which  $\mathbf{b}(t) \neq 0$ .



### Definitions

The application of the change of observer, Eq. 4.3, may modify physical quantities. Particular dependencies can be categorized as follows:

- *invariant* quantities: a change of observer has no influence on the quantity observed in either frame. Typical example may be any scalar, specific vector or tensorial quantity  $\phi$  for which:

$$\phi^* = \phi$$

In fluid mechanics, invariant quantities can be for instance density  $\rho$  or temperature  $T$ .

- *objective* quantities: quantities that are invariant under translation  $\mathbf{b}(t)$  (or change of origin), i.e.:

$$\begin{aligned} \phi^* &= \phi && \text{for scalars,} \\ \phi^* &= \mathbf{Q}\phi && \text{for vectors,} \\ \Phi^* &= \mathbf{Q}\Phi\mathbf{Q}^T && \text{for second order tensors.} \end{aligned}$$

Examples of objective quantities are again density  $\rho$ , the heat flux vector  $\mathbf{q}$  or the strain rate tensor  $\mathbf{S}$ .

Note that quantities like the velocity vector  $\mathbf{u}$  or its gradient are not objective (and therefore not invariant) and will change under the action of  $\mathbf{Q}(t)$  and  $\mathbf{b}(t)$ . More details on their properties can be found in the work of Bertram [7].

#### 4.1.2 Governing equations in rotating frames

In this part, we will consider the governing equations of a fluid particle in a frame of reference  $\mathcal{R}^*$  rotating with a constant rotation speed around an axis  $\boldsymbol{\Omega}$  with respect to an inertial reference frame  $\mathcal{R}$ . Assuming a z-axis rotation with  $\boldsymbol{\Omega} = \Omega\mathbf{e}_3$ , which will be always the case in this chapter, the transformation applied is the following:

$$\mathbf{x}^* = \mathbf{Q}(t)\mathbf{x} \tag{4.5}$$

where  $\mathbf{Q}(t)$  is recast in a rotation matrix which simply writes:

$$\mathbf{Q}(t) = \begin{pmatrix} \cos(\Omega t) & -\sin(\Omega t) & 0 \\ \sin(\Omega t) & \cos(\Omega t) & 0 \\ 0 & 0 & 1 \end{pmatrix} \tag{4.6}$$

with  $\Omega t$  the rotation angle  $(\mathbf{e}_1, \mathbf{e}_1^*) = (\mathbf{e}_2, \mathbf{e}_2^*)$  between  $\mathcal{B}$  and  $\mathcal{B}^*$ .

### Navier-Stokes equations in a rotating frame

The expression of the NS equations 3.9 already assumes the presence of inertial forces caused by rotation for example if grouped in the body force term. Here, details are given on the expression of these inertial forces and a summary of the method required to identify them. Note that if needed more details on the observer change are given by de Laage de Meux [32].

Derivating the  $\mathbf{x}$  position of a particle in  $\mathcal{R}$  as a function of  $\mathcal{R}^*$ :

$$\mathbf{x} = \mathbf{Q}^T \mathbf{x}^* \quad (4.7)$$

one obtains the expression for velocity in the rotating frame  $\mathcal{R}^*$ :

$$\mathbf{u} = \mathbf{Q}^T (\mathbf{u}^* + \boldsymbol{\Omega} \times \mathbf{x}^*). \quad (4.8)$$

Likewise for acceleration and noting that density is invariant, i.e.  $\rho = \rho^*$  one gets:

$$\frac{D(\rho \mathbf{u})}{Dt} = \mathbf{Q}^T \left( \frac{D(\rho \mathbf{u}^*)}{Dt} + 2\rho \boldsymbol{\Omega} \times \mathbf{u}^* + \rho \boldsymbol{\Omega} \times (\boldsymbol{\Omega} \times \mathbf{x}^*) \right) \quad (4.9)$$

From Eq. 4.8 and 4.9, neither the velocity nor the acceleration are objective: a change of observer introduces the addition of a solid rotation term for the former, and two acceleration terms for the latter known respectively as Coriolis acceleration  $2\boldsymbol{\Omega} \times \mathbf{u}^*$  and centrifugal acceleration  $\boldsymbol{\Omega} \times (\boldsymbol{\Omega} \times \mathbf{x}^*)$ . Both accelerations are non-inertial forces usually included in body forces  $f_i$  introduced in Eq. 3.9. Note that to consider entirely the change of observer of the NS equations, two terms still remain and need to be evaluated: the pressure gradient and the viscous stress tensor. Pressure is invariant, since being a material and a thermodynamical scalar property, which leads to:

$$\nabla p = \mathbf{Q}^T (\nabla p)^* \quad (4.10)$$

The change of observer effects on the viscous stress tensor  $\boldsymbol{\tau}$  is not so direct. However, for a Newtonian fluid,  $\boldsymbol{\tau}$  is assumed to be proportional to the strain rate tensor, i.e. the symmetrical part of the velocity gradient  $\nabla \mathbf{u}$ . De Laage de Meux [32] shows that for a change of observer, with  $\dot{\mathbf{Q}}$  being the time derivative of  $\mathbf{Q}$  the latter can be expressed as :

$$\nabla \mathbf{u} = \mathbf{Q}^T ((\nabla \mathbf{u})^* + (\dot{\mathbf{Q}} \mathbf{Q}^T)) \mathbf{Q} \quad (4.11)$$

revealing that  $\nabla \mathbf{u}$  is not an objective variable. However noting that  $\dot{\mathbf{Q}} \mathbf{Q}^T$  is antisymmetric, one can decompose  $\nabla \mathbf{u}$  into  $\mathbf{S}$  and  $\mathbf{W}$ , respectively, its symmetric and antisymmetric parts, so that:

$$\mathbf{W} = \mathbf{Q}^T (\mathbf{W}^* + (\dot{\mathbf{Q}} \mathbf{Q}^T)) \mathbf{Q} \quad (4.12)$$

and

$$\mathbf{S} = \mathbf{Q}^T \mathbf{S}^* \mathbf{Q}. \quad (4.13)$$

Therefore, even if the antisymmetric part  $\mathbf{W}$  is modified just like  $\nabla \mathbf{u}$  by the change of observer, it is shown that the symmetric tensor  $\mathbf{S}$  is objective. Finally, thanks to the Newtonian fluid assumption where the viscous stress tensor is considered linearly dependent on the strain rate tensor  $\mathbf{S}$ , one can write:

$$\boldsymbol{\tau} = \mathbf{Q}^T \boldsymbol{\tau}^* \mathbf{Q} \quad (4.14)$$

Replacing the above expression terms in Eq. 3.9, one obtains the NS equations in a constant rotating frame of reference:

$$\frac{\partial(\rho \mathbf{u}^*)}{\partial t} + \nabla \cdot (\rho \mathbf{u}^* \otimes \mathbf{u}^*) = -\nabla p + \nabla \cdot \boldsymbol{\tau}^* - 2\rho \boldsymbol{\Omega} \times \mathbf{u}^* - \rho \boldsymbol{\Omega} \times (\boldsymbol{\Omega} \times \mathbf{x}^*) \quad (4.15)$$

In comparison to the NS equations written in an inertial frame of reference, two new additional terms previously introduced as body forces and function of the rotation vector  $\boldsymbol{\Omega}$  appear:

- *Coriolis force*  $\mathbf{f}_{co} = -2\rho \boldsymbol{\Omega} \times \mathbf{u}^*$ : applies perpendicularly to the velocity vector  $\mathbf{u}^*$  and the rotation vector  $\boldsymbol{\Omega}$ . This force will hence tend to curve the particle trajectories in the rotating frame relatively to the particle velocity magnitude and to the angle between this velocity and the rotation vectors. The amplitude of this bending depends on the Coriolis force magnitude reading:

$$\|\mathbf{f}_{co}\| = 2\rho \Omega \|\mathbf{u}^*\| \sin((\boldsymbol{\Omega}, \mathbf{u}^*)) \quad (4.16)$$

It has to be noted that since  $\mathbf{f}_{co}$  is perpendicular to the velocity vector, no work is created and therefore no energy is provided to the flow. A common manifestation of this force is observable in large scale motions of the Earth atmosphere: the moving air mass attracted by a low-pressure area is deflected by the Coriolis force to finally wind around the low-pressure region where an equilibrium between Coriolis and pressure forces exists.

- *Centrifugal force*  $\mathbf{f}_{ce} = -\rho \boldsymbol{\Omega} \times (\boldsymbol{\Omega} \times \mathbf{x}^*)$ : in contrast to the Coriolis force, the centrifugal force does not depend on the flow velocity, but only on the distance  $r$  from the rotation axis which is in our case  $r = \|\mathbf{x}^*\| \sin((\boldsymbol{\Omega}, \mathbf{x}^*))$ . Any fluid particle not on the rotation axis will hence feel the centrifugal force whose amplitude equals:

$$\|\mathbf{f}_{ce}\| = \rho \Omega^2 r \quad (4.17)$$

This time, since the centrifugal force does not depend on velocity, creation of work is possible and energy can be transferred to or extracted from the flow resulting in a pressure gradient. The centrifugal force is commonly used to increase the fluid pressure (good examples are radial compressors of gas turbines) or to separate components of different densities present in a mixture.

### Effect of rotation on turbulence and on energy transfer

The influence of rotation on turbulence can be observed by decomposing the velocity vector in its mean and fluctuating parts. For rotating frames, one can show that the mean velocity has the same transformation as the instantaneous velocity, i.e.:

$$\bar{\mathbf{u}} = \mathbf{Q}^T (\bar{\mathbf{u}}^* + \boldsymbol{\Omega} \times \mathbf{x}^*) \quad (4.18)$$

and the fluctuating part is objective:

$$\mathbf{u}' = \mathbf{Q}^T (\mathbf{u}')^* \quad (4.19)$$

Therefore one can deduce that the Reynolds stress tensor  $\bar{\boldsymbol{\tau}}^t$  such as  $\bar{\tau}_{ij}^t = -\bar{\rho} \widetilde{u'_i u'_j}$ , which is obtained from operations preserving objectivity in the NS equations, is also an objective tensor:

$$\bar{\boldsymbol{\tau}}^t = \mathbf{Q}^T (\bar{\boldsymbol{\tau}}^t)^* \mathbf{Q}^T \quad (4.20)$$

These deductions allow to write the Reynolds stress tensor transport equation in the rotating frame as detailed by de Laage de Meux [32]. Only the Coriolis force remains in this equation through a term  $\mathbf{G}^*$  called *Coriolis production*:

$$\mathbf{G}^* = -2\boldsymbol{\Omega} \times (\bar{\boldsymbol{\tau}}^t)^* - 2(\boldsymbol{\Omega} \times (\bar{\boldsymbol{\tau}}^t)^*)^T \quad (4.21)$$

It has to be noticed that  $\mathbf{G}^*$  is traceless, which means that it does not appear in the turbulent kinetic energy transport equation. The Coriolis production term is thus a redistribution term. The Coriolis effect, and therefore rotation, has only a role on the turbulence anisotropy redistributing energy between the different components of the Reynolds stress tensor, without increasing or decreasing its trace.

Note that it has been observed that rotation modifies the turbulence energy spectrum through more complex phenomena which are still under debate. The common observation is that rotation decreases the energy decay rate [128].

#### 4.1.3 Rotation and shear

In channel configurations, the flow is also exposed to shear due to the boundary layer on walls for example. The superimposition of the rotating background with the shear present in a flow has already been widely studied [65, 109, 127, 131]. In general, rotation impacts greatly such flows when the gradient is normal to the plane  $(\bar{\mathbf{u}}, \boldsymbol{\Omega})$ , i.e. when the rotation vector  $\boldsymbol{\Omega}$  and the main flow vorticity due to the shear are aligned. When the mean flow tends to rotate in a sense identical / opposite to that of the background flow, the rotation is called cyclonic / anti-cyclonic respectively, following the meteorology terminology to describe a rotating air mass in comparison to the rotation of the earth. Well-known behaviors are then induced: the flow can be rather *stabilized* or *destabilized*, and the Coriolis force tends to damp or amplify respectively a fluctuation of a fluid particle. In terms of terminology, a cyclonic

rotation is associated with the amplification process, while anti-cyclonic rotation is linked to damping.

This categorization is however limited, in the sense that destabilization only occurs in an interval of anti-cyclonic rotation as shown by Bradshaw in 1969 [11] with a common criterion based on an analogy on stabilization/destabilization of gravity stratified flows, Eq. 4.22. This criterion uses  $R = 2\Omega/W$ , the ratio between twice the background rotation rate and the local vorticity, which is equal to the opposite of the shear rate in pure shear flows.

$$B = R(R + 1) \quad (4.22)$$

Bradshaw's criterion indicates that the flow is unstable for  $B < 0$  and stable for  $B > 0$ , while  $B = 0$  is a neutral case. This leads to a condition on  $R$  for destabilization  $-1 < R < 0$ , i.e. when the background vorticity is opposite and lower than the local vorticity. This conclusion is supported by the work of Cambon et al. [15] where a linear stability analysis is performed to assess Bradshaw's criterion on more general flows (other than pure shear with rotation).

### Application to a channel flow

As introduced in the previous paragraph, the stabilization and destabilization of a shear layer influence rotating flows. Here rotating flows in channels are addressed for the case of orthogonally rotating channels for which the background rotation and the local vorticity are aligned. Academical rotating channel flows are first described below and the hypothese for more realistic channels are proposed.

**Developed infinite aspect ratio channel** Let's first consider the simple case of a 2D channel flow in the  $(x, y)$  plane or an infinite 3D channel rotating around the  $z$  axis, Fig. 4.2. In such a channel, the Coriolis force is balanced by a wall-normal pressure gradient. As a consequence and following the direction of the flow (i.e. radially outward or inward), the leading and trailing walls become pressure (or anti-cyclonic) and suction (or cyclonic) sides. Based on the stability behaviors identified above, boundary layers on the pressure side will be destabilized, while the one on the suction side will be stabilized.

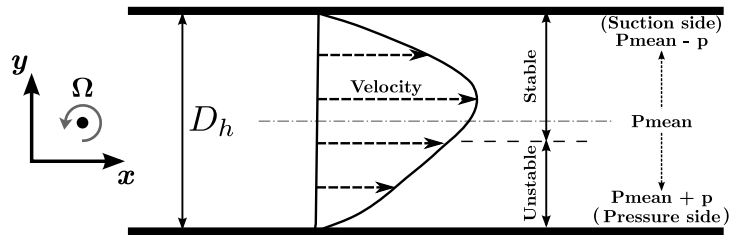


Figure 4.1: A schematic of the 2D rotating channel with mean flow.

The main impact on the flow quantities is a change of near wall turbulence level. More precisely, the stabilized (destabilized) side sees a decrease (increase) in turbulence intensity, implying a symmetry loss of the main flow velocity profile. Previous observations have been experimentally reported by Johnston [65] and later confirmed by the DNS of Kristoffersen [72]. Between both walls, one can also notice the presence of a zero absolute vorticity region where local vorticity is balanced by the background vorticity, i.e. when  $W = -2\Omega$  ( $R = -1$ ). This region is visible on the mean velocity profile where the slope  $d\bar{U}/dy = -W$  is equal to  $2\Omega$ . Other and more recent DNS computations by Lamballais [75] and Grundestam [52] have permitted to explore a wider range of rotation rates revealing different regimes leading to a possible classification, summarized below.

- $Ro < 0.2$ , low rotation rate: flow stabilization and destabilization is already observed with the above mentioned consequences on turbulence and velocity profile. An other flow feature appearing at this regime has been noticed, like long streamwise vortices commonly called Taylor-Görtler (TG) vortices [37]. These unstable structures are preferentially spotted on the pressure side according to the work of Kristoffersen [72].
- $0.5 < Ro < 1.5$ , moderate rotation rate: TG vortices are no more present and the zero absolute vorticity region extends. The flow on the suction (stabilized) side gets closer to a laminar flow, while a peak of turbulence is reached on the pressure (destabilized) side. For  $1.5 < Ro < 2$  all turbulent quantities are seen to decrease.
- $Ro > 2$ , high rotation rate: the laminar flow grows and takes over the turbulent part so that the velocity profile becomes similar to the Poiseuille parabolic profile. Grundestam [52] introduces the rotation number  $Ro_{lam}$  for which the total laminarization occurs: assuming that the laminar velocity profile is the asymptotic limit of the flow solution, he determines the point where the  $2\Omega$ -slope zone is confined near the wall and is equal to the laminar velocity profile slope at the wall, i.e.  $2\Omega = dU_{wall}^{lam}/dy$ . For a plane channel, this equation leads to  $Ro_{lam} = 3$ , which has been confirmed by DNS.

Figure 4.2 presents the mean velocity profiles computed by Grundestam [52] for eight rotation rates from  $Ro = 0$  to  $Ro = 3.0$ . The aforementioned description is recognizable with a large  $2\Omega$ -slope turbulent zone for  $0.5 < Ro < 1.5$  and the gradual transition to the laminar profile for  $Ro > 2$ .

**Realistic channel** This paragraph presents some limitations and modifications of the previous analysis made for fully developed infinite aspect ratio channels. Although of great value, these observations may have limited impact on real industrial configurations and the intent is to get closer to the more realistic case of this thesis. For helicopter turbine cooling channels, two main assumptions are more likely not applicable: the *developed flow* and the *infinite aspect-ratio*. For the first property, a

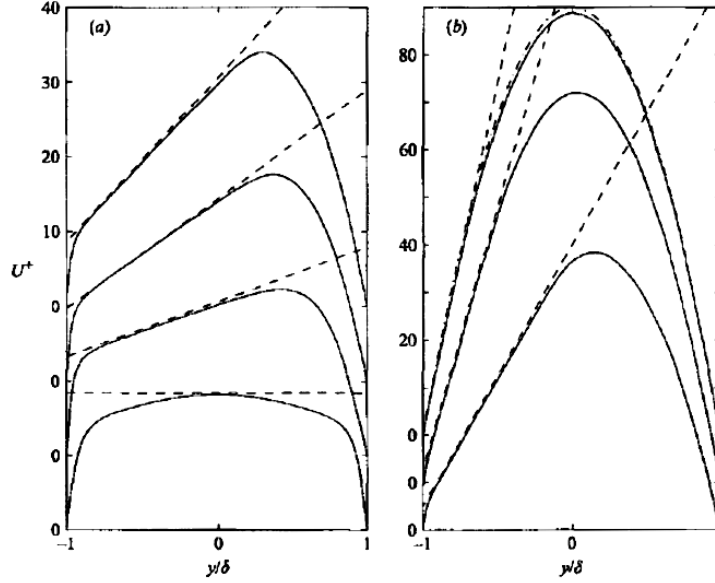


Figure 4.2: Mean velocity profiles,  $U^+$ , (a) for  $Ro = 0, 0.43, 0.77$  and  $0.98$  (—) and (b) for  $Ro = 1.5, 2.06, 2.49$  (—) and  $3.0$  (-·-). ---,  $2\Omega$ -slope lines. From the DNS of Grundestam [52].

developed flow can be assumed only in significantly long channels. In the rotating ribbed channel case of interest, Sewall [115] has measured a turbulent developed flow near the ribbed wall after the third rib, and only after the eighth rib on the channel centerline. In our application, a turbine blade cooling channel in a aircraft engine, the length of the channel may thus not be long enough if compared to this last criterion. The second property of infinite aspect ratio may also not be valid. Experimental and industrial channels of this thesis have aspect ratios between 1 and 3. So, side walls have clearly to be taken into account and the slower moving fluid particles will induce non-uniform Coriolis forces in the spanwise direction (i.e.  $z$  direction following the simplified notation of this chapter). An imbalance between the Coriolis forces and the pressure forces is expected which will deviate fluid from the pressure side toward the suction side, generating a large streamwise secondary flows (Ekman layer flows [38]).

## 4.2 Simulation of rotating channels with AVBP: method and sensitivity

The theoretical rotating channel flow behavior has been presented in the previous section. Here, the modeling of such flows by LES and with the AVBP solver is introduced. The primary objective of the section is thus to describe the numerical procedure adopted while providing a first assessment of the method. Note that in

the following, the rotating frame is chosen as the default frame of reference, and the star symbol will be omitted for corresponding variables.

#### 4.2.1 Modeling of rotating flows

The main approach used in numerical studies of rotating flows is classically to choose the rotating frame as the reference frame, and therefore to add the Coriolis and the centrifugal forces to the NS equations to take into account the change of frame (see all the references of rotating channels in Tab. 2.4 in Chapter 2). Naturally, this simple method is sufficient considering a DNS computation for which geometrical simplifications are introduced. For real industrial flows, turbulence modeling is mandatory, which raises new questions: what does the change of frame imply on the modeling? This question has been studied very early on [122] and has led to the conclusion that most of the classical models are, in their original form, incompatible with the rotating frame of reference. Indeed, closures are often obtained without taking into account the rotating frame, or simply performed with objective variables. This is for example the case for the classical  $k - \varepsilon$  RANS model where the Reynolds stress tensor is modeled considering that it is proportional to the shear stress tensor. As shown before this tensor is objective, and the turbulent viscosity, being the factor of proportionality, is built from energetic quantities  $k$  and  $\varepsilon$  modeled also from objective quantities. Therefore, even if the Coriolis force is added and seen by the mean flow, it can be concluded that rotation is invisible to the turbulence  $k - \varepsilon$  modeling. De Laage de Meux [32] gives a detailed analysis of classical RANS and LES models used in a rotating frame. Original and corrected models are compared in an academic rotating channel configuration using DNS validation data.

For our cases, a non-conventional approach is adopted to simulate rotating flow: instead of the rotation frame, an inertial frame is used as reference frame. Indeed thanks to a numerical tool already implemented in the AVBP solver, the numerical domain can be set in rotation, which means practically that a circular movement is given to all the mesh points. This approach removes the need for correcting the NS equations and the turbulence modeling since rotation is transmitted implicitly to the flow through moving boundaries and mesh points.

#### 4.2.2 Numerical method in AVBP

To set numerically a rotating channel, the Arbitrary Lagrangian Eulerian (ALE) description given by Hirt et al. [56] is used thanks to its implementation by Moureau [90]. This approach allows mesh nodes to be moved in some arbitrary fashion regardless of the particle motions. This ALE method has already been validated in previous works on piston and rocket engines [51, 106]. In our case, the mesh movement is chosen to be equivalent to a constant rotation, chosen in this chapter around the  $z$  axis. This type of motion has not been performed before within CERFACS, so a validation test case is provided in the following. The advantage is that the flow is solved in a fixed frame of reference, and no need of direct correction due to the change of



frame is required for the NS equations and the turbulence modeling. The disadvantage is the need to reconstruct the field in the rotating frame for post-processing. Since AVBP solves the compressible NS equations, a smooth ramp is also applied before reaching the final constant rotation speed to avoid pressure oscillations due to spurious transitional steps between the initial stationary and rotating states.

Note that the ALE induces additional computational time, giving in the present work a cost increase between 1.4 and 1.5 times the static case. The ALE used here is a general formulation taking into account at the same time the node movement and the cell volume variation. Only the former is required for a solid rotation motion, so the latter should be suppressed in a computational time optimization strategy.

### 4.2.3 Validation test cases

Physical modifications appearing in rotating flows are represented by two distinct effects caused by the centrifugal and Coriolis forces. In this section, each of them are investigated separately in order to assess the validity of the numerical method chosen for rotation. Simplified geometries are used following the experimental VKI ribbed channel test case characteristics [33] which will be used for comparison and presented in the Section 4.3.

#### Centrifugal effect

As explained previously (Section 4.1.2), the centrifugal force generates an additional pressure gradient in a flow regardless of the fluid motion. Therefore, a simple numerical test case has been set up consisting of a rotating rectangular box filled with air with all boundaries being adiabatic walls, Fig. 4.12. The dimensions of the box are the same as for the experimental test case, i.e. 760 mm  $\times$  83 mm  $\times$  75 mm following respectively  $x$ ,  $y$ , and  $z$  directions at the initial position. The box is also set in rotation with the same rotation rate as in the experiment, that is 13.5 rad/s with respect to the  $z$  axis. Note that the box center is located 580 mm away from the rotation axis.

Theoretically, assuming that  $\mathbf{u} = 0$  in the rotating reference frame, Eq. 4.15 becomes:

$$\nabla p + \rho \mathbf{\Omega} \times (\mathbf{\Omega} \times \mathbf{x}) = 0 \quad (4.23)$$

In a cylindrical coordinate system with associated basis  $(\mathbf{e}_r, \mathbf{e}_\theta, \mathbf{e}_z)$ , the case can be reduced to a one dimensional problem in  $\mathbf{e}_r$ . Therefore with  $\mathbf{\Omega} = \Omega \mathbf{e}_z$  and  $\mathbf{x} = r \mathbf{e}_r$  one obtains the radial pressure gradient expression to be:

$$\frac{\partial p}{\partial r} = \rho r \Omega^2 \quad (4.24)$$

Figure 4.4 gives a comparison between the theoretical centrifugal pressure gradient from Eq. 4.24 and the LES pressure gradient in the rotating rectangular box determined on a radius. The superposition of the two lines shows that the centrifugal effect is correctly reproduced with the ALE rotating method.

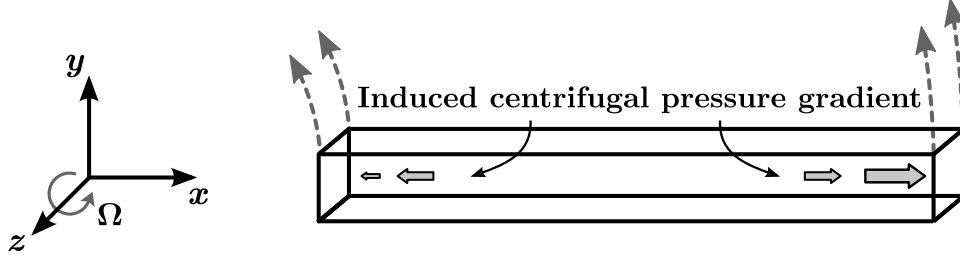


Figure 4.3: Scheme of the centrifugal effect validation test case: z-axis rotating rectangular box. Filled grey arrows show the expected direction and strength of the induced centrifugal pressure.

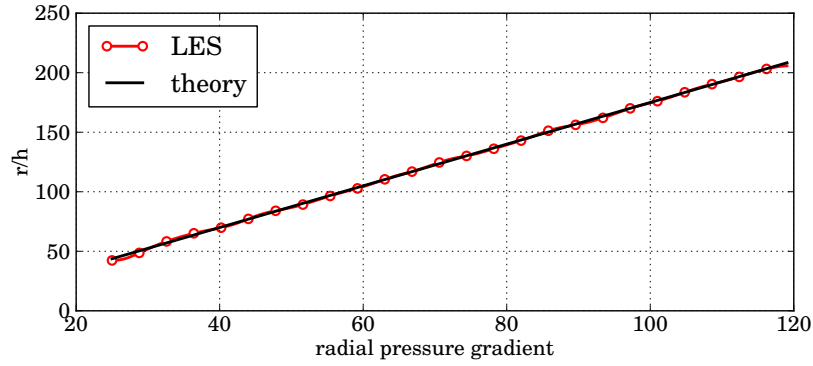


Figure 4.4: Comparison between the theoretical centrifugal pressure gradient of Eq. 4.24 and the pressure gradient in the rotating rectangular box determined on a radius.

### Coriolis effect

A validation of the Coriolis effect requires a non-zero velocity, so the previous closed rectangular box is modified by replacing two opposite parallel walls into a flow inlet and a flow outlet to create a channel. Figure 4.5 depicts the test case with fluid flowing radially outward in the same fashion as in the experimental ribbed channel, i.e.  $Re = 15\,000$  and  $Ro = 0.38$ .

In this case, assuming that  $u \gg v, w$  in the rotating frame of reference, and looking at the  $y$  component of Eq. 4.15 to suppress the centrifugal term, one obtains (with  $\frac{\partial v}{\partial t} \sim \frac{\partial v}{\partial x_i} \sim 0$ ) an approximation of the  $y$ -axis pressure gradient:

$$\frac{\partial p}{\partial y} \approx -2\rho\Omega u \quad (4.25)$$

Figure 4.6 presents the mean pressure gradient profile extracted from a mean LES result along 15 regularly spaced  $y$  lines in comparison to the analytic pressure gradient solution of Eq. 4.25. The mean of the 15 profiles shows a very good agreement under the assumed hypotheses. Small discrepancies can be caused by the

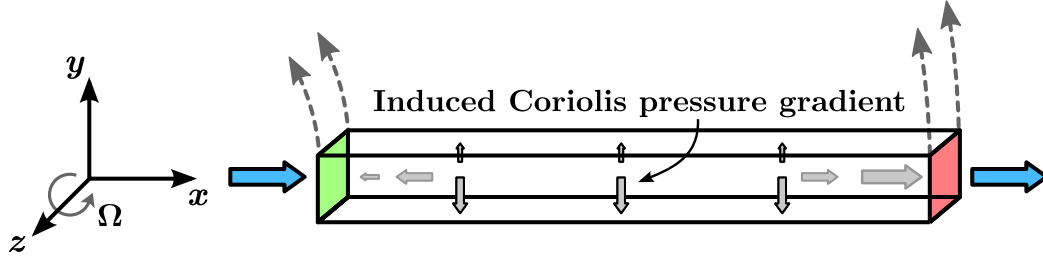


Figure 4.5: Scheme of the Coriolis effect validation test case: z-axis rotating smooth channel. Fluid flows radially outward following blue arrows from green face to red face. Filled grey arrows show expected direction and strength of the induced centrifugal and Coriolis pressure, with respectively light and dark contour.

influence of secondary flows appearing in such rotating channel flows (i.e. streamwise counter rotating vortices) making a non-negligible velocity component  $v$ .

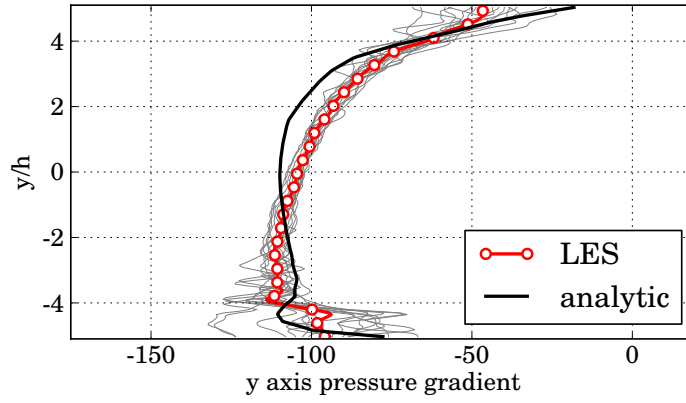


Figure 4.6: Comparison between computed and analytic Coriolis pressure gradient  $2\rho u\Omega$  in a smooth rectangular channel. The red line with symbols represents the mean of 15 pressure gradients determined along the channel (grey curves)

#### 4.2.4 Conclusion

In this section, a numerical methodology is proposed to handle rotation with the AVBP solver based on the existing ALE method. Both centrifugal and Coriolis terms appearing in the rotating frame of reference have been found to be in good agreement with the theory in geometrical configurations similar to the experimental ribbed channel, described in more details in the following sections.

### 4.3 Experimental rotating test bench

From the discussion of Section 4.2.3, a need for a representative experimental setup is clearly required to explicitly assess the LES of rotating complex ribbed channels.

To evaluate LES in this rotating context the experimental test case of the recent VKI rotating bench by Di Sante [33] is proposed. This facility has the particularity of having an on-board PIV system allowing measurement of classical mean quantities from uncorrelated time windows, but also of fluctuating quantities resolved in time. These two aspects are ideal to compare unsteady results obtained by LES. This section is dedicated to the presentation of the experimental test bench including its geometrical description and its measurement abilities.

Figure 4.7(a) depicts the apparatus of the rotating facility. The model is a straight one-ribbed wall channel fixed to a wooden disk, which can rotate. The air flow is generated by a stationary centrifugal pump and sent in the disk hollow rotating shaft. A 90° elbow allows to connect the shaft to the channel where air flows outwards in the radial direction. Honeycombs are located at the entrance and at the outlet of the channel to reduce the disturbances coming from the elbow and the ambient cross flow respectively. The wooden disk can rotate in the clockwise / counter-clockwise direction allowing to set the ribbed wall respectively as the leading / trailing wall. Figure 4.7 (b) shows a lateral sketch of the test channel. It is a 760 mm rectangular channel made of Plexiglas with a hydraulic diameter  $D_h = 4ab/2(a+b) = 79$  mm, with  $a = 83$  mm the height of the channel and  $b = 75$  mm its depth. Eight ribs perpendicular to the flow direction are fixed to the short wall and are parallel to the axis of rotation. Ribs have an  $8 \times 8$  mm<sup>2</sup> section and are spaced with a pitch of 80 mm. The characteristics of the channel are summarized in Tab 4.1.

Table 4.1: Summary of ribbed channel characteristics used for rotational analysis

height	$a = 83$ mm
depth	$b = 75$ mm
$D_h$	79 mm
length	760 mm ( $9.6D_h$ )
rib height $h$	8 mm
pitch $p/h$	10
blockage ratio $h/D_h$	0.1

The flow considered has a Reynolds number  $Re = U_0 D_h / \nu = 15\,000$ , based on  $U_0$  the bulk velocity,  $D_h$  the hydraulic diameter and  $\nu$  the kinematic viscosity. The measurements for this study are performed at 130 rpm leading to a rotation number  $Ro = 0.38$ . These two parameters are representative of internal cooling channels within industrial turbine blades. For this condition, flow measurements have been carried out with Particle Image Velocimetry (PIV) in the channel symmetry plane thanks to a system directly mounted on the disk (therefore stationary with respect to the channel even if it is rotating). Several windows, shown in Fig. 4.7 (b), have been measured:  $pa$  and  $pb$  to measure inlet flow injection and  $p1$  to  $p4$  to analyze the flow around rib 6 and rib 7. Besides classical average measurements and thanks to the embedded PIV system, time-resolved recordings have also been performed

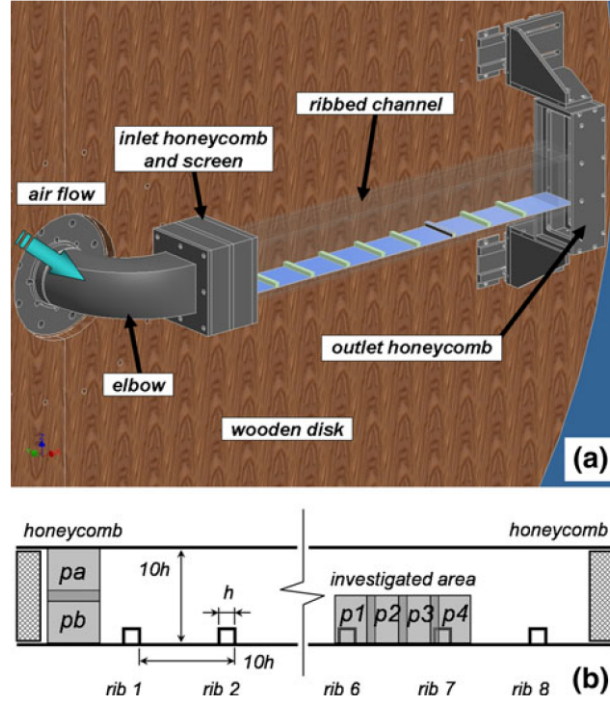


Figure 4.7: Experimental test bench: three dimensional view (a) and schematic lateral view (b, not in scale) - with the courtesy of Coletti [23]

and can thus be compared to the unsteady LES flow predictions. Further details on the experimental procedure are given by Coletti [23].

#### 4.4 Application of the rotating numerical methodology to the experimental ribbed channel

The smooth and fully developed rotating channel theory has been recalled and is the subject of numerous existing studies as well as validations of numerical methods [65, 127, 72, 75, 64, 52]. However and as already discussed at the end of Section 4.1.3, these experimental cases introduce some assumptions more likely invalid for turbine blade cooling channels indicating the need of further preliminary numerical analyses and validation to determine the best methodology to adopt in the final industrial application. To measure the influence of the different physical and numerical parameters, this section provides a sensitivity analysis of one of the turbulent rotating cases, i.e. the destabilized one. Below and before this study, a description of the numerical setup is given to justify the choice of the believed dominant parameters.

#### 4.4.1 Domain and boundary conditions

**Numerical domain** The numerical domain for the LES is chosen to be the entire channel of the experiment, which means that all the geometrical parameters of Table 4.1 are used accordingly and as illustrated by Fig. 4.8. The domain is discretized following the hybrid method proposed in Chapter 3 consisting in tetrahedral cells in the main channel and a single prismatic layer on all walls.

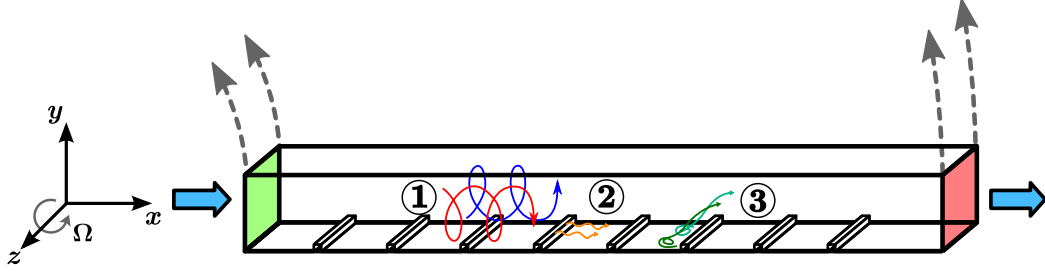


Figure 4.8: Numerical domain: channel with 8 ribs, fluid inlet in green near rotation axis, fluid outlet in red far from rotation axis. Numbers indicate flow mechanisms observed in rotating ribbed channel.

To satisfy the compromise between a wall-resolved LES computation and an industrial requirement of a not too expensive computational cost, the global mean  $y^+$  is set under 5 in the region of interest: i.e. around the ribs. With the present hybrid mesh,  $x^+$  and  $z^+$  are around  $5y^+$ . The opposite smooth near wall region is discretized with the same or lightly coarser wall resolutions (mean  $y^+$  equal to 6). Note that two resolutions for the top wall lead to similar results and the coarser resolution is used for computational efficiency.

**Boundary conditions** A priori reference boundary conditions are presented here following the methodology of the static channel. The position of the different boundary conditions of the domain is given in Fig. 4.8. In green, the inlet boundary condition imposes a theoretical turbulent mean velocity profile with a bulk velocity of 2.8 m/s and a temperature of 293 K. Outlet boundary condition (in red) imposes a uniform ambient static pressure (ie. 1013 hPa) with the NSCBC conditions [101]. All other (white) surfaces are set as adiabatic no-slip wall conditions.

#### 4.4.2 Expected flow topology

In comparison to a smooth infinite aspect ratio channel, new major flow features are expected in the rotating ribbed channel portrayed in Fig. 4.8. Some are already present in static channels. Shear layers behind the ribs give rise to a large recirculation bubble, Fig. 4.8 ②, which is then deviated by the near side wall of the following rib, Fig. 4.8 ③. Note also that as previously introduced, side walls induce non-uniform Coriolis forces which generate new large secondary flows: two stream-wise counter rotating vortices are superimposed onto the mean flow, Fig. 4.8 ①.

These two counter rotating vortices will tend to push the flow toward the pressure side, that is the ribbed / smooth wall for counter-clockwise / clockwise respectively, where the velocity and turbulence are expected to be increased.

#### 4.4.3 Sensitivity analysis

New parameters absent or non-significant in the static case have to be assessed in the context of rotation as described in the list below. Their influence will be observed on the mean global flow first and then locally around the ribs where experimental data are available.

- Rotation rate: as explained in the rotation regime classification of Section 4.1.3, different rotation rates induce different flow behaviors. A computation has therefore been done at a higher rotation rate than in the experiment (namely  $Ro = 0.54$  versus  $Ro = 0.38$  for the experiment) to confirm this influence which needs to be captured numerically.
- Channel length: one of the difficult points of the experimental channel modeling is its outlet where the flow comes out in the laboratory room through a honey comb. In the reference case the numerical domain stops before the honey comb and the potential influence of a longer outlet boundary condition with uniform pressure is evaluated.
- Velocity profile of the inlet boundary condition: in the stationary case of the last chapter, no experimental inlet information was available and the turbulent flow was assumed to be mainly generated by the ribs, because of their high blockage ratio (30%). Here, experimental measurements provide an inlet velocity profile so it is possible to assess the previous assumption which may be emphasized because of the lower blockage ratio (10%). A computation with a theoretical  $1/7^{th}$  turbulent velocity profile is thus tested. Fluctuations have also been measured by PIV (1% in the core flow, 3% near the wall), but here only the mean velocity profile is changed.
- Pressure outlet boundary condition: in rotating domains a wall-normal pressure gradient is present because the Coriolis forces act along the channel. The potential effect due to the imposition of a constant pressure gradient equal to the theoretical one has thus been evaluated and compared to the uniform outlet pressure computation.

#### 4.4.4 Results and interpretations

To quantify the influence of the retained parameters, the choice has been done to compare the modification of the axial velocity in the symmetry plane of the channel. The reasons are that the axial velocity component is the major contributor to the Coriolis force in this channel and the symmetry plane is the location where experimental data is available.

Before looking at the comparisons, a presentation of the reference case has to be done. Figure 4.9 displays the non-dimensional mean axial velocity component computed in the symmetry plane of the rotating channel (reference value). One can notice several observations:

1. The flow does not reach a fully developed state in the computational result, even if the zone above the two last ribs seems to approach it. Only comparisons with experimental data will therefore be thoroughly made in these cases.
2. Imposing a theoretical turbulent inlet velocity profile results in a high velocity core flow (circled zone on the left). This induces higher Coriolis forces in the channel center than with a flatter inflow profile which may yield more importance to the secondary flows.
3. Two streamwise near wall counter rotating vortices appear on the smooth wall around the half of the channel length. Their trace is visible in the second circled zone where the axial velocity reincreases near the top wall. These vortices seem to be generated by the large secondary flow and may therefore be a footprint of the strength of the latter.

The three points listed above are chosen to be indicators for the global comparison of the mean flow response in the symmetry plane to the parameters summarized in Table 4.2.

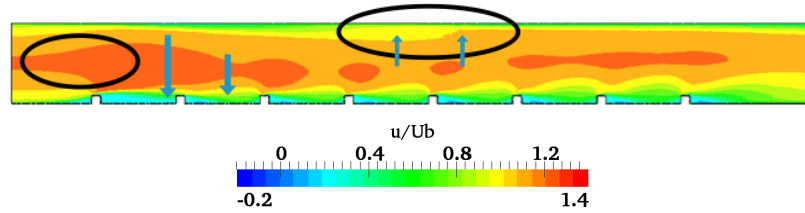


Figure 4.9: Non-dimensional mean axial velocity component in the symmetry plane of the rotating channel reference case

Figure 4.10 presents comparisons between the physical parameters of the two first lines of Table 4.2: the rotation rate and the channel outlet length. Compared to the reference case of Fig. 4.10a or the extended case of Fig. 4.10c, these two different conditions do not yield major changes in the axial velocity distribution in the symmetry plane. The flow development reaches the same level and smooth wall vortices appear at the same location. On the other hand, a change of the rotation rate, Fig. 4.10b, modifies the mean flow globally. This is expected since the rotation rate directly plays on the Coriolis force, which is one of the major actors of this rotating flow topology. For this case, differences are visible above the first rib where the high velocity zone is smaller than in the reference case, indicating that more mass flow is already captured by the secondary flow on the sides, not detectable in the symmetry plane. A direct consequence is the appearance of smooth wall vortices



Table 4.2: Summary of the sensitivity analysis parameters

Parameter	Reference	Modified
rotation rate	$Ro = 0.38$	$Ro = 0.54$
channel length	length of the experiment ( $9.6D_h$ )	outlet extension $+1.4D_h$
outlet pressure	uniform pressure	theoretical Coriolis induced wall-normal pressure gradient
inlet velocity	PIV profile	theoretical $1/7^{th}$ turbulent profile

that is much earlier than in the reference case, confirming that the secondary flows develop faster when the rotation rate increases.

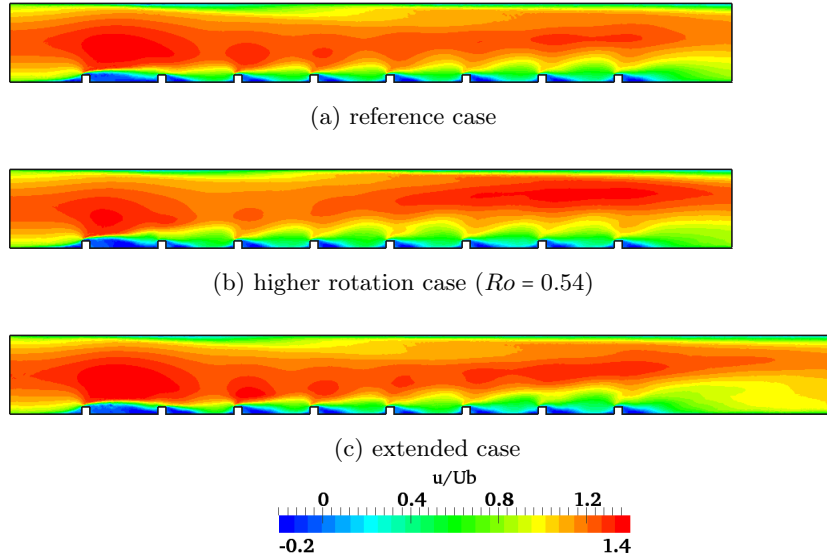


Figure 4.10: Modification of the non-dimensional axial velocity in the symmetry plane of the rotating channel reference case (a), with higher rotation rate (b) and outlet extension (c).

Figure 4.11 presents comparisons between the physical parameters linked the two last lines of Table 4.2: the inlet velocity profile and the outlet pressure. The addition of the theoretical pressure gradient in the exit plane corresponding to the balance with the Coriolis force, Fig. 4.11c, induces only small isobar curvature differences at the end of the channel and after the last rib. However such adaptations do not really change the main flow in the symmetry plane. This could be expected looking at the value of the pressure obtained with the pressure gradient formula of Section 4.2.3. Between suction and pressure sides, a difference of 8 Pa is computed. This is a relatively small difference in comparison to the ambient pressure in the channel.

Changes in the inlet profile, Fig. 4.11b, have a more visible influence on the main flow. As one can see, the PIV inlet velocity profile is flatter than the theoretical turbulent 1/7-power profile. Lower Coriolis forces and potentially weaker secondary flows are expected. This assumption is confirmed if looking at the smooth wall vortices: their trace in the symmetry plane is much less underlined than in the reference case. Also, the high velocity zone above the two last ribs in the reference case is moved upstream toward the middle of the channel.

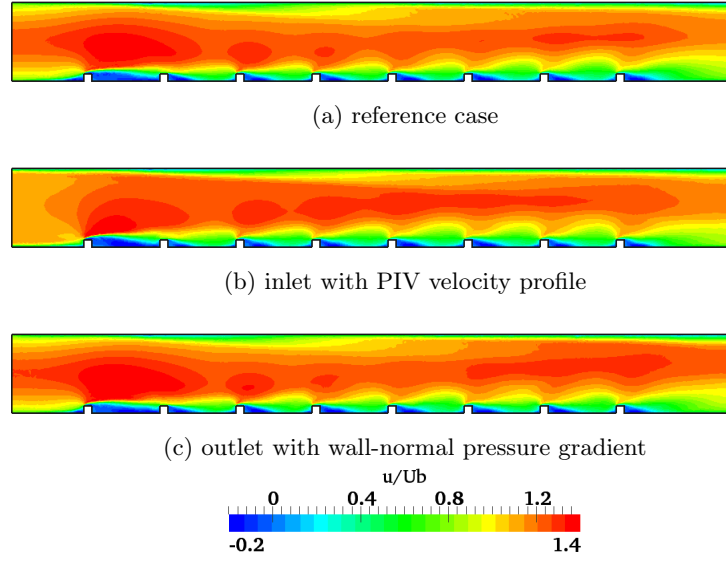


Figure 4.11: Modification of the non-dimensional axial velocity in the symmetry plane of the rotating channel reference case (a), with PIV inlet velocity profile (b), and theoretical outlet Coriolis induced wall-normal pressure gradient (c).

#### 4.4.5 Conclusion




Based on the previous study, it has been decided that the LES of the experimental rotating channel needs to satisfy at least the following requirements:

- Imposition of the exact measured profile at the inlet of the channel: different profiles will clearly result in different high/low velocity zones generating different Coriolis force magnitudes with important consequences on the mean flow predictions and spatial development.
- Imposition of the wall-normal pressure gradient: physically more realistic because of the presence of the honey comb, although of no major influence.

## 4.5 LES of the VKI isothermal rotating ribbed channel: validation against experiment

This section provides different levels of validation of the rotating LES numerical methodology by use of a hybrid grid and the ALE approach. For the validation, three cases are assessed and discussed in the following (Table 4.3): the reference non-rotating case and two isothermal rotating cases, one with stabilizing and the other with destabilizing rotation.

Table 4.3: Summary of the comparison cases for the isothermal rotating study

Case name	$Re$	$Ro$	$Bo$	Nomenclature
rotating case w/o buoyancy	15000	+0.38	0	
non-rotating case	15000	0	0	
rotating case w/o buoyancy	15000	-0.38	0	

In this section, the focus is mainly given on the region of interest corresponding to the measurement window located in the symmetry plane between the sixth and the seventh rib. The following paragraphs present first the influence of the rotation on the mean flow topology, followed by several types of measurements in comparison to the isothermal LES predictions. Confrontations are obtained not only for mean flow fields but also for spatial two-point correlations and time resolved vortex tracking techniques.

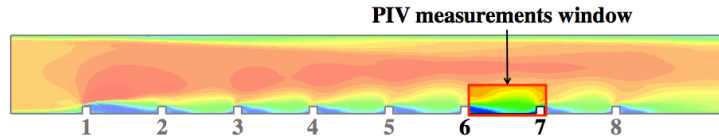


Figure 4.12: Investigation zone for LES / PIV comparisons: bottom third of the symmetry plane between rib#6 and rib#7. Window size  $(x, y) = (10h, 3h)$ .

### 4.5.1 Mean effects of rotation on the near wall flow topology

Three dimensional computations do provide access to mean flow fields in the entire domain and since the flow in rotating ribbed channels is clearly 3D with large secondary flows, it is also of interest to analyze the whole channel with and without rotation. In the specific context of cooling systems, wall regions are critical and will be the focus of the following discussion to see how rotation impacts this region.

First, let us observe the non-rotating case to consider the reference near wall flow topology, Figure 4.13. Wall streamlines are presented on the top, side and ribbed walls and may be observed as being an image of the near wall flow in the channel. They are plotted according to the vector  $\mathbf{d}_w$  computed as follows:

$$\mathbf{d}_w = \nabla \mathbf{u} \cdot \mathbf{n}_w \quad (4.26)$$

$\mathbf{u}$  being the time averaged velocity vector and  $\mathbf{n}_w$  the wall normal vector. Therefore and for the reference case, one can see on the side wall the influence of the ribs on the near wall flow. After a transition at the entrance over the two first ribs, a tilted streamline periodic pattern appears which can be seen as the mark of the flow being deflected by the rib on the side wall. In this pattern, the streamlines are first oriented in the upstream direction in front of the rib, then curve vertically above it to finally be redirected in the streamwise direction keeping an angle with the main flow until two-third of the channel height. Note that the third rib side wall does not seem to be influenced by the previous ribs and has the same streamwise orientation as at the entrance. The top smooth wall streamlines do not show any change in their orientation which allows to conclude that the ribs do not modify the wall flow anymore. However, this is not the case on the ribbed wall where three characteristic spanwise lines are visible between each rib, visible on the magnified region between the 6<sup>th</sup> and the 7<sup>th</sup> ribs. Following the streamwise direction, there are: a separation line (S1), a reattachment line (R2) and another separation line (S3). These lines are the marks of the secondary flows described in Chapter 3. Namely, the trace of the large recirculation bubble present behind the rib between S1 and R2 and the associated smaller counter rotating vortex between the upstream rib bottom corner and S1. The flow then reattaches between R2 and S3 while the other rib corner recirculation appears between S3 and the downstream rib. This pattern is clearly observable and periodic after the third rib.

The reference topology being described, the positive rotation leading to the destabilization of the flow on the ribbed wall can be addressed, Fig. 4.14. Looking at the side wall, the patterns show a similar bottom up streamline orientation as in the non rotating case: i.e. the streamlines flow around the rib and go in the direction of the top wall. But in this case, they do not reorient reaching the top wall with a constant angle. This typical pattern appears almost instantaneously at the channel entrance before the first rib and is the mark of the large streamwise secondary flows generated by the imbalance between the Coriolis forces and the pressure gradient in the channel. While the channel core flow is pushed to the ribbed wall, the near side wall low velocity fluid particles are pushed toward the top wall. Prediction of both counter rotating streamwise vortices is confirmed by the top wall streamlines where friction marks are visible on each side of the top wall following the same orientation as on the side wall. Note that these marks are present only on about one fourth of the top wall width. In the middle, the streamlines keep their initial streamwise orientation even if this is also the region where the small counter rotating streamwise vortices are generated. This indicates that they are not in contact with the top wall. Finally, as assumed with the velocity comparisons in the symmetry plane, there is no obvious difference between the non-rotating and the destabilizing ribbed wall streamline pattern: both predictions present two separation lines and one reattachment line in-between at equivalent positions.

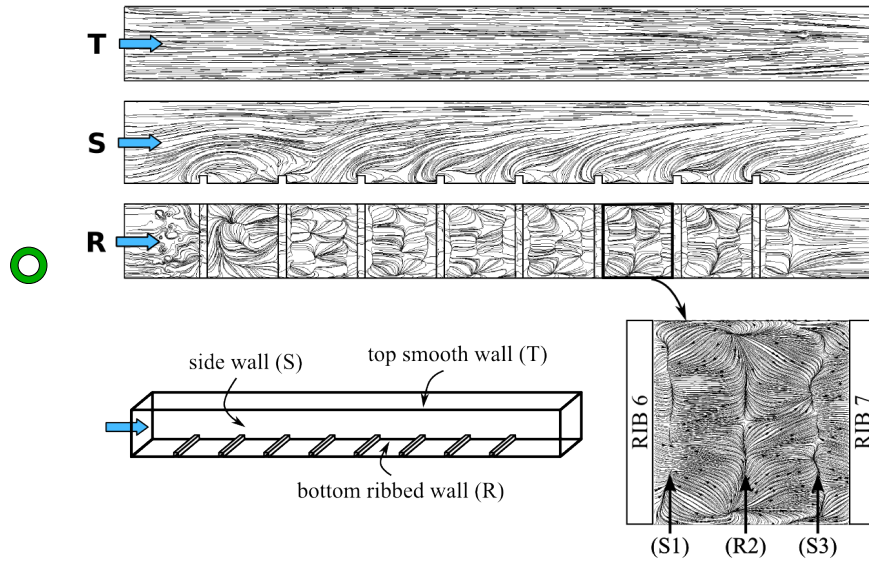


Figure 4.13: Wall streamlines computed from the LES computation for the reference non-rotating case. Top, side and ribbed walls are given following the 3D channel scheme below and near wall flow topology features between the 6<sup>th</sup> and the 7<sup>th</sup> ribs are presented.

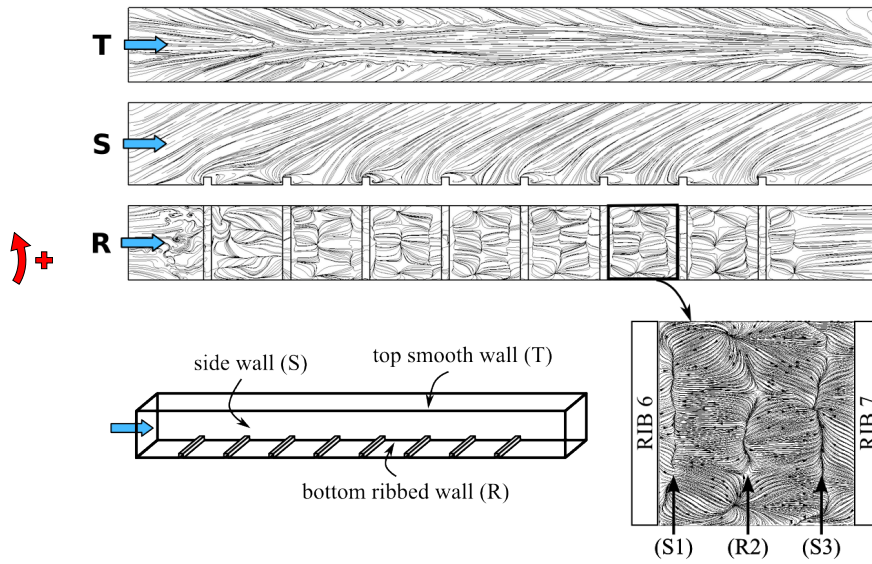


Figure 4.14: Wall streamlines computed from the LES computation for the destabilizing case. Top, side and ribbed walls are given following the 3D channel scheme below and near wall flow topology features between the 6<sup>th</sup> and the 7<sup>th</sup> ribs are presented.

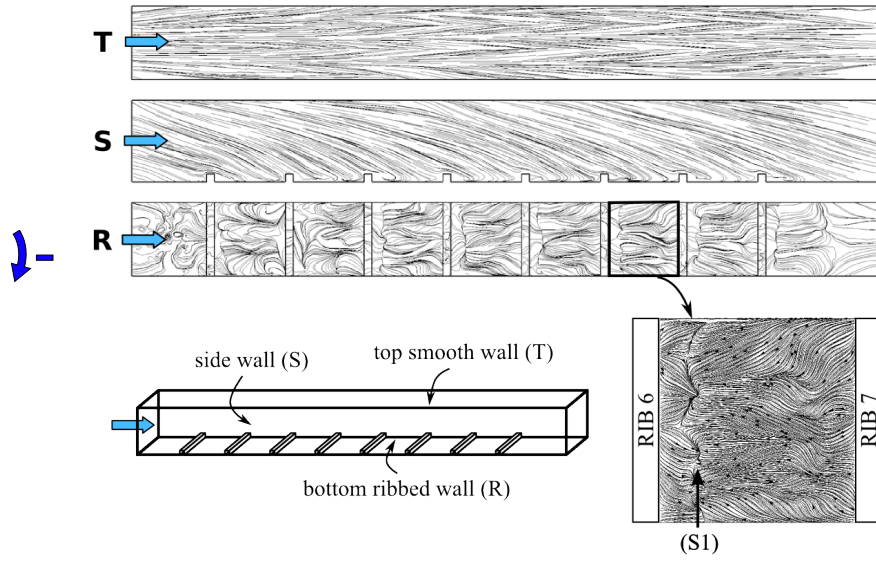


Figure 4.15: Wall streamlines computed from the LES computation for the stabilizing case. Top, side and ribbed walls are given following the 3D channel scheme below and near wall flow topology features between the 6<sup>th</sup> and the 7<sup>th</sup> ribs are presented.

To finish, the stabilizing case (with the negative rotation) is considered in Fig. 4.15. Looking at the side wall and considering two large counter rotating streamwise vortices as for the destabilizing case but with an opposite rotation direction, one can expect a balance between the top down flow and the deflected bottom up flow from the ribs. The first observation to be made based on the LES results is that the near side wall streamlines follow entirely the top down orientation until the ribbed wall while the near wall rib deflected flow is non-existing. This can be explained considering that in the stabilizing rotation, the flow around the ribs is slower and less turbulent than for the other two cases. That being said, the rib deflection is weaker and the near side wall flow is constrained near the ribbed wall. One can note that streamlines do curve when arriving between the ribs, indicating the presence of a large recirculation between them as shown with the PIV comparisons. The footprint of this recirculation is more visible on the ribbed wall streamline representation where no reattachment line is actually present on the inter rib wall and only one separation line (S1). The top smooth wall does not present the same pattern as for the other cases: there is no mark of the streamwise vortices and no streamwise oriented streamlines. What we observe here are V-shape streamlines, and one can suppose that they are the mark of turbulent structures as TG vortices, since located on the top wall which is here the destabilized wall.

Finally, focusing on the global channel flow topology, one can conclude from the wall streamline analysis that the positive, destabilizing rotation generates large secondary flows reinforcing the natural flow deflection created by the ribs, while the



negative, stabilizing rotation secondary flows suppress this effect maintaining the near wall flow between the ribs. Note that experimental visualization of the wall streamlines could be an interesting comparison to be made looking at the a priori complex near wall flow topology observed here.

#### 4.5.2 Effect of rotation on the flow field around the ribs

The LES mean results are computed for each case averaging identically over a time corresponding five flow through. The computed mean and fluctuating velocities are compared with the PIV measurements for each case.

##### Mean velocity comparison

Figure 4.16 presents contours and streamlines from the mean velocity field respectively from LES and PIV for the destabilizing, stabilizing and non-rotating cases. One can see that for the reference non-rotating case, Fig. 4.16c and Fig. 4.16d, mean velocity results match very well PIV measurements with a good large recirculation bubble extension prediction of  $x/h = 4$ . This is consistent with the previous results of Chapter 3 for a non-rotating channel with the same numerical procedure but an aspect ratio of 30%. For the stabilizing case, Fig. 4.16e and Fig. 4.16f, LES is in very good agreement with PIV, predicting the correct recirculation bubble size equals to  $x/h = 6 - 6.5$ . These observations are supported by Fig 4.17a and 4.17a where streamwise velocity profiles fit experimental data at all locations. Differences appear for the destabilizing rotating case for which Fig. 4.16a and Fig. 4.16b are to be compared. Even if flow reattachment is correctly predicted at a position of  $x/h = 4$  (not different from the non-rotating case), flow velocity magnitudes in the channel are clearly underestimated. These conclusions appear also on Fig 4.17b where LES matches PIV at all locations near the wall under  $y/h = 0.25$  but move away from measurements with increasing discrepancies further of the wall. One potential origin of such differences could be that mesh requirements dedicated to non-rotating cases may not be sufficient for destabilizing cases where velocity gradients and flow curvature are present, two characteristics that are reduced around the rib in the case of stabilizing rotation. A second possible reason considered here could be the SGS modeling since no modification has been applied here for the rotation, whereas the turbulence behavior is known to be changed in this rotating condition.

##### Fluctuating velocity components comparisons

Going further into the flow analysis, one can look at velocity fluctuations in the streamwise and wall-normal directions, Fig. 4.18 and 4.19. The first obvious conclusion coming from such comparisons is that LES slightly over-predicts fluctuating velocities for all cases, except for the wall-normal component of the stabilizing rotation. Overestimations go from 15% to 35% for the streamwise fluctuating velocity and from 30% to 40% for the wall normal component. Despite these observed limitations that would require more investigations, the LES does capture effects of rotation

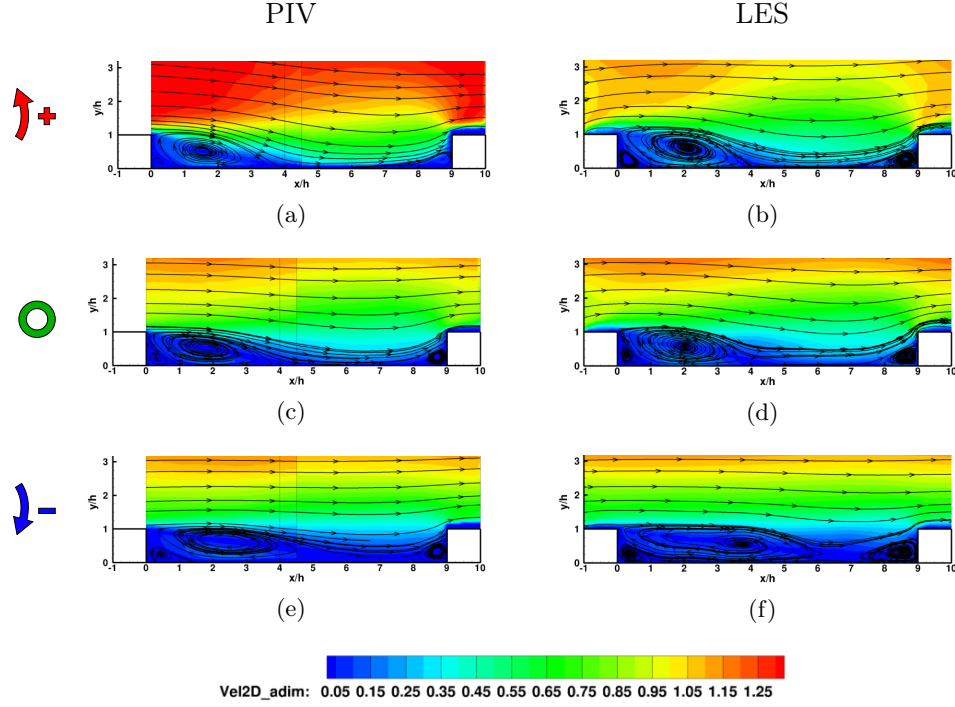


Figure 4.16: Two dimensional contours of velocity magnitude in the channel symmetry plane between the 6<sup>th</sup> and the 7<sup>th</sup> ribs: PIV and LES with destabilizing rotation (first row), non-rotating case (middle row) and stabilizing rotation (last row)

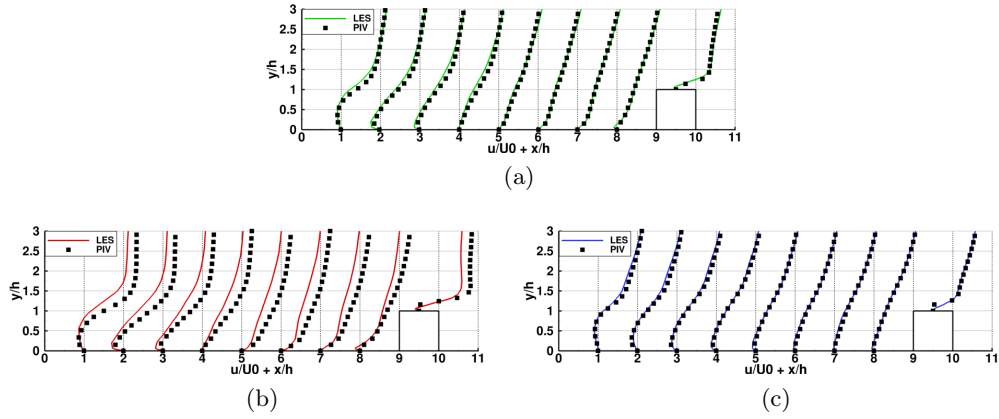


Figure 4.17: Comparison of LES (lines) and PIV (symbols) mean streamwise velocity profiles in the channel symmetry plane between the 6<sup>th</sup> and the 7<sup>th</sup> ribs: non-rotating case (a), destabilizing rotation (b) and stabilizing rotation (c)

on the flow with increasing/decreasing turbulence caused by destabilizing/stabilizing rotation. The maps of normal stresses contours, Fig 4.18, indicate that maxima are correctly located, i.e. in the shear layer behind the rib for the streamwise fluctuations. Note that one maximum is located above the rib for the non-rotating case,



and two maxima appear above the rib and in zones of the rib wake between  $x/h = 2$  and 3 where flow brought by Coriolis forces reactivates mixing in the destabilizing rotation. The result for stabilizing rotation is a quasi-uniform zone joining both ribs between  $y/h = 1$  and 2. Maxima of wall normal fluctuations, Fig 4.19, are well predicted for each case and all  $x/h$  locations corresponding to a part of the large recirculation bubble mean boundary where strong curvature is present.

Figure 4.20 gives a more quantitative view of the TKE evolution as a function of the position on the  $x$ -axis for each case non dimensionalized by the initial value at  $x/h = 0$  location. One can see that despite the overestimation of the fluctuating velocity, the LES is able to reproduce the streamwise evolution of the turbulence for all three cases:

- a turbulence peak is well reproduced at  $x/h = 3$  in the destabilizing case with distinct different slopes on each side.
- In the non-rotating case, a maximum is detected near the same  $x/h$  location but around this point the curve has a bulge shape rather than a clear peak.
- Finally, for the stabilizing case even if a maximum is visible at a similar location near  $x/h = 3$ , a low turbulence decrease is present after that location, and there is no reincreased above the downstream rib.

Note that the non-rotating and the destabilizing cases present a turbulence reincrease above the downstream rib which is predicted numerically. In the stabilizing case, a discontinuity also exists in the PIV measurement at  $x/h = 4.5$  location (due to the fact that several measurement windows were used).

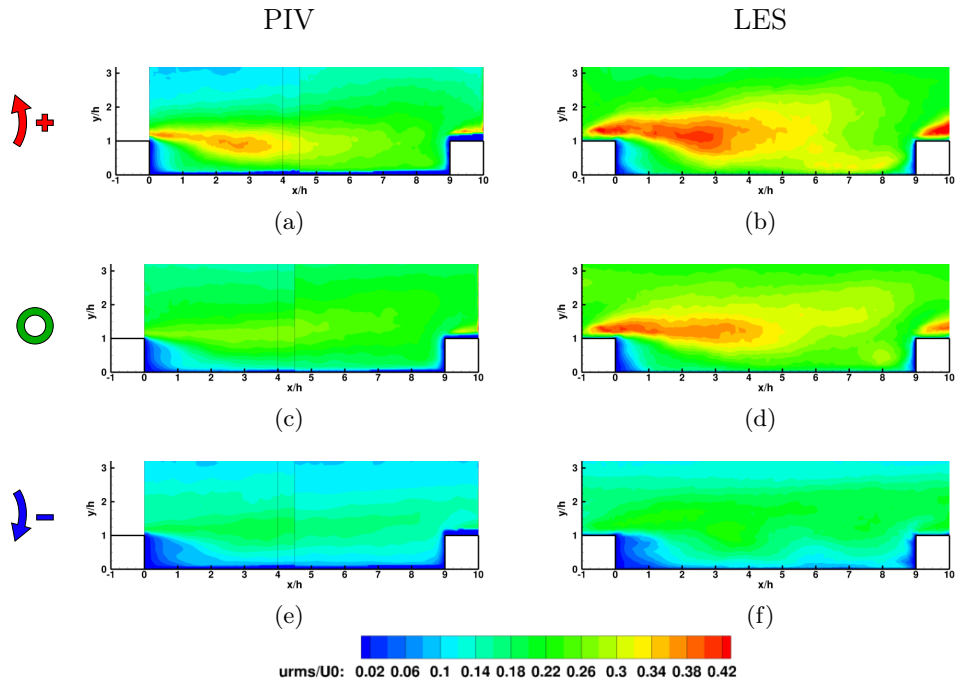


Figure 4.18: Two dimensional contours of streamwise fluctuating velocity  $u'u'$  in the channel symmetry plane between the 6<sup>th</sup> and the 7<sup>th</sup> ribs: LES and PIV with destabilizing rotation (top row), non-rotating case (middle row) and stabilizing rotation (bottom row)

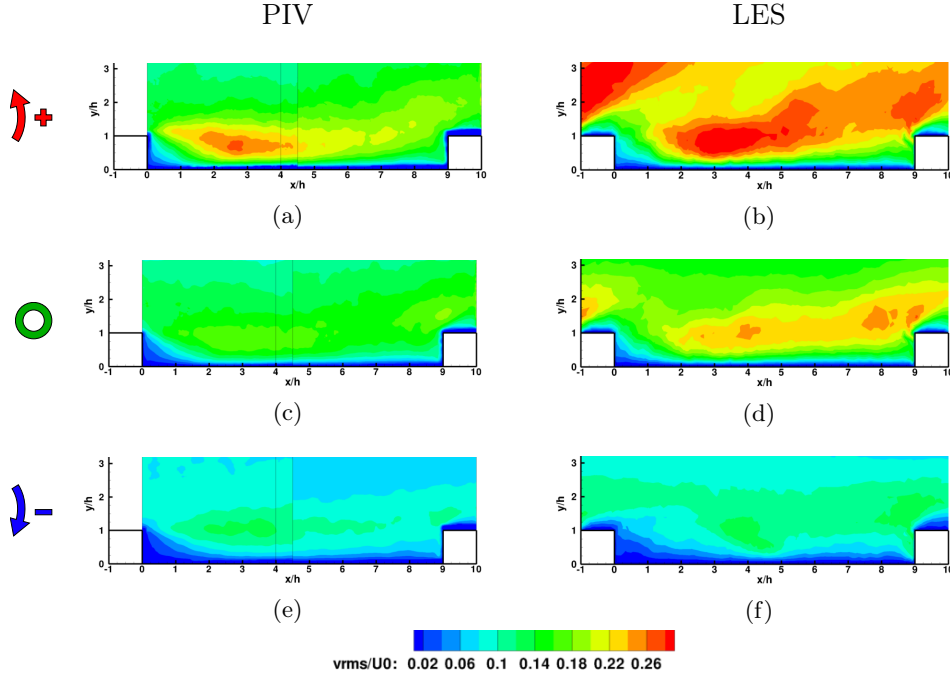


Figure 4.19: Two dimensional contours of wall-normal fluctuating velocity  $v'v'$  in the channel symmetry plane between the 6<sup>th</sup> and the 7<sup>th</sup> ribs: LES and PIV with destabilizing rotation (top row), non-rotating case (middle row) and stabilizing rotation (bottom row)

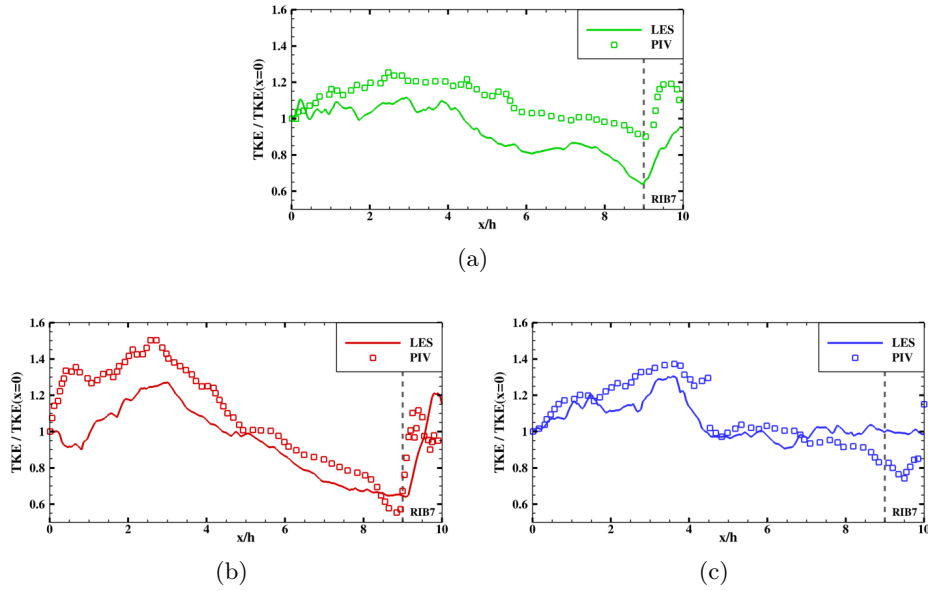


Figure 4.20: Comparison between LES (lines) and PIV (symbols) TKE evolution computed as a function of the position on the  $x$ -axis in the channel symmetry plane between the 6<sup>th</sup> and the 7<sup>th</sup> ribs: non-rotating case (a), destabilizing rotation (b) and stabilizing rotation (c)

### 4.5.3 Two-point correlations

Having validated and compared mean, fluctuating and near wall quantities in the previous paragraphs, it is possible to investigate the spatial organization of the flow generated by the ribs as well as the coherent structure alteration in the different cases. To do so, Coletti [24] has performed two-point correlations based on PIV data at a point located in the region of maximum turbulence in the shear layer behind the rib. LES flow predictions can also attain such quantities giving access to more in-depth comparative validations. The spatial correlation coefficient  $R_{AB}$  between two flow field values  $A$  and  $B$  is defined as follows:

$$R_{AB} = \frac{\overline{A(\vec{X}_0) \cdot B(\vec{X}_0 + \Delta\vec{X})}}{\sqrt{\overline{A(\vec{X}_0)^2}} \cdot \sqrt{\overline{B(\vec{X}_0 + \Delta\vec{X})^2}}} \quad (4.27)$$

PIV spatial correlation are provided at the location  $(x/h; y/h) = (1; 1.2)$  in the channel symmetry plane for the two flow fields available which are the streamwise  $u'$  and the wall normal  $v'$  velocity fluctuations. Figure 4.21 presents the streamwise fluctuating velocity spatial correlation  $R_{u'u'}$  2D map with blanked regions where  $R_{u'u'} < 0.5$ . Comparing first the shape of the  $R_{u'u'} > 0.5$  contour, one can see that the present LES predictions provide similar  $x$ -stretched highly correlated regions like the PIV, but with a larger extend. As observed experimentally, for each rotating case the oval shape of the correlation contour is tilted downward or upward for the destabilizing or stabilizing rotation respectively, reflecting the orientation of the mean flow. The larger correlation zones provided by LES are coherent with the differences observed for the fluctuating velocities in the previous paragraph indicating a lack of mesh resolution or SGS modeling issue in this region.

Wall normal two-point velocity correlation maps of Fig. 4.22 provide the same conclusions with an overestimated  $R_{v'v'}$  contour size with no clear increasing size trend from the stabilizing case to the destabilizing case. One can however note that the destabilized contour is lightly shifted upward if compared to the other two cases, which is visible experimentally.

Two-point correlations may also provide access to a characteristic integral length scale to qualify turbulence. Following the indications of Pope [102], streamwise integral length scale  $L_{XX}$  for example may be expressed as:

$$L_{XX} = \int_0^\infty R_{u'u'}(X) dX \quad (4.28)$$

This estimation requires however a domain extension where the correlation coefficients fall to zero, which may not be evident in a ribbed channel case with periodic patterns. Figure 4.23 presents therefore  $R_{u'u'}$  and  $R_{v'v'}$  correlations in a full ribbed wall pitch and still centered at the point  $(x/h; y/h) = (1; 1.2)$ . One can see that the streamwise coefficients for each case of Fig. 4.23a do not show proper convergence after  $x/h = 5$ , which may be caused by the proximity of the next rib. Equation 4.28 is therefore not necessarily the adapted method to quantify the integral length scale.

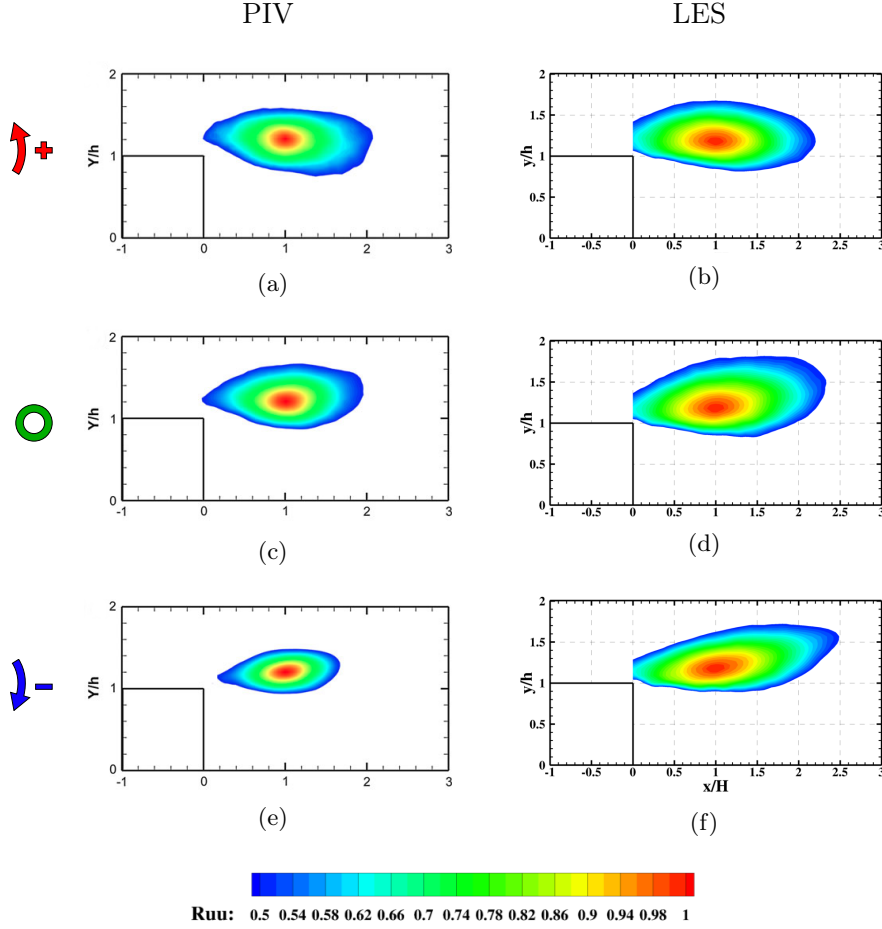


Figure 4.21: Comparison of PIV and LES streamwise two-point correlation function  $R_{u'u'}$  contours centered at  $(x/h; y/h) = (1; 1.2)$  for the non-rotating, stabilizing and destabilizing cases.

Volino [134] has proposed a methodology to evaluate this length scale based on the size of the 0.5 correlation contours presented in Fig. 4.21 and Fig. 4.22. For the streamwise scale  $L_{XX}$ , one may consider the distance from the most upstream to the most downstream location on the  $R_{u'u'} = 0.5$  contour. In the same fashion, the wall normal integral length scale  $L_{YY}$  may be determined with the distance between the lowest and the highest  $y$  location of the  $R_{v'v'} = 0.5$  contour.

Table 4.4 gives a comparison of the integral turbulent length scale  $L_{XX}$  and  $L_{YY}$  using Volino's proposition as obtained from LES and PIV results. It can be seen that experimental measurements find an increase in the highly correlated region size from the stabilizing and the destabilizing cases, concluding that regions of coherent large-scale motions in the separated shear layer are more and more extended. However, for  $1 < R_{u'u'} < 0.5$ , no significantly increasing trend is found between the LES cases in comparison to the PIV, even if a good tendency is seen for the dissipative behaviors for  $R_{u'u'} < 0.5$  and  $2 < x/h < 4$ .

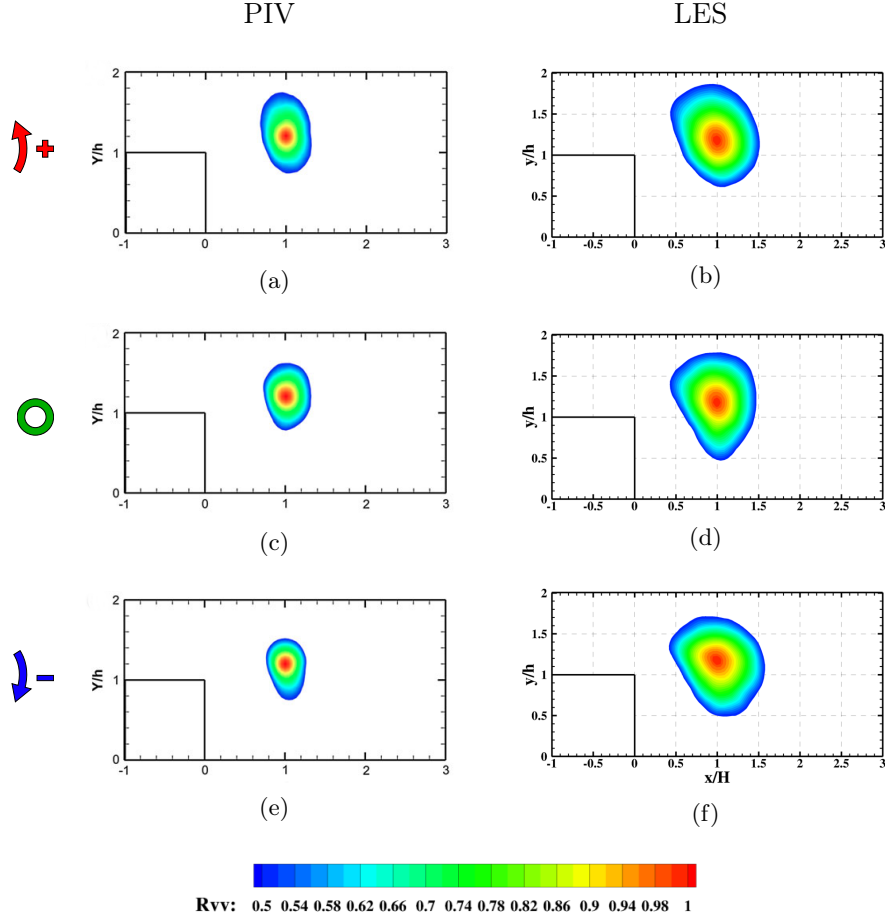


Figure 4.22: Comparison of PIV and LES wall-normal two-point correlation function  $R_{v'v'}$  contours centered at  $(x/h; y/h) = (1; 1.2)$  for the non-rotating, stabilizing and destabilizing cases.

#### 4.5.4 Temporal vortex tracking

The previous results addressed flow analyses based on time or spatially averaged quantities. These analyses however do not fully take advantage of the unsteady data provided by LES. Thanks to the available experimental data, the following subsection proposes therefore to study and validate the unsteady flow predictions generated by LES in the framework of coherent structure tracking.

##### Space time vortex tracking

Time-resolved PIV measurements carried out by Coletti [22] for the rotating channel allow to perform deeper unsteady flow analyses. One possibility is presented in Fig. 4.24 with space-time domains for the non-rotating case. This 3D view allows to track vortices in space and time thanks to the swirling strength criterion  $\lambda_{ci}$ , introduced by Zhou [140] and equal to the imaginary part of the locally cal-

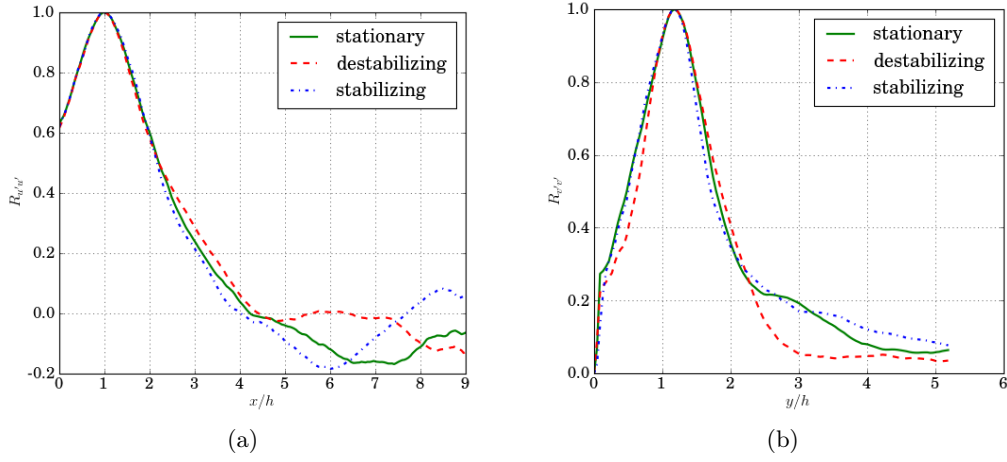


Figure 4.23: Comparison of the LES predicted correlation coefficients for the non-rotating, stabilizing and destabilizing cases.  $R_{u'u'}$  along the streamwise direction at  $y/h = 1.2$  location (a) and  $R_{v'v'}$  along the wall normal direction at  $x/h = 1$  location (b).

Table 4.4: Comparison of PIV and LES Turbulent length scales evaluated from two-point correlations centered at  $(x/h; y/h) = (1; 1.2)$

	Stabilizing rotation	Non-rotating	Destabilizing rotation
$L_{xx}$ PIV	1.52	1.98	2.08
$L_{xx}$ LES	2.16	2.21	2.21
error	42%	12%	6%
$L_{yy}$ PIV	0.77	0.85	1.01
$L_{yy}$ LES	1.25	1.31	1.21
error	62%	54%	20%

culated complex conjugate eigenvalues of the velocity gradient. A positive value of this criterion is a measure of fluid rotation excluding shear. In the PIV data, only two components of the velocity have been measured (streamwise and wall-normal), so only vortical structures with a rotation axis normal to the symmetry plane are accessible. The LES data reduction has been performed to make visualizations comparable and validation possible. Vortices plotted in Fig. 4.24 are finally colored by the local vorticity value: positive vorticity in red (i.e. rotating counter-clockwise in the XY plane), and negative vorticity in blue (i.e. rotating clockwise). LES counterparts are shown in Fig. 4.25a for the non-rotating case. Note that in Fig. 4.24, two space-time domains are presented since both PIV windows are not time-correlated. For LES one unique volume covers the entire space between rib 6 and rib 7.

Comparing both space-time volumes for the non-rotating case (i.e. Fig. 4.24 and 4.25a) by identifying an isosurface of  $\lambda_{ci} = 10\%$  of the maximum value of the

dataset, one can see a similar density and orientation of the vortices. A large majority of negative vortical structures is present in the domain because of the mean shear of the flow behind the rib. Clockwise vortices are more present after  $x/h = 4$  where flow reattaches so such vortices can be generated by the shear layer flapping. Coletti [22] also proposes as an explanation the convection of streamwise structures oriented in the quasi-spanwise direction by the mean flow. As in the experiment, the more one looks at decreasing  $y/h$ , the more vortices seem to be aligned with the time axis, pointing at the same time fast-moving structures carried by the mean flow and stationary vortices near the wall. One can also notice that the diameter of the structures is larger in LES than in the experiment partly confirming the excess of fluctuating velocities reported earlier.

Keeping the same level of  $\lambda_{ci}$  and applying it to the destabilizing and stabilizing cases, one obtains respectively Fig. 4.25b and Fig. 4.25c. The lower fluctuating velocity observed in Fig. 4.19 can be here linked to the lower number of high vortical structures in comparison to Fig. 4.25a. Vortices have also a lower advection velocity since they are more aligned with the time axis compared to what is observed for the non-rotating case. Looking at the destabilizing rotation, Fig. 4.25b, one does not observe obvious differences with the non-rotating case. The only thing noticed is a lower advection velocity difference between mean flow and near wall structures since the majority of vortices are aligned in the same direction. This is consistent with Fig. 4.17(a) where higher mean near-wall velocity is predicted in comparison with the non-rotating case. In the experimental data (not presented here for the destabilizing case), vortical structures appear to have a shorter life time than predicted by LES.



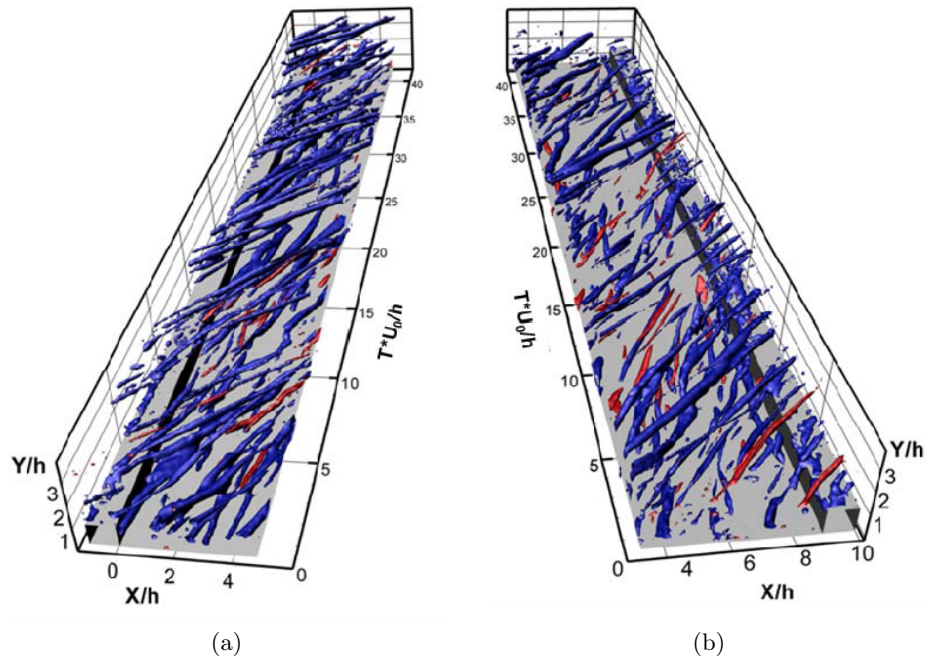


Figure 4.24: Spanwise vortices travelling in spacetime in the non rotating case, visualized by means of iso-contours of positive swirling strength  $\lambda_{ci}$  computed from the PIV measurements. Top: downstream of rib 6 (position a); bottom: upstream of rib 7 (position b).

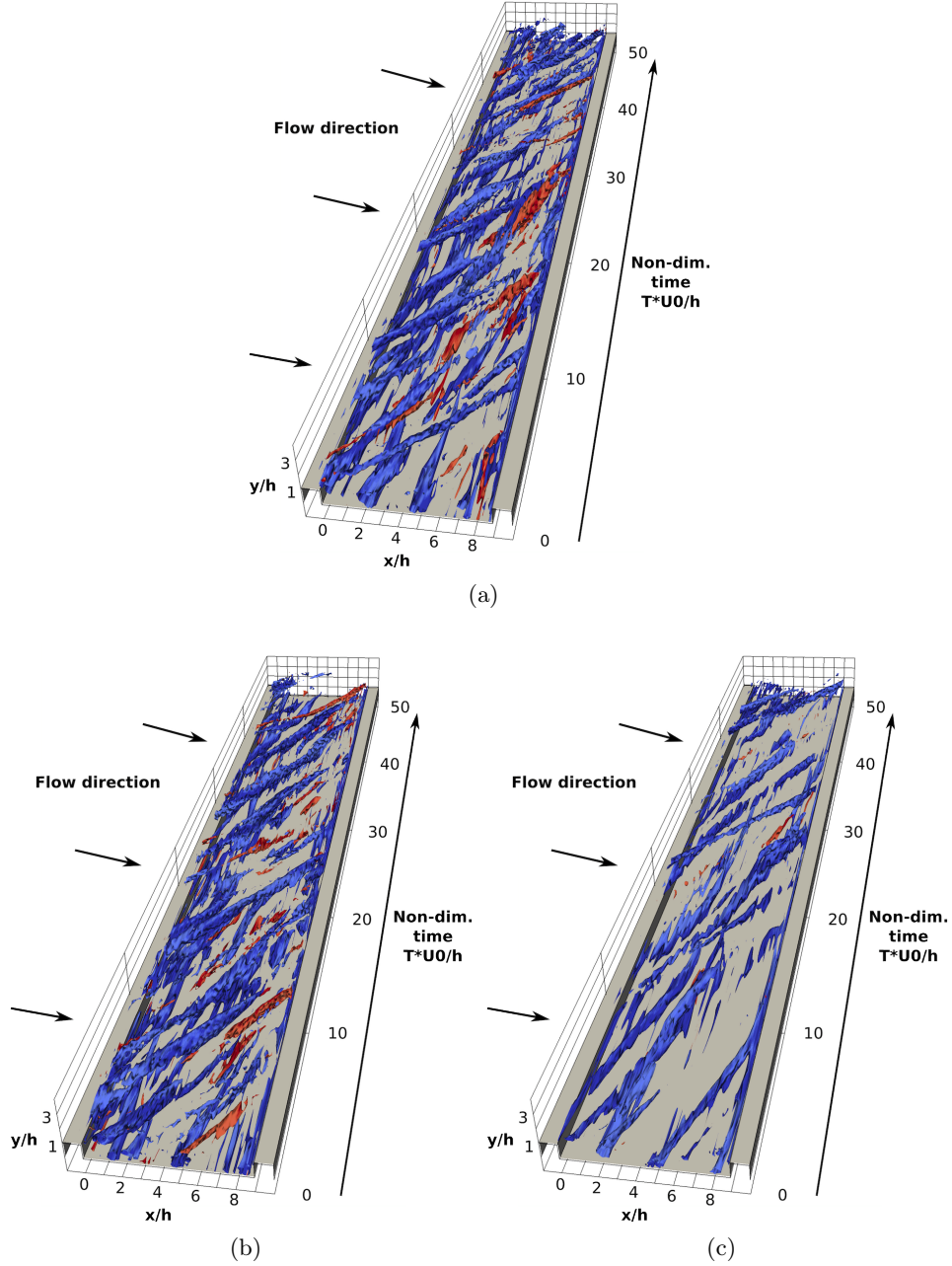


Figure 4.25: Spanwise vortices travelling in spacetime between rib 6 and rib 7, visualized by means of iso-contours of positive swirling strength  $\lambda_{ci}$  computed from the LES results. Reference non rotating case(a), destabilizing rotation (b) and stabilizing rotation (c).

### Three dimensional vortex tracking

The previous time resolved vortex analysis has yield information on the coherent structures in the channel symmetry plane. However, since the near rib flow is highly three dimensional as seen on the wall streamline maps, it may be interesting to extend the vortices analysis to a 3D volume. The CFD tool allows to perform such analysis thanks to available data in the entire domain. For simplicity, one keeps focusing here on the fluid region between the 6th and the 7th ribs, but enlarging the domain in the third spatial dimension to cover the entire flow volume. The resulting domain of interest is given in Fig. 4.26.

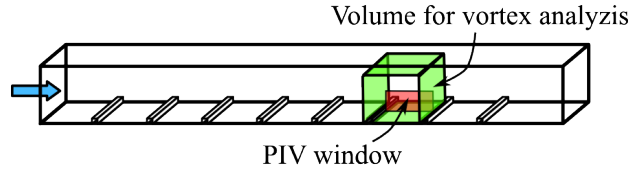


Figure 4.26: Volume selected for the 3D vortex analysis.

Since turbulence through fluctuating velocity has shown a dependency to the rotation, one proposes here to study if a correlation exists between the number of vortices which may be detected and the studied case: destabilizing, non-rotating and stabilizing. To do so, identification of vortices is first performed using the common  $Q$ -criterion [57]. For a specific positive  $Q$ -criterion value, it results a complex set of 3D surfaces representing the location of 3D rotating coherent structures. Then, all non connected 3D surfaces are isolated and counted in order to get for a specific time instant a coherent structure number. Naturally the given diagnostic is a function of  $Q$  which needs to be made explicit and will differentiate the three flows.

In the present study, vortices have been counted for 20 discrete  $Q$ -criterion values at 40 instants to produce a density map as shown in Fig. 4.27. The mean density plot for each case shows clearly a trend in vortex number between the three cases: in comparison to the non-rotating case, the destabilizing case generates more vortices and the stabilizing case less vortices. These modifications are however not symmetric: if the destabilizing case increases lightly the vortex number and maximum strength, stabilizing rotation shows much less vortices and reduces by half the strength of the most powerful vortices. Although intuitively resolution dependent at this resolution, one can note a vortex number decreasing exponentially with increasing square root of the non dimensional  $Q$ -criterion  $Q_{adim} = Q/(0.5(U_b/h)^2)$ .

In conclusion, this study provides a clear influence of the rotation on the coherent structure generation and the LES captures adequately such effects. The generated data may then be correlated to heat transfer rates since near wall vortices are responsible for improved or improper heat exchanges.

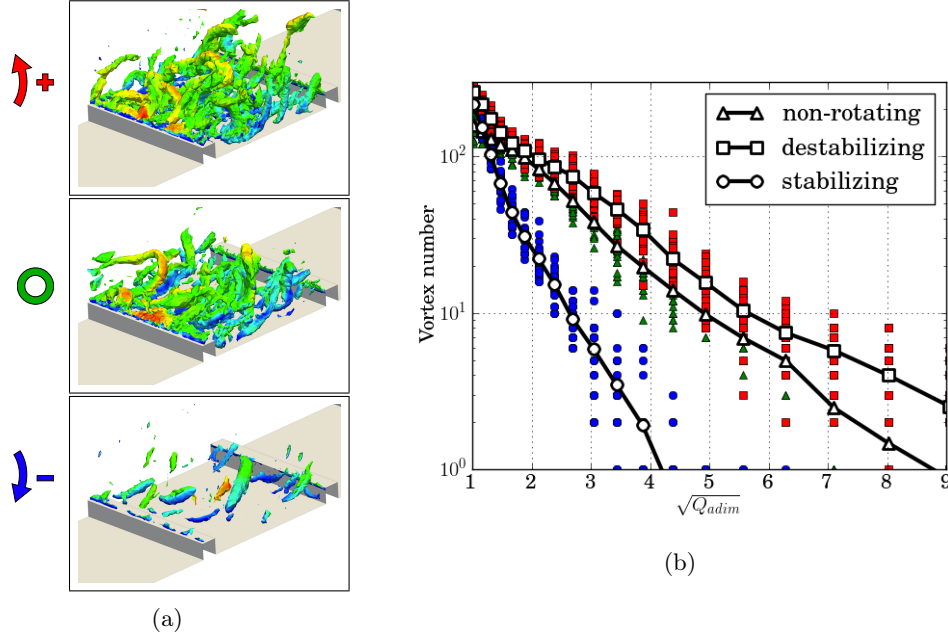


Figure 4.27: Vortex number identified with non dimensional Q criterion  $Q_{adim} = Q/(0.5(U_b/h)^2)$  in the non-rotating, stabilizing and destabilizing cases: example of 3D unsteady snapshots for the vortex count (a) and vortex number mean trend over 40 snapshots (b).

#### 4.5.5 Conclusions on LES of rotating isothermal flows

The different flow investigations presented in this section provide the following conclusions about LES for rotating cooling channels:







- Mean flow velocity: the predictions are good for the stabilizing and non rotating cases, underestimate the central profile of the axial velocity component for the destabilizing case. The overall effect of rotation on the recirculation bubble length and topology is well reproduced by LES.
- Fluctuating velocity: overall the LES overestimates the peaks of all rotating cases, but the turbulence increase / decrease, resulting from the destabilizing / stabilizing rotation is observed.
- Wall streamlines: the marks of the large secondary flows provide a better comprehension of the near wall flow, which is known to be of great importance in the next section where the temperature transport is addressed.
- Two-point correlations: two point correlations indicate that the LES overestimates the flow coherence, which may be an explanation for the fluctuating velocity overestimations. The mean flow feature reflected by the highly correlated region orientation which is a function of the sense of rotation and rotation rate is well reproduced by the numerical model.

- Temporal vortex tracking: LES analysis of the vortex temporal trajectories provides a coherent structure behavior in relatively good agreement with the experimental observations, i.e an increase / decrease in number and strength for the destabilizing / stabilizing cases respectively. The size of these structures is shown to be larger than those measured experimentally, confirming the too strong coherence of the computed flow.

## 4.6 LES of the VKI anisothermal rotating ribbed channel: validation against experiment

The previous section presented a range of diagnoses on the flow behavior for isothermal rotating channels. This section provides an extension of the rotating flows for which the ribbed wall is heated bringing it closer to the industrial case. Table 4.5 gives a summary of the case addressed or recalled in this section where three anisothermal rotating cases are added to the isothermal cases studied in the previous chapter.

Table 4.5: Summary of the comparison cases for the anisothermal rotating study

Case name	$Re$	$Ro$	$Bo$	Nomenclature
anisothermal rotating case	15000	+0.38	0.31	
isothermal rotating case	15000	+0.38	0	
anisothermal non-rotating case	15000	0	0	
isothermal non-rotating case	15000	0	0	
isothermal rotating case w/o buoyancy	15000	-0.38	0	
anisothermal rotating case w/ buoyancy	15000	-0.38	0.31	

Following the experiment of Coletti [24], in the anisothermal cases the only modification is the heating of the entire ribbed wall (i.e. the ribs and the inter-rib wall) at a constant temperature  $T_w = 368$  K. All other boundary conditions, i.e. velocity inlet, pressure outlet and the three others smooth adiabatic walls stay unchanged following the same rotating methodology used in the previous section. The inlet flow being at  $T_i = 293$  K, the chosen parameters lead to a Buoyancy number  $Bo = 0.31$ .

The organization of this section proposes comparative results between both the anisothermal rotating cases and the reference non-rotating heated case as well as experimental measurements when available. Results are given by presenting first the mean temperature repartition in the whole channel, then detailed flow field modifications near the ribs in the symmetry plane (with PIV validation data), to finally conclude the study with wall heat transfer performance.

#### 4.6.1 Mean temperature in the channel

Figure 4.28 displays the non-dimensional mean temperature  $T_{adim}$  defined by:

$$T_{adim} = \frac{T - T_i}{T_w - T_i} \quad (4.29)$$

with  $T_i$  the inlet temperature and  $T_w$  the constant end uniform wall temperature.  $T_{adim}$  is given for the heated non-rotating, destabilizing and stabilizing cases at three different locations: the symmetry plane, the top wall and a side wall.

The overview of the mean temperature fields in the symmetry plane (Sy) for the three cases show a hot fluid layer for which  $T_{adim} > 0.5$  located around the ribs with a thickness approaching  $2h$ . Looking closely, one can see for each case that a mean temperature isocontour regular pattern is visible behind each rib, except the first one, with a small hot gases pocket due to the fluid recirculation and the lack of mixing with colder air. In contrast, behind the first rib, the hot pocket extends along the whole rib pitch because of the larger recirculation bubble issued by the strong flow deflection behind the first rib. In comparison to the reference non-rotating case, the hot pocket is slightly reduced in the destabilizing case and slightly extended over the second rib in the stabilizing case.

While the thermal layer slowly grows over the ribbed wall in the non-rotating and stabilizing cases, an interesting phenomenon is detected above the two last ribs of the destabilizing case: a hot fluid region is seen to grow near the top wall (T). The observation of the symmetry plane (Sy) is not sufficient to understand the phenomenon origin: combining the mean temperature traces on the side and top walls of the destabilizing rotation shows that hot fluid ascends much more above the ribs near the side wall than in the symmetry plane, reaching the top wall after the fourth rib in the channel middle length. This hot fluid movement is actually caused by the streamwise large secondary flows in the channel, for which the near wall traces have been evidenced in a previous section using the wall streamline analysis. In contrast, no major difference is observed between the symmetry plane and the side wall in the stabilizing case. As shown before, the secondary flows tend to confine the fluid near the ribbed wall, and no hot gas reaches the top wall before the end of the channel. Following the same interpretation, the reference case side wall mean temperature isocontours are in agreement with the corresponding wall streamlines since hot fluid is raised along the side walls without reaching the top wall.

This hot fluid strong extraction / weak extraction / confinement behavior for the destabilizing / non-rotating / stabilizing cases respectively is presented in Fig. 4.29 with an isosurface of temperature  $T_{adim} = 0.16$ . In the destabilizing case, the initial flat surface at the channel inlet rolls up near the side walls to finally form a tube at the channel outlet. In the stabilizing case, the surface keeps an overall flat shape all along the channel, even if it tends to curve downward near the side walls due to the secondary flow entrainment. The reference case isosurface presents a behavior similar to the destabilizing case with an upward curving shape near the side walls, but without merging before the outlet of the channel.

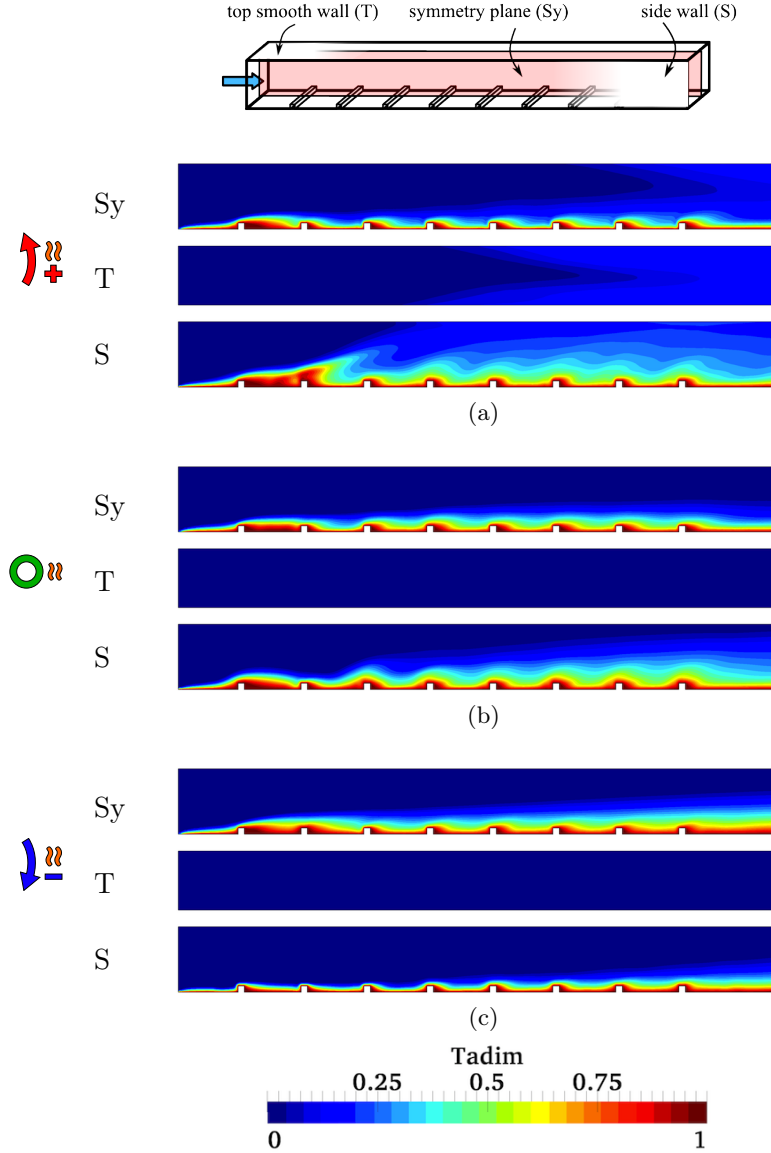


Figure 4.28: Mean temperature computed from the LES for the destabilizing (a), non-rotating (b) and stabilizing (c) cases. Symmetry plane (Sy), top wall (T) and side wall (S) are given following the 3D channel description above.

As a conclusion, mean flow topology clearly impairs visible differences on the bulk temperature evolution along the channel, Fig. 4.30. To quantify these effects, the bulk temperature is computed following the expression of Section 3.5.4, integrating the enthalpy flow rate in several channel cross sections. One can see that rotation has a strong impact on the fluid heating, since the outlet-inlet temperature difference is 1.5 times higher in the destabilizing case and 0.7 times lower in the stabilizing case if compared to the reference case. The LES predictions therefore clearly show how rotation may modify fluid heating through the strong influence of the induced



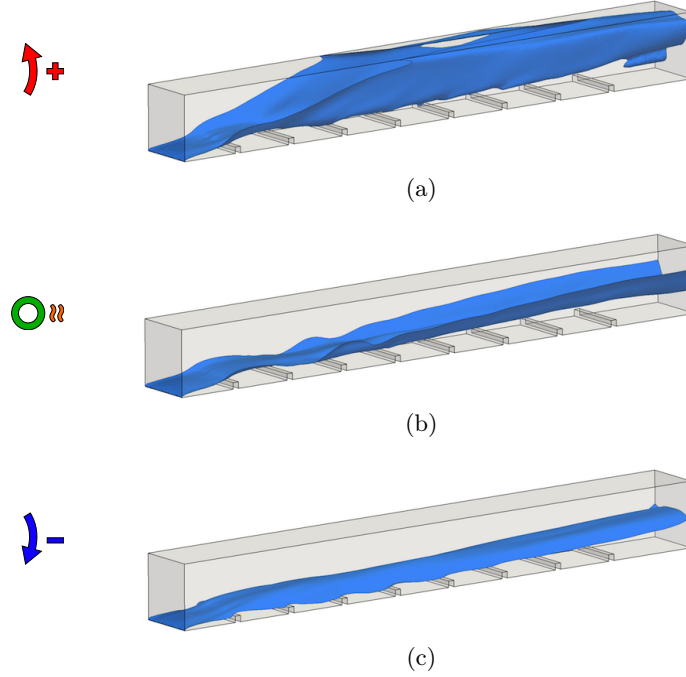


Figure 4.29: Mean temperature isosurface from the LES computation for the destabilizing (a), non-rotating (b) and stabilizing (c) cases.

secondary flows interacting with the ribbed hot wall which can be enhanced or damped depending on the sense of rotation.

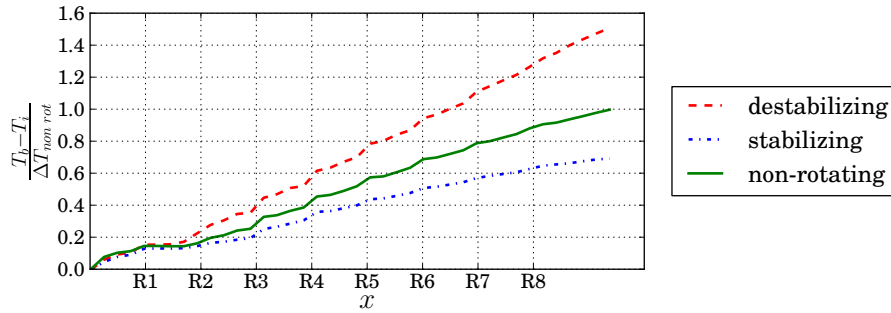


Figure 4.30: Dimensionless bulk temperature along the channel for the destabilizing, stabilizing and non-rotating cases.  $\Delta T_{non\ rot}$  is the reference fluid heating in the non-rotating case and  $x$ -axis labels indicate the rib locations.

#### 4.6.2 Flow field around the ribs

In this section, one focuses on the flow modification around the ribs with anisothermal conditions. PIV measurements are available for validation at this operating point for both rotating heated cases, so following observations are provided in the



PIV measurement window in the symmetry plane. Figure 4.31 presents therefore the 2D velocity magnitude between the 6<sup>th</sup> and the 7<sup>th</sup> ribs for the already presented isothermal cases and compared to both additional rotating heated cases (no aerodynamic experimental data are available for the anisothermal non-rotating case).

Looking first at the comparison between the isothermal and anisothermal destabilizing rotation for PIV and LES, Fig. 4.31c, 4.31d and 4.31a 4.31b respectively, no major thermal influence is visible: the flow velocity is not strongly impacted and the main recirculation bubble size is not modified (length =  $4x/h$ ). Minor changes are however detected, as for example the slightly thicker recirculation bubble in front of the downstream rib, and a lower maximum velocity just above the rib.

The addition of heated walls in the stabilizing rotation produces a more visible difference if compared to the isothermal case, Fig. 4.31k, 4.31h and 4.31i 4.31j. With hot fluid, the LES predicts a 25% lower velocity than the isothermal case, which appears above the rib around  $y/h = 3$ . However, the large recirculation bubble does not seem to be strongly impacted by heating: LES provides a similar reattachment length around  $x/h = 6$ , while the PIV measurements show that the recirculation bubble fills the entire space between both ribs.

### 4.6.3 Heat transfer at the ribbed wall

The previous sections presented all the main flow features encountered in anisothermal rotating ribbed channels with emphases on the fluid temperature and velocity distributions. This section investigates the consequences of the previously studied flow behaviors looking at the heat transfer occurring on the ribbed wall.

Figure 4.32 presents the time averaged wall heat flux for the reference non-rotating, destabilizing and stabilizing cases on the heated ribbed wall, and non-dimensionalized by the channel-averaged heat flux of the reference case  $q_{w,ref}$ . As anticipated in the previous mean flow temperature analyses, significant heat transfer differences are observed between the three cases. In comparison to the reference non-rotating case, the destabilizing or stabilizing rotation increases the heat transfer rate by 28% or decreases it by 22% respectively. This observation is the consequence of all the previous flow analyses with enhanced or reduced turbulence and flow deflection due to secondary flows present in such pipes.

Looking at the heat flux patterns in the different inter-rib regions, one can note that for each case different behaviors are observed respectively upstream and downstream of the third rib location:

Before the third rib, one can look distinctly at each wall between the ribs. First, the inlet smooth channel flow undergoes the first rib disturbance: this rib strongly deflects the flow which does not fully reattaches before the second rib, leading to low heat-transfer region between both of them. Note that the destabilizing rotation presents however high heat transfer spots before the second rib, indicating that in this case the core flow is more likely to reattach. Then, between the second and the third rib, the wall heat flux increases for all three cases.

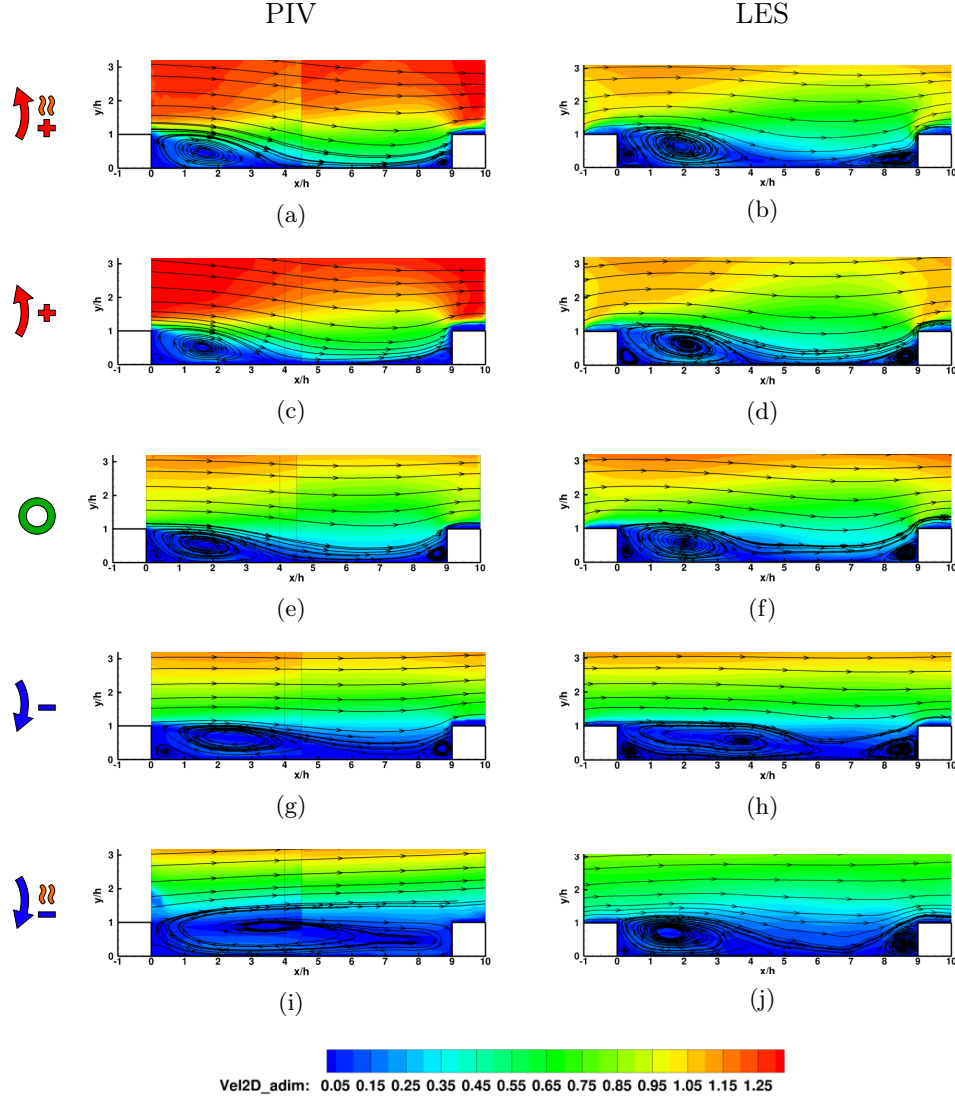


Figure 4.31: Two dimensional contours of velocity magnitude in the channel symmetry plane between the 6<sup>th</sup> and the 7<sup>th</sup> rib: PIV and LES with from the top: destabilizing rotation w/ buoyancy, destabilizing rotation w/o buoyancy, non-rotating case, stabilizing rotation w/o buoyancy and stabilizing rotation w/ buoyancy

From the third rib to the channel outlet, a similar periodic pattern appears in all cases. The pattern can be divided in three zones with a low heat transfer region just behind the rib, two symmetric high heat transfer regions near the side walls and an intermediate heat transfer zone everywhere else.

The topology of the latter periodic heat flux pattern can be explained thanks to the wall streamline analyses presented in Section 4.5.1. Figure 4.33 shows a comparison of the ribbed wall between the 6<sup>th</sup> and the 7<sup>th</sup> rib for each case with the corresponding wall streamline topology. One can note that for the three cases,

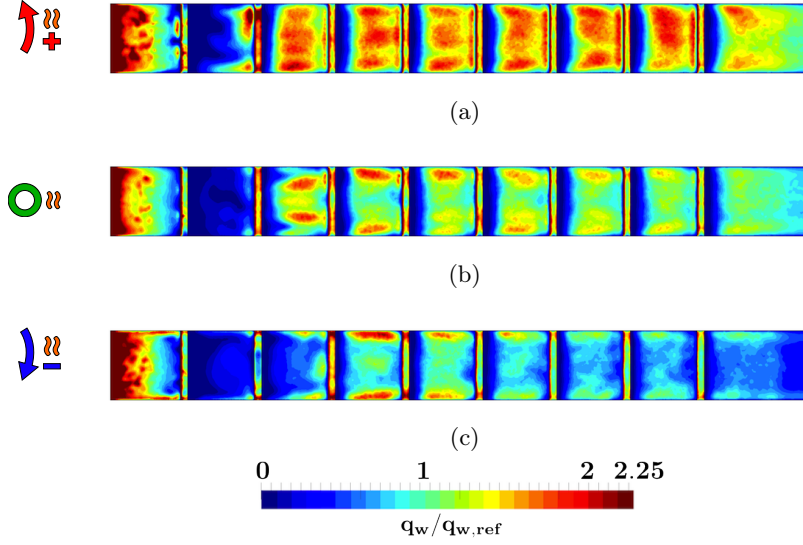


Figure 4.32: Non dimensionalized wall heat flux on the ribbed wall for the destabilizing (a), reference non-rotating (b) and stabilizing (c) cases.  $q_{w,ref}$  is the channel-averaged heat flux value of the reference case.

regions of maximum heat transfer are strongly correlated with the reattachment zones, and more specifically with two symmetric repelling foci located near both lateral sides walls. In contrast, separation lines and attracting foci do not present specific correspondence to neither high nor low heat transfer regions. This behavior can be explained since reattachment lines and repelling foci are the traces of the impinging colder core fluid on the hot wall increasing therefore the near wall temperature gradient, while separation lines and attracting foci represent the extraction of the near wall hot fluid with lower near wall temperature gradient.

Finally, the rib-averaged  $Nu/Nu_0$  ratios representing the heat transfer augmentation of the three cases are given in Fig. 4.34 along the channel. As a reference, the non-rotating case shows a roughly constant heat transfer augmentation between 2 and 2.5 in the channel, except between the two first ribs where the flow does not reattach yet as explained above. Looking at the stabilizing case, the  $Nu/Nu_0$  ratios are lower than in the reference case and is also roughly predicted constant downstream the fourth rib at a value around 1.5 (−30% if compared to the non-rotating case). By contrast, the destabilizing case presents an enhanced heat transfer rate which increases all along the channel from 3 after the second rib to 4 after the seventh rib (from +30% to +60% if compared to the non-rotating case). Note that the behavior with the clearly lower heat transfer observed behind the first rib is also reproduced in the two rotating cases (2 and 1.3 for the destabilizing and stabilizing rotation respectively).

Since no experimental data are available here, the present LES heat transfer results may be compared to an other similar LES study, as for example these proposed

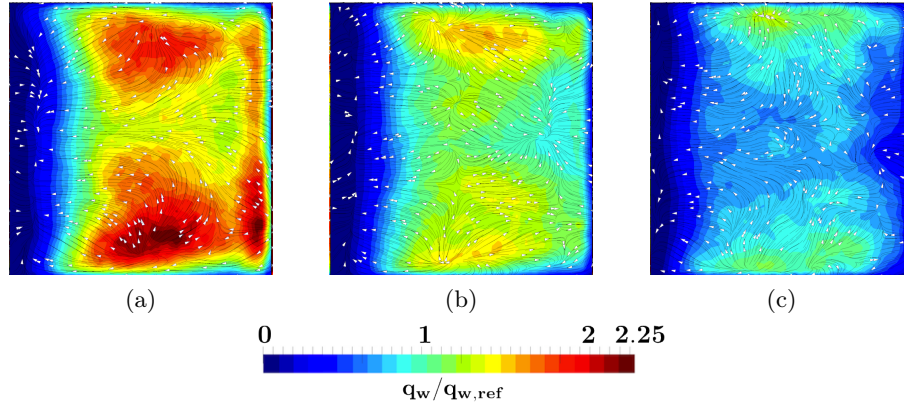


Figure 4.33: Details of wall heat flux on the ribbed wall for the destabilizing (a), reference non-rotating (b) and stabilizing (c) cases with corresponding wall streamlines.

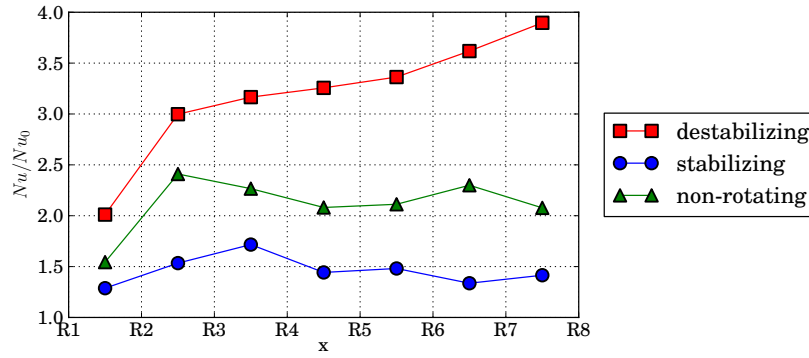


Figure 4.34: Rib-averaged heat transfer augmentation for the non-rotating, destabilizing and stabilizing cases from the present LES at  $Re = 15\,000$ ,  $Ro = 0.38$  and  $Bo = 0.31$ .

by Sewall [116]. In his work, Sewall investigated a developing rotating ribbed channel with the same rib characteristics, i.e.  $h/D_h = 0.1$ ,  $p/h = 10$  and perpendicular to the flow, except that two faced ribbed walls were used. The resulting  $Nu/Nu_0$  ratios are presented in Fig. 4.35. Comparisons of the heat transfer augmentation with the present LES show a good agreement: the  $Nu/Nu_0$  ratios for the non rotating channel are predicted in both cases mainly constant at the same level between 2 and 2.5 with a minimum after the first rib (under 2) and a maximum after the second rib. Similarities are also observed for the stabilizing case with a constant lower heat transfer around 1.5 and an increasing heat transfer rate on the destabilizing side, from 3 to 4 with the corresponding operating conditions. Note that in the Sewall's channel the entrance length and the inlet velocity profile are not the same than in the present study, so one can not really further compare both LES results. Without experimental validation data and following the previous observations, one can

however conclude on the potential good validity of the predictions provided by the LES with the ALE rotating methodology proposed in the present work.

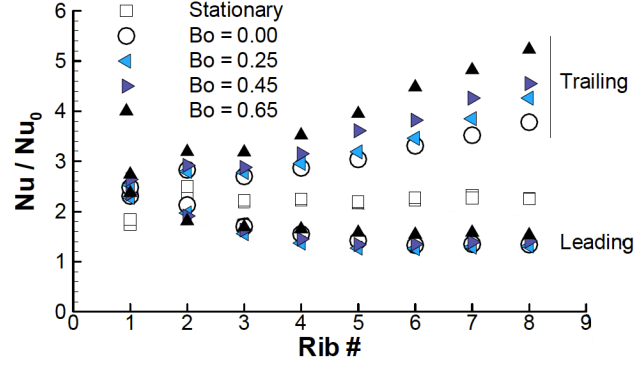


Figure 4.35: Rib-averaged heat transfer augmentation for the non-rotating, destabilizing and stabilizing cases from Sewall's LES at  $Re = 20\,000$ ,  $Ro = 0.3$  and various  $Bo$  between 0.0 and 0.65 [116].

#### 4.6.4 Conclusions on the anisothermal study

The LES of a rotating ribbed channel with anisothermal flow has been conducted in this section. The following observations can be drawn:

- Mean temperature evolutions predicted by the LES in the channel show large disparity in comparison to the reference non rotating case: in destabilized rotation the fluid mixing enhancement increases the fluid heating, while stabilizing rotation does not heat the fluid as much as for the reference case.
- The LES provides a flow description around the ribs in agreement with the results of the isothermal computations, but do not predict exactly the buoyancy effect observed experimentally in the stabilizing case. Further turbulence modeling study should be carried out to understand this difference.
- The overall wall heat exchange is coherent with the above flow conclusions with respectively higher and lower heat transfer in destabilizing and stabilizing rotation, and quantitative values of heat transfer augmentation are found identical to previous similar LES results.

### 4.7 Conclusions on LES of rotating cooling channels

This chapter has introduced the problematic of LES computation of a rotating configuration. Numerical requirements, validations and comparisons with experimental data have been performed for a typical academic cooling ribbed channel.

- The rotation movement has been implemented and validated in the ALE tool of AVBP on a simplified channel comparable to the VKI experimental one. The ALE approach is used here to simulate rotating flows in a inertial frame of reference, without *a priori* modification requirement of the NS equations since inertial forces are implicitly taken into account.
- The methodology proposed in the Chapter 3 for the LES of non-rotating cooling channels has been validated to predict the correct isothermal mean flow and unsteady structure behaviors for the non rotating case and for the rotating case implying stabilizing flow around the ribs. For the destabilizing isothermal case, mean flow and turbulence intensity level show more differences than anticipated. The lack of mesh resolution and the need for a better SGS modeling are pointed out as possible reasons of such discrepancies. Despite this observation, advanced LES results analyses show that the large scale mean flow behavior and unsteady turbulence evolution are well predict by LES.
- The anisothermal LES predictions of the ribbed channel show a strong correlated behavior with the aerodynamic flow field. Again, despite disparities observed on the flow topology around the ribs in comparison to the experimental data, evolution of the mean wall heat transfer efficiency with rotation is found in good agreement with other work on similar configurations, i.e.  $Nu/Nu_0$  ratio constant slightly above 2 for the reference non-rotating case while this ratio is reduced around 1.5 in stabilizing rotation, and increases from 2.5 to almost 4 in destabilizing rotation.
- In the industrial computation presented in the next chapter, since CHT analysis is expected the most useful thermal information will be the wall thermal data. Even if corrections may have to be brought to improve the flow predictions inside the channel, the present numerical methodology for rotating internal cooling channel is found relevant for the industrial CHT computation.



# General conclusion and future works

---

Gas turbine design is a work which consists in finding the best balance between the maximum power generation and the engine resistance capabilities. The power being directly linked to flow with high temperature, the resistance of an engine often translates into the thermal resistance of the engine. In addition to the high temperature, if mechanical stresses caused by the high speed rotation are also taken into account, the rotor of the first turbine stage may be considered as one of the most critical parts in the turbine design. On top of that, the rotor blades which face directly the combustor hot gases require an even more particular attention since their lifetime may be dramatically reduced if their temperature becomes too high. Cooling of such a part has therefore become a priority to ensure the reliability of the engine and new technologies as blade internal air cooling systems have been developed to save the blade lifetime.

In the conception process of such cooled blades, the turbine designers have to predict the behavior of the blade material which is strongly subjected to the surrounding flow. The engineers are helped in their task by numerical tools which model the thermal physical phenomena in presence. If the thermal diffusion process in the blade is well mastered, the convective behavior around and inside it is still widely studied, particularly through the Computational Fluid Dynamics (CFD) field which is able to provide numerical flow predictions.

Current state-of-the-art CFD tools used in the industry (RANS methods) rely on strong theoretical assumptions of isotropic flow and perform practically the resolution of the mean flow while all the unsteady turbulent scales are modeled. The main advantage of these approaches is the low computational cost required to obtain a flow prediction. Thanks to the exponential development of the computational power, advanced flow modeling becomes available. Among them, LES is a very promising one according to its formalism where the large unsteady scales of the flow are solved while the modeling through the isotropic assumption is dedicated to the small scales only. This advantage over the RANS allows LES to be more universal and thereby to be more easily adaptable to any turbulent flow configuration. The case of interest of turbine blade cooling channels addressed in this thesis is a particular configuration where large separated flows in presence may provide some pitfalls to the RANS models. LES, which has already been validated in gas turbine applications with



combustion predictions, is here a potential candidate to improve the resolution of the complex flows encountered in cooling channels.

In this framework, the aims of the works presented in this manuscript were to examine the application, validation and comparison to the current RANS industrial tools of the LES approach for the aerothermal modeling of turbine blade cooling. The objectives of the study were determined as follows: (1) Analyze the physical phenomenon in blade cooling channel flows and propose a suitable numerical approach for LES targeting the application capabilities to a realistic industrial turbine blade. Evaluate the LES predictions provided using this approach on simplified static typical cooling channel geometries from the dynamic and thermal points of view. (2) Extend the chosen LES modeling in the case of rotating channels and underline the physical changes. Validate the predictions with available experimental data. (3) Apply the previous LES analysis to a realistic cooling channel to describe the complex flow and estimate the consequent heat transfer. Perform finally the CHT computation of a turbine blade with the LES results and compare it to industrial RANS results. The conclusions raised from the present work follow these three points:

### LES of static cooling channel

- The turbulence is a first order physical phenomenon responsible of heat transfer increase at the wall in cooling channels. Resolution of this turbulence in the near-wall regions becomes the LES bottle neck for  $Re > 10\,000$  and requires most of the computational time [100]. An approach using a hybrid discretization of the cooling channel is proposed to reduce the computational requirement using a prism layer on all the channel walls, tetrahedron filling the remaining fluid volume. The assumption proposed here is to solve the flow at the wall with the SGS WALE model without wall-law, imposing all first off-wall points in the viscous sublayer (i.e. setup the prism layer such as  $y^+ < 10$ ). The choices of a wall-resolved approach is preferred to a wall-law approach due to the complex near-wall flows (multiple reattachments and separations with adverse pressure gradients) for which classical log wall-laws are not specifically dedicated. Note that the use of the latter have however shown to be of acceptable accuracy to reduce the computational cost for larger configurations.
- Two academic geometries which are typical of blade cooling channels are chosen for the assessment of the LES in this configuration type: a U-bend and a straight ribbed channel, both designed by the VKI. Measurements and RANS results are available for both of them. For the flow dynamic predictions, massive separations created in the cooling channels by the ribs and the bend are seen to be handled with difficulties by the RANS models: even if it is possible to obtain a good prediction with a particular modeling, the lack of universal

closure makes it a dangerous option to simulate such complex flows. By contrast, every LES test case (even a poorly designed one) leads to similar mean and fluctuating flows in good agreement with measurements, showing its good reliability for this typical configuration. Note that if unsteady LES modeling has proven its interest, the requirement of more realistic unsteady boundary conditions for more accurate results has also been highlighted. The thermal behavior at the wall is the direct consequence of the flow topology: the latter being correctly predicted by LES in the ribbed channel, the resulting thermal efficiency at the wall is found to be in very good agreement with experiments, as well for heat transfer levels or maps (for the ribbed channel case: two high heat transfer regions with heat transfer enhancement above 2 are correctly predicted between two ribs).

### LES of rotating cooling channel

- The derivation of the NS equations relatively to a rotating frame generates two additional non-inertial forces: the Coriolis and the centrifugal forces. The consequences in the particular case of a channel with spanwise rotation is the stabilization or destabilization of the shear regions, leading to turbulence intensity decrease or increase respectively.
- The common approach used in the literature to solve rotating flows is in the rotating frame of reference. This method implies the modification of the NS equations to be solved and of the turbulence model to take into account the change of frame. Instead, the ALE approach, available in AVBP, is proposed here to simulate rotating flows directly in a inertial frame of reference, without an *a priori* modification requirement of the solved NS equations since inertial forces are implicitly taken into account. ALE rotation movement has been therefore implemented and the validation in a simplified channel configuration shows a satisfactory recovering of the analytical centrifugal and Coriolis forces.
- A VKI rotating ribbed channel is chosen as the reference test bench to evaluate the ALE method on a cooling configuration. The results of adiabatic flow computations using the hybrid discretization and the ALE method with LES are compared to PIV measurements of non-rotating, stabilized and destabilized rotations. LES provides predictions with a good agreement of the mean flow and unsteady structure behaviors for the non rotating case and for the rotating case implying stabilizing flow around the ribs. For the destabilizing case, mean flow and turbulence intensity level show more differences than anticipated. The lack of mesh resolution and the need of better SGS modeling are pointed out as possible reasons of such discrepancies. Despite this observation and thanks to the available VKI experimental data, advanced LES results analyses as two-point correlations and vortex tracking show that the large scale mean flow behavior and unsteady turbulence evolution are well predicted by LES.

- LES predictions of the ribbed channel with heated walls show a strong correlated behavior to the aerodynamic flow field, especially to the near wall singular topologies (separations and reattachments being correlated with lower and higher heat transfer respectively). The evolution of the mean wall heat transfer efficiency is found to be significantly affected by the rotation: in comparison to the non rotating case, heat transfer is uniformly 30% lower on the stabilized wall, and from 30% to 60% higher on the destabilized wall. An other LES study on a similar configuration provided similar thermal predictions. Despite the disparities observed on the flow topology around the ribs in comparison to the experimental data and the need of better SGS analysis, the present approach with the hybrid mesh, ALE and LES WALE model for rotating ribbed channels is found relevant for the industrial CHT computation chosen since only wall thermal quantities are used for the solid thermal computation.

### LES of realistic rotating cooling channel

- The setup of a full industrial blade cooling channel with the ALE based rotation and the hybrid mesh methods has been successfully applied. The resulting LES predictions yield the changes induced by rotation on the flow (i.e. stabilization and destabilization) and a consequent modification of the wall heat flux repartition. The mesh resolution at the wall is found to be of first importance for the heat flux estimations and the resulting blade temperature distribution. A mesh with  $y^+ < 10$ , accordingly to the wall-resolved approach proposed in this thesis, is seen here to be a minimal requirement to perform the turbine blade cooling CHT computation.
- A LES based CHT computation is proposed using the chaining method where only time averaged thermal values are exchanged between a fluid solver and a solid thermal solver (AVBP and AVTP respectively). This approach is sufficient to solve the present CHT problem of the turbine blade regarding the characteristic time scales of the fluid and the solid. The first comparisons with the reference industrial RANS tool show global similar levels of predicted temperature. However local important difference are obtained all along the channel on the heat flux and temperature estimations. The main difference is observed in the blade root where high heat transfer rates are predicted by LES leading to a significant increase of the air temperature inside the channel. Since no experimental data is available and according to the satisfactory thermal validation of LES in the rotating academic channel, these differences should be further investigated.

### Future works

Results of the study on the aerothermal modeling of cooling channel with LES summarized in the previous conclusions have raised the following improvement areas:

- The ALE method to model rotating fluid with LES has shown the possible need for a better comprehension of the SGS modeling in this specific framework. The modification of the SGS dissipation may be one of the first axes to explore.
- Rotating wall thermal measurements on the VKI ribbed channel were not available yet in the time range of this work. Comparisons should offer interesting additional validations to this study.
- The works presented in this thesis have particularly focused on the LES thermal predictions. In turbine cooling design, pressure losses are the other first order parameter. Further investigations of the LES prediction capabilities on the pressures loss estimations in the cooling channels, also related to the wall resolution, could therefore be proposed.
- The wall modeling has been enlightened as being the key-point of the LES of wall bounded flows. Besides the hybrid discretization proposed in this manuscript, other more complex wall modeling than the log wall-law could be studied. On this line, numerous works are in progress on the LES/RANS coupling. A review of the available variety is proposed by Fröhlich [43].
- A different direction for improvement of the LES accuracy is also available considering an increasing resolution of the mesh. Smaller mesh cells and larger point number near the wall are likely to reduce the modeled part of the LES predictions. Of course, this higher resolution has a cost which has already been underlined as unaffordable for the industry yet. However, looking at the Mach number present in the cooling channels, the compressible approach of AVBP may be an obstacle to this rise in resolution. It should therefore be worth considering an incompressible solver to perform LES in such internal cooling channels. In the present case, short investigations with the incompressible YALES2 solver [89] on the VKI ribbed channels, using the identical meshes and the same LES model, has shown a computational time reduced by a factor around 10 with similar accuracy.



# Appendices



# RANS and LES modeling details

---

## A.1 Physics and modeling of turbulent flows

### Governing equations

Starting point of the turbulence modeling in this thesis are the three-dimensionnal compressible NS equations:

$$\frac{\partial(\rho \mathbf{u})}{\partial t} + \nabla \cdot (\rho \mathbf{u} \otimes \mathbf{u}) = -\nabla p + \nabla \cdot \boldsymbol{\tau} + \rho \mathbf{f} \quad (\text{A.1})$$

which in Cartesian coordinates and using the Einstein notations (indices ranging over the set  $\{1, 2, 3\}$  for the three space coordinates) read:

$$\frac{\partial}{\partial t}(\rho u_i) + \frac{\partial}{\partial x_j}(\rho u_i u_j + p \delta_{ij} - \tau_{ji}) = \rho f_i \quad (\text{A.2})$$

In A.2  $u_i$  is the  $i$ th velocity component of the fluid,  $\rho$  its density,  $p$  the pressure,  $\tau_{ij}$  the viscous stress tensor and  $f_i$  the body forces. In order to fully describe fluid flows, one adds to the previous equations the following conservation laws for mass, Eq. A.3, and energy, Eq. A.4:

$$\frac{\partial \rho}{\partial t} + \frac{\partial}{\partial x_j}(\rho u_j) = 0 \quad (\text{A.3})$$

$$\frac{\partial}{\partial t}(\rho E) + \frac{\partial}{\partial x_j}(\rho u_j E + u_i p \delta_{ij} + q_j - u_i \tau_{ij}) = \rho u_j f_j + r \quad (\text{A.4})$$

$E$  is here the total energy, which depends in addition to pressure, on the viscous dissipation, the body forces already present in the momentum equations, as well as on the flux vector  $q_j$  and radiative transfers  $r$ .

In the following, the entire set of conservation equations will be called as Navier-Stokes (NS) equations.

### Simplifications and assumptions

**Newtonian fluid** In this aerothermal study, the only operating fluid will be pure air. It will thus be considered as a Newtonian fluid [6], which implies the viscous stress tensor which becomes linearly dependent on the strain rate  $\mathbf{S}$  with its components  $s_{ij}$ :



$$s_{ij} = \frac{1}{2} \left( \frac{\partial u_i}{\partial x_j} + \frac{\partial u_j}{\partial x_i} \right) \quad (\text{A.5})$$

Using fluid particle isotropic considerations one obtains the following expression for the viscous stress tensor [44]:

$$\tau_{ij} = 2\mu s_{ij} + \eta s_{kk} \delta_{ij} \quad (\text{A.6})$$

with  $\mu$  the dynamic coefficient of viscosity for the shear and  $\eta$  the second coefficient of viscosity link to the dilatation.

**Stokes' hypothesis** Stokes' hypothesis [125, 44] assumes that for such a fluid, mechanical pressure could be equal to the thermodynamical pressure neglecting the damping of volumetric vibration of a fluid particle, yielding simply:

$$3\eta + 2\mu = 0 \quad (\text{A.7})$$

so that:

$$\tau_{ij} = 2\mu \left( s_{ij} - \frac{1}{3} s_{kk} \delta_{ij} \right) \quad (\text{A.8})$$

**Viscosity** Dynamic viscosity  $\mu$  is assumed to depend on temperature following the Sutherland's law, valid from 100 K to 1900 K [45]:

$$\frac{\mu(T)}{\mu(T_{ref})} = \left( \frac{T}{T_{ref}} \right)^{3/2} \frac{T_{ref} + S}{T + S} \text{ with } S = 110.4 \text{ K} \quad (\text{A.9})$$

**Equation of state** Temperature  $T$ , pressure  $p$  and density  $\rho$  are also linked by the equation of state for perfect gases:

$$p = \rho \frac{R}{M} T \quad (\text{A.10})$$

with  $R = 8.3145 \text{ J/mol/K}$  the gas constant and  $M$  the molar mass in  $\text{kg/mol}$  of the gas/mixture.

**Body forces** Body forces  $f_i$  are in general associated to the gravity, electromagnetic and inertial forces. In this study, we will only deal with air in earth's magnetic field so magnetic forces will always taken as zero. For the two other forces, since we will study thermal and rotating configurations, we will verify their influence in the following chapters through dimensionless numbers.

## A.2 RANS

RANS modeling introduces the notion of *average* so only mean flow values are solved while all turbulent scales are modeled leading to a low computational time. The principle is based on the Favre averaging of the compressible NS equations [41], splitting each quantity, except density, into a Favre averaged mean and a fluctuating component:

$$\phi = \tilde{\phi} + \phi'' \quad (\text{A.11})$$

with the Favre averaged component defined by:

$$\tilde{\phi} = \frac{\overline{\rho\phi}}{\bar{\rho}} \quad (\text{A.12})$$

The fluctuating part  $\phi''$  therefore satisfies:

$$\overline{\rho\phi''} = 0 \quad (\text{A.13})$$

Overline denoting classical time (Reynolds) or ensemble average with the following properties (with  $a$  constant and  $\phi$  an  $\psi$  function of time):

1. Constant conservation:

$$\bar{a} = a$$

2. Linearity:

$$\overline{a\phi + \psi} = a\bar{\phi} + \bar{\psi}$$

3. Commutation with temporal and spatial derivative:

$$\overline{\frac{\partial\phi}{\partial t}} = \frac{\partial\bar{\phi}}{\partial t}$$

$$\overline{\frac{\partial\phi}{\partial x_j}} = \frac{\partial\bar{\phi}}{\partial x_j}$$

4. Idempotence:

$$\overline{\overline{\phi\psi}} = \overline{\phi\psi}$$

$$\overline{\overline{\phi}} = \bar{\phi}$$

Substituting Eq. A.11 into the NS equations and averaging, one obtains the following set of equations to be solved numerically:

$$\frac{\partial\bar{\rho}}{\partial t} + \frac{\partial}{\partial x_j} (\bar{\rho}\tilde{u}_j) = 0 \quad (\text{A.14})$$

$$\frac{\partial}{\partial t} (\bar{\rho}\tilde{u}_i) + \frac{\partial}{\partial x_j} (\bar{\rho}\tilde{u}_i\tilde{u}_j + \bar{p}\delta_{ij} - \bar{\tau}_{ji} - \overline{\tau_{ji}^t}) = \bar{\rho}\tilde{f}_i \quad (\text{A.15})$$

$$\frac{\partial}{\partial t}(\bar{\rho}\tilde{E}) + \frac{\partial}{\partial x_j}(\bar{\rho}\tilde{u}_j\tilde{E} + \tilde{u}_j\bar{p} + \bar{q}_j + \bar{q}_j^t - \tilde{u}_i(\bar{\tau}_{ij} - \bar{\tau}_{ij}^t)) = \bar{\rho}\tilde{u}_j\tilde{f}_j \quad (\text{A.16})$$

Due to non-linearity of the NS equations, Favre averaging introduces new terms which some of them can be neglected. The primary unknowns to be modeled for a proper numerical integration and flow simulation are:  $\bar{\tau}_{ij}^t = -\bar{\rho}\tilde{u}_i''\tilde{u}_j''$  and  $\bar{q}_j^t = -C_p\bar{\rho}\tilde{u}_j''T$ . For the first term, also called Reynolds stress tensor, common modeling employs the Boussinesq hypothesis [112] based on the resolved strain rate tensor  $\tilde{s}_{ij}$  and leading to a similar expression as for  $\tau_{ij}$ :

$$\bar{\tau}_{ij}^t = 2\bar{\rho}\nu_t\left(\tilde{s}_{ij} - \frac{1}{3}\tilde{s}_{kk}\delta_{ij}\right) \quad (\text{A.17})$$

With this assumption, a new scalar  $\nu_t$  also known as the turbulent viscosity is introduced and is usually evaluated from available quantities. The turbulent heat flux,  $\bar{q}_j^t$  can be modeled using a turbulent thermal conductivity and the turbulent Prandtl number ( $\lambda_t = \nu_t\bar{C}_p/Pr_t$ ), which leads to:

$$\bar{q}_j^t = -\lambda_t\frac{\partial\tilde{T}}{\partial x_j} \quad (\text{A.18})$$

Note that in the mean NS equations other terms are approximated. Typically,

$$\bar{\tau}_{ij} \approx \widetilde{\tau_{ij}} = 2\bar{\mu}\left(\tilde{s}_{ij} - \frac{1}{3}\tilde{s}_{kk}\delta_{ij}\right) \quad (\text{A.19})$$

for the momentum Eq. A.15, and

$$\bar{q}_j \approx -\bar{\lambda}\frac{\partial\tilde{T}}{\partial x_j} \quad (\text{A.20})$$

for total energy Eq. A.16.

Numerous types of closures are possible. They are usually classified in terms of number of transport equations solved (in addition to the RANS equations) to compute  $\nu_t$  (as among others works [76, 121, 36]). In some circumstances it can also be of interest to solve for the 6 modeled transport equations of the Reynolds stress tensor directly [77, 31].

### A.3 LES

LES modeling relies on the filtering of the NS equations so the most energetic part of the flow is resolved and directly simulated. The assumption behind this method is that all turbulent length scales can be divided into two parts:

- a high energy anisotropic large scales range, above the filter length scale
- a lower energy and dissipative isotropic small scale range, below the filter length scale

Generally filtering is linked to the mesh cells size and the first geometry-dependent range of scales can be resolved without paying too expensive a computational price thanks to a not too fine mesh. Note that scales smaller than the grid size still need to be modeled to simulate the turbulent dissipation effect of the removed information which is done using a so-called subgrid scale (SGS) model. To do so, LES for compressible flows involves the same formalism as RANS with the spatial Favre filtering:

$$\phi = \tilde{\phi} + \phi'' \quad (\text{A.21})$$

with this time  $\tilde{\phi}$  the low frequency part and  $\phi''$  the high frequency part of  $\phi$ . In simple cases the filtering operation reduces for spatially, temporally invariant and localized filter functions to:

$$\widetilde{\phi(\mathbf{x}, t)} = \frac{1}{\rho(\mathbf{x}, t)} \int_{-\infty}^{+\infty} \rho(\mathbf{x}', t) \phi(\mathbf{x}', t) G(\mathbf{x}' - \mathbf{x}) d\mathbf{x}', \quad (\text{A.22})$$

where  $G$  denotes the filter function. In comparison to RANS average operator, the filtering operator follows the three first properties of the latter (constant conservation, linearity and commutation), but not the idempotence, ie:

$$\begin{aligned} \widetilde{\tilde{\phi} \psi} &\neq \tilde{\phi} \tilde{\psi} \\ \widetilde{\tilde{\phi}} &\neq \tilde{\phi} \end{aligned}$$

It has also to be noticed that in practical applications (i.e. with bounded domain and irregular space discretization), Favre filtering does not commute with space derivatives [110].

Then, filtering NS equations leads to the same set of equations than RANS, except the non linear term representing here the unresolved SGS stress tensor:

$$\bar{\tau}_{ij}^{SGS} = -\bar{\rho}(\widetilde{u_i u_j} - \tilde{u}_i \tilde{u}_j) \quad (\text{A.23})$$

Even if several modeling method exists, Boussinesq assumption [118] is commonly used in the same way as RANS to model  $\bar{\tau}_{ij}^{SGS}$ , here from the unsteady filtered strain rate tensor  $\tilde{s}_{ij}$ .

**Subgrid scale viscosity modeling** Since LES pretends to be a more universal turbulence modeling than RANS, there are a narrower range of method to model non linear term than for the latter. In this framework, the most famous SGS viscosity model is probably the Smagorinsky model [118]. Based on the assumption that energy production and dissipation are in equilibrium, Smagorinsky proposed the following expression for  $\nu_{SGS}$ :

$$\nu_{SGS} = (C_s \Delta)^2 \sqrt{2 \tilde{s}_{ij} \tilde{s}_{ij}} \quad (\text{A.24})$$

Where  $\Delta$  stands for the filter length ( $\propto$  the cubic-root of the cell volume) and  $C_s$  is the model constant set to 0.18.

But in this thesis implying internal cooling channel, an especially wall bounded flow designed model has been preferred: SGS turbulent viscosity is thus computed with the WALE model introduced by Nicoud [94]. This model allows indeed to recover the  $y^3$  near-wall scaling law for turbulent viscosity with the following expression:

$$\nu_t = (C_w \Delta)^2 \frac{(s_{ij}^d s_{ij}^d)^{3/2}}{(\tilde{S}_{ij} \tilde{S}_{ij})^{5/2} + (s_{ij}^d s_{ij}^d)^{5/4}}, \quad (\text{A.25})$$

$$s_{ij}^d = \frac{1}{2}(\tilde{g}_{ij}^2 + \tilde{g}_{ji}^2) - \frac{1}{3}\tilde{g}_{kk}^2 \delta_{ij}, \quad (\text{A.26})$$

$C_w$  is the model constant equal to 0.4929 and  $\tilde{g}_{ij}$  is the resolved velocity gradient. The SGS energy flux is then modeled from the turbulent viscosity as for RANS method, with here the filtered quantities [88, 35, 27].

# AVBP solver presentation

---

The main code used in this manuscript to compute internal cooling flow is the AVBP code [113]. Today property of CERFACS and Institut Français du Pétrole (IFP), this code was designed from the very beginning to be used for parallel computing. It is dedicated and have been widely validated on reactive flow numerical simulation, mainly for combustion application, in complex geometries with its hybrid unstructured grid management. But the code versatility has also permitted to compute configurations with Lagrangian flow and mesh movement, and further from reactive flows the present subject on aerothermal study of coolant flow.

The code solves the full compressible, multi species, reactive Navier-Stokes (NS) equations, presented in the section 3.1.2 in the simplified mono species and non reactive form suitable for our study. Available numerical methods allow to solve NS equations on both structured and unstructured grid with finite volume and finite element schemes. Formulation used is cell-vertex type, with data stored at mesh nodes, giving among other advantages a better robustness against mesh distortion.

Following two numerical schemes available in AVBP based on this formulation have been used in this thesis. They are briefly described here but further properties analysis can be found in the Lamarque thesis [74].

- Lax-Wendroff (LW) scheme: LW scheme is a space and time  $2^d$  order centered scheme [79, 80] adapted to the cell-vertex method. Time march has only one step giving to this scheme a relatively good accuracy for a low computational time, even if its dissipation and dispersion properties are mean. These characteristics make this scheme a good candidate to initialize a computation in the transient time without wasting computational time with higher order and expensive schemes.
- Two-step Taylor-Galerkin (TTG) schemes: this scheme family is a predictor-corrector type. In AVBP, space and time  $3^d$  TTGC [25] is often used for production computation after LW initializing thanks to its good dissipation and dispersion properties (low dispersion and low dissipation of small flow length scale). Its computational time is 2.3 times higher than LW scheme.

Employing these explicit schemes involves to keep the CFL number below 0.7 to ensure stability, which lead to the main disadvantage to use time steps very low: for example  $\propto 10^{-7}$ s for aerodynamical applications where the viscous sub-layer needs to be computed accurately, inducing even with LW scheme high computational costs.

In AVBP, the use of centered schemes with low dissipation requires the addition of artificial diffusion operator. Indeed, transport of high gradient may lead to the

Gibbs phenomenon [114] with the apparition of non physical node-to-node oscillations called wiggles. To help the diffusion operator in its task, artificial viscosity can be added locally in the field to remove numerical oscillations. A sensor specifically dedicated to unsteady turbulent flow can automatically detect numerical anomalies and increase local viscosity in the limitation of an user defined threshold.

### Details on equation closure in AVBP

Some additional details are given here on the AVBP physical implementation.

- For thermal diffusion, space and time constant Prandtl number is assumed, which is a common hypothesis even if its value may change with local composition and thermodynamical state. Thermal diffusion coefficient is so computed from viscosity with the formula  $\lambda = \mu C_p / Pr$ .
- Dynamic viscosity can be computed from Sutherland or power law being a temperature function. In this thesis, power law has been used.
- To improve computational time, species enthalpies are stored in tables from 0 to 5000 K with a 100 K step.  $C_p$  are obtained from derivation of these tables leading to piece-wise values each 100 K.

### Details of the wall log-law implemented in AVBP

Classical near wall log-law [102] is implemented in AVBP as following:

- Viscous linear sublayer where  $y^+ \leq 11.445$  :

$$u^+ = y^+ \tag{B.1}$$

- log-law region where  $y^+ \geq 11.445$  :

$$u^+ = \kappa^{-1} \ln(E y^+) \text{ with } \kappa = 0.41 \text{ and } E = 9.2 \tag{B.2}$$

All additional information on numerical method and physics modeling in AVBP can be found in the code handbook [17].

# Periodicity of compressible flow in a ribbed channel

---

## Entropy increase in the periodic channel

Entropy increase caused by the source term is considered negligible in the time range used to compute flow statistics in the periodic ribbed channel. Indeed, a constant increase rate of 0.35 K/s has been observed in the present computations. which gives an increase of 0.53 K in the time range used to converge LES statistics. This has no major influence on the flow since it represents only twice the mean temperature range at a given moment (0.223 K).

## Axial source term influence

Using a constant source term on the x-momentum equation everywhere in the domain may be a plausible option for a periodic smooth channel configuration where axial pressure gradient is constant, but here in our case the rib causes strong flow bifurcations and contraction leading to a no more uniform pressure gradient. So in order to check if its addition would influence the pressure field viewed by the flow, fictive pressure  $P_f$  is created from  $P_p$  the pressure in the periodic domain using the formula  $P_f = P_p - x \cdot S_x^{cst}$ . Figure C.1 presents  $P_f$  field and the mean pressure around a rib computed in the spatial case. Comparison shows that similar pressure loss is recovered in the periodic case as well as isobar line shapes. A difference is however observed in the shear layer behind the rib where mean fictive pressure has a lower minimum than in the spatial case, with a difference about 15 Pa.

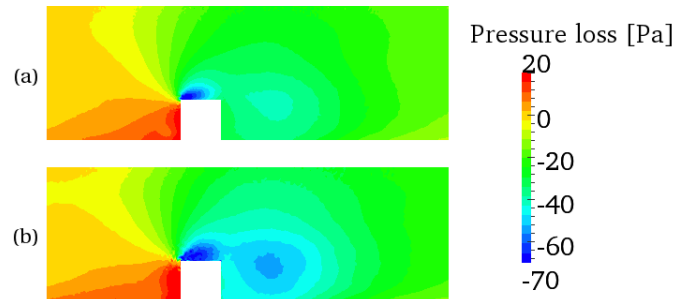


Figure C.1: Comparison of pressure around a rib in (a) periodic and (b) spatial computations. Pressure in periodic case is rebuilt with constant source term.





# Comparison of LES simulations on full-tetra meshes with PIV measurement

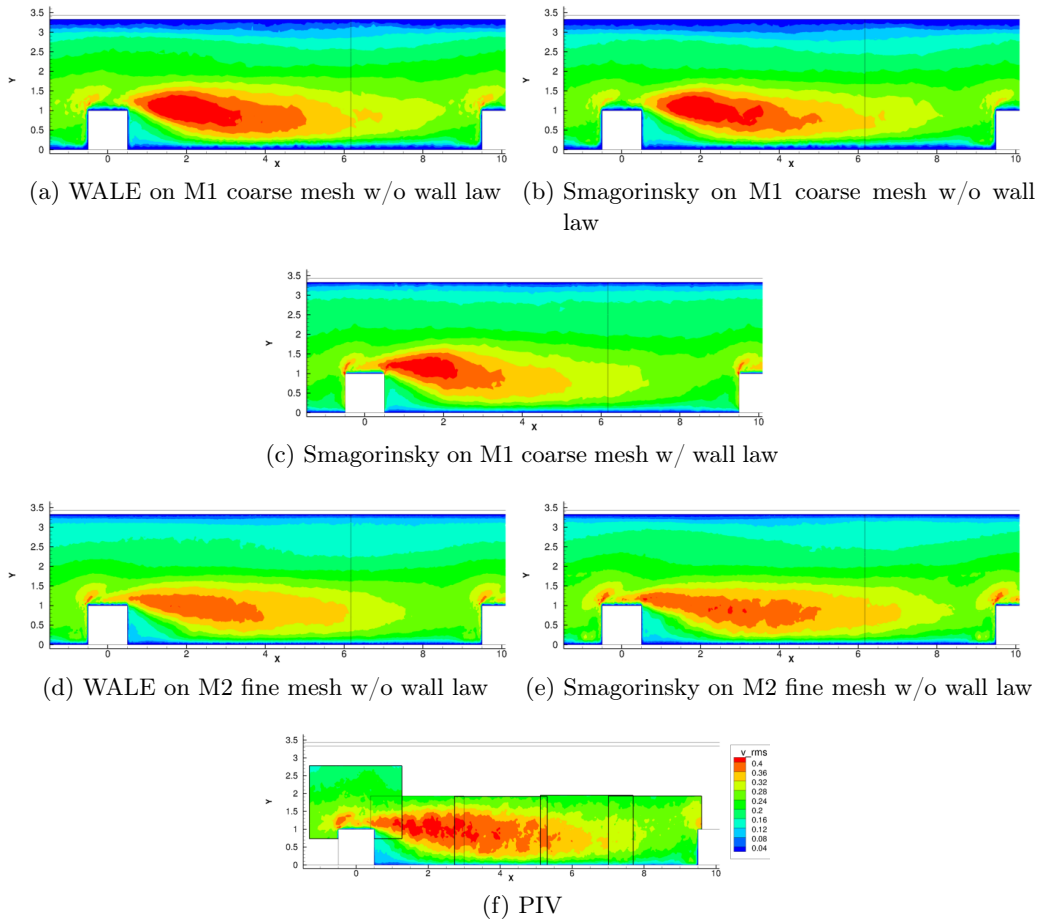


Figure D.1: Non-dimensionalized fluctuating wall-normal velocity  $\overline{v'v'}$  in 1XY plane: comparison of WALE and Smagorinsky modeling with PIV.

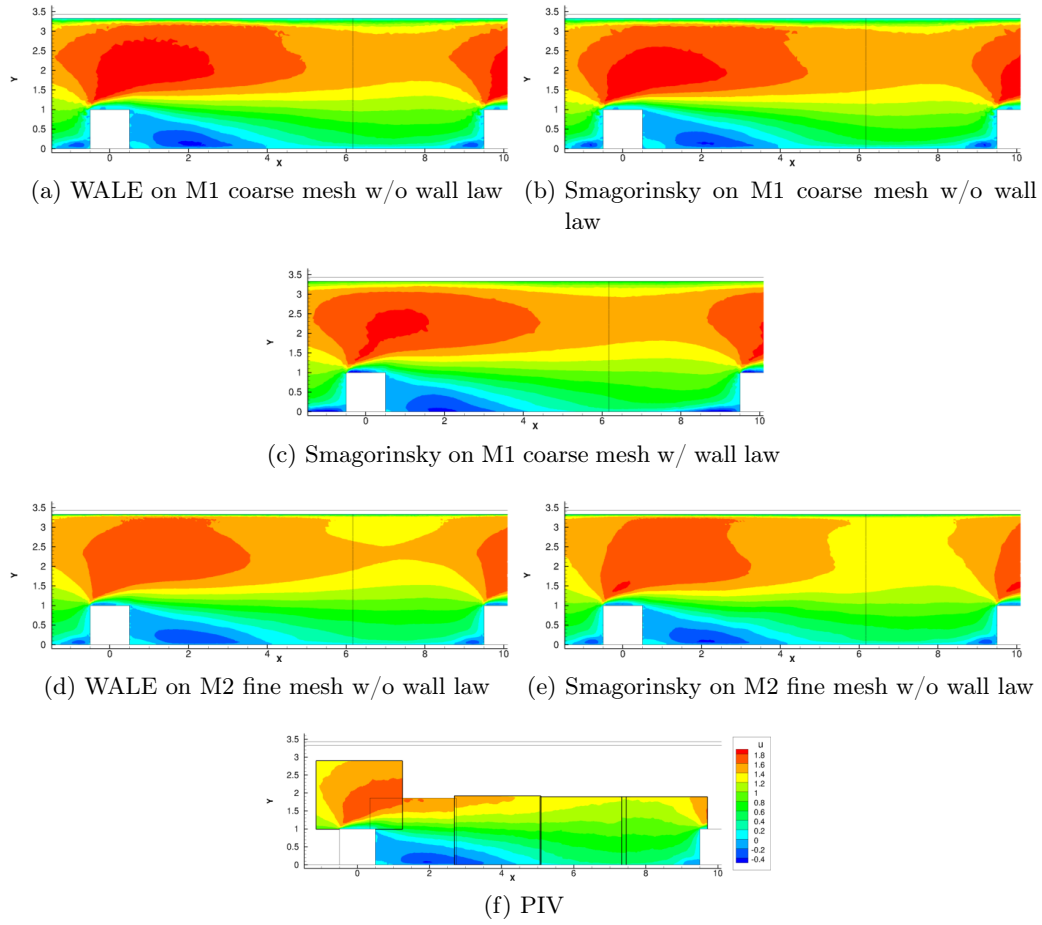


Figure D.2: Non-dimensionalized mean streamwise velocity  $\bar{u}$  in 2XY plane: comparison of WALE and Smagorinsky modeling with PIV.

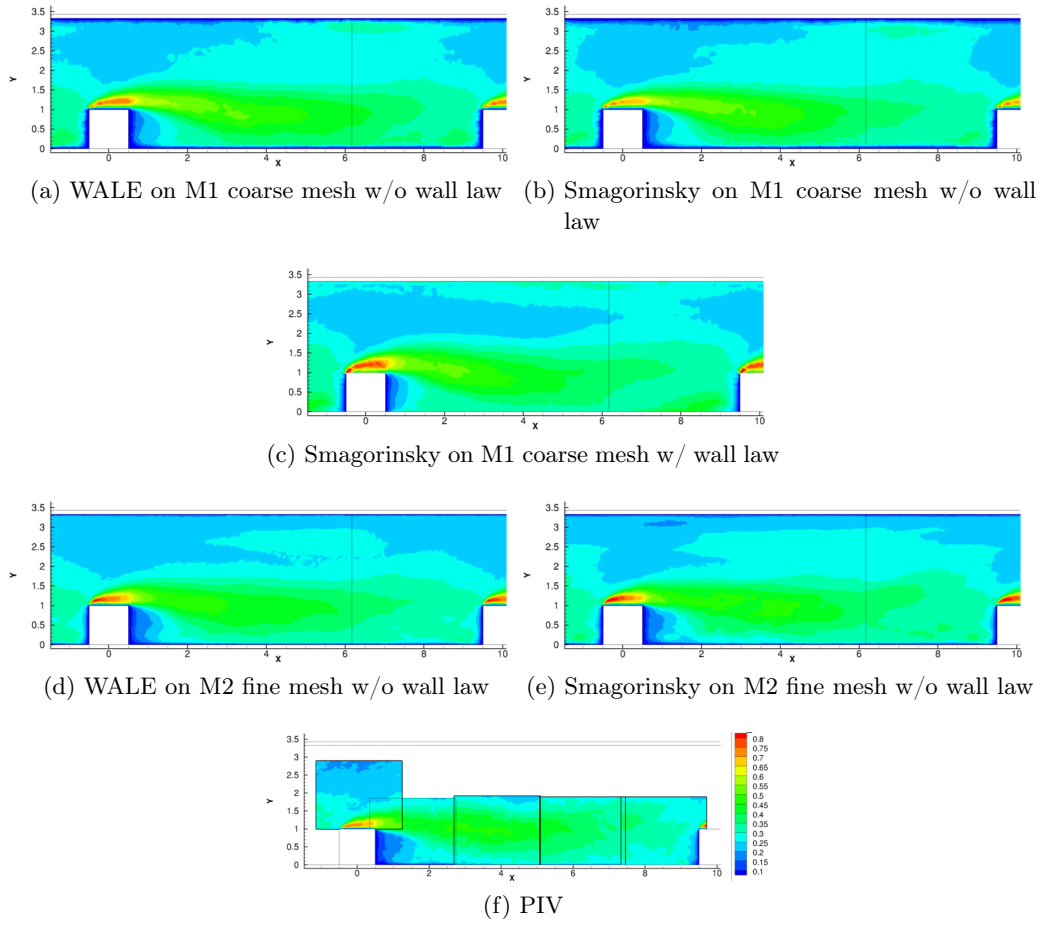


Figure D.3: Non-dimensionalized fluctuating streamwise velocity  $\overline{u'u'}$  in 2XY plane: comparison of WALE and Smagorinsky modeling with PIV.

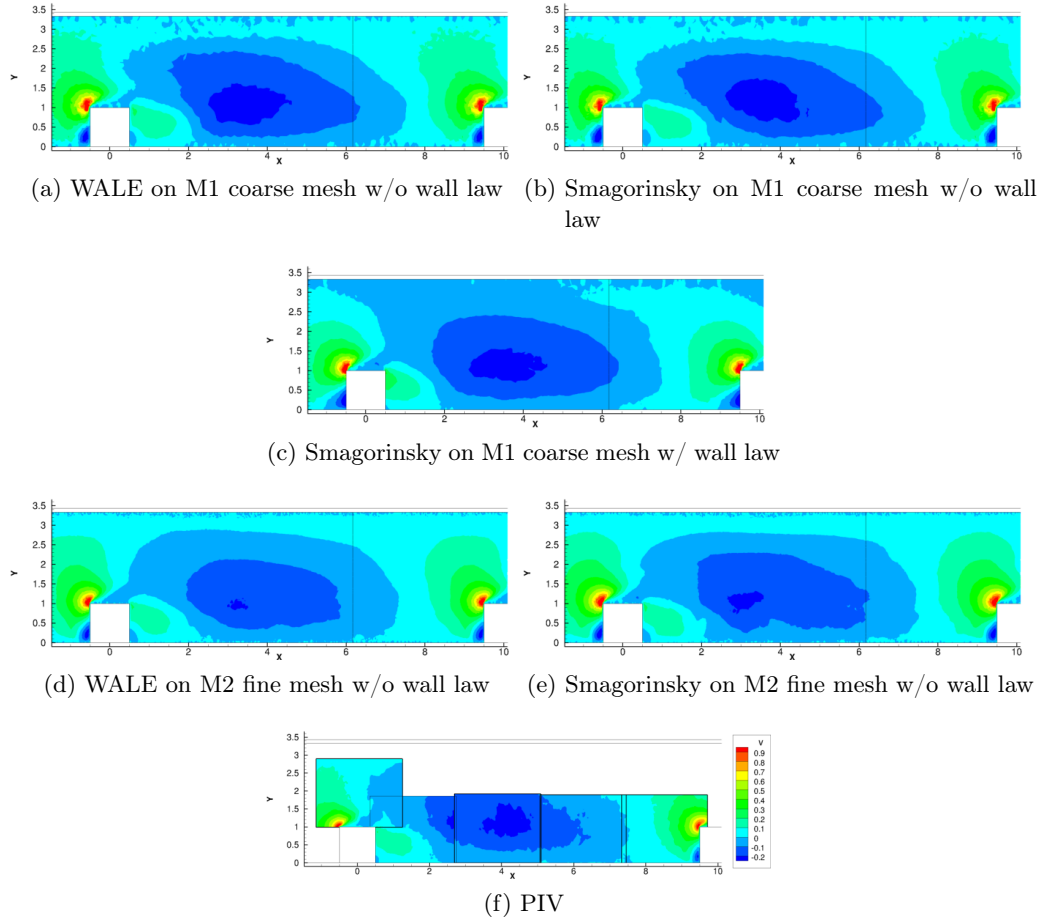


Figure D.4: Non-dimensionalized mean wall-normal velocity  $\bar{v}$  in 2XY plane: comparison of WALE and Smagorinsky modeling with PIV.

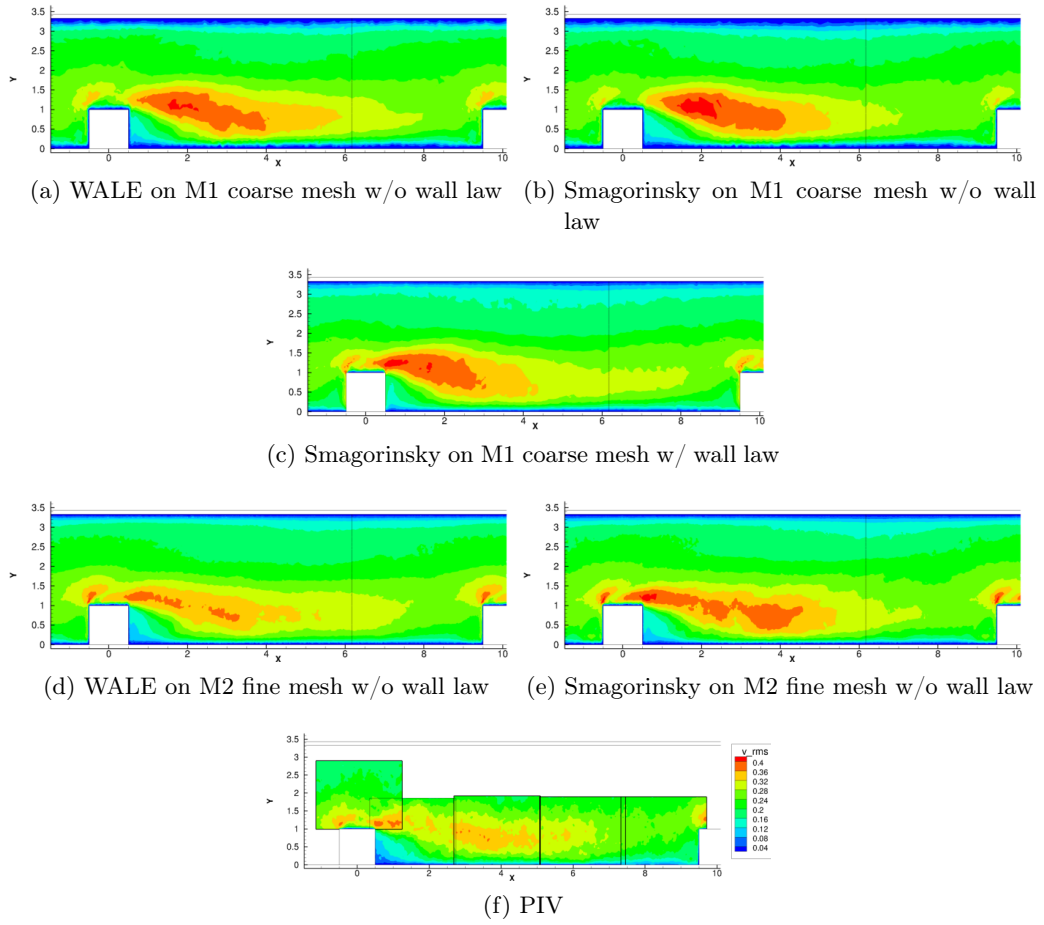


Figure D.5: Non-dimensionalized fluctuating wall-normal velocity  $\overline{v'v'}$  in 2XY plane: comparison of WALE and Smagorinsky modeling with PIV.

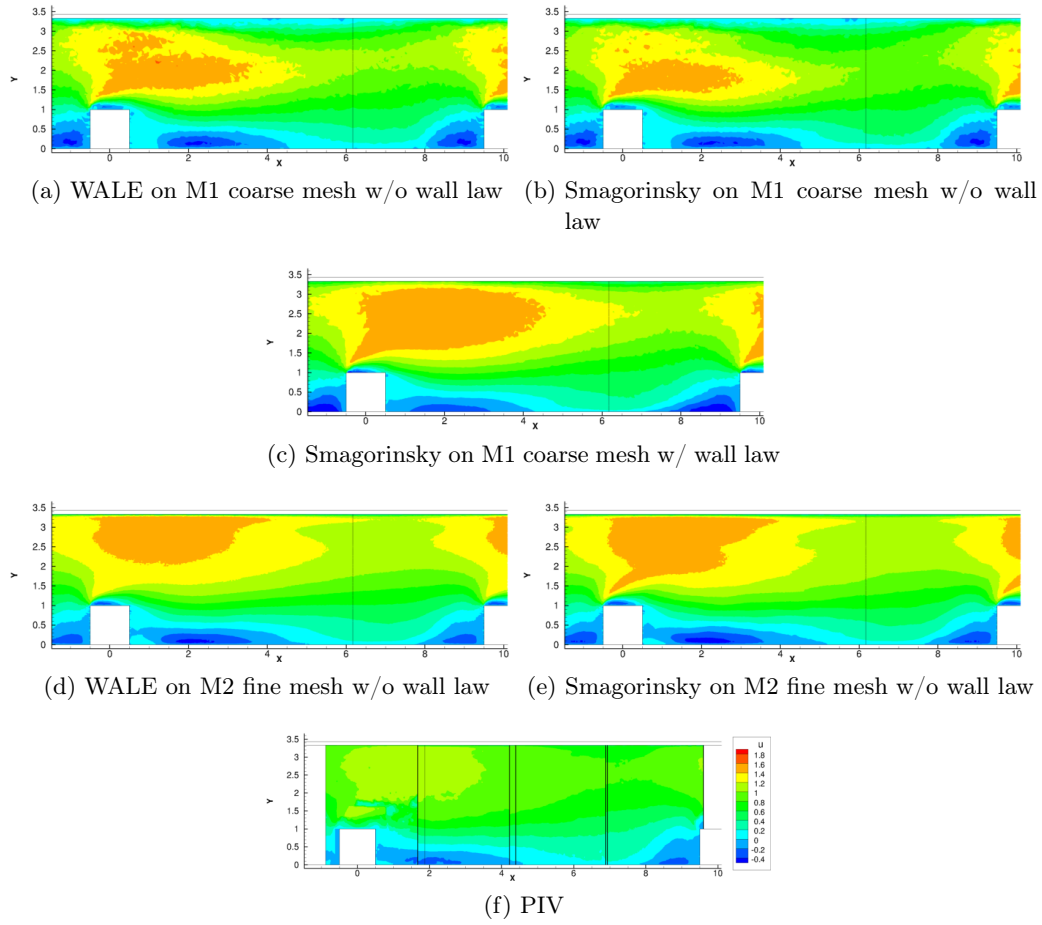


Figure D.6: Non-dimensionalized mean streamwise velocity  $\bar{u}$  in 3XY plane: comparison of WALE and Smagorinsky modeling with PIV.

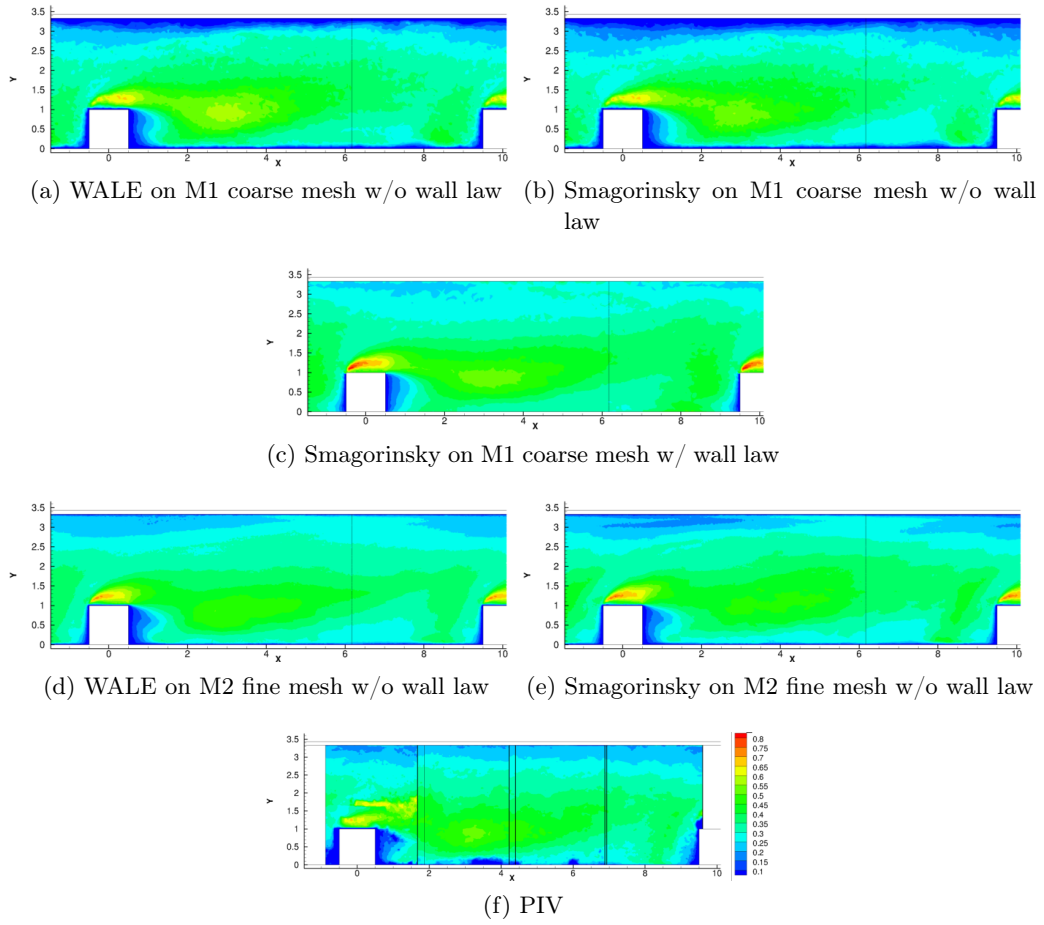


Figure D.7: Non-dimensionalized fluctuating streamwise velocity  $\overline{u'u'}$  in 3XY plane: comparison of WALE and Smagorinsky modeling with PIV.



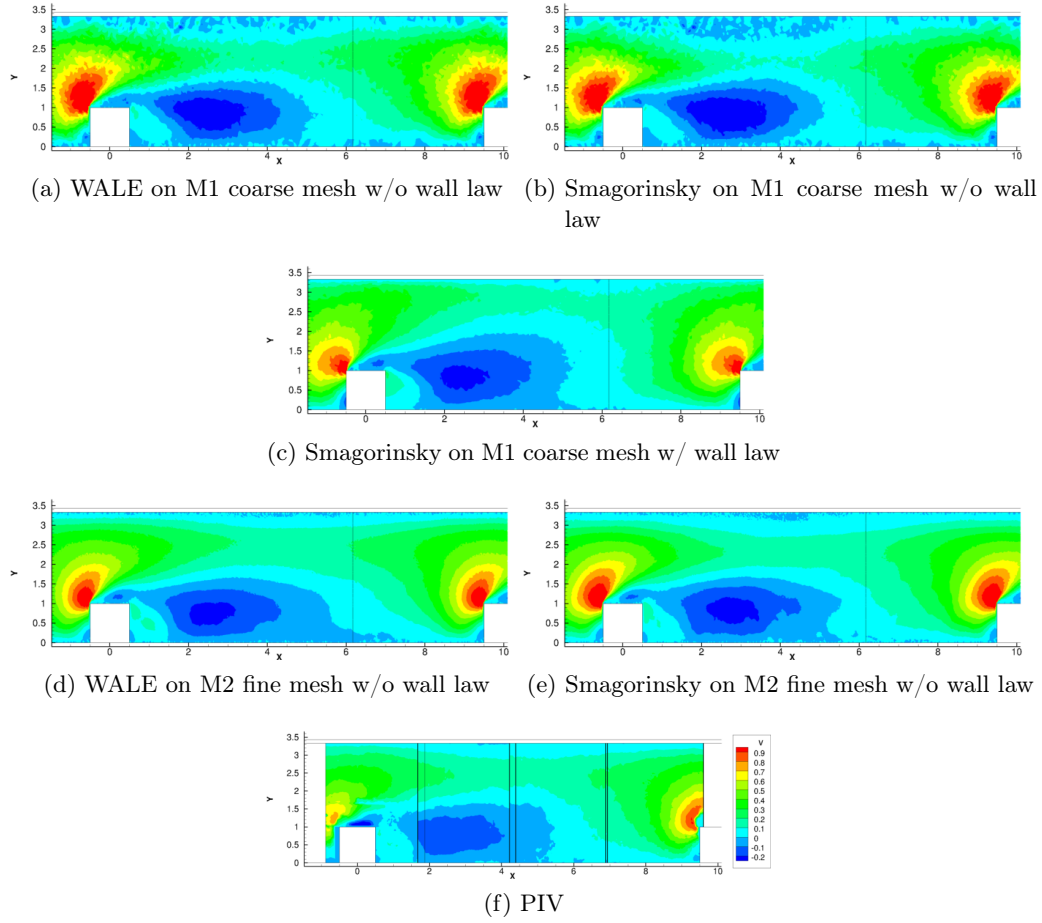


Figure D.8: Non-dimensionalized mean wall-normal velocity  $\bar{v}$  in 3XY plane: comparison of WALE and Smagorinsky modeling with PIV.

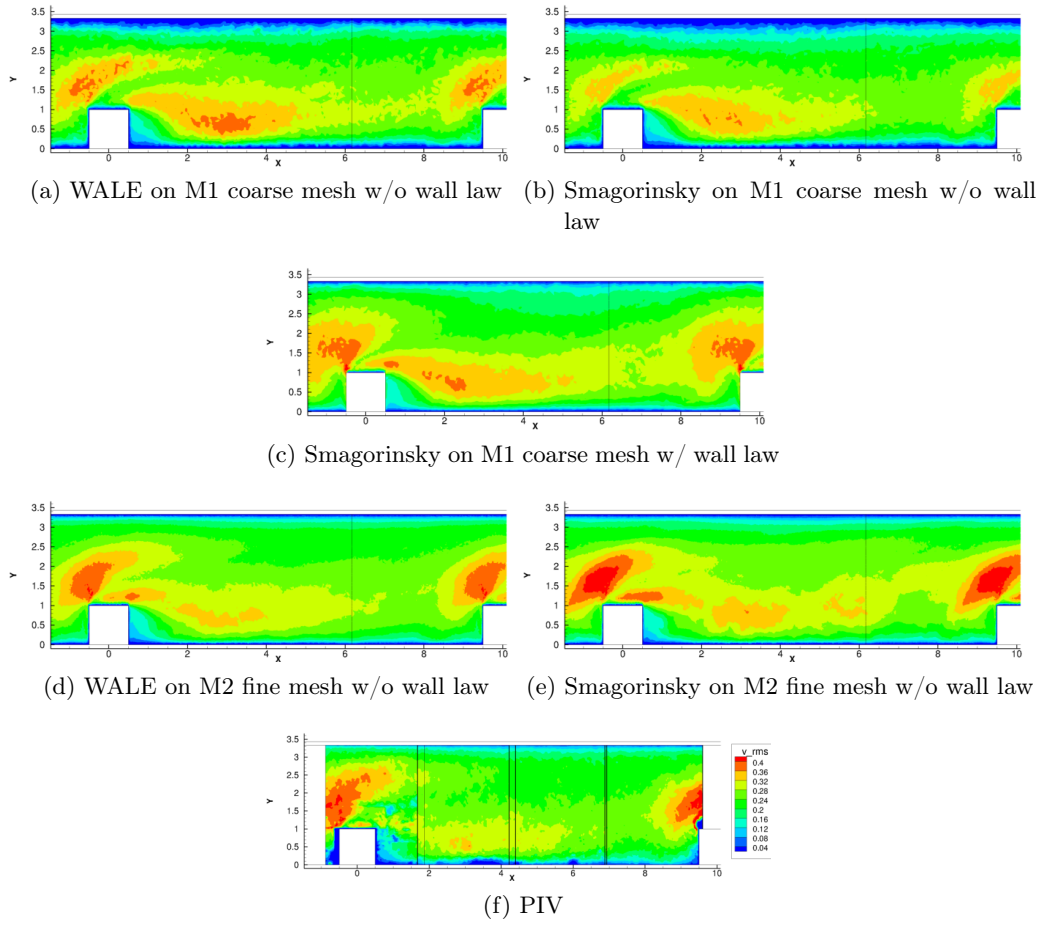


Figure D.9: Non-dimensionalized fluctuating wall-normal velocity  $\overline{v'v'}$  in 3XY plane: comparison of WALE and Smagorinsky modeling with PIV.



# Bibliography

- [1] AFANASYEV, V., CHUDNOVSKY, Y., LEONTIEV, A., AND ROGANOV, P. Turbulent flow friction and heat transfer characteristics for spherical cavities on a flat plate. *Experimental Thermal and Fluid Science* 7, 1 (July 1993), 1–8. (Cited on page 12.)
- [2] AHN, J., CHOI, H., AND LEE, J. S. Large eddy simulation of flow and heat transfer in a rotating ribbed channel. *International Journal of Heat and Mass Transfer* 50, 25-26 (Dec. 2007), 4937–4947. (Cited on pages 18 and 21.)
- [3] AHN, J., AND LEE, J. S. Large eddy simulation of flow and heat transfer in a channel with a detached rib array. *International Journal of Heat and Mass Transfer* 53, 1-3 (Jan. 2010), 445–452. (Cited on pages 18 and 21.)
- [4] AL-QAHTANI, M., JANG, Y.-J., CHEN, H.-C., AND HAN, J.-C. Flow and heat transfer in rotating two-pass rectangular channels (AR=2) by reynolds stress turbulence model. *International Journal of Heat and Mass Transfer* 45, 9 (Apr. 2002), 1823–1838. (Cited on page 21.)
- [5] AL-QAHTANI, M. S., CHEN, H.-C., AND HAN, J.-C. Heat transfer prediction of rotating rectangular channels using reynolds stress model. *Journal of Thermophysics and Heat Transfer* 19, 1 (Jan. 2005), 36–47. (Cited on page 21.)
- [6] BATCHELOR, G. K. *An Introduction to Fluid Dynamics*, new ed ed. Cambridge University Press, Feb. 2000. (Cited on page 131.)
- [7] BERTRAM, A., AND SVENDSEN, B. On material objectivity and reduced constitutive equations. *Archives of Mechanics* 53, 6 (2001), 653–675. (Cited on page 76.)
- [8] BONINI, A., ANDREINI, A., CARCASI, C., FACCHINI, B., CIANI, A., AND INNOCENTI, L. Conjugate heat transfer calculations on gt rotor blade for industrial applications. part i: Equivalent internal fluid network setup and procedure description. In *ASME Turbo Expo 2012* (Copenhagen, 2012), A. GT2012-69846, Ed. (Cited on page 20.)
- [9] BOUDIER, G., GICQUEL, L. Y. M., POINSOT, T., BISSIÈRES, D., AND BÉRAT, C. Comparison of LES, RANS and experiments in an aeronautical gas turbine combustion chamber. *Proc. Combust. Inst.* 31 (2007), 3075–3082. (Cited on page 33.)
- [10] BOYCE, M. P. *Gas Turbine Engineering Handbook, Second Edition*, 2 ed. Gulf Professional Publishing, Jan. 2002. (Cited on page 3.)

- [11] BRADSHAW, P. The analogy between streamline curvature and buoyancy in turbulent shear flow. *Journal of Fluid Mechanics* 36, 01 (1969), 177–191. (Cited on page 80.)
- [12] CABRIT, O., AND NICOUD, F. Direct simulations for wall modeling of multicomponent reacting compressible turbulent flows. *Phys. Fluids* 21, 5 (May 2009), 055108. (Cited on pages 45 and 46.)
- [13] CAKAN, M. *Aero-thermal Investigation of Fixed Rib-roughened Internal Cooling Passages*. PhD thesis, Université Catholique de Louvain, Von Karman Institute for Fluid Dynamics, 2000. (Cited on pages 41, 69, 70 and 71.)
- [14] CAMBIER, L., AND VEUILLOT, J. Status of the elsa software for flow simulation and multi-disciplinary applications. In *46th AIAA Aerospace Sciences Meeting and Exhibit* (Reno, Nevada, January 2008), no. AIAA-2008-0664. (Cited on page 64.)
- [15] CAMBON, C., BENOIT, J.-P., SHAO, L., AND JACQUIN, L. Stability analysis and large-eddy simulation of rotating turbulence with organized eddies. *Journal of Fluid Mechanics* 278 (1994), 175–200. (Cited on page 80.)
- [16] CASARSA, L. *Aerodynamic performance investigation of a fixed rib-roughened internal cooling Passage*. PhD thesis, Università degli Studi di Udine, Von Karman Institute for Fluid Dynamics, 2003. (Cited on pages 39, 41 and 65.)
- [17] CERFACS. *AVBP Handbook* - <http://cerfacs.fr/~avbp/>. CERFACS, 2009. (Cited on page 138.)
- [18] CHANG, S., LIOU, T.-M., AND LEE, T.-H. Thermal performance of developing flow in a radially rotating parallelogram channel with 45° ribs. *International Journal of Thermal Sciences* 52, 0 (Feb. 2012), 186–204. (Cited on page 15.)
- [19] CHASSAING, P. *Turbulence en mécanique des fluides, analyse du phénomène en vue de sa modélisation à l’usage de l’ingénieur*. Cépaduès-éditions, Toulouse, France, 2000. (Cited on pages 29 and 30.)
- [20] CHATELAIN, A. *Simulation des Grandes Echelles d’Ecoulements Turbulents avec Transferts de Chaleur*. PhD thesis, INP Grenoble, 2004. (Cited on page 20.)
- [21] Clean sky website. <http://www.cleansky.eu/>, 2008. (Cited on page 1.)
- [22] COLETTI, F., CRESCI, I., AND ARTS, T. Time-resolved piv measurements of turbulent flow in rotating rib-roughened channel with coriolis and buoyancy forces. In *ASME Turbo Expo 2012* (Copenhagen, 2012), A. GT2012-69406, Ed. (Cited on pages 105 and 107.)

- [23] COLETTI, F., MAURER, T., ARTS, T., AND DI SANTE, A. Flow field investigation in rotating rib-roughened channel by means of particle image velocimetry. *Experiments in Fluids* 52, 4 (Sept. 2011), 1043–1061. (Cited on page 88.)
- [24] COLETTI, F., VERSTRAETE, T., VANDERWIELEN, T., BULLE, J., AND ARTS, T. Optimization of a u-bend for minimal pressure loss in internal cooling channels: Part II — Experimental validation. *ASME Conference Proceedings 2011*, 54655 (2011), 1689–1699. (Cited on pages 16, 38, 43, 103 and 112.)
- [25] COLIN, O., AND RUDGYARD, M. Development of high-order taylor-galerkin schemes for unsteady calculations. *J. Comput. Phys.* 162, 2 (2000), 338–371. (Cited on page 137.)
- [26] COLLADO, E. *Analyse de l'impact de l'environnement aérothermique sur la température des pales de turbine HP*. PhD thesis, Institut National Polytechnique de Toulouse, Oct. 2012. (Cited on pages 4 and 13.)
- [27] COMTE, P. *New tools in turbulence modelling. vortices in incompressible les and non-trivial geometries*. Course of Ecole de Physique des Houches. Springer-Verlag, France, 1996. (Cited on page 136.)
- [28] CORSON, D., JAIMAN, R., AND SHAKIB, F. Industrial application of RANS modelling: capabilities and needs. *International Journal of Computational Fluid Dynamics* 23, 4 (2009), 337–347. (Cited on pages 17 and 33.)
- [29] CUI, J., PATEL, V. C., AND LIN, C.-L. Large-eddy simulation of turbulent flow in a channel with rib roughness. *International Journal of Heat and Fluid Flow* 24, 3 (June 2003), 372–388. (Cited on pages 18 and 21.)
- [30] CUSHMAN-ROISIN, B. *Introduction to Geophysical Fluid Dynamics*, 1 ed. Prentice Hall, Apr. 1994. (Cited on page 74.)
- [31] DAFALIAS, Y. F., AND YOUNIS, B. A. Objective model for the fluctuating pressure-strain-rate correlations. *Journal of Engineering Mechanics* 135, 9 (Sept. 2009), 1006–1014. (Cited on pages 49 and 134.)
- [32] DE LAAGE DE MEUX, B. *Modélisation des écoulements turbulents en rotation et en présence de transferts thermiques par approche hybride RANS/LES zonale*. PhD thesis, École nationale supérieure de mécanique et d'aérotechnique, 2012. (Cited on pages 77, 79 and 83.)
- [33] DI SANTE, A., THEUNISSEN, R., AND VAN DEN BRAEMBUSSCHE, R. A. A new facility for time-resolved PIV measurements in rotating channels. *Experiments in Fluids* 44, 2 (Sept. 2007), 179–188. (Cited on pages 84 and 87.)

- [34] DUCHAINE, F., CORPRON, A., PONS, L., MOUREAU, V., NICOUD, F., AND POINSOT, T. Development and assessment of a coupled strategy for conjugate heat transfer with Large Eddy Simulation. application to a cooled turbine blade. *International Journal of Heat and Fluid Flow* 30, 6 (2009), Pages 1129–1141. (Cited on page 20.)
- [35] DUCROS, F., COMTE, P., AND LESIEUR, M. Large-eddy simulation of transition to turbulence in a boundary layer developing spatially over a flat plate. *J. Fluid Mech.* 326 (1996), 1–36. (Cited on page 136.)
- [36] DURBIN, P. A. Near-wall turbulence closure modeling without damping functions. *Theoretical and Computational Fluid Dynamics* 3 (1991), 1–13. 10.1007/BF00271513. (Cited on page 134.)
- [37] EDO, Y., OBI, S., AND MASUDA, S. Heat transfer experiments in rotating boundary layer flow. *International Journal of Heat and Fluid Flow* 21, 6 (Dec. 2000), 684–692. (Cited on page 81.)
- [38] EKMAN, V. On the influence of the earth’s rotation on ocean currents. *Ark. Mat. Astron. Fys.* 2 (1905), 1–53. (Cited on page 82.)
- [39] ELYYAN, M. A., AND TAFTI, D. K. Investigation of coriolis forces effect of flow structure and heat transfer distribution in a rotating dimpled channel. *Journal of Turbomachinery* 134, 3 (2012), 031007. (Cited on page 21.)
- [40] Opinion of the european economic and social committee on the european aeronautics industry: current situation and prospects, oj c 175, 28.7.2009, p. 50-56, 2009. (Cited on page 1.)
- [41] FAVRE, A. Statistical equations of turbulent gases. In *Problems of hydrodynamics and continuum mechanics*. SIAM, Philadelphia, 1969, pp. 231–266. (Cited on pages 33 and 133.)
- [42] FLACK, R. D. *Fundamentals of Jet Propulsion with Applications*. Cambridge University Press, Apr. 2005. (Cited on pages 9 and 10.)
- [43] FRÖHLICH, J., AND VON TERZI, D. Hybrid LES/RANS methods for the simulation of turbulent flows. *Progress in Aerospace Sciences* 44, 5 (July 2008), 349–377. (Cited on page 127.)
- [44] GAD-EL HAK, M. Questions in fluid mechanics: Stokes’ hypothesis for a newtonian, isotropic fluid. *Journal of Fluids Engineering* 117, 1 (Mar. 1995), 3–5. (Cited on page 132.)
- [45] GARNIER, E., ADAMS, N., AND SAGAUT, P. *Large Eddy Simulation for Compressible Flows*, 1 ed. Springer, Aug. 2009. (Cited on page 132.)

- [46] GATSKI, T. B., AND SPEZIALE, C. G. On explicit algebraic stress models for complex turbulent flows. *J. Fluid Mech.* 254 (1993), 59–78. (Cited on page 64.)
- [47] GE website. [http://www.geaviation.com/press/ge90/ge90\\_200325a.html/](http://www.geaviation.com/press/ge90/ge90_200325a.html/), 2003. (Cited on page 1.)
- [48] GHIGHI, J. *Modelisation du fluage de superalliages monocristallins : effets d'anisotropie et de microstructure*. PhD thesis, ISAE-ENSMA, 2013. (Cited on page 9.)
- [49] GILL, A. E. *Atmosphere-Ocean Dynamics*, 1 ed. Academic Press, Dec. 1982. (Cited on page 74.)
- [50] GOLDSTEIN, R. J. Film cooling. In *Advances in Heat Transfer*, vol. 7. Academic Press, New York, 1971, pp. 321–379. (Cited on page 10.)
- [51] GRANET, V. *La Simulation aux Grandes Echelles : un outil pour la prédiction des variabilités cycliques dans les moteurs á allumage commandé ?* PhD thesis, Université de Toulouse, 2011. (Cited on page 83.)
- [52] GRUNDESTAM, O., WALLIN, S., AND JOHANSSON, A. V. Direct numerical simulations of rotating turbulent channel flow. *Journal of Fluid Mechanics* 598 (2008), 177–199. (Cited on pages 81, 82 and 88.)
- [53] HAN, J.-C. Recent studies in turbine blade cooling. *International Journal of Rotating Machinery* 10, 6 (2004), 443–457. (Cited on pages 12 and 14.)
- [54] HAN, J.-C., DUTTA, S., EKKAD, S., AND DUTTA, S. E. S. *Gas Turbine Heat Transfer and Cooling Technology*. Taylor & Francis Inc, Apr. 2001. (Cited on pages 9, 10, 12, 13 and 15.)
- [55] HEDLUND, C. R., AND LIGRANI, P. M. Local swirl chamber heat transfer and flow structure at different reynolds numbers. *Journal of Turbomachinery* 122, 2 (Feb. 1999), 375–385. (Cited on page 12.)
- [56] HIRT, C. W., AMSDEN, A., AND COOK, J. L. An arbitrary lagrangian-eulerian computing method for all flow speeds. *J. Comput. Phys.* 131, 4 (1974), 371–385. (Cited on page 83.)
- [57] HUNT, J. C. R., WRAY, A. A., AND MOIN, P. Eddies, streams, and convergence zones in turbulent flows. In *Proc. of the Summer Program* (1988), Center for Turbulence Research, NASA Ames/Stanford Univ., pp. 193–208. (Cited on page 110.)
- [58] IACOVIDES, H., AND RAISEE, M. Recent progress in the computation of flow and heat transfer in internal cooling passages of turbine blades. *International Journal of Heat and Fluid Flow* 20, 3 (June 1999), 320–328. (Cited on pages 17 and 21.)



- [59] INCROPERA, F. P. *Fundamentals of Heat and Mass Transfer*, 6th revised edition ed. John Wiley & Sons Ltd, Jan. 2007. (Cited on pages 25 and 26.)
- [60] IRELAND, P., AND DAILEY, G. Aerothermal performance of internal cooling systems in turbomachines. In *Internal Cooling In Turbomachinery* (von Karman Institute, Belgium, May 2010), vol. 2010-05 of *VKI Lecture Series*. (Cited on pages 8, 9, 11 and 12.)
- [61] JACKSON, D., AND LAUNDER, B. Osborne reynolds and the publication of his papers on turbulent flow. *Annual Review of Fluid Mechanics* 39, 1 (Jan. 2007), 19–35. (Cited on page 28.)
- [62] JANG, Y.-J., CHEN, H.-C., AND HAN, J.-C. Flow and heat transfer in a rotating square channel with 45 deg angled ribs by reynolds stress turbulence model. *Journal of Turbomachinery* 123, 1 (2001), 124–132. (Cited on page 21.)
- [63] JAURÉ, S. *Conjugate heat transfer in gas turbine combustion chamber. Identification of coupling strategies for massively parallel computations*. PhD thesis, INP Toulouse, 2012. (Cited on pages 20 and 22.)
- [64] JOHNSTON, J. P. Effects of system rotation on turbulence structure: A review relevant to turbomachinery flows. *International Journal of Rotating Machinery* 4, 2 (1998), 97–112. (Cited on page 88.)
- [65] JOHNSTON, J. P., HALLEENT, R. M., AND LEZIUS, D. K. Effects of spanwise rotation on the structure of two-dimensional fully developed turbulent channel flow. *Journal of Fluid Mechanics* 56, 03 (1972), 533–557. (Cited on pages 15, 79, 81 and 88.)
- [66] KANE, M., AND YAVUZKURT, S. Calculation of gas turbine blade temperatures using an iterative conjugate heat transfer approach. In *Proceedings of International Symposium on Heat Transfer in Gas Turbine Systems* (2009), Begellhouse, pp. 1–14. (Cited on page 20.)
- [67] KAYS, K. Turbulent Prandtl number. Where are we ? *J. Heat Trans.* 116 (May 1994), 284–295. (Cited on page 37.)
- [68] KERCHER, D. M. Turbine blade having transpiration strip cooling and method of manufacture, Nov. 1997. Patent number: 5690473. (Cited on page 12.)
- [69] KOLMOGOROV, A. N. The local structure of turbulence in incompressible viscous fluid for very large reynolds numbers. *C. R. Acad. Sci. , USSR* 30 (1941), 301. (Cited on page 29.)
- [70] KOMI, P. *Strength and Power in Sport: Olympic Encyclopedia of Sports Medicine*, 2nd edition, volume III ed. Wiley-Blackwell, Dec. 2002. (Cited on page 1.)

- [71] KRAICHNAN, R. Diffusion by a random velocity field. *Phys. Fluids* 13 (1970), 22–31. (Cited on page 48.)
- [72] KRISTOFFERSEN, R., AND ANDERSSON, H. I. Direct simulations of low-reynolds-number turbulent flow in a rotating channel. *Journal of Fluid Mechanics* 256 (1993), 163–197. (Cited on pages 19, 21, 81 and 88.)
- [73] LABBÉ, O., RYAN, J., AND SAGAUT, P. Direct numerical simulation of flow in a ribbed channel. *International Journal of Computational Fluid Dynamics* 11, 3-4 (1999), 275–284. (Cited on page 19.)
- [74] LAMARQUE, N. *Schémas numériques et conditions limites pour la simulation aux grandes échelles de la combustion diphasique dans les foyers d’hélicoptère*. Phd thesis, INP Toulouse, 2007. (Cited on page 137.)
- [75] LAMBALLAIS, E., LESIEUR, M., AND MÉTAIS, O. Effects of spanwise rotation on the vorticity stretching in transitional and turbulent channel flow. *International Journal of Heat and Fluid Flow* 17, 3 (June 1996), 324–332. (Cited on pages 81 and 88.)
- [76] LAUNDER, B. E., AND JONES, W. P. The prediction of laminarisation with a two-equations model of turbulence. *Int. J. Heat and Mass Transfer* 15 (1972), 301–314. (Cited on page 134.)
- [77] LAUNDER, B. E., REECE, G. J., AND RODI, W. Progress in the development of a reynolds stress turbulence closure. *J. Fluid Mech.* 68, 3 (1975), 537–566. (Cited on pages 17 and 134.)
- [78] LAWSON, S. A., THRIFT, A. A., THOLE, K. A., AND KOHLI, A. Heat transfer from multiple row arrays of low aspect ratio pin fins. *International Journal of Heat and Mass Transfer* 54, 17–18 (Aug. 2011), 4099–4109. (Cited on page 12.)
- [79] LAX, P. D., AND WENDROFF, B. Systems of conservation laws. *Commun. Pure Appl. Math.* 13 (1960), 217–237. (Cited on page 137.)
- [80] LAX, P. D., AND WENDROFF, B. Difference schemes for hyperbolic equations with high order of accuracy. *Commun. Pure Appl. Math.* 17 (1964), 381–398. (Cited on page 137.)
- [81] LEBLANC, C., EKKAD, S. V., LAMBERT, T., AND RAJENDRAN, V. Detailed heat transfer distributions in engine similar cooling channels for a turbine rotor blade with different rib orientations. *ASME 2011 Turbo Expo: Turbine Technical Conference and Exposition* 5 (June 2011), 1109–1116. (Cited on page 16.)
- [82] LIEN, F. S., AND A., D. P. Non-linear  $k - \varepsilon - v^2$  modeling with application to high lift. In *Center for Turbulence Research, Proceedings of the Summer 1996* (1996). (Cited on page 69.)

- [83] LIGRANI, P. Internal cooling - surface heat transfer augmentation. <http://www.ligrani.com/Research/Groups/internalcooling.html>. (Cited on pages 12 and 13.)
- [84] LUO, J., AND RAZINSKY, E. H. Conjugate heat transfer analysis of a cooled turbine vane using the V2F turbulence model. *Journal of Turbomachinery* 129, 4 (July 2006), 773–781. (Cited on page 20.)
- [85] MAHESH, K., CONSTANTINESCU, G., APTE, S., IACCARINO, G., AND MOIN, P. Large-eddy simulation of gas turbine combustors. In *Annual Research Briefs*. Center for Turbulence Research, NASA Ames/Stanford Univ., 2001, pp. 3–17. (Cited on page 4.)
- [86] MCADAMS, W. H. *Heat Transmission*, 2nd ed. New York : McGraw-Hill, 1942. (Cited on page 42.)
- [87] MENDEZ, S., AND NICLOUD, F. Large-eddy simulation of a bi-periodic turbulent flow with effusion. *J. Fluid Mech.* 598 (2008), 27–65. (Cited on page 46.)
- [88] MOIN, P., SQUIRES, K. D., CABOT, W., AND LEE, S. A dynamic subgrid-scale model for compressible turbulence and scalar transport. *Phys. Fluids A* 3, 11 (1991), 2746–2757. (Cited on page 136.)
- [89] MOUREAU, V., DOMINGO, P., AND VERVISCH, L. Design of a massively parallel CFD code for complex geometries. *Comptes Rendus Mécanique* 339, 2–3 (Feb. 2011), 141–148. (Cited on page 127.)
- [90] MOUREAU, V., LARTIGUE, G., SOMMERER, Y., ANGELBERGER, C., COLIN, O., AND POINSOT, T. Numerical methods for unsteady compressible multi-component reacting flows on fixed and moving grids. *J. Comput. Phys.* 202, 2 (2005), 710–736. (Cited on page 83.)
- [91] MOUSTAPHA, H., ZELESKY, M. F., BAINES, N. C., AND JAPIKSE, D. *Axial and Radial Turbines*. Concepts ETI, Inc., June 2003. (Cited on page 14.)
- [92] MURATA, A., AND MOCHIZUKI, S. Large eddy simulation with a dynamic subgrid-scale model of turbulent heat transfer in an orthogonally rotating rectangular duct with transverse rib turbulators. *International Journal of Heat and Mass Transfer* 43, 7 (Apr. 2000), 1243–1259. (Cited on pages 17 and 21.)
- [93] NAGANO, Y., HATTORI, H., AND HOURA, T. DNS of velocity and thermal fields in turbulent channel flow with transverse-rib roughness. *International Journal of Heat and Fluid Flow* 25, 3 (June 2004), 393–403. (Cited on pages 19 and 21.)
- [94] NICLOUD, F., AND DUCROS, F. Subgrid-scale stress modelling based on the square of the velocity gradient. *Flow, Turb. and Combustion* 62, 3 (1999), 183–200. (Cited on pages 43, 53 and 136.)

- [95] OOI, A., IACCARINO, G., DURBIN, P., AND BEHNIA, M. Reynolds averaged simulation of flow and heat transfer in ribbed ducts. *International Journal of Heat and Fluid Flow* 23, 6 (Dec. 2002), 750–757. (Cited on pages 17 and 21.)
- [96] OPENFOAM. <http://www.openfoam.com/>. (Cited on page 49.)
- [97] PARK, J., HAN, J., HUANG, Y., OU, S., AND BOYLE, R. Heat transfer performance comparisons of five different rectangular channels with parallel angled ribs. *International Journal of Heat and Mass Transfer* 35, 11 (Nov. 1992), 2891–2903. (Cited on page 14.)
- [98] PARSONS, J. A., HAN, J.-C., AND ZHANG, Y. Effect of model orientation and wall heating condition on local heat transfer in a rotating two-pass square channel with rib turbulators. *International Journal of Heat and Mass Transfer* 38, 7 (May 1995), 1151–1159. (Cited on pages 15 and 16.)
- [99] PHIBEL, R., LAROCHE, E., CASARSA, L., AND ARTS, T. Numerical investigation on flow and heat transfer in a rib-roughened channel with high blockage ratio. In *6th European Conference on Turbomachinery: Fluid Dynamics and Thermodynamics* (Lille, France, March 2005). (Cited on pages 17, 69, 70 and 71.)
- [100] PIOMELLI, U. Wall-layer models for large-eddy simulations. *Prog. Aerospace Sci.* 44, 6 (2008), 437–446. (Cited on pages 34, 35, 61, 63 and 124.)
- [101] POINSOT, T., AND LELE, S. Boundary conditions for direct simulations of compressible viscous flows. *J. Comput. Phys.* 101, 1 (1992), 104–129. (Cited on pages 46 and 89.)
- [102] POPE, S. B. *Turbulent flows*. Cambridge University Press, 2000. (Cited on pages 4, 32, 103 and 138.)
- [103] QIN, Z., AND PLETCHER, R. H. Large eddy simulation of turbulent heat transfer in a rotating square duct. *International Journal of Heat and Fluid Flow* 27, 3 (June 2006), 371–390. (Cited on page 21.)
- [104] RAMA KUMAR, B. V. N., AND PRASAD, B. V. S. S. A combined CFD and network approach for a simulated turbine blade cooling system. *Indian Journal of Engineering & Materials Sciences* 13 (June 2006), 195–201. (Cited on page 20.)
- [105] REYNOLDS, O. On the dynamical theory of incompressible viscous fluids and the determination of the criterion. *Phil. Trans. R. Soc. London A* 186 (1895), 123–164. (Cited on pages 28 and 29.)
- [106] RICHARD, J. *Développement d’une chaîne de calcul pour les interactions fluide-structure et application aux instabilités aéro-acoustiques d’un moteur à propergol solide*. PhD thesis, Université de Montpellier II, 2012. (Cited on page 83.)

- [107] RICHTER, J. P. *The Notebooks of Leonardo da Vinci*. Dover Publications, June 1970. (Cited on pages 28 and 30.)
- [108] RICKLICK, M., AND KAPAT, J. S. Determination of a local bulk temperature based heat transfer coefficient for the wetted surfaces in a single inline row impingement channel. *Journal of Turbomachinery* 133, 3 (2011), 031008. (Cited on page 25.)
- [109] ROTHE, P. H., AND JOHNSTON, J. P. Free shear layer behavior in rotating systems. *Journal of Fluids Engineering* 101, 1 (Mar. 1979), 117–120. (Cited on page 79.)
- [110] SAGAUT, P. *Large eddy simulation for incompressible flows*. Springer, 2002. (Cited on page 135.)
- [111] SAHA, A. K., AND ACHARYA, S. Unsteady RANS simulation of turbulent flow and heat transfer in ribbed coolant passages of different aspect ratios. *International Journal of Heat and Mass Transfer* 48, 23–24 (Nov. 2005), 4704–4725. (Cited on pages 17 and 21.)
- [112] SCHMITT, F. About boussinesq’s turbulent viscosity hypothesis: historical remarks and a direct evaluation of its validity. *Comptes Rendus Mécanique* 335, 9–10 (Oct. 2007), 617–627. (Cited on page 134.)
- [113] SCHØNFELD, T., AND POINSOT, T. Influence of boundary conditions in LES of premixed combustion instabilities. In *Annual Research Briefs*. Center for Turbulence Research, NASA Ames/Stanford Univ., 1999, pp. 73–84. (Cited on page 137.)
- [114] SENGUPTA, T. K., GANERWAL, G., AND DIPANKAR, A. High accuracy compact schemes and gibbs’ phenomenon. *J. Sci. Comput.* 21, 3 (2004), 253–268. (Cited on page 138.)
- [115] SEWALL, E. A. *Large Eddy Simulations of Flow and Heat Transfer in the Developing and 180° Bend Regions of Ribbed Gas Turbine Blade Internal Cooling Ducts with Rotation – Effect of Coriolis and Centrifugal Buoyancy Forces*. PhD thesis, Virginia Tech, 2005. (Cited on page 82.)
- [116] SEWALL, E. A., AND TAFTI, D. K. Large eddy simulation of flow and heat transfer in the developing flow region of a rotating gas turbine blade internal cooling duct with coriolis and buoyancy forces. *Journal of Turbomachinery* 130, 1 (2008), 011005. (Cited on pages 16, 18, 19, 21, 119 and 120.)
- [117] SLEITI, A., AND KAPAT, J. Effect of coriolis and centrifugal forces on turbulence and transport at high rotation and density ratios in a rib-roughened channel. *International Journal of Thermal Sciences* 47, 5 (May 2008), 609–619. (Cited on pages 17 and 21.)

- [118] SMAGORINSKY, J. General circulation experiments with the primitive equations: 1. the basic experiment. *Mon. Weather Rev.* 91 (1963), 99–164. (Cited on pages 53, 74 and 135.)
- [119] SMIRNOV, A., SHI, S., AND CELIK, I. Random flow generation technique for large eddy simulations and particle-dynamics modeling. *Trans. ASME. J. Fluids Eng.* 123 (2001), 359–371. (Cited on page 48.)
- [120] SMITH, M. W., AND SMITS, A. J. Visualization of structure of supersonic turbulent boundary layers. *Exp. Fluids* 18, 4 (February 1995), 288–302. (Cited on page 64.)
- [121] SPALART, P., AND ALLMARAS, S. A one-equation turbulence model for aerodynamic flows. *AIAA Paper 1992-0439* (1992). (Cited on page 134.)
- [122] SPEZIALE, C. G. Galilean invariance of subgrid-scale stress models in the large-eddy simulation of turbulence. *J. Fluid Mech.* 156 (1985), 55–62. (Cited on page 83.)
- [123] STAFFELBACH, G., GICQUEL, L., BOUDIER, G., AND POINSOT, T. Large eddy simulation of self-excited azimuthal modes in annular combustors. *Proc. Combust. Inst.* 32 (2009), 2909–2916. (Cited on page 4.)
- [124] STEPHENS, M., SHIH, T., AND CIVINSKAS, K. Computation of flow and heat transfer in a rectangular channel with ribs. *AIAA-1995-0180* (Jan. 1995). (Cited on page 65.)
- [125] STOKES, G. On the theories of internal friction of fluids in motion. *Transactions of the Cambridge Philosophical Society* 8 (1845), 287–305. (Cited on page 132.)
- [126] TAFTI, D. Evaluating the role of subgrid stress modeling in a ribbed duct for the internal cooling of turbine blades. *International Journal of Heat and Fluid Flow* 26, 1 (Feb. 2005), 92–104. (Cited on page 21.)
- [127] TAFTI, D. K., AND VANKA, S. P. A numerical study of the effects of spanwise rotation on turbulent channel flow. *Physics of Fluids A: Fluid Dynamics* 3, 4 (Apr. 1991), 642–656. (Cited on pages 79 and 88.)
- [128] TEITELBAUM, T., AND MININNI, P. D. The decay of turbulence in rotating flows. *Physics of Fluids* 23, 6 (June 2011), 065105–065105–15. (Cited on page 79.)
- [129] THOM, A. The flow past circular cylinders at low speeds. *Proceedings of the Royal Society of London. Series A* 141, 845 (Sept. 1933), 651–669. (Cited on page 3.)
- [130] Top500 website. <http://www.top500.org/>, 2012. (Cited on page 5.)

- [131] TRITTON, D. J. Stabilization and destabilization of turbulent shear flow in a rotating fluid. *Journal of Fluid Mechanics* 241 (1992), 503–523. (Cited on page 79.)
- [132] TUCKER, P. G., AND LARDEAU, S. Applied large eddy simulation. *Philosophical Transactions of the Royal Society A: Mathematical, Physical and Engineering Sciences* 367, 1899 (July 2009), 2809–2818. (Cited on page 4.)
- [133] VERSTRAETE, T., COLETTI, F., BULLE, J., VANDERWIELEN, T., AND ARTS, T. Optimization of a u-bend for minimal pressure loss in internal cooling channels: Part I—Numerical method. *ASME Conference Proceedings* 2011, 54655 (2011), 1665–1676. (Cited on pages 38 and 49.)
- [134] VOLINO, R. J., SCHULTZ, M. P., AND FLACK, K. A. Turbulence structure in rough- and smooth-wall boundary layers. *Journal of Fluid Mechanics* 592 (2007), 263–293. (Cited on page 104.)
- [135] WEBB, R., AND ECKERT, E. Application of rough surfaces to heat exchanger design. *International Journal of Heat and Mass Transfer* 15, 9 (Sept. 1972), 1647–1658. (Cited on pages 11 and 12.)
- [136] WEIGAND, B., AND SPRING, S. Multiple jet impingement - a review. *Heat Transfer Research* 42, 2 (2011), 101–142. (Cited on page 12.)
- [137] WLASSOW, F. *Analyse instationnaire aérothermique d'un étage de turbine avec transport de points chauds*. PhD thesis, Ecole centrale de Lyon, 2012. (Cited on page 4.)
- [138] WU, H., AND KASAGI, N. Effects of arbitrary directional system rotation on turbulent channel flow. *Physics of Fluids* 16, 4 (Mar. 2004), 979–990. (Cited on page 15.)
- [139] YANG, C.-Y., AND LIN, T.-Y. Heat transfer characteristics of water flow in microtubes. *Experimental Thermal and Fluid Science* 32, 2 (Nov. 2007), 432–439. (Cited on page 29.)
- [140] ZHOU, J., ADRIAN, R. J., BALACHANDAR, S., AND KENDALL, T. M. Mechanisms for generating coherent packets of hairpin vortices in channel flow. *J. Fluid Mech.* 387 (1999), 353–396. (Cited on page 105.)

# Publications

The works presented in this thesis have led to several publications in different proceedings of the ASME Turbo Expo conferences. The corresponding references are listed below while [b] and [c] are reproduced in the following pages.

- [a]. GOURDAIN, N., GICQUEL, L., FRANSEN, R., COLLADO, E., AND ARTS, T. Application of RANS and LES to the prediction of flows in high pressure turbines components. In *ASME Turbo Expo 2011* (Vancouver, 2011), GT2011-46518, ASME, Ed.
- [b]. FRANSEN, R., GOURDAIN, N., AND GICQUEL, L. Steady and unsteady modeling for heat transfer predictions of high pressure turbine blade internal cooling. In *ASME Turbo Expo 2012* (Copenhagen, 2012), GT2012-69482, ASME, Ed.
- [c]. FRANSEN, R., AND GICQUEL, L. Large eddy simulation of rotating ribbed channel. In *ASME Turbo Expo 2013* (San Antonio, 2013), GT2013-95076, ASME, Ed.



GT2012-69482

## STEADY AND UNSTEADY MODELING FOR HEAT TRANSFER PREDICTIONS OF HIGH PRESSURE TURBINE BLADE INTERNAL COOLING

Rémy Fransen\*

SAFRAN Turbomeca  
 DT/MD/MO

64511 Bordes Cedex 1  
 France

Email: remy.fransen@cerfacs.fr

Nicolas Gourdain

Laurent Y.M. Gicquel  
 CERFACS

Computational Fluid Dynamics Team  
 31057 Toulouse Cedex 1  
 France

### ABSTRACT

*This work focuses on numerical simulations of flows in blade internal cooling system. Large Eddy Simulation (LES) and Reynolds-Averaged Navier Stokes (RANS) approaches are compared in a typical blade cooling related problem. The case is a straight rib-roughened channel with high blockage ratio, computed and compared for both a periodic and full spatial domains. The configuration was measured at the Von Karman Institute (VKI) using Particle Image Velocimetry (PIV) in near gas turbine operating conditions. Results show that RANS models used fail to predict the full evolution of the flow within the channels where massive separation and large scale unsteady features are evidenced. In contrast LES succeeds in reproducing these complex flow motions and both mean and fluctuating components are clearly improved in the channels and in the near wall region. Periodic computations are gauged against the spatial computational domain and results on the heat transfer problem are addressed.*

### NOMENCLATURE

$D_h$  Hydraulic diameter (m)

$h$  Rib height (m)

$Nu$  Nusselt number :  $Nu = \frac{q_w D_h}{\lambda (T_w - T_{ref})}$

$Re$  Reynolds number :  $Re = \frac{U_0 D_h}{\nu}$

$Pr$  Prandtl number

$q_w$  Wall heat flux ( $W.m^{-2}$ )

$U_0$  Bulk velocity ( $m.s^{-1}$ )

$U_x, U_y, U_z$  Streamwise, normal and spanwise components of mean velocity ( $m.s^{-1}$ )

$u_x, u_y, u_z$  Streamwise, normal and spanwise components of fluctuating velocity ( $m.s^{-1}$ )

$\nu$  Cinematic viscosity ( $m^2.s^{-1}$ )

$\lambda$  Thermal conductivity ( $W.m^{-2}.K^{-1}$ )

$T_w$  Wall temperature (K)

$T_{ref}$  Reference temperature (K)

RANS Reynolds-Averaged Navier Stokes

LES Large Eddy Simulation

DNS Direct Numerical Simulation

NRMSD Normalized Root-Mean-Square Deviation

### INTRODUCTION

Output power increase and improved efficiency of aeronautical engine can be obtained by increasing the combustor outlet temperature. This rise in temperature however imposes new constraints on the turbine design since the blade material melting point is often well surpassed. Life duration of the turbine can hence greatly be reduced if the cooling system is poorly designed. Providing improved design tools and better predictions in this part of the engine becomes therefore more and more critical. Today, design engineers heavily rely on computational

\*Address all correspondence to this author.

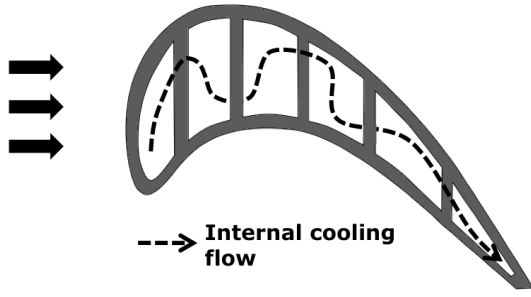


**FIGURE 1.** EXAMPLE OF APPLICATION OF THIS STUDY : FLOW INSIDE A TURBINE BLADE (DASHED ARROW).

tools to dimension these complex systems. For the fluid in the main vein and within the cooling ducts, RANS modeling is routinely used and conjugated heat transfer problems are possible. Although RANS has known limitations for these two types of flows, it clearly benefits from a computational efficiency and the modeling experience gained in this specific context: 2D and 3D computations (Ooi et al. [1]), specific modeling for wall bounded flows with low-Re turbulence model (Iacovides et Raisee [2] and unsteady computations with U-RANS methods (Saha. et al. [3]). However and with the advent of LES, a fully unsteady modeling approach, improvement in the flow prediction can be expected in this configuration, as already shown by Sewall et al. [4]. Further analysis of LES on ribbed channel configuration have also been carried out, as for example the study of Tasti on the subgrid stress [5], and in a more applied way the design study of Ahn and Lee [6] with detached ribs.

In this context, this article provides a comparison of RANS and LES computations on a cooling channel configuration representative of the industrial case of Fig. 1. A quick description of RANS and LES modeling is first presented, then the ribbed channel physical and numerical parameters are introduced to compute adiabatic and imposed heat flux operating point. The two last sections show the results of these pure aerodynamic and aerothermal computations, and compare them to 2D experimental fields of velocity and heat transfer enhancement factor.

## MODELLISATION AND TOOLS

In the context of practical engineering calculations, the high Reynolds numbers involved are too computationally expensive to be simulated directly with Direct Numerical Simulation. The instantaneous (exact) governing equations need thus to be time-averaged, ensemble-averaged, or otherwise manipulated to remove the small scales, resulting in a modified set of equations that are computationally less expensive to solve. However, the modified equations contain additional unknown variables and turbulence models are needed to close the system before being sim-

ulated numerically. The most common approach for complex configurations is still RANS that proposes to model the effect of all the turbulent scales on the mean flow. An alternative and more universal method is LES that introduces a separation between the resolved (large) turbulent scales and the modeled (small) scales (see Sagaut, Pope and Poinso [7–9]). Both RANS and LES methods, detailed below, have been heavily tested on aerodynamic setups and to a lesser extent on thermal problems. For our work, two flow solvers are considered: a structured multi-block solver (elsA, see Cambier [10] for further description) and an unstructured solver (AVBP, detailed in the works of Mendez and Schonfeld [11, 12]).

The governing equations for both approaches are the unsteady / steady compressible Navier-Stokes equations that describe the conservation of mass, momentum and energy. In conservative form, it can be expressed in three-dimensional coordinates as:

$$\frac{dW}{dt} + \text{div}F = 0 \quad (1)$$

where  $W$  is the vector of primary variables,  $F = (f - f_v, g - g_v, h - h_v)$  is the flux tensor;  $f, g, h$  are the inviscid fluxes and  $f_v, g_v, h_v$  are the viscous fluxes. The fluid follows the ideal gas law  $p = \rho r T$ , where  $r$  is the mixture gas constant. The fluid viscosity follows Sutherland's law and the heat flux follows Fourier's law.

## RANS approach

This modeling is one of the most used for engineering work. The principle is based for compressible flow on the Favre averaging of the Navier-Stokes equations, splitting each quantity (velocity, pressure...) into a Favre averaged and a fluctuating component:

$$F = \tilde{f} + f'' \text{ with } \tilde{f} = \frac{\bar{\rho} \bar{f}}{\bar{\rho}} \quad (2)$$

With overline denoting Reynolds average. Substituting (2) into the Navier-Stokes equations (1) and averaging, one obtains the evolution equations to be solved numerically. Favre averaging introduces a new term  $\overline{\rho u_i'' u_j''} = -\overline{\rho} \tau_{ij}$  in the momentum equation, also called the Reynolds stresses. A common model employs the Boussinesq hypothesis (see Schmitt [13]) based on the mean strain rate tensor  $\bar{S}_{ij}$ . With this assumption, a new scalar  $\nu_t$  also known as the turbulent viscosity is introduced and is usually evaluated from available quantities. There are numerous types of modelling, classified in terms of number of transport equations

solved (in addition to the RANS equations) to compute  $v_t$  (as among others works of Launder, Spalart and Durbin [14–17]). Here the  $k - L$  model of Smith [18] is used.

The turbulent energy flux  $\bar{q}_i'$  present in the energy equation is modeled using a turbulent heat conductivity obtained from  $v_t$  by  $\lambda_t = \bar{\rho} v_t C_p / Pr_t$ , where  $Pr_t = 0.7$  is a constant turbulent Prandtl number, and the gradient of the Reynolds averaged temperature coming from the averaged state equation  $\bar{p} = \bar{\rho} r \bar{T}$ :

$$\bar{q}_i' = -\lambda_t \frac{\partial \bar{T}}{\partial x_i} \quad (3)$$

### LES approach

LES involves the spatial Favre filtering operation that reduces for spatially, temporally invariant and localised filter functions to:

$$\widetilde{f(\mathbf{x}, t)} = \frac{1}{\bar{\rho}(\mathbf{x}, t)} \int_{-\infty}^{+\infty} \rho(\mathbf{x}', t) f(\mathbf{x}', t) G(\mathbf{x}' - \mathbf{x}) d\mathbf{x}', \quad (4)$$

where  $G$  denotes the filter function. Within this specific context, the unresolved SGS stress tensor  $\bar{\tau}_{ij}$  is modeled using the Boussinesq assumption [19] in the same way as RANS but from filtered strain rate tensor  $\widetilde{S}_{ij}$ . The SGS turbulent viscosity is then computed in our case with the WALE model introduced by Nicoud [20], especially designed for wall bounded flow:

$$v_t = (C_w \Delta)^2 \frac{(s_{ij}^d s_{ij}^d)^{3/2}}{(\widetilde{S}_{ij} \widetilde{S}_{ij})^{5/2} + (s_{ij}^d s_{ij}^d)^{5/4}}, \quad (5)$$

$$s_{ij}^d = \frac{1}{2} (\widetilde{g}_{ij}^2 + \widetilde{g}_{ji}^2) - \frac{1}{3} \widetilde{g}_{kk}^2 \delta_{ij}, \quad (6)$$

In Eq. (5),  $\Delta$  stands for the filter length ( $\propto$  the cubic-root of the cell volume),  $C_w$  is the model constant equal to 0.4929 and  $\widetilde{g}_{ij}$  is the resolved velocity gradient. The SGS energy flux is modeled from the turbulent viscosity as for RANS method, with here the filtered quantities [21–23].

### Structured RANS solver

The *elsA* software uses a cell centered approach on structured multiblock meshes. More information about this flow solver are presented by Cambier [10]. Convective fluxes are computed with an upstream scheme based on the Advection Upstream Splitting Method (AUSM) introduced by Liou [24]. Diffusive fluxes are computed with a second-order centered scheme.

The pseudo time-marching is performed by using an efficient implicit time integration scheme, based on the backward Euler scheme and a scalar Lower-Upper (LU) Symmetric Successive Over-Relaxation (SSOR) method as proposed by Yoon [25]. The turbulent viscosity is computed with the two equations model of Smith [18] based on a  $k - L$  formulation.

### Unstructured LES solver

The parallel LES code, AVBP [11, 12], solves the full compressible Navier-Stokes equations using finite element schemes TTG4A and TTGC based on a two step Taylor Galerkin formulation for the convection [26] in a cell-vertex formulation [27, 28]. It is especially designed for LES on hybrid meshes. Indeed, these explicit low diffusion and low dispersion properties provide 3<sup>rd</sup> order space and time accuracy. Employing explicit schemes involves to keep the CFL number below 0.7 to ensure stability, which lead to the main disadvantage to use time steps very low: for example  $\propto 10^{-7}$ s for aerodynamical applications where the viscous sub-layer needs to be computed accurately, inducing high computational costs.

### RIB-ROUGHENED COOLING CHANNEL CASE

The ribbed configuration used in this study, Fig. 2, is a square channel with an hydraulic diameter  $D_h = 0.1$  m, an aspect ratio of 1 and for which experimental measurements have been carried out at the Von Karman Institute. Square ribs normal to the flow are mounted on one wall with a pitch-to-height ratio ( $p/h$ ) of 10 leading to a high-blockage ratio,  $h/D_h = 0.3$ ,  $h$  being the rib height. The Reynolds number of the mean flow based on the bulk velocity and  $D_h$  is set to 40000, a regime similar of flows inside real cooling channels. Aerodynamic flow measurements have been performed using PIV by Casarsa [29] and thermal analysis using Liquid Crystal Thermography (LCT) by Çakan [30]. Mean flow velocity and fluctuations in the channel and Enhancement Factor (EF) at the wall characterizing the heat-transfer are provided at the same operating point for comparisons with numerical predictions. EF is the ratio between the measured Nusselt number at the wall and  $Nu_0$ , the Nusselt number computed from the Dittus-Boelter correlation for a smooth circular duct, as introduced by McAdams [31]:

$$Nu_0 = 0.023 \cdot Re^{0.8} \cdot Pr^{0.4} \quad (7)$$

### Computational domain and mesh generation

Measurements were performed in a section of the channel where the flow is assumed to be periodic. In order to reduce computational cost and allow finner mesh in LES, a first numerical

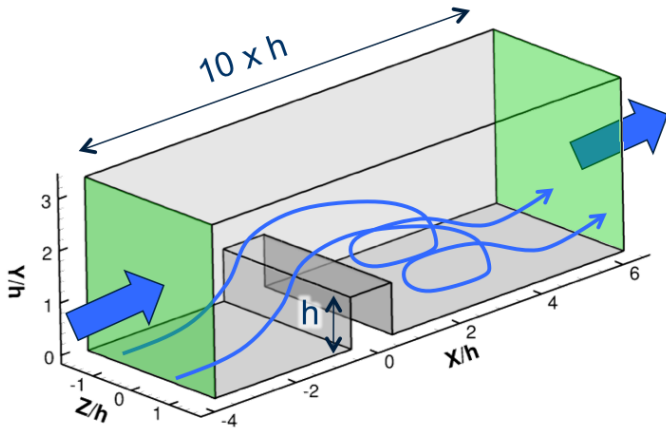


**FIGURE 2.** COMPUTATIONAL DOMAIN OF THE RIBBED CHANNEL

domain is chosen to be only one section of the channel corresponding to one periodic pattern of the channel geometry, Fig. 2. In reality, turbine blade cooling channel may not reach a periodic regime due to a few number of ribs in one straight channel. A second case has thus been computed to analyse the periodicity hypothesis as a good approximation for a more realistic configuration. The domain of study has been here chosen to be composed of 7 ribs and is called the spatial case.

**Periodic case** Figure 2 gives a representation of the periodic domain. Periodicity is applied between both flow inlet and outlet sections. Since there is no inlet/outlet condition in this case, fluid displacement is obtained by adding a source term similar to a fictive pressure gradient in the momentum equation, following the method of Cabrit [32]. All other boundaries are walls following the adiabatic no-slip condition.

Three periodic meshes are tested to see the influence of the discretization on the LES results. The first one, called M1, is a coarse full-tetra mesh with low wall resolution and a small number of cells allowing longer simulated physical time and fast simulations, Fig. 3(a). The second mesh, M2, is a fine full-tetra mesh with better wall resolution and approximately ten times more cells than M1, Fig. 3(b). Finally, M3 is an hybrid mesh made of one layer of prisms on all walls and tetrahedrons everywhere else, Fig. 3(c). This mesh combines a relative small number of cells with good wall resolution thanks to the use of prisms at the wall. Characteristics of these three meshes are summarized in Tab. 1. Since RANS simulation requests less computation time, no periodic reduction is applied and a full channel with four ribs is discretized with  $18.5 \cdot 10^6$  points and a  $y^+$  near 1 on walls.

**Spatial case** The spatial geometry is made of 7 repetitions of the domain seen on Fig.2, lightly extended at both ex-

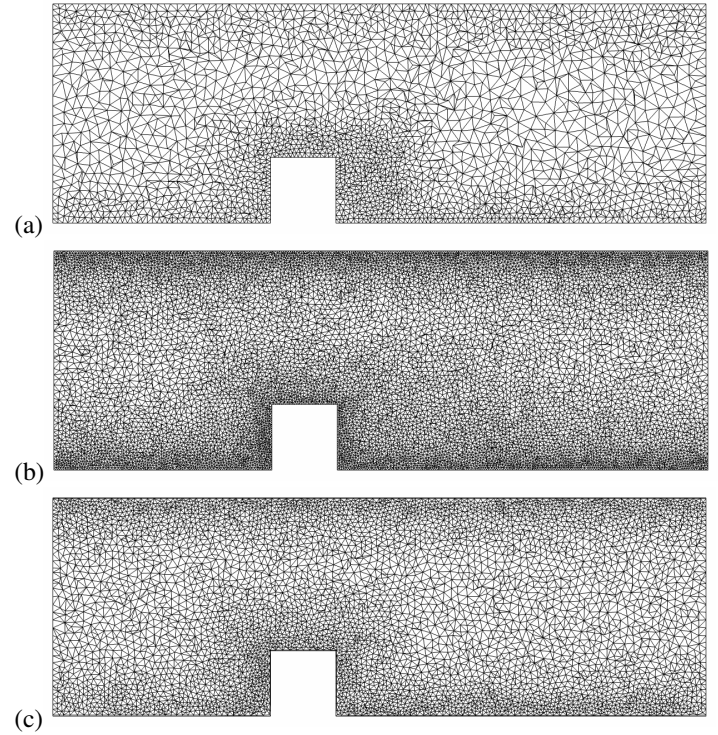


**FIGURE 3.** MESHES USED FOR LES: (a) M1, (b) M2 AND (c) M3

**TABLE 1.** CHARACTERISTICS OF THE MESHES USED FOR COMPUTATION OF THE RIBBED CHANNEL.

Mesh	Nb. of cells / rib	$y^+$	$x^+, z^+$
M1	550 000	[5; 20]	$\sim 1y^+$
M2	5 500 000	[2.5; 10]	$\sim 1y^+$
M3	1 800 000	[1; 5]	$\sim 5y^+$
RANS	4 500 000	$\sim 1$	$\sim 40y^+$

tremities (inlet located at  $3D_h$  before rib#1 and outlet at  $4D_h$  after rib#7). As for the periodic case, all the walls are set with the same adiabatic no slip condition but inlet imposes an air mean turbulent velocity profile at 293K keeping the same operating point ( $Re = 40000$ ). Outlet uses ambient static pressure (ie. 1013 hPa) with the NSCBC conditions [33]. Only one mesh is used for the spatial case, based on the same characteristics as for the M3 hybrid periodic mesh to ensure good wall resolution and affordable computational cost.

Spatial mesh is then used for heat transfer computation, changing only all adiabatic wall with  $650 \text{ W m}^{-2}$  imposed heat flux condition, corresponding to the condition used in experi-

**TABLE 2.** SUMMARY OF COMPARED CASES WITH TURBULENT MODELS USED

	Aerodynamics	Heat transfer
LES	periodic (WALE)	spatial (WALE)
RANS	spatial ( $k - L$ )	spatial ( $k - \epsilon$ and $v2f$ )
Experiment	PIV measurements	LCT measurements

mental measurements. Available and computed data compared in this study are summarized in Tab. 2.

## AERODYNAMIC RESULTS

The first following section presents mean velocity comparisons of periodic LES cases against RANS and PIV. Then turbulence evolution is described for LES, using PIV validation on the same configuration. Lastly, periodicity assumption is quantified by comparing LES periodic and spatial cases.

### Mean velocity comparisons

An overview of the different phenomena appearing in the flow caused by the rib will be analysed based on the PIV measurements, Fig. 4 and 5 (a). First, the narrowing of the section due to the rib forces the fluid velocity to increase and a maximum is detected in the middle of the channel. A boundary layer separation appears at the upstream rib top corner coinciding with a small flattened recirculation bubble on the top surface of the rib, Fig. 4 ①. Then, just after the rib a second large flow separation occurs at the rib downstream top corner due to the sharp widening, as encountered in a backward facing step flow. An elongated recirculation bubble takes place behind the rib, Fig. 4 ②, with an associated smaller counter-rotating vortice at the rib downstream bottom corner, Fig. 4 ③. Further downstream the flow fully re-expands in the channel and reattaches on the bottom wall near  $x/h = 4.5$ . Finally, when the fluid reaches the next rib, flow streamlines strongly curve upward, leading to a new small recirculation bubble near the upstream bottom corner of the rib, Fig. 4 ④.

Comparing the numerical simulations with these observations yields important information about the quality of the model. Both LES computations on M2 and M3, Figs. 5 (c) & (d); show very good agreement with PIV, when RANS with  $k - L$  modeling miss represents all the features previously described. Indeed on Fig. 5 (b) RANS detects the acceleration near the top wall while LES averages give exactly the good position. Figure 6 details the comparison in of the middle plane and shows the excellent agreement of the LES in the channel, even if small discrepancies may occur in the near-wall region. Nevertheless, it has to be

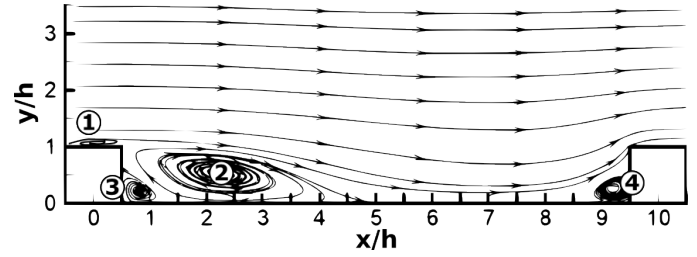


**FIGURE 4.** MEAN FLOW TOPOLOGY IN THE RIBBED CHANNEL SYMMETRY PLANE WITH THE FOUR CHARACTERISTIC VORTICES.

noticed that previous computations on rectangular ribbed channel with low Reynolds  $k - \omega$  RANS modeling could give better predictions of velocity field, see for example Stephens [34].

### Turbulence intensity comparisons

Figure 7 shows the position and the value of Turbulent Intensity (TI) predicted by LES and measured with PIV. On Fig. 7 (a), the maximum of TI has been computed on one periodic pattern from the upstream top corner of a rib ( $x/h = -0.5$ ) until the next one ( $x/h = 9.5$ ). Comparisons with PIV give very good predictions of both position and size of the zone where most turbulent structures occur and travel. This zone begins in a thin layer at the location of the recirculation bubble, Fig. 4 ①, above the rib and then spreads vertically. The zone envelope increases from  $0.5h$  at position  $x/h = 0.5$  to  $1.5h$  at  $x/h = 4.5$  where the zone reaches the bottom wall. After this point, the envelope grows more slowly but stays mainly in the bottom half part of the channel while the maximum line keeps a constant position between  $y/h = 0.5$  and  $y/h = 1.5$ .

Figure 7 (b) presents TI evolutions along the maximum line. Reference measurements from PIV detect high turbulence levels above the rib between 0.55 and 0.6, then TI decreases until it levels off between  $x/h = 1$  and  $x/h = 2.5$  to a mean value of 0.48. These two parts coincide mainly with the location of the shear layers generated by the two vortices identified on Figs. 4 ① & ②. In the second part of the channel where there is no more intense recirculation, TI follows a linear decrease until 0.3 in front of the next rib. LES results give the same evolution of TI but with lower levels. Computations on the finer meshes M2 and M3 reproduce the peak of turbulence above the rib, the lower flat portion and the linear decrease being very well captured. M1 predictions show a not so contrasted difference between the peak and the flat portion but a good decrease. Note that these results do not take into account the subgrid scale contribution for TI, which could reduce the discrepancy between PIV and LES values.

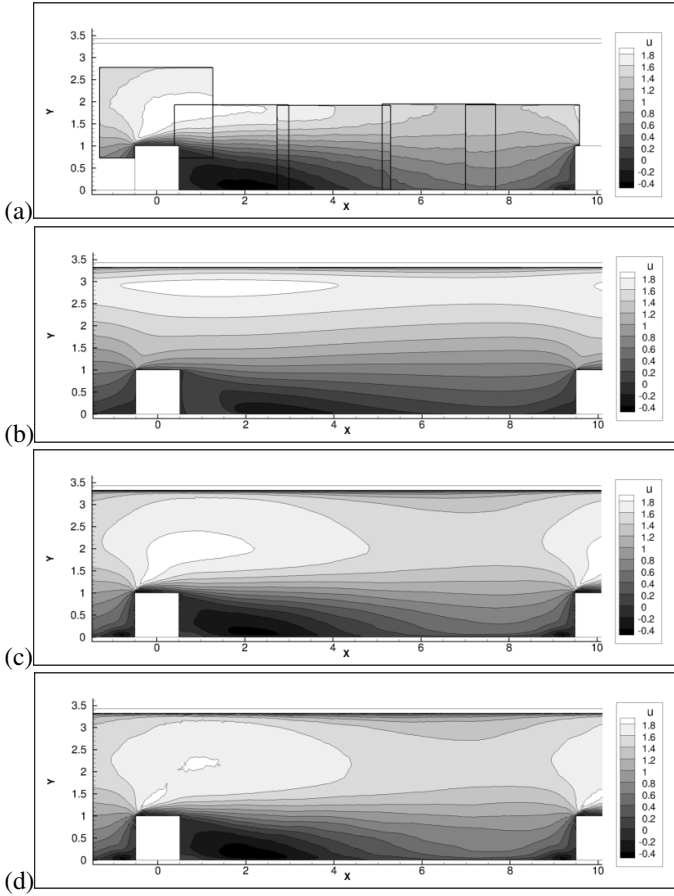


**FIGURE 5.** COMPARISON OF THE NON DIMENSIONALIZED STREAMWISE VELOCITY IN THE SYMMETRY PLANE FOR (a) PIV [29], (b) RANS AND LES WITH (c) M2 AND (d) M3 MESHES.

### Periodicity analysis

Establishment of the periodicity is investigated from statistically converged mean LES solutions obtained with the periodic M3 and spatial meshes. To do so, the finer mesh M2 is used as comparison domain: periodic solution from M3 and each of the 7 ribs of the spatial mesh are interpolated on M2 and a Normalized Root-Mean-Square Deviation (NRMSD) is computed between 3D fields of the periodic rib and each of the spatial ribs for mean and fluctuating velocity components. If  $X_i^P$  is the value of the periodic mean solution (P) interpolated on the  $i^{th}$  point of the neutral mesh M2 made of  $N$  points, and  $X_i^{Sj}$  the value of the spatial mean solution of the  $j^{th}$  rib ( $Sj$ ) interpolated on the  $i^{th}$  point of M2, then one obtains NRMSD for each spatial rib normalizing the Root-Mean-Square Deviation (RMSD) of Eq. 8 with  $\max(X_i^P) - \min(X_i^P)$ .

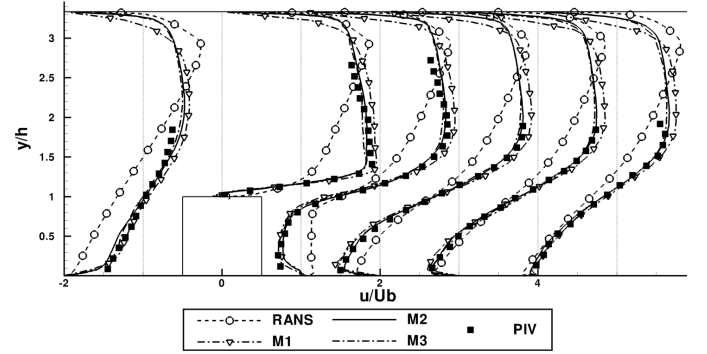


**FIGURE 6.** COMPARISON OF LES, RANS AND PIV STREAMWISE MEAN VELOCITY AT DIFFERENT POSITIONS IN THE CHANNEL SYMMETRY PLANE ( $x/h = -2, 0, 1, 2, 3, 4$ )

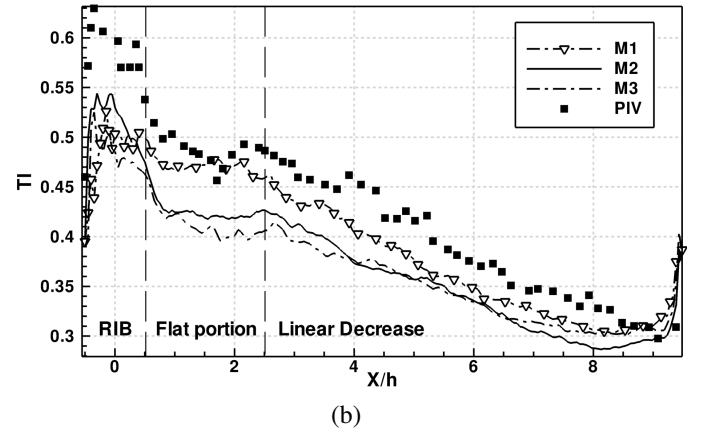
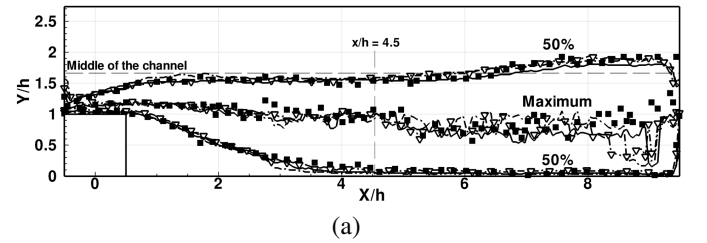


**FIGURE 7.** COMPARISON OF TURBULENCE INTENSITY ( $TI = \sqrt{\frac{1}{3}(u_{x,rms}^2 + u_{y,rms}^2 + u_{z,rms}^2)}/U_b$ ) COMPUTED WITH LES: (a) MAXIMUM LINE AND ENVELOPE (50% OF MAXIMUM) AND (b) VALUE ON THE MAXIMUM LINE (SAME LEGEND FOR BOTH GRAPHS).

$$RMSD(P, Sj) = \sqrt{\frac{\sum_{i=1}^N (X_i^P - X_i^{Sj})^2}{N}} \quad (8)$$

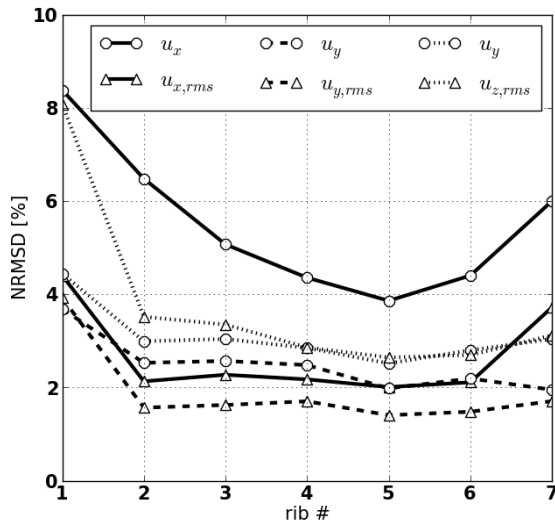


**FIGURE 8.** DEVIATION BETWEEN PERIODIC AND SPATIAL FLOW FOR MEAN AND FLUCTUATING VELOCITY COMPONENTS

Figure 8 shows the result of this analysis. All 6 curves follow the same evolution, i.e. a high NRMSD at the first rib, then a decreasing or more or less flat evolution from rib#2 to rib#5 with a NRMSD between 1.5% and 3.5%, to finally increase around the two last ribs (except for the  $u_z$  component which stays flat at the end and even gets a bit lower). This shape allows to draw two conclusions for this case: first, since all the 6 components do not have a flat portion, 7 ribs are not enough and boundary effect avoids to reach a reference periodic regime in this LES simulation. The most pathological case is for the  $u_x$  component, which has an inverted bell shape curve. The second conclusion is that there is nevertheless a rib where one can assume a flow near of periodicity conditions: for all curves NRMSD falls down to a minimum at rib#5 with values under 3% for 5 of the 6 components, and under 4% for  $u_x$ .

It must be noticed that for the needs of this analysis, since the periodic and spatial meshes were not exactly identical an interpolation has been used so error has been introduced. Both cases are comparable here since they had the same process, but employing another neutral mesh for interpolation could lightly change the values of the results.

## HEAT TRANSFER RESULTS

Heat transfer is compared using Nusselt number which needs temperature on the wall  $T_w$  and reference temperature in the channel  $T_{ref}$ .  $T_w$  is built from fluid values near the wall, and  $T_{ref}$  from the temperature increase stepwise approximation in the channel computed with inlet and outlet bulk temperatures. Since experimental data were carried on established periodic flow, data

are extracted on and downstream of the 5<sup>th</sup> rib where flow is the most periodic as concluded in the previous section. Figure 9 shows a snapshot of the unsteady LES simulation used to compute mean thermal values presented in the following paragraphs. In this section, RANS results are computed by Phibel [35]. Two models have been tested in his study: the common  $k - \epsilon$  and the  $v2f$  [36] which uses the normal velocity fluctuation rather than the turbulent kinetic energy to compute the turbulent viscosity and damping at the wall for the redistribution terms in the Reynolds stress equation is introduced.

## Heat transfer on the wall between two ribs

Figure 10 shows the comparison of  $EF = Nu/Nu_0$  obtained from RANS, LES and experimental measurements. Both RANS simulations give the same main pattern of EF on the wall between the two ribs: only one zone of high Nusselt is detected in the middle of the wall, which is not the case on the experimental thermography where a second high heat transfer zone in front of the rib is measured. In contrast, LES reproduces both patterns very well and at better location than RANS: between  $x/h = 3$  and 4.5 for LES and measurements but after  $x/h = 4.5$  for both RANS computations. The tightening of the isolines between  $x/h = 7$  and 8 towards the center of the channel is also well predicted with LES, which allows to draw the overall fish-tail shape of the pattern visible in the experiment.

Note that the maximum of enhancement factor is as well as predicted by the RANS  $v2f$  model than LES ( $\sim 2.8 - 2.9$ ), whereas  $k - \epsilon$  underestimates it by more than 20%. However, LES overestimates the second zone in front of the rib with a level comparable to the maximum between  $x/h = 3$  and 4.5 instead of 2.19 in the measurements, that is an error of 30%.

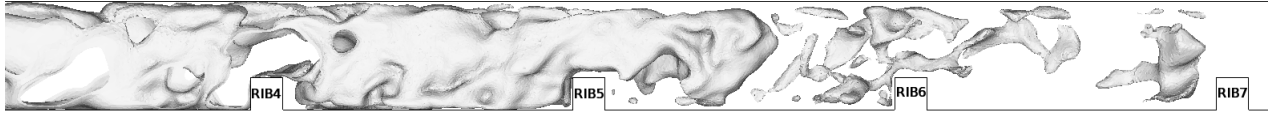
## Heat transfer on the rib

Figure 11 presents the comparison of the EF on the 3 faces of the rib. This part is a very differential zone to test the models since the fluid impacts it with very different angles and velocities depending on the faces.

LES and RANS show the same isoline pattern on the upstream surface, Fig. 11 (b) and Fig. 11 (a) respectively, which are not the same as for the experiment: the latter presents a bulge near both channel side wall (on top and bottom side of Fig. 11 (c)) while isoline curvature of the computations does not invert. Both models also overestimate experimental findings since EF is measured between 1.9 and almost 3 and numerics predict respectively more than 5 and 12 for RANS and LES.

It is noticed that LES detects very high EF values on the upstream corner of the rib (the right side of the upstream surface and the left side of the top surface). This behaviour is due to the fluid acceleration over the rib, for which mesh refinement at the upstream corner becomes too coarse for the high gradient in





**FIGURE 9.** INSTANTANEOUS ISOSURFACE OF TEMPERATURE OF CONSTANT HEAT FLUX LES COMPUTATION (ONLY RIB#4 TO RIB#7 PRESENTED HERE)

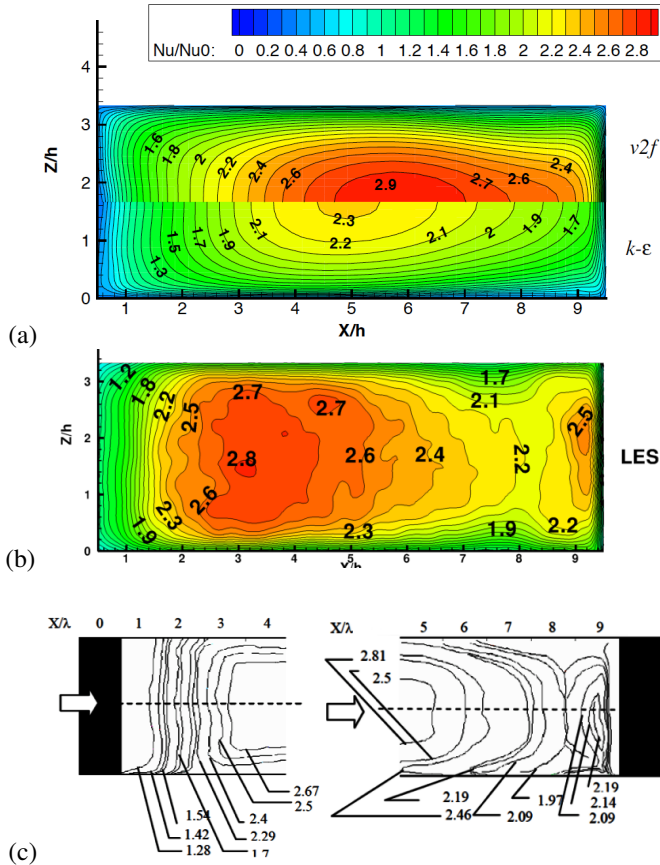


**FIGURE 10.** ENHANCEMENT FACTOR ON THE WALL BETWEEN TWO RIB FOR (a) RANS [35], (b) LES AND (c) EXPERIMENTAL DATA [30]

presence combined to the tricky sharp corner treatment of the code cell-vertex formulation.

On the top surface, none of the models detect the maximum located the middle of the rib. However, the order of magnitude is relatively well predicted, even it is slightly overestimated for the maximum value: measurements show EF being mainly between 2.5 and 3.1, and LES and RANS give a range from 2.5 to 3.5 (without taking into account the overpredicted left side).

The backface analysis shows more difference between RANS and LES. Indeed, RANS predicts very low EF, mainly

less than 1.1, whereas measurements give a range from 1.5 to 2. Patterns of RANS isolines are also completely different. Limits of this modeling are here pointed out: the massive recirculation, Fig. 4 (2), is badly computed by RANS resulting in wrong estimates of heat transfer behind the rib. In contrast, as seen in the aerodynamic results section, LES predicts very well all the recirculation zones in the channel yielding here a better EF fields on the downstream face. Values from 1 to 2 are computed on the main part of the face, which is in good agreement with thermal measurements, even if the elongated maximum zone in the middle of the face is not predicted.

## CONCLUSIONS

An evaluation of RANS and LES modeling for the flow inside an academic turbine blade cooling channel was performed and compared with complete aerodynamical and thermal experimental measurements. Results show the following points:

- The different RANS model used in this study ( $k-L$ ,  $k-\epsilon$  and  $v2f$ ) are not able to predict correctly the flow inside a cooling channel because of the massive separations and recirculations present in such flows. In contrast, LES reproduces very well all the features of the flow inside the channel.
- As well as mean quantities, LES has provided good estimates of fluctuating velocities and has proved to be a expedient tool to analyse unsteady isothermal complex flows.
- The use of a periodic configuration for LES has permitted to computed precise reference cases to afterwards describe flow establishment in more realistic cooling channel and adapt further thermal post-processing.
- Thermal results have shown that, as with RANS computations of this study, bad flow topology predictions would jeopardize good thermal estimates. Nevertheless, using a more efficient modeling like LES may not be sufficient. Even if results are clearly improved in comparison to RANS, particular attention should be turned to critical geometry zone where high velocity appears.

## ACKNOWLEDGMENT

The financial support of Turbomeca (Safran Group) and ANRT for the CIFRE Ph.D is gratefully acknowledged. Many



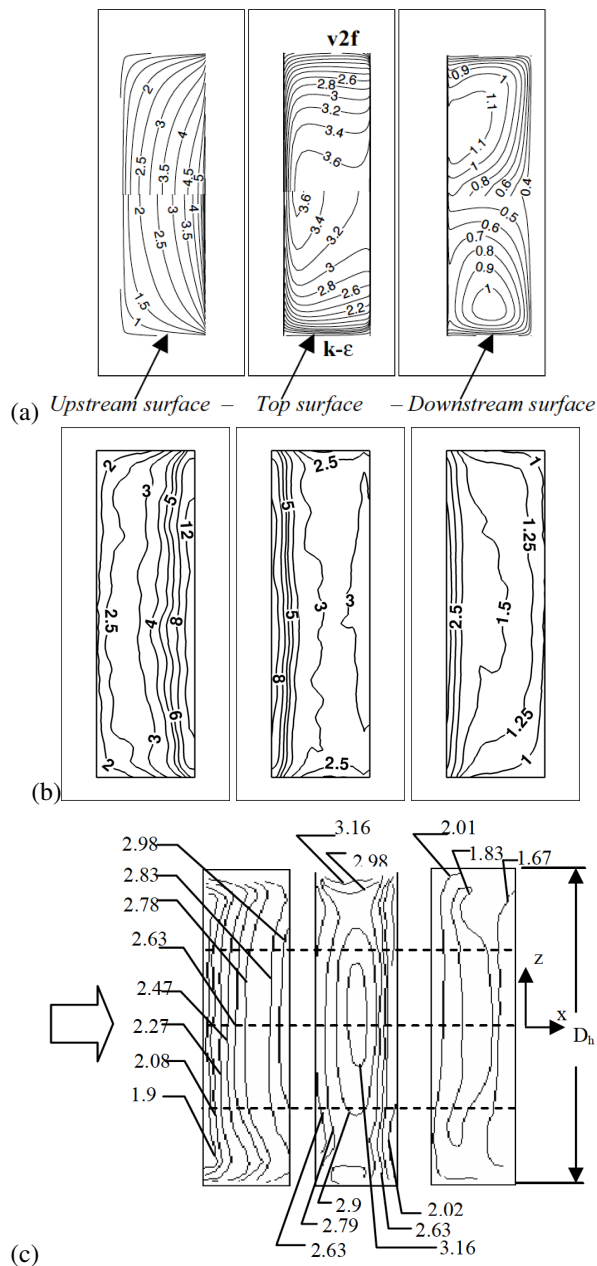


**FIGURE 11.** ENHANCEMENT FACTOR ON THE RIB WALL FOR (a) RANS [35], (b) LES AND (c) EXPERIMENTAL DATA [30]

thanks to the VKI team for the experimental data that are used in this paper. The work presented has also largely benefited from CERFACS internal and GENCI-CINES computing facilities (under the project fac 2554). The authors also thank the CERFACS CFD team, for helpful discussions about LES and flow physics.

## REFERENCES

- [1] Ooi, A., Iaccarino, G., Durbin, P., and Behnia, M., 2002. "Reynolds averaged simulation of flow and heat transfer in ribbed ducts". *International Journal of Heat and Fluid Flow*, **23**(6), Dec., pp. 750–757.
- [2] Iacovides, H., and Raisee, M., 1999. "Recent progress in the computation of flow and heat transfer in internal cooling passages of turbine blades". *International Journal of Heat and Fluid Flow*, **20**(3), June, pp. 320–328.
- [3] Saha, A. K., and Acharya, S., 2005. "Unsteady RANS simulation of turbulent flow and heat transfer in ribbed coolant passages of different aspect ratios". *International Journal of Heat and Mass Transfer*, **48**(2324), Nov., pp. 4704–4725.
- [4] Sewall, E. A., Tafti, D. K., Graham, A. B., and Thole, K. A., 2006. "Experimental validation of large eddy simulations of flow and heat transfer in a stationary ribbed duct". *International Journal of Heat and Fluid Flow*, **27**(2), Apr., pp. 243–258.
- [5] Tafti, D., 2005. "Evaluating the role of subgrid stress modeling in a ribbed duct for the internal cooling of turbine blades". *International Journal of Heat and Fluid Flow*, **26**(1), Feb., pp. 92–104.
- [6] Ahn, J., and Lee, J. S., 2010. "Large eddy simulation of flow and heat transfer in a channel with a detached rib array". *International Journal of Heat and Mass Transfer*, **53**(13), Jan., pp. 445–452.
- [7] Sagaut, P., 2000. *Large Eddy Simulation for incompressible flows*. Scientific computation series. Springer-Verlag.
- [8] Pope, S. B., 2000. *Turbulent flows*. Cambridge University Press.
- [9] Poinot, T., and Veynante, D., 2005. *Theoretical and Numerical Combustion*. R.T. Edwards, 2nd edition.
- [10] Cambier, L., and Veuillot, J., 2008. "Status of the elsa software for flow simulation and multi-disciplinary applications". In 46th AIAA Aerospace Sciences Meeting and Exhibit, no. AIAA-2008-0664.
- [11] Mendez, S., and Nicoud, F., 2008. "Large-eddy simulation of a bi-periodic turbulent flow with effusion". *J. Fluid Mech.*, **598**, pp. 27–65.
- [12] Schöfeld, T., and Poinot, T., 1999. "Influence of boundary conditions in LES of premixed combustion instabilities". In *Annual Research Briefs*. Center for Turbulence Research, NASA Ames/Stanford Univ., pp. 73–84.
- [13] Schmitt, F., 2007. "About boussinesq's turbulent viscosity hypothesis: historical remarks and a direct evaluation of its validity". *Comptes Rendus Mécanique*, **335**(910), Oct., pp. 617–627.
- [14] Launder, B. E., and Jones, W. P., 1972. "The prediction of laminarisation with a two-equations model of turbulence". *Int. J. Heat and Mass Transfer*, **15**, pp. 301–314.
- [15] Launder, B. E., Reece, G. J., and Rodi, W., 1975. "Progress

- in the development of a reynolds stress turbulence closure". *J. Fluid Mech.* , **68**(3), pp. 537–566.
- [16] Spalart, P., and Allmaras, S., 1992. "A one-equation turbulence model for aerodynamic flows". *AIAA Paper 1992-0439*.
- [17] Durbin, P. A., 1991. "Near-wall turbulence closure modeling without damping functions". *Theoretical and Computational Fluid Dynamics*, **3**, pp. 1–13. 10.1007/BF00271513.
- [18] Smith, M. W., and Smits, A. J., 1995. "Visualization of structure of supersonic turbulent boundary layers". *Exp. Fluids* , **18**(4), February, pp. 288–302.
- [19] Smagorinsky, J., 1963. "General circulation experiments with the primitive equations: 1. the basic experiment". *Mon. Weather Rev.* , **91**, pp. 99–164.
- [20] Nicoud, F., and Ducros, F., 1999. "Subgrid-scale stress modelling based on the square of the velocity gradient". *Flow, Turb. and Combustion* , **62**(3), pp. 183–200.
- [21] Moin, P., Squires, K. D., Cabot, W., and Lee, S., 1991. "A dynamic subgrid-scale model for compressible turbulence and scalar transport". *Phys. Fluids* , **A 3**(11), pp. 2746–2757.
- [22] Ducros, F., Comte, P., and Lesieur, M., 1996. "Large-eddy simulation of transition to turbulence in a boundary layer developing spatially over a flat plate". *J. Fluid Mech.* , **326**, pp. 1–36.
- [23] Comte, P., 1996. *New tools in turbulence modelling. vortices in incompressible les and non-trivial geometries*. Course of Ecole de Physique des Houches. Springer-Verlag, France.
- [24] Liou, M., 1996. "A sequel to AUSM: AUSM+". *Journal of Computational Physics*, **129**(2), Dec., pp. 364–382.
- [25] Yoon, S., and Jameson, A., 1987. "An lu-ssor scheme for the euler and navierstokes equations". *AIAA Paper 87-0600*.
- [26] Colin, O., and Rudgyard, M., 2000. "Development of high-order taylor-galerkin schemes for unsteady calculations". *J. Comput. Phys.* , **162**(2), pp. 338–371.
- [27] Donea, J., 1984. "Taylor-galerkin method for convective transport problems". *Int. J. Numer. Meth. Fluids* , **20**(1), pp. 101–119.
- [28] Lamarque, N., 2007. "Schémas numériques et conditions limites pour la simulation aux grandes échelles de la combustion diphasique dans les foyers d'hélicoptère". PhD thesis, INP Toulouse.
- [29] Casarsa, L., 2003. "Aerodynamic performance investigation of a fixed rib-roughened internal cooling passage". PhD thesis, Università degli Studi di Udine, Von Karman Institute for Fluid Dynamics.
- [30] Cakan, M., 2000. "Aero-thermal investigation of fixed rib-roughened internal cooling passages". PhD thesis, Université Catholique de Louvain, Von Karman Institute for Fluid Dynamics.
- [31] McAdams, W. H., 1942. *Heat Transmission*, 2nd ed. New York : McGraw-Hill.
- [32] Cabrit, O., and Nicoud, F., 2009. "Direct simulations for wall modeling of multicomponent reacting compressible turbulent flows". *Phys. Fluids* , **21**(5), p. 055108.
- [33] Poinso, T., and Lele, S., 1992. "Boundary conditions for direct simulations of compressible viscous flows". *J. Comput. Phys.* , **101**(1), pp. 104–129.
- [34] Stephens, M., Shih, T., and Civinskas, K., 1995. "Computation of flow and heat transfer in a rectangular channel with ribs". *AIAA-1995-0180*, Jan.
- [35] Phibel, R., Laroche, E., Casarsa, L., and Arts, T., 2005. "Numerical investigation on flow and heat transfer in a rib-roughened channel with high blockage ratio". In 6th European Conference on Turbomachinery: Fluid Dynamics and Thermodynamics.
- [36] Lien, F. S., and A., D. P., 1996. "Non-linear  $k - \epsilon - v^2$  modeling with application to high lift". In Center for Turbulence Research, Proceedings of the Summer 1996.

GT2013-95076

## LARGE EDDY SIMULATION OF ROTATING RIBBED CHANNEL

Rémy Fransen\*, Laurence Vial  
SAFRAN Turbomeca  
DT/MD  
64511 Bordes Cedex1  
France  
Email: remy.fransen@cerfacs.fr

Laurent Y.M. Gicquel  
CERFACS  
Computational Fluid Dynamics Team  
31057 Toulouse Cedex 1  
France

### ABSTRACT

*Large Eddy Simulation (LES) of isothermal flow in stationary and wall-normal rotating blade internal cooling system is evaluated against experimental data. The studied case is a 3D one wall ribbed straight channel for which time resolved two-dimensional Particle Image Velocimetry (PIV) measurements have been performed at the Von Karman Institute (VKI) in a near gas turbine operating condition. Thanks to these experimental mean and time-resolved quantities, advanced numerical computations can be adequately evaluated. In this work LES results show that this high fidelity CFD model is able to reproduce the turbulence increase (decrease) around the rib in destabilizing (stabilizing) rotation of the ribbed channel. Such effects are not only captured at the mean level but also at the unsteady level as confirmed by the comparison of the LES large-scale coherent motions with these obtained by PIV.*

### NOMENCLATURE

$D_h$  Hydraulic diameter (m)  
 $h$  Rib height (m)  
 $Re$  Reynolds number :  $Re = \frac{U_0 D_h}{\nu}$   
 $Ro$  Rotation number :  $Ro = \frac{\Omega D_h}{U_0}$   
 $U_0$  Bulk velocity ( $m.s^{-1}$ )  
 $\nu$  kinematic viscosity ( $m^2.s^{-1}$ )  
 $\Omega$  Rotation speed ( $rad/s$ )  
RANS Reynolds-Averaged Navier Stokes

LES Large Eddy Simulation  
DNS Direct Numerical Simulation  
SGS Sub Grid Scale  
PIV Particle Image Velocimetry

### INTRODUCTION

Aeronautical engine designers are constantly subject to increasing power demands from aircraft manufacturers. To satisfy this requirement, combustor outlet temperature can be increased to improve efficiency and output energy of the engine. This rise in temperature however also increases the thermal load on the turbine, which can surpass the material melting point. Turbine blades, which also face large mechanical and non thermal stresses, can be dramatically damaged if their cooling system is poorly designed. Turbine blade cooling often uses internal channels for cold air from the compressor flow to cool it down. Therefore, design problematic becomes to maximize heat transfer enhancement while minimizing air flow rate to avoid engine power penalties. Today to design such complex air systems, engineers heavily rely on computational tools to dimension the geometry and improve the flow comprehension and cooling efficiency.

In practice, RANS modeling is routinely used and conjugate heat transfer problems are possible. Although RANS has known limitations for channel flows with turbulent promoters like ribs leading to large recirculations (see for example Phibel [1]), it clearly benefits from computational efficiency and modeling experience. Causes of discrepancies are usually ascribed to the turbulence isotropy assumption used in classical two-equation

---

\*Address all correspondence to this author.

RANS model like  $k - \varepsilon$ , which is confirmed by often improved results with the use of Reynolds Stress Model, see Sleiti [2]. However and thanks to increasing computational power, more universal LES modeling can today greatly improve such flow predictions, as shown by Sewall et al. [3] and more recently by Fransen et al. [4]. Other LES of ribbed channel configurations have also been carried out, with emphasis on the subgrid stress model [5], or in a design study by Ahn and Lee [6].

In the present study, we focus on an other characteristic of such cooling flows: their rotation. In order to simulate industrial cooling system, we only consider wall normal rotation of straight channels, with air flowing radially outward. To measure rotation rate of such flows, the rotation number  $Ro$  is usually introduced:

$$Ro = \frac{\Omega D_h}{U_0} \quad (1)$$

where  $\Omega$ ,  $D_h$  and  $U_0$  are respectively rotation speed, channel hydraulic diameter and bulk velocity of the flow. This type of flow has been already widely studied and modification of turbulence near leading and trailing walls are well known. In finite aspect ratio channels, imbalance between the fluid near side walls and the fluid central core particles creates a secondary flow in the form of large streamwise counter-rotating cells causing a flow disymmetry between the leading and trailing walls. Note also that a background vorticity (equal to twice the system rotation rate  $\Omega$ ) and superimposed onto the mean flow vorticity in the relative frame of reference can have a significant impact if their axis are aligned. Shear layers present in such channels or separated flows can be strongly affected. Bradshaw, based on an analogy of curved flows, gave a criterion using the rotational Richardson number to determine a state where a shear flow could be stabilized or destabilized by a background rotation [7]. In term of design, all these effects have of course a great influence on the thermal efficiency of the cooling channel: in comparison to a stationary channel, Chang has shown experimentally that heat transfer enhancement can be increased/decreased or decreased/increased on the trailing/leading side respectively following the flow radial direction [8].

Objectives of this papers is then to compare mean and unsteady LES flow predictions of rotating ribbed channels with a corresponding full set of PIV measurements. LES modeling is firstly presented, then experimental and numerical procedures are described. Finally time-averaged and coherent structures time tracking comparison analysis are given.

## MODELLISATION AND TOOLS

### LES approach

In the context of practical engineering calculations, the high Reynolds numbers involved induce too computationally intensive efforts to be simulated with Direct Numerical Simulation

(DNS). The instantaneous (exact) governing equations need thus to be time-averaged, ensemble-averaged, or otherwise manipulated to remove the small scales to yield a modified set of equations that are computationally less expensive to solve. However, these modified equations contain additional unknown and turbulence models are needed to close the system before to be solved numerically. The most common approach for complex configurations is still RANS that proposes to model the effect of all the turbulent scales solving only for the mean flow. An alternative and more universal method is LES that introduces a separation between the resolved (large) turbulent scales and the modeled (small) scales (see Sagaut, Pope and Poinso [9–11]). By nature, LES computations yield unsteady flow predictions providing access to part of the turbulent data allowing better flow comprehension. In the present study LES is evaluated for rotating flows prediction to qualify its ability from the mean and the unsteady point of view thanks to available mean and time-resolved PIV validation data.

The solved governing equations are the unsteady / steady compressible Navier-Stokes equations that describe the conservation of mass, momentum and energy. In conservative form, it can be expressed in three-dimensional coordinates as:

$$\frac{dW}{dt} + \text{div} F = 0 \quad (2)$$

where  $W$  is the vector of primary variables,  $F = (f - f_v, g - g_v, h - h_v)$  is the flux tensor;  $f, g, h$  are the inviscid fluxes and  $f_v, g_v, h_v$  are the viscous fluxes. The fluid follows the ideal gas law  $p = \rho r T$ , where  $r$  is the mixture gas constant. The fluid viscosity follows Sutherland's law and the heat flux follows Fourier's law. In this study, turbulent Prandtl number is set constant and equal to 0.75.

LES for compressible flow involves the spatial Favre filtering operation of the Navier-Stokes equations, splitting each quantity  $\phi$  (velocity, pressure...) into a low frequency part  $\bar{\phi}$  and high frequency part  $\phi''$ :  $\phi = \bar{\phi} + \phi''$ . This filtering operation reduces for spatially, temporally invariant and localized filter functions to:

$$\widetilde{f(\mathbf{x}, t)} = \frac{1}{\rho(\mathbf{x}, t)} \int_{-\infty}^{+\infty} \rho(\mathbf{x}', t) f(\mathbf{x}', t) G(\mathbf{x}' - \mathbf{x}) d\mathbf{x}', \quad (3)$$

where  $G$  denotes the filter function. The Favre filtering introduces new terms in the governing equations because of the non linearity of the NS equations which represent the unresolved Sub Grid Scale (SGS) stress tensor:

$$\bar{\tau}_{ij}^{SGS} = -\bar{\rho}(\widetilde{u_i u_j} - \widetilde{u_i} \widetilde{u_j}) \quad (4)$$

Even if several modeling method exists, Boussinesq assumption [12] is commonly used to model  $\bar{\tau}_{ij}^{SGS}$ . With these closure the unsteady filtered (resolved) strain rate tensor  $\tilde{S}_{ij}$  is introduced as well as a new scalar playing the role of a SGS turbulent viscosity [13–15].

Eddy viscosity models of LES approach in such a flow have been early studied by Speziale [16] and he concluded that these models could not take into account rotation effect on turbulence dissipation. Several modeling have been developed to correct the subgrid scale behavior using statistical approach like Kobayashi [17] or transport equations for each component of the subgrid stress with Tsubokura [18]. In our study, a classical model will be tested.

In this study and following the conclusions of Fransen [4], SGS turbulent viscosity is computed with the WALE model introduced by Nicoud [19], especially designed for wall bounded flow:

$$\nu_t = (C_w \Delta)^2 \frac{(s_{ij}^d s_{ij}^d)^{3/2}}{(\tilde{S}_{ij} \tilde{S}_{ij})^{5/2} + (s_{ij}^d s_{ij}^d)^{5/4}}, \quad (5)$$

$$s_{ij}^d = \frac{1}{2}(\tilde{g}_{ij}^2 + \tilde{g}_{ji}^2) - \frac{1}{3}\tilde{g}_{kk}^2 \delta_{ij}, \quad (6)$$

In Eq. (5),  $\Delta$  stands for the filter length ( $\propto$  the cubic-root of the cell volume),  $C_w$  is the model constant equal to 0.4929,  $\tilde{g}_{ij}$  is the resolved velocity gradient tensor and  $\tilde{S}_{ij}$  the resolved strain rate tensor. Then, SGS energy flux is modeled from the turbulent viscosity using here a constant turbulent Prandtl number equal to 0.75.

### Unstructured LES solver

The parallel LES code, AVBP [20, 21], is used here to solve the full compressible Navier-Stokes equations using the finite element scheme TTGC based on a two step Taylor Galerkin formulation for the convection [22] in a cell-vertex formulation [23, 24]. It is especially designed for LES on hybrid meshes and is explicit. It yields low diffusion and low dispersion properties provided by a 3<sup>rd</sup> order space and time accuracy. Employing such explicit schemes involves to keep the CFL number below 0.7 to ensure stability, which leads to the main disadvantage, i.e. time steps of the order of  $10^{-7}$ s. For aerodynamical applications of interest where the viscous sub-layer needs to be computed accurately, this clearly induces high computational costs.

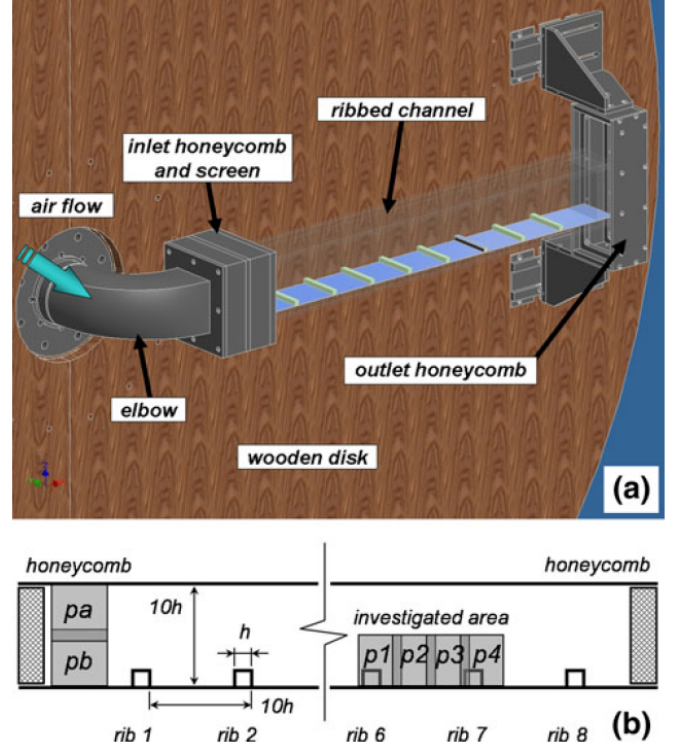


**FIGURE 1.** EXPERIMENTAL TEST BENCH: THREE DIMENSIONAL VIEW (a) AND SCHEMATIC LATERAL VIEW (b, NOT IN SCALE) - WITH THE COURTESY OF COLETTI [26]

### EXPERIMENTAL TEST CASE

#### Rotating facility

Application of LES has been done for the Von Karman (VKI) Institute rotating test bench shown on Fig. 1(a). The case is a straight one-ribbed wall channel fixed to a wooden disk, which can rotate. Air flow is generated by a stationary centrifugal pump and sent in the disk hollow rotating shaft. A 90° elbow allows to connect the shaft to the channel for which air flows outwards in the radial direction. Honeycombs are located at the entrance and at the outlet of the channel to reduce disturbances coming from the elbow and ambient cross flow respectively. The wooden disk can rotate in the clockwise / counter-clockwise direction allowing to set the ribbed wall respectively as the leading / trailing wall. More details on the apparatus can be found in Di Sante [25]. Figure 1 (b) shows a lateral sketch of the test channel. It is a 760 mm rectangular channel made of Plexiglas with a hydraulic diameter  $D_h = 4ab/2(a+b) = 79$  mm, with  $a = 83$  mm the height of the channel and  $b = 75$  mm its depth. Eight ribs perpendicular to the flow direction are fixed to the short wall and parallel to the axis of rotation. Ribs have a 8x8 mm<sup>2</sup> section and spaced with a pitch of 80 mm. Characteristics of the channel are summarized in Tab 1.

**TABLE 1.** SUMMARY OF RIBBED CHANNEL CHARACTERISTICS USED FOR ROTATIONAL ANALYSIS

length	760 mm
height	$a = 83$ mm
depth	$b = 75$ mm
$D_h$	79 mm
rib height $h$	8 mm
pitch $p/h$	10
blockage ratio $h/D_h$	0.1

### Flow conditions and measurements

The flow considered has a Reynolds number  $Re = U_0 D_h / \nu$  based on  $U_0$  the bulk velocity,  $D_h$  the hydraulic diameter and  $\nu$  the kinematic viscosity of 15000. Measurements for this study are performed at 130 rpm leading to a rotation number  $Ro = 0.38$ . These two parameters are representative of internal cooling channel of industrial turbine blades. For this condition, flow measurements have been carried out with Particle Image Velocimetry (PIV) technic in the channel symmetry plane thanks to a system directly mounted on the disk, therefore stationary with respect to the channel even if it is rotating. Several windows, shown on Fig. 1 (b), have been measured:  $pa$  and  $pb$  to measure inlet flow injection and  $p1$  to  $p4$  to analyze the flow around rib 6 and rib 7. Besides classical average measurements and thanks to the embedded PIV system, time-resolved recordings have also been performed and can thus be compared to the unsteady LES flow predictions. Further details on the experimental procedure are given by Coletti [26].

Major flow features expected in the rotating channel are portrayed on Fig. 2. Some are already present in stationary channel: shear layer behind the rib, Fig. 2 ②, and deviated flow near side walls due to the rib, Fig. 2 ③. Moreover, at this rotation rate Coriolis force generates a new large secondary flow: two stream-wise counter rotating vortices are superimposed on the mean flow, Fig. 2 ①. Therefore both counter rotating vortices tend to push the flow toward the trailing side, that is the ribbed / smooth wall for counter-clockwise / clockwise respectively, where then velocity and turbulence is expected to be increase.

### NUMERICAL SETUP

#### Domain and boundary conditions for the non rotating case

The numerical domain for LES has been chosen to be the entire channel of the experiment, which means that all the geometrical parameters of Tab. 1 have been used accordingly to

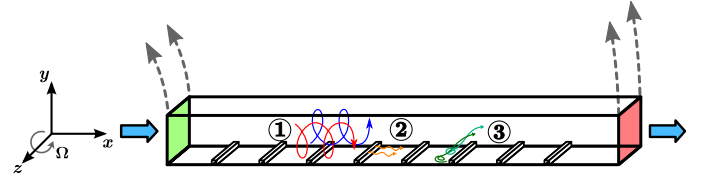


**FIGURE 2.** NUMERICAL DOMAIN: CHANNEL WITH 8 RIBS, FLUID INLET IN GREEN, FLUID OUTLET IN RED

Fig. 2. The domain is discretized by a hybrid mesh consisting of tetrahedral cells in the main channel and a single prismatic layer on all walls. This methodology has been chosen from previous work [4] where mesh convergence analysis has been performed for another cooling channel study. Figure 3 shows a sample of the resulting mesh leading to 3.6 million cells.

The position of the different boundary conditions of the domain are portrayed on Fig. 2. In green, the inlet boundary condition reproduces air inlet mean velocity profile measured with PIV on plane  $pa$  and  $pb$  as shown on Fig. 1(b) and for a bulk velocity of 2.8 m/s and a temperature of 293 K. Fluctuations have been measured in the PIV (1% in the core flow, 3% near the wall), but here only mean velocity has been imposed: no major influence have been observed on the main flow and in the PIV measurement zone. Outlet (in red) imposes ambient static pressure (ie. 1013 hPa) with the NSCBC conditions [27]. All others (white) surfaces are set with an adiabatic no-slip condition. To satisfy a compromise between a wall-resolved LES computation and an industrial requirement of a not too expensive computational cost, the global mean  $y^+$  is equal to 4.4 in the region of interest: i.e. around the ribs delimited by the dashed rectangle on Fig. 3, and as confirmed by the histogram of  $y^+$  presented on Fig. 4.  $y^+$  less than 4 is commonly accepted by the LES modeling community as being an acceptable criteria for fully turbulent boundary layers and provided that the SGS model degenerates in these regions according to known theoretical behaviors. Still in the framework of the chosen compromise, overall all points have a mean  $y^+$  which varies in time in the computation that is under 9, i.e. mainly in the viscous sublayer. With the present hybrid mesh,  $x^+$  and  $z^+$  are around  $5y^+$ . Opposite smooth wall has been tested with same and lightly coarser wall resolution (mean  $y^+$  is equal to 6), leading to similar results. Coarser wall has therefore been used for computational efficiency.

#### Methodology for the rotating case

To set numerically a rotating channel, classical Arbitrary Lagrangian Eulerian (ALE) description given by Hirt et al. [28] is used and implemented in the AVBP solver. This approach allows the mesh nodes to be moved in some arbitrary fashion regardless of the particle motions. ALE method has already been validated in the AVBP solver in previous works on piston and rocket en-



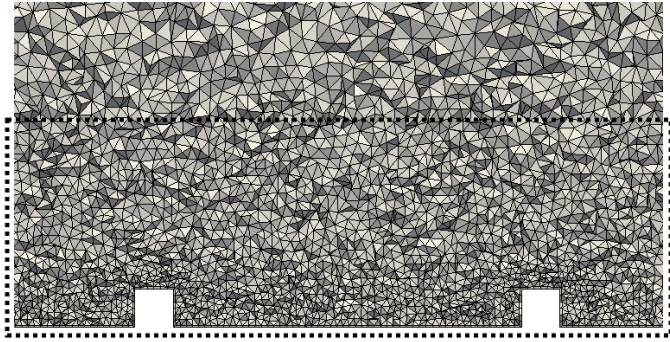


**FIGURE 3.** MESH SAMPLE OF THE DISCRETIZED CHANNEL: ZOOM ON TWO RIBS IN THE SYMMETRY PLANE

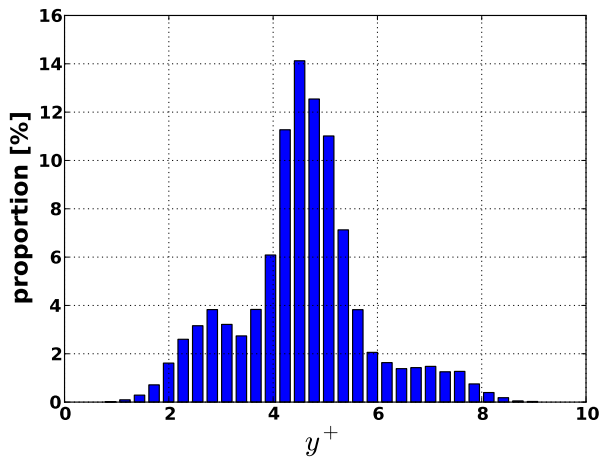


**FIGURE 4.**  $y^+$  DISTRIBUTION ON THE WALL AROUND THE RIBS

gines [29, 30]. In our case, mesh movement is chosen to be a constant ribbed-wall normal rotation, around the  $z$  axis of Fig. 2. To avoid pressure oscillations due to transitional step between stationary and rotating state, a smooth symmetric function with zero derivatives at each extremity is applied before reaching the final constant rotation speed of 13.5 rad/s. Validation test cases have been performed to ensure the correct influence of the rotation on the flow based on the Coriolis and centrifugal forces. Note however that rotation being imposed and fully known and at a constant speed, no specific issue is present in terms of ALE procedure that is 2nd order in time and space hence exact in this case. The only advantage is that the flow is due to ALE solved in a fixed frame of reference the geometry being in motion. The disadvantage is in reconstructing the field in the rotating frame whenever needed for post-processing for example.

Note also that ALE require additional computational time, in the present case 7 000 hours for a flow through time instead of 5 700 for the stationary case on a HP AMD MagnyCours cluster.

## MEAN RESULTS

### Mean velocity comparison

Figures 5 and 6 present contours and streamlines of mean velocity respectively from LES and the PIV measurements for destabilizing, stabilizing and non-rotating cases in the symmetry plane of the duct. One can see that for the reference non-rotating case, Fig. 5(b) and Fig. 6(b), mean velocity results match very well the PIV measurements. This is consistent with previous results [4] on a non-rotating channel with the same numerical procedure. For the stabilizing case, Fig. 5(c) and Fig. 6(c), LES leads again to a very good agreement with PIV, predicting the correct large recirculation bubble extension from  $x/h = 4$  for the non-rotating case to  $x/h = 6 - 6.5$ . These observations are supported looking at Fig 7(b) and (c) where streamwise velocity profiles fit experimental data at every location.

Differences appear for the destabilizing rotation case for which Fig. 5(a) and Fig. 6(a) are to be compared. Even if flow reattachment is correctly predicted at  $x/h = 4$ , i.e. no difference with the non-rotating case, flow velocity magnitudes in the channel are clearly underestimated. These conclusions appear also on Fig 7(a) where LES matches PIV at all locations near the wall under  $y/h = 0.25$  but move away from measurements with increasing discrepancies further of the wall. A brief observation is that mesh requirements dedicated to non-rotating cases may not be sufficient for destabilizing cases where velocity gradients and flow curvature are present, two characteristics that are reduced around the rib in the case of stabilizing rotation.

### Fluctuating velocity

Going further into the flow analysis, one can look at velocity fluctuations in the streamwise and wall-normal direction, on Fig. 8 and Fig. 9 respectively. The first obvious conclusion coming from such comparisons is that LES over-predict fluctuating velocity for all cases, except for the wall-normal component for the stabilizing rotation. Overestimations go from 15% to 35% for the streamwise fluctuating velocity and from 30% to 40% for the wall normal fluctuation. Despite limitations, LES does capture effects of rotation on the flow with increasing/decreasing turbulence caused by destabilizing/stabilizing rotation. The maps of turbulence contours and thus turbulence maxima are also correctly located, i.e. in a wake in the shear layer behind the rib for the streamwise fluctuations. Note that one maximum is located above the rib for the non-rotating case, and two maxima appear above the rib and in zones in the wake between  $x/h = 2$  and 3 where flow brought by Coriolis forces reactivates mixing in the destabilizing rotation. The result for stabilizing rotation is a con-

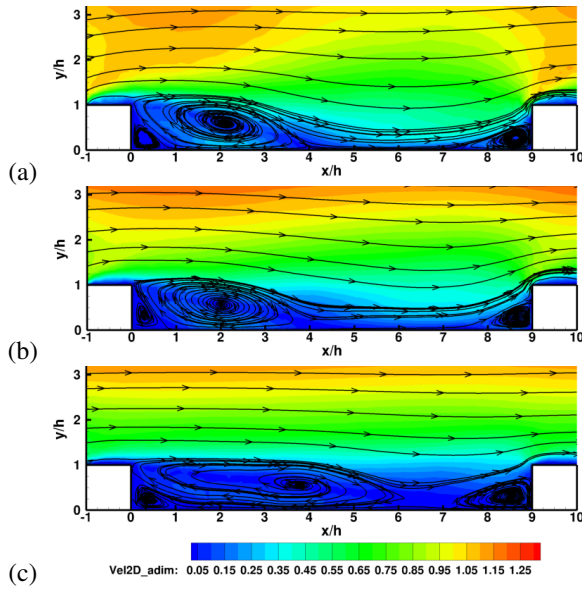


**FIGURE 5.** TWO DIMENSIONAL CONTOURS AND STREAM-LINES OF THE LES MEAN VELOCITY IN THE SYMMETRY PLANE: DESTABILIZING ROTATION (a), NON-ROTATING CASE (b) AND STABILIZING ROTATION (c)

stant stripe joining both ribs between  $y/h = 1$  and 2. Maxima of wall normal fluctuations are well predicted for each case in at  $x/h$  location corresponding to a part of the large recirculation bubble mean boundary with strong curvature. Possible reasons proposed for these results is the mesh resolution: grid spacing seems to be too coarse for simulating small fluctuations, leading to the prediction of large coherent structures behind the ribs and so higher velocity fluctuations. However, these structures are then correctly convected since mean flow is well predicted.

## UNSTEADY RESULTS COMPARISON

Time-resolved PIV measurements carried out by Coletti [31] on this configuration for the rotating channels allow to performed deeper unsteady flow analysis. One possibilities is presented on Fig. 10 with space time-domains for the non-rotating case. This 3D view allows to track vortices in space and time thanks to the criterion of swirling strength, introduced by Zhou [32]. Figure 10 portrays iso-contours of  $\lambda ci$ , the imaginary part of the locally calculated complex conjugate eigenvalues of the velocity gradient. A positive value of this criterion is then a measure of fluid rotation excluding shear. In the PIV data, only two components of the velocity have been measured (streamwise and wall-normal), so only vortical structures with a rotation axis normal to the symmetry plane are accessible. LES data reduction has been performed to make visualization comparable. Vortices plotted on Fig. 10 are finally colored by vorticity: positive vorticity is in

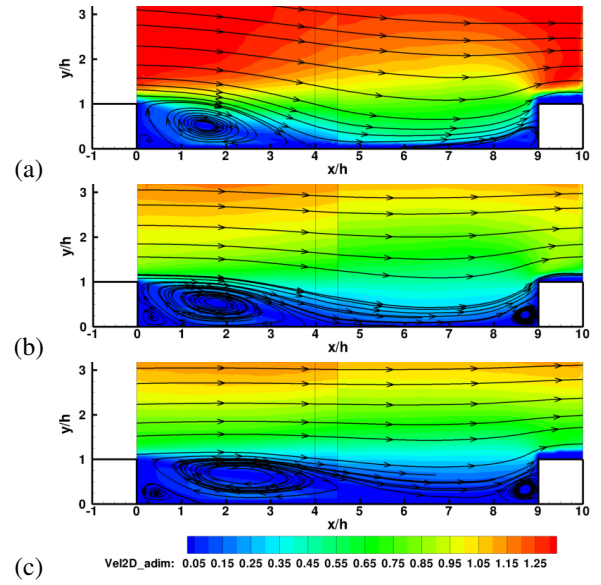


**FIGURE 6.** TWO DIMENSIONAL CONTOURS AND STREAM-LINES OF THE PIV MEAN VELOCITY IN THE SYMMETRY PLANE: DESTABILIZING ROTATION (a), NON-ROTATING CASE (b) AND STABILIZING ROTATION (c)

red (i.e. rotating counter-clockwise in the XY plane), and negative vorticity is in blue (i.e. rotating clockwise). LES equivalent quantities are shown on Fig. 11 for the same non-rotating case. Note that in Fig. 10, two space-time domains are presented since both PIV windows are not time-correlated. For LES one simple volume covers the entire space between rib 6 and rib 7. It has also to be noticed that the LES non-dimension time  $T \cdot U_0/h$  runs only to 25 whereas PIV goes to 40. Comparing both space-time volumes for non-rotating case where an isosurface of  $\lambda ci = 10\%$  of the maximum value of the dataset is shown, one can see a similar density and orientation of the vortices. A large majority of negative vortical structures is present in the domain because of the mean shear of the flow behind the rib. Clockwise vortices are more present after  $x/h = 4$  where flow reattaches and so can be generated by shear layer flapping. Coletti [31] also proposes as explanation the convection of streamwise structures oriented in the quasi-spanwise direction by the mean flow. As in the experiment, the more one looks at decreasing  $y/h$ , the more vortices seem to be aligned with the time axis, pointing at the same time fast-moving structures carried by the mean flow and stationary vortices near the wall. One can also notice that the diameter of the structures is larger in LES than in the experiment partly confirming the excess in RMS reported earlier.

Keeping the same level of  $\lambda ci$  and applying it to the stabilizing and destabilizing cases, one obtains respectively Fig. 12 and Fig. 13. The lower fluctuating velocity observed in Fig. 8 and Fig. 9 can be here linked to the lower number of high vorticity



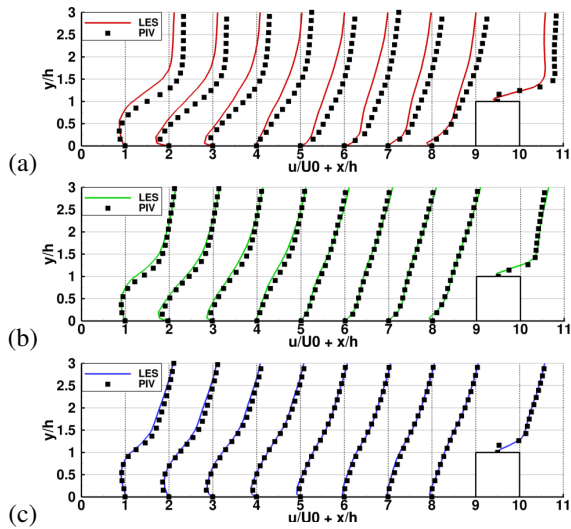


**FIGURE 7.** COMPARISON OF LES (LINES) AND PIV (SYMBOLS) MEAN VELOCITY PROFILES IN THE SYMMETRY PLANE: DESTABILIZING ROTATION (a), NON-ROTATING CASE (b) AND STABILIZING ROTATION (c)

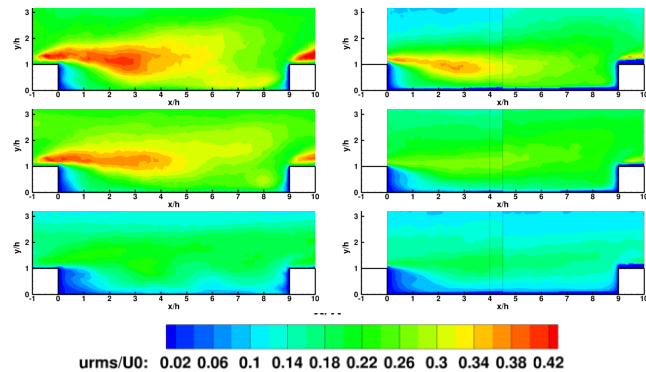


**FIGURE 8.** TWO DIMENSIONAL CONTOURS OF STREAM-WISE FLUCTUATING VELOCITY IN THE SYMMETRY PLANE: LES (LEFT COLUMN) AND PIV (RIGHT COLUMN) WITH DESTABILIZING ROTATION (FIRST ROW), NON-ROTATING CASE (MIDDLE ROW) AND STABILIZING ROTATION (LAST ROW)

structures in comparison to Fig. 11. Vortices have also a lower advection velocity since they are more parallel to the time axis compared to what is observed for the rotating case. Looking at the destabilizing domain, Fig. 13, one does not observe obvious differences with the non-rotating case. The only thing noticed is a lower advection velocity difference between mean flow and near wall structures since the majority of vortices are aligned in the same direction. This is consistent with Fig. 7(a) where higher mean near-wall velocity is predicted in comparison with the non-

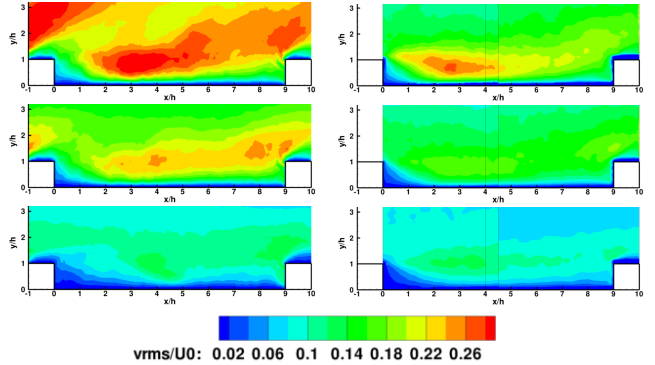


**FIGURE 9.** TWO DIMENSIONAL CONTOURS OF WALL-NORMAL FLUCTUATING VELOCITY IN THE SYMMETRY PLANE: LES (LEFT COLUMN) AND PIV (RIGHT COLUMN) WITH DESTABILIZING ROTATION (FIRST ROW), NON-ROTATING CASE (MIDDLE ROW) AND STABILIZING ROTATION (LAST ROW)

rotating case. In the experimental data (not presented here for the destabilizing case), vortical structures appear to have a shorter life time than LES. This may also be a consequence of the lack of resolution that is designed for non-rotating flows.

## CONCLUSIONS

LES have been carried out on stationary and clockwise/counter-clockwise rotating cooling channels. Comparisons with time-averaged and time-resolved PIV data yield the following observations:

- The methodology proposed by [4] for LES of non-rotating cooling channels has been validated to predict the correct mean flow and unsteady structures behavior for the non rotating case and for the rotating case implying stabilizing flow around the ribs.
- For destabilizing cases, grid resolution needs to be verified as turbulence intensity level show more difference than anticipated. Despite this observation the unsteady large scale turbulence evolution is well predict by LES. Neglecting rotation effect on SGS model or the lack of mesh resolution are pointed out as possible reasons of such discrepancies.
- These different turbulent rates observed experimentally and numerically on opposite faces in rotating channel would encourage new design of cooling channel with uneven repartition between leading and trailing side to optimize heat transfer.

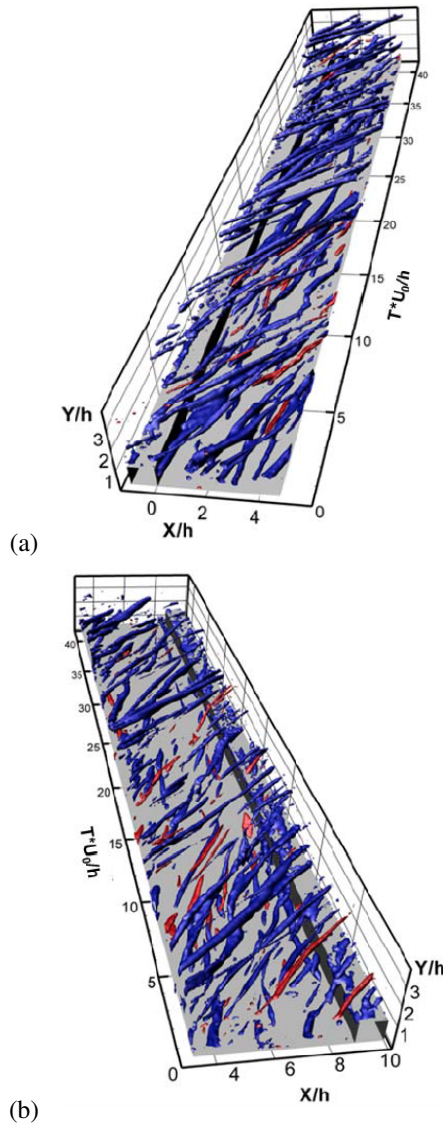


**FIGURE 10.** SPANWISE VORTICES TRAVELLING IN SPACE-TIME, VISUALIZED BY MEANS OF ISO-CONTOURS OF POSITIVE SWIRLING STRENGTH, IN THE NON ROTATING CASE. TOP: DOWNSTREAM OF RIB 6 (POSITION a); BOTTOM: UPSTREAM OF RIB 7 (POSITION b).

#### ACKNOWLEDGMENT

The financial support of Safran Turbomeca and ANRT for the CIFRE Ph.D is gratefully acknowledged. Many thanks to the VKI team for the experimental data that are used in this paper, especially to Filippo Coletti for helpful discussions about flow physics. The work presented has also largely benefited from CERFACS internal and GENCI-CINES computing facilities (under the project fac 2554).

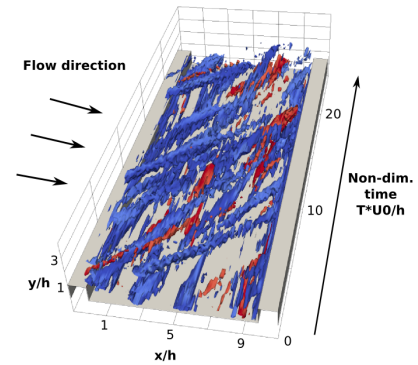


**FIGURE 11.** SPANWISE VORTICES TRAVELLING IN SPACE-TIME BETWEEN RIB 6 AND RIB 7, VISUALIZED BY MEANS OF ISO-CONTOURS OF POSITIVE SWIRLING STRENGTH, IN THE NON ROTATING CASE

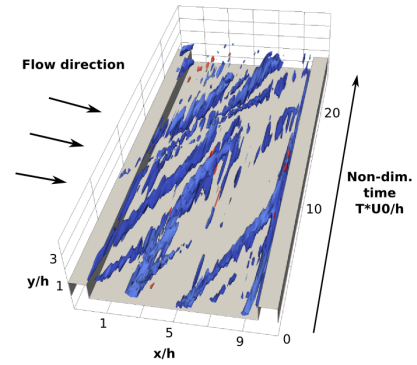


**FIGURE 12.** SPANWISE VORTICES TRAVELLING IN SPACE-TIME BETWEEN RIB 6 AND RIB 7, VISUALIZED BY MEANS OF ISO-CONTOURS OF POSITIVE SWIRLING STRENGTH, IN THE STABILIZING CASE

#### REFERENCES

- [1] Phibel, R., Laroche, E., Casarsa, L., and Arts, T., 2005. "Numerical investigation on flow and heat transfer in a rib-roughened channel with high blockage ratio". In 6th European Conference on Turbomachinery: Fluid Dynamics and Thermodynamics.
- [2] Sleiti, A. K., and Kapat, J. S., 2006. "Comparison between EVM and RSM turbulence models in predicting flow and heat transfer in rib-roughened channels". *Journal of Turbulence*, p. N29.
- [3] Sewall, E. A., Tafti, D. K., Graham, A. B., and Thole, K. A., 2006. "Experimental validation of large eddy simulations of flow and heat transfer in a stationary ribbed duct". *International Journal of Heat and Fluid Flow*, 27(2), Apr., pp. 243–258.

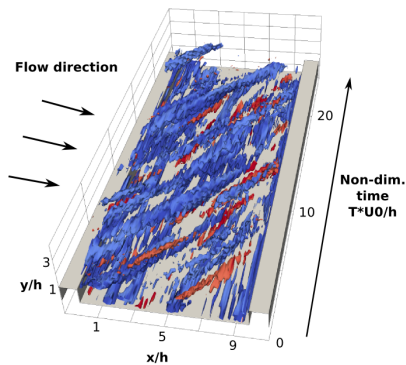


**FIGURE 13.** SPANWISE VORTICES TRAVELLING IN SPACE-TIME BETWEEN RIB 6 AND RIB 7, VISUALIZED BY MEANS OF ISO-CONTOURS OF POSITIVE SWIRLING STRENGTH, IN THE DESTABILIZING CASE

- [4] Fransen, R., Gourdain, N., and Gicquel, L., 2012. "Steady and unsteady modeling for heat transfer predictions of high pressure turbine blade internal cooling". In ASME Turbo Expo 2012, A. GT2012-69482, ed.
- [5] Tafti, D., 2005. "Evaluating the role of subgrid stress modeling in a ribbed duct for the internal cooling of turbine blades". *International Journal of Heat and Fluid Flow*, **26**(1), Feb., pp. 92–104.
- [6] Ahn, J., and Lee, J. S., 2010. "Large eddy simulation of flow and heat transfer in a channel with a detached rib array". *International Journal of Heat and Mass Transfer*, **53**(13), Jan., pp. 445–452.
- [7] Bradshaw, P., 1969. "The analogy between streamline curvature and buoyancy in turbulent shear flow". *Journal of Fluid Mechanics*, **36**(01), pp. 177–191.
- [8] Chang, S. W., Liou, T.-M., and Po, Y., 2010. "Coriolis and rotating buoyancy effect on detailed heat transfer distributions in a two-pass square channel roughened by 45 ribs at high rotation numbers". *International Journal of Heat and Mass Transfer*, **53**(7-8), Mar., pp. 1349–1363.
- [9] Sagaut, P., 2000. *Large Eddy Simulation for incompressible flows*. Scientific computation series. Springer-Verlag.
- [10] Pope, S. B., 2000. *Turbulent flows*. Cambridge University Press.
- [11] Poinot, T., and Veynante, D., 2005. *Theoretical and Numerical Combustion*. R.T. Edwards, 2nd edition.
- [12] Smagorinsky, J., 1963. "General circulation experiments with the primitive equations: 1. the basic experiment.". *Mon. Weather Rev.*, **91**, pp. 99–164.
- [13] Moin, P., Squires, K. D., Cabot, W., and Lee, S., 1991. "A dynamic subgrid-scale model for compressible turbulence and scalar transport". *Phys. Fluids*, **A 3**(11), pp. 2746–2757.
- [14] Ducros, F., Comte, P., and Lesieur, M., 1996. "Large-eddy simulation of transition to turbulence in a boundary layer developing spatially over a flat plate". *J. Fluid Mech.*, **326**, pp. 1–36.
- [15] Comte, P., 1996. *New tools in turbulence modelling. vortices in incompressible les and non-trivial geometries*. Course of Ecole de Physique des Houches. Springer-Verlag, France.
- [16] Speziale, C. G., 1985. "Galilean invariance of subgrid-scale stress models in the large-eddy simulation of turbulence". *J. Fluid Mech.*, **156**, pp. 55–62.
- [17] Kobayashi, H., 2005. "The subgrid-scale models based on coherent structures for rotating homogeneous turbulence and turbulent channel flow". *Physics of Fluids*, **17**(4), Mar., pp. 045104–045104–12.
- [18] Tsubokura, M., Kobayashi, T., Taniguchi, N., and Kogaki, T., 1999. "Subgrid scale modeling for the turbulence in rotating reference frames". *Journal of Wind Engineering and Industrial Aerodynamics*, **81**(13), May, pp. 361–375.
- [19] Nicoud, F., and Ducros, F., 1999. "Subgrid-scale stress modelling based on the square of the velocity gradient". *Flow, Turb. and Combustion*, **62**(3), pp. 183–200.
- [20] Mendez, S., and Nicoud, F., 2008. "Large-eddy simulation of a bi-periodic turbulent flow with effusion". *J. Fluid Mech.*, **598**, pp. 27–65.
- [21] Schöenfeld, T., and Poinot, T., 1999. "Influence of boundary conditions in LES of premixed combustion instabilities". In *Annual Research Briefs*. Center for Turbulence Research, NASA Ames/Stanford Univ., pp. 73–84.
- [22] Colin, O., and Rudgyard, M., 2000. "Development of high-order taylor-galerkin schemes for unsteady calculations". *J. Comput. Phys.*, **162**(2), pp. 338–371.
- [23] Donea, J., 1984. "Taylor-galerkin method for convective transport problems". *Int. J. Numer. Meth. Fluids*, **20**(1), pp. 101–119.
- [24] Lamarque, N., 2007. "Schémas numériques et conditions limites pour la simulation aux grandes échelles de la combustion diphasique dans les foyers d'hélicoptère". Phd thesis, INP Toulouse.
- [25] Di Sante, A., Theunissen, R., and Van den Braembussche, R. A., 2007. "A new facility for time-resolved PIV measurements in rotating channels". *Experiments in Fluids*, **44**(2), Sept., pp. 179–188.
- [26] Coletti, F., Maurer, T., Arts, T., and Di Sante, A., 2011. "Flow field investigation in rotating rib-roughened channel by means of particle image velocimetry". *Experiments in Fluids*, **52**(4), Sept., pp. 1043–1061.
- [27] Poinot, T., and Lele, S., 1992. "Boundary conditions for direct simulations of compressible viscous flows". *J. Comput. Phys.*, **101**(1), pp. 104–129.
- [28] Hirt, C. W., Amsden, A., and Cook, J. L., 1974. "An arbitrary lagrangian-eulerian computing method for all flow

- speeds”. *J. Comput. Phys.* , **131**(4), pp. 371–385.
- [29] Granet, V., 2011. “La simulation aux grandes echelles : un outil pour la prédiction des variabilités cycliques dans les moteurs á allumage commandé ?”. PhD thesis, Université de Toulouse.
  - [30] Richard, J., 2012. “Développement d’une chaine de calcul pour les interactions fluide-structure et application aux instabilités aéro-acoustiques d’un moteur á propergol solide”. PhD thesis, Université de Montpellier II.
  - [31] Coletti, F., Cresci, I., and Arts, T., 2012. “Time-resolved piv measurements of turbulent flow in rotating rib-roughened channel with coriolis and buoyancy forces”. In *ASME Turbo Expo 2012*, A. GT2012-69406, ed.
  - [32] Zhou, J., Adrian, R. J., Balachandar, S., and Kendall, T. M., 1999. “Mechanisms for generating coherent packets of hairpin vortices in channel flow”. *J. Fluid Mech.* , **387**, pp. 353–396.

